Volume Imaging Lidar Observations and Large-eddy Simulations of Convective Internal Boundary Layers

by

Shane D. Mayor

A dissertation submitted in partial fulfillment of the
requirements for the degree of

Doctor of Philosophy
(Atmospheric and Oceanic Sciences)

at the

University of Wisconsin – Madison

2001

Abstract

Volume imaging lidar data collected from a site on the western shore of Lake Michigan during the Lake-Induced Convection Experiment provide new observations of convective internal boundary layers and are used to test large-eddy simulations (LESs). Two-dimensional correlation functions of the aerosol backscattering data on horizontal planes reveal the mean motion, orientation, size, spacing and lifetime of the aerosol structures as a function of altitude and offshore distance. Observations show the flow accelerating as a result of the increase in convective mixing and decrease in surface roughness. Although individual lidar backscatter images show remarkable detail of the eddy structure, the averaged backscatter is very homogeneous and does not indicate a well-defined edge to the internal boundary layer despite the tremendous increase in surface heat and moisture flux over the lake.

LESs of January 13 were performed using the University of Wisconsin's nonhydrostatic scalable model. To simulate the horizontal homogeneity of turbulence over the land and the inhomogeneity over the lake, a perturbation recycling method was added to the inflow boundary condition. Optical aerosol scattering was estimated from the model output to enable comparison with the lidar data. The simulated lidar backscattering is used for computing correlation functions that can be compared with those from the observed backscatter data. Comparisons show that the LES (1) tends to have smaller and more elongated convective structures at the smallest scales simulated, (2) tends to produce more linear structures that are aligned with the mean wind direction, and (3) fails to simulate the apparent organization of structures by gravity waves. The absence of strong gravity waves in the simulations is probably caused by the limited depth of the model domain and limitations of the lateral boundary conditions.

Acknowledgements

Special thanks goes to Ed Eloranta for inviting and giving me the opportunity to earn a Ph.D. at UW and insisting that I work with both lidar and LES. Special thanks also to Greg Tripoli for his patient help with learning how to use his model and his enthusiastic support for trying so many LES experiments over the years. John Young has been a terriffic coach throughout the experience. Thanks to committee members John Norman, Pao Wang, Patrick Farrell and Leslie Smith for helpful discussions. Thanks also to Philippe Spalart for his help with the perturbation recycler.

The Lake-ICE VIL dataset was made possible through the hard work of Patrick Ponsardin, Ralph Kuehn, and Jim Hedrick. Genie Tubal helped with the initial data processing. Joe Garcia bailed me out of countless computer problems and never complained when I asked for help. Thanks also to the SSEC technical computing staff, the AOS staff, Pete Pokerandt, and lidar comrades Igor Razenkov and Bob Holz. Many colleagues at NCAR and NOAA supported me in one way or another including Erik Miller, Peter Sullivan, Don Lenschow, Chin-Hoh Moeng, Larry Mahrt, Janet Intrieri and Mike Hardesty.

I enjoyed many friendships in Madison including those with Susan Jensen, Tom Daniels, Jim Olsen, Kurt Brueske, Kathy Webster, Tracy Twine, Ed Mierkiewicz, and Alejandro Dussaillant. Friends in other cities who stayed in close contact include Nitin Gautam, Steven Mang, Christoph Senff, Joyce Jay, and Ron and Nancy Schwiesow. Special thanks to Colin Mcleod for editing during the last month.

I thank my Mother, Father and sister, Kelly, for their constant support and encouragement. The *biggest* thanks goes to Heather McCullough for her love and patience every day of the last 2.285 years. Her terrific sense of humor and smiles make the best memories.

Contents

List of Figures

List of Tables

Chapter 1

Introduction

1.1 Motivation

The turbulent atmospheric boundary layer (ABL) is driven by the surface of the earth. Heat, moisture, momentum, and trace gases are added to or removed from the atmosphere at its lower boundary. These fluxes directly influence weather and climate. Therefore, accurate simulation of the boundary layer is an important skill, whether it be a parameterization in a general circulation model or the explicit simulation of eddies in a fine resolution model.

This dissertation presents rapid-scanning aerosol-backscatter lidar observations of ABL structure and shows how they can be used to test numerical simulations of inhomogeneous ABLs. The simulations employ simple but effective boundary conditions that enable a realistic simulation of ABLs that experience a single, abrupt, spatial change in at least one surface forcing. *The primary objective of the research is to demonstrate the usefulness of volume imaging lidar for resolving aerosol scattering structure and motion in the atmospheric boundary layer and using these measurements to test the large-eddy simulations.* A secondary objective of this research is to use the observations and simulations in concert to improve characterizations of convective internal boundary layer (CIBL) structure.

The motivation to collect the lidar data was to obtain four-dimensional (4-D, space and time) measurements of CIBL structure that could be used to test large-eddy simulations (LESs) of CIBLs. Unlike homogeneous convective boundary layers (CBLs), which develops *temporally*, a CIBL develops *spatially* (i.e. with increasing downstream distance). It was hypothesized by experiment planners that the growth of the convective boundary layer could be observed as a function of downstream distance with the spatial imaging capability of the lidar. This hypothesis was formed with the presumption that the boundary layer upwind of the lake would be stable, and, therefore, not turbulent during the intensive operation periods of the experiment.

The field campaign, *Lake Induced Convection Experiment* (Lake-ICE, Kristovich et al. 2000), took place during the winter of 1997-98 and studied the entire convective boundary layer (CBL) over the approximately 100 to 140 km wide Lake Michigan

during cold air outbreaks. The deployment of the UW lidar on the upwind shore was just one part of a much larger project which included research aircraft, radars, and other surface-based observing systems.

The remainder of this chapter will be devoted to describing at an introductory level the main tools and concepts used in the research and the plan for the remainder of the dissertation.

1.2 Lidar

Lidar is an acronym for Light Detection and Ranging. Lidars are the optical counterparts of radars (an acronym for Radio Detection and Ranging). Both lidars and radars are *active* remote sensors because they transmit pulses of energy in order to detect properties of the atmosphere at a distance. Passive remote sensors such as interferometers are able to measure properties of the atmosphere only by receiving information.

Lidars transmit pulses of laser light and detect and record backscattered[1] light from molecules and aerosol particles in the atmosphere. This basic measurement capability of backscatter intensity is common to all lidars. However, some lidars offer additional measurement capabilities such as the ability to detect frequency shift, depolarization, and backscatter intensity from multiple wavelengths.

For example, lidars that detect the frequency shift of the backscattered light for the purpose of measuring the wind are called Doppler lidars. Lidars which can detect changes in the polarization of the backscatter are able to distinguish between spherical (droplets) and non-spherical (i.e. ice-crystals) particles (Sassen, 1991). Lidars that transmit two wavelengths, one of which is strongly absorbed by the gas of interest (water vapor or ozone for example), are called differential absorption lidars (DIALs) (Wulfmeyer and Bosenberg, 1998). Lidars which are capable of measuring molecular and aerosol scattering simultaneously are called high spectral resolution lidars (HSRLs) and provide absolutely calibrated backscatter intensity information (Grund and Eloranta, 1991). There are also lidars which transmit at one wavelength and receive at several wavelengths in order to detect flouresence and Raman signals from gases of interest (Grant, 1991). These advanced capabilities provide measurements of important atmospheric properties but come with increased technical complexity.

The University of Wisconsin's Volume Imaging lidar (UW-VIL) is relatively simple when compared to the above types of lidars. It only transmits and detects one wavelength. It does not measure frequency shift or depolarization of the backscatter. It does not measure molecular scattering and cannot provide any information regarding absolute concentration of aerosol or optical scattering intensity. It only provides relative[2] backscattering. Yet, it is a unique lidar because of its powerful laser, large

[1]When a ray of light hits a small particle, photons are scattered in all directions. The photons that are scattered back toward the source of light are *backscattered* photons.

[2]Relative because the measurement is uncalibrated. It only provides backscatter intensity information with no units.

receiving optics, a fast beam-steering unit, and a log amplifier. The configuration of the VIL used in Lake-ICE allowed us to record backscatter intensity at 15-m intervals out to 18-km ranges to map the 4-D (space and time) structure of the boundary layer.

1.3 Large-eddy simulation

Numerical simulation of atmospheric motion enjoys success in two broad categories: *pattern predictibility* and *statistical results from pattern forecasts* (Stull, 1988). As an example of the first category, weather prediction models are initialized with the most important flow features, synoptic-scale disturbances which are typically 1000's of km wide, in the simulation being highly resolved from a relatively dense network of observations. The distance between the observations over land is typically on the order of 100 km and weather forecast models also use horizontal grid-spacing on the order of 100 km. Therefore the positions, shapes and intensities of cyclones and anticyclones are described quite accurately at the beginning (the *initialization*) of the simulation. As the model runs, the virtual weather systems move and evolve according to the equations governing fluid motion. The forecast simulation lasts for approximately the length of one Lagrangian lifetime of these features (48-96 hours) which have the largest impact on the weather forecast. The forecast can be verified by comparing the positions, shapes and intensities of the synoptic systems with a new set of observations from the same network that was used to initialize the model. The accuracy of the prediction is determined by how well the forecast pattern matches the observed pattern at specific times.

In contrast, LES and climate models fall into the second category. They are initialized without any knowledge of the positions, shapes and intensities of the important turbulent flow features which the model is intended to simulate. These perturbations develop from instabilities in the model's horizontally homogeneous initial condition, which is representative of the mean atmospheric properties of the local environment. The time to develop the turbulent eddies is often called *spin-up*. Only after mature, or fully-developed, turbulence is created (requiring the simulation of many eddy lifetimes) can the solution be verified in terms of *flow statistics*.

Although rapid-scanning lidars are capable of making 3D measurements with LES-like resolution, lidars are still not able to initialize LESs because LESs require a complete set of velocity and thermodynamic information with spatial resolution and precision beyond the capability of present lidars. This dissertation will show, however, that volumetric lidar backscatter data can be used to check the LES solutions for spatial and temporal statistics.

LESs are four-dimensional (time and space) explicit simulations of eddies that comprise turbulence. The phrase *large-eddy* is used because the large and medium sized eddies in the modeled flow are resolved while the effects of the smallest eddies are parameterized. The gridpoint spacing of an atmospheric LES is typically on the order of 100 m and the domains several kilometers wide. Because the largest eddies, which are responsible for most of the turbulent flux, are explicitly resolved, most of

the turbulent flux is explicitly simulated in an LES (as oppopsed to fluxes which are often parameterized in models with larger grid-spacing).

Turbulent flow consists of eddies of all different sizes interacting simultaneously. The largest eddies of the turbulent flow exist in the *energy containing* range of the spectrum where turbulent energy is generated. The large eddies interact nonlinearly and produce smaller eddies in the *inertial subrange* part of the spectrum. Kinetic energy is neither created nor destroyed in the inertial subrange and the spectrum in this region holds the well-known frequency$^{-5/3}$ power law dependence. In the inertial subrange, energy only cascades to smaller scales where is it eventually received by the *dissipative range*. Here, viscous forces convert the inertial energy into thermal energy. Since the LES is not capable of resolving the energy cascade at the small-scale end of the inertial subrange or the energy dissipation range, a subgrid scale turbulence parameterization must be used to receive the resolved downscale transport of kinetic energy.

Typically, the largest eddies in a boundary layer are on the order of the boundary layer depth and LES grid-spacing is approximately one order magnitude smaller than the boundary layer depth. Because the most important (flux carrying) eddies are resolved, LESs can be very useful tools for studying boundary layers and developing flux parameterizations for global climate and weather forecast models (Ayotte et al., 1996). The high resolution 4-D LES results can be used to compute fluxes with sampling errors that are much smaller than those made from in situ measurements.

LESs, however, are only viable if we have confidence in their solutions. Inaccuracies may occur because of code bugs, inappropriate boundary conditions, numerical schemes or parameterizations, and an infinite number of influences present in the real world but absent in the simulation. Traditional tests of LESs include computing vertical profiles of higher order moments, fluxes of heat and momentum, and velocity power spectra (for example, see Nieuwstadt et al. 1993 and Andren et al. 1994). These statistics can be compared with those from in situ sensors but suffer from large sampling errors. Unfortunately, in situ sensors are not capable of measuring the 4-D structure of turbulence. At best they provide 2-D (time versus one spatial dimension) information (for example, a series of anemometers on a tower.) Therefore, high resolution 4-D measurements are needed to test the LESs ability to accurately simulate the organization of convection such as linear and cellular boundary layer circulations or surface layer streaks in the shear-driven mixed layer. Although the VIL does not provide both wind and thermodynamic data, it does provide information on the structure of aerosol backscatter which is strongly related to the former variables.

Because of the difficulty in making three-dimensional descriptions of turbulence for dynamic and thermodynamic quantities simultaneously, most LESs employ *periodic*, or *cyclic*, lateral boundary conditions. This method of connecting opposing sides of the domain effectively makes the domain infinitely wide because it removes lateral boundaries but limits the largest possible length scale which can be simulated. Boundary conditions are the required specification of all predictive variables on the edges of

the LES grid. To run a periodic simulation, the variables on one side of the domain are duplicated on the opposing side. This commonly-used method passes the flow back into the model domain on the opposing side, thus eliminating the requirement for an independent description of turbulence on the edges. Unfortunately, this style of simulation can require substantial computer time to reach mature turbulence because the eddies develop upward from the surface. Furthermore, models using lateral periodic boundaries either require unreasonably large domain sizes or very short sampling times in order to simulate mesoscale internal boundary layers. This dilemma and a solution will be discussed more in section 1.5.

LES is a well-established technique pioneered by Deardorff (1972; 1974b; 1974a). Since then several LES codes (Mason, 1989; Moeng, 1984; Nieuwstadt and Brost, 1986; Schmidt and Schumann, 1989) have been developed and used for many atmospheric studies. There are also many uses of LES in the engineering community to assist designers (Moin and Lin, 1997) . In the atmospheric community, Sommeria (1976) extended Deardorff's work by adding moisture and then used the model to simulate the cumulus capped trade-wind boundary layer. Lamb (1978) used Deardorff's LES results to simulate the dispersion of nonbuoyant particles released from an elevated point source. Moeng (1984) wrote an LES code which uses spectral solutions in the horizontal thereby eliminating possible truncation error accumulation. Wyngaard and Brost (1984) used LES to study top-down-bottom-up diffusion. Later, more complex boundary layer types were examined including those forced by a combination of buoyancy and shear (Moeng and Sullivan, 1994; Khanna and Brasseur, 1998) and stratocumulus-capped (Moeng et al., 1996). Some additional important studies that used LES include Schmidt and Schumann (1989) and Mason (1989) on the structure of the convective boundary layer, Lin et al. (1996; 1997) and Lin (1999) on coherent structures in neutral and convective boundary layers, and Coleman et al. (1990; 1992) and Andren et al. (1994) on Ekman boundary layers.

More recently, perhaps because of the availability of computer power, many investigators are using several model codes that were originally designed for mesoscale simulations with grid-spacing near LES. As the interest in local predictions increase, the requirement for LES-like grid-spacing will increase. Therefore, as more computer power becomes available, it appears that LES will continue to become more popular.

1.4 Internal Boundary Layers

Internal boundary layers (IBLs) are the result of horizontal advection across a discontinuity in some surface property (Garratt, 1990) that influences the air such as roughness, temperature or moisture. For a parcel of air moving across the discontinuity, the change in surface property may lead to a sudden change in surface flux. In most of the literature discussing IBLs, the surface properties are homogeneous on either side of the discontinuity. When the surface heat flux changes, a *thermal* IBL forms, and when the roughness length changes, a *momentum* IBL forms. When the surface sensible heat flux *increases* across the discontinuity, the new boundary layer

is called a CIBL. The observations and simulations presented in this dissertation are a combination of intense convective and momentum IBLs because of the extreme increase in surface heat flux and the decrease in surface roughness.

IBLs can also be classified as *mesoscale* or *local* (Mahrt, 2000). Mesoscale BLs are associated with large-scale surface features, such as onshore or offshore flow, and eventually the IBL engulfs the entire pre-existing boundary layer. Such is the case for the CIBLs presented here. Local IBLs only grow to a depth that is small compared to the height of upstream boundary layer depth because the along-wind dimension of the surface change feature is small compared to the boundary layer depth. Small agricultural fields or lakes can create local IBLs.

Mesoscale IBLs usually form near coastlines and can exist over the water or the land depending on the direction of the flow. Cities, industrial areas, power generation facilities, and airports are often located on coastlines and, therefore, it may be useful to have a model for the prediction of dispersion of pollutants or in navigation planning when an IBL is present. IBLs also play an important role in the Arctic. Leads, narrow channels of open water in an otherwise ice-covered sea, cause intense internal boundary layers which result in large clouds that alter the radiative properties of the atmosphere downwind of the lead (Pinto and Curry, 1995). Schnell (1989) observed plumes at altitudes of 3 km and ranges of 200 km downwind of leads north of Ellesmere Island. Glendening and Burk (1992) report on a LES over an Arctic lead.

There has been a lot of work characterizing the mean properties of IBLs starting with Elliott (1958). Other papers which present formulations for the height of the atmospheric internal boundary layer as a function of downstream distance include Venkatram (1977), Raynor et al. (1979), Hsu (1983a; 1983b; 1986), Ogawa and Ohara (1985), Stunder (1985), and Smedman et al. (1997). These works typically employ analytic models for mixed-layer growth or surface layer profile change.

Fig. 1.1 is a idealized diagram of a CIBL developing within a stable boundary layer. The approximately parabolic scalloped line, which begins at the shore and rises to the right, represents the mean approximate position of the top of the internal boundary layer. In this diagram, a stable boundary layer exists over the land on the upwind side of the lake. In the upwind region, thermal stratification suppresses turbulence. The IBL can be clearly identified by the region in which mixing occurs. Fig. 1.1 represents the situation that experiment planners expected to observe. In contrast, fig. 1.2 is based on lidar observations during the three days of intense cold air outbreaks in the field campaign. The upwind boundary layer, which ranged in depth from 200 m to 1 km depending on the day, was well mixed. Therefore, the edge of the IBL was not as clearly defined.

As Mahrt (2000) points out, the position of the top of the plumes in the CIBL varies in time apparently in response to individual thermals and fluctuations in wind speed. Therefore, the properties of the time-averaged flow are characterized by more gradual changes compared to the instantaneous distribution. Mahrt says, "In this sense, the top of the IBL represents the upper limit of the measurable influence of

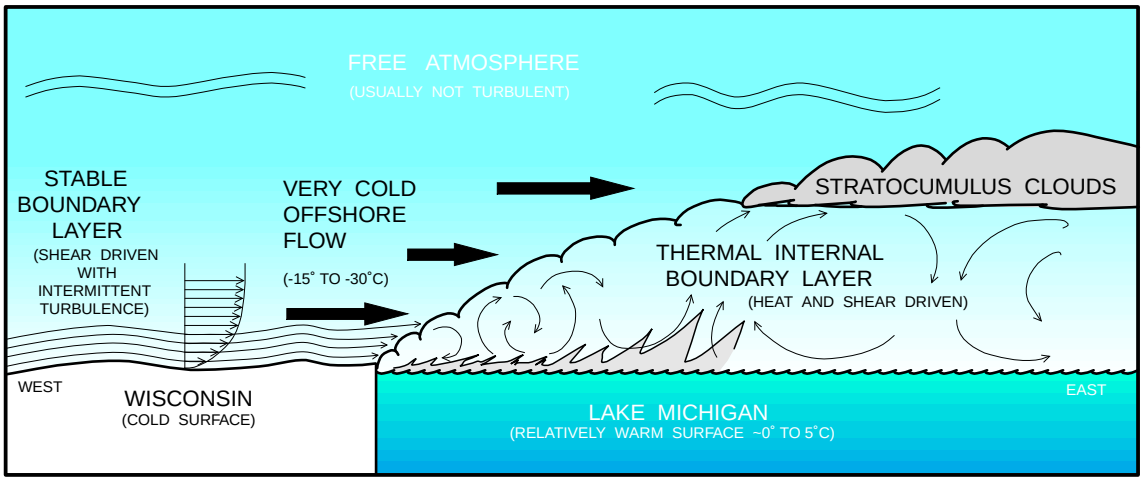

Figure 1.1: Idealized diagram of a convective internal boundary layer growing inside a stable offshore flow.

thermals during the averaging period." He concludes that the time-averaged top of the IBL is (1) not associated with a sharp change in properties, (2) may rise with any slope including nearly vertical in weak-wind convective conditions, and (3) rises more vertically with greater averaging time, which increases the probability of capturing vertically-oriented thermals. The observations and simulations presented here support this hypothesis.

The boundary layer over Lake Michigan has been the focus of attention in a number of observational studies (Lenschow, 1973; Agee and Hart, 1990; Chang and R. R. Braham, 1991). In a recent paper, Young et al. (2000) examines NCAR Electra aircraft in situ data from the BL entrainment zone over Lake Michigan on 13 January 1998. This date is one of the three days for which VIL observations are presented and the same day that was chosen for large-eddy simulation here.

1.5 LES of the IBL

One approach to LES of an IBL used previously (see, for example, Lin et al. 1997) is to simulate a horizontally homogeneous boundary layer in which the entire surface boundary condition is altered at some point in time. This Lagrangian (i.e. the domain is moving with the mean flow) approach assumes that the temporal evolution of turbulence is equivalent to the spatial evolution by a factor of one over the mean advection time. This approach allows the use of spectral solutions in the horizontal directions (Moeng, 1984). The spectral and periodic method is convenient and numerically accurate, but the Lagrangian approach lacks the physical realism of a spatially-evolving boundary layer. Unfortunately, spectral methods require periodic lateral boundaries as discussed above.

It is possible to generate horizontally inhomogeneous turbulence using laterally

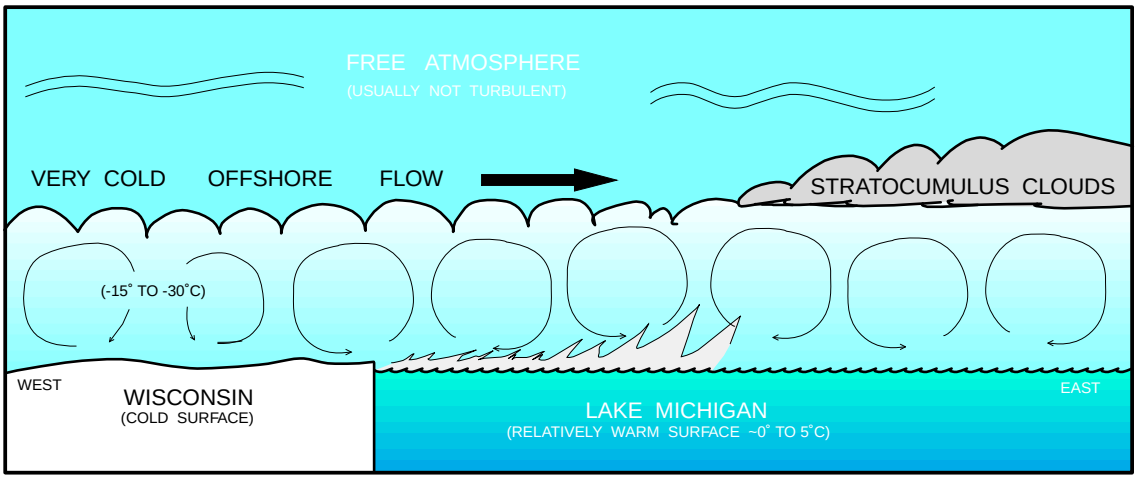

Figure 1.2: Idealized diagram of what was observed on 10, 11 and 13 January. A well-mixed boundary layer advected offshore and the lidar observations did not show a clearly defined internal boundary layer. The circles in the boundary layer represent idealized large eddies.

periodic domains. Glendening (1995), for example, presents a LES of a plume emanating from a narrow Arctic lead. In this case, the atmosphere upwind of the lead is assumed to be strongly stably stratified. The left 200 m of the domain has a water surface, and the right 300 m has an ice surface, and the flow is from the left. The lead causes a buoyant plume above and downstream of itself. This modeling approach works if the atmosphere upwind of the lead is not turbulent and the LES handles the transition from non-turbulent to turbulent flow correctly. Furthermore, because of the periodic domain, he may only use model results from a period prior to the time when the plume re-enters the domain over the lead.

In a more recent paper, Glendening (1999) uses a periodic domain divided into two equal areas, each of different surface roughness. He allows the simulation to run long beyond the time it takes for a parcel of air to advect across the entire domain. This style of simulation is analogous to simulating over an infinitely-wide plane with a patchwork of two surface roughnesses–each patch half the size of the domain and contributing its own local IBL. It is a good example of what might happen over a large agricultural region with two types of crops.

Mesoscale IBLs present a different challenge. The periodic approach can only be used if the flow just before the outflow wall is restored to the mean properties of the boundary layer over the upwind surface. Although this can be done, the method is not efficient because a substantial number of grid-points are used in the ends of the domain to gradually remove perturbations before they propagate or advect into the opposing end. Furthermore, because this method removes all the turbulence near the inlet, a much longer domain must be used for the spatial development of eddies over the upstream surface. Therefore, a more efficient method to generate a homogeneous

fully-developed turbulent boundary layer before the flow reaches the change in surface conditions was desired.

Recently, Fedorovich et al. (2001) performed a LES of a spatially evolving convective boundary layer. These authors constructed a LES domain with boundary conditions designed to duplicate wind-tunnel experiments. Their mean inflow boundary condition was prescribed as constant and their outflow boundary condition was *open*, or *radiative* (Klemp and Lilly, 1980). This means that perturbations cannot propagate upstream through the inflow wall, but they do move through the outlet wall freely. They added uncorrelated random values to the inflow condition to simulate the effect of small perturbations in the experimental flow.

For this dissertation research, the modeling challenge was to generate horizontally-homogeneous turbulence that could flow over an abrupt change in surface properties whereby the turbulence would become inhomogeneous and then exit the domain freely without disturbing the upstream flow. The surface conditions on either side of the discontinuity were homogeneous and extended for distances much larger than the boundary layer depth. Therefore, in contrast to the experiments of Fedorovich et al. (2001), the simulation required a steady supply of horizontally-homogeneous, fully-developed boundary layer turbulence over the upwind side of the domain.

1.6 The Plan

This introduction has described the motivation of this research, the two main tools (lidar and LES), and the main phenomena of interest (CIBL) in the dissertation. In chapter 2, the VIL and data collection methods will be described. In chapter 3, VIL observations of cold-air outbreak events are presented for three cases: 10, 11 and 13 January 1998. Chapter three also discusses the synoptic setting and conventional observations of the events as well as the mean structure and qualitative descriptions of the lidar data. In chapter 4, 2D VIL scans are used to obtain the spatially-evolving vector wind field. A segment of data from 21 December 1997 is used to show when this technique fails. In chapter 5, the numerical model and LES experiments are described. In chapter 6, the 2D cross-correlation technique for data which are inhomogeneous in one direction is presented. The technique is applied to horizontal slices of gridded data extracted from the lidar's volume scans and to simulated aerosol backscatter on horizontal planes from the LES output. The eddy structure information from the correlation functions are compared to those of the simulations. In chapter 7, the motion of aerosol structure in the model is compared to model wind. Conclusions and recommendations for future work are in chapter 8.

Chapter 2

Volume Imaging Lidar

The VIL is designed to make multi-dimensional images of atmospheric aerosol backscatter. The images of aerosol backscatter are useful for determining the top of the planetary boundary layer, mapping the edges of clouds, and identifying elevated layers of pollutants and plumes. In addition to these, because of the VIL's sensitivity and ability to quickly repeat scans of a region, it can be used to explore the patterns and motion of aerosol structure within the boundary layer.

The VIL transmits and receives at 1.064 microns wavelength. This wavelength makes it most sensitive to particles that are about 1-micron and larger. Dense clouds, such as cumulus, severely attenuate the lidar.

One part of the VIL's uniqueness comes from pushing only the most basic requirements of any lidar (transmission and detection) to extreme levels. This is achieved by using a high-power commercial laser, 0.5 m diameter receiving optics, and a custom log-amplifier. The other part is a very fast mechanical "beam steering-unit" (BSU) which enables the VIL to point to anywhere in the sky and construct two and three-dimensional images by moving the laser beam quickly.

2.1 History

Lidar measurements at the University of Wisconsin began in the mid-1960's as a joint project between the Department of Electrical Engineering and the Department of Meteorology. At that time, a ruby laser was used to transmit 1-J pulses approximately 1–3 times per minute. A photomultiplier tube was located at the prime focus of a 6 inch diameter telescope. Data were recorded on Polariod film. The data from this system was used to make the first measurements of aerosol radial motion by cross-correlation of the aerosol structures along a fixed line-of-sight (Eloranta et al., 1975).

In 1967, Dr. Ed Eloranta, then a graduate student in meteorology, inherited the lidar and added an 8 inch telescope, transient digitizer, and paper tape data recording. After earning his Ph.D. and joining the department of meteorology staff, Dr. Eloranta and his adviser, Professor James Wienman, obtained funding from the U.S. Army in the early 1970's to upgrade the laser to a 1-watt ruby system transmitting once per second. Limited scanning capability was added with a larger 12 inch diameter tele-

Figure 2.1: The University of Wisconsin volume imaging lidar in July of 1979.

scope. Data collection hardware was upgraded to a PDP-1140 and 9-track magnetic tapes. During these early years the lidar system was deployed in a van as shown in Fig. 2.1.

During the mid-1970's, the improvements which allowed movement of the laser beam enabled the first two-dimensional images of aerosol scattering through convective boundary layers (Kunkel et al., 1977). These measurements revealed structural information about the convective plumes such as the observation that they often have large vertical coherence with roots in the surface layer. The new observations enabled testing of simple boundary layer models (Boers et al., 1984; Boers and Eloranta, 1986). Sroga et al. (1980) showed aerosol structure motion derived from three-shot RHI scans.

The configuration of the VIL used to collect the data analyzed in this dissertation came to shape in the mid 1980's. The transmitter was replaced by a 20-watt Nd:YAG with a pulse repetition frequency (PRF) of 30 Hz. A DEC VAX replaced the PDP computer. The BSU was designed and constructed, and the system moved to a semi-trailer van. This system was first deployed in the 1987 FIFE experiment.

In 1995, an Air Force grant allowed the VIL to make greatly improved measurements by purchasing a new laser and SGI workstation with optical disk for data recording. The Infinity Coherent 40-100 laser is a diode pumped Nd:YAG laser. The diode pump uses a ring configuration to ensure single longitudinal mode output. This light then passes multiple times through a pair of flash-lamp pumped Nd:YAG rods for amplification. Moreover, the laser employs a phase conjugate mirror to produce excellent quality pulses at all repetition rates. The laser is capable of producing 40-watts at a PRF of 100 Hz. The laser is water cooled and requires three-phase power. The PRF and pulse energy are controlled by a program running on a PC which also monitors and displays the laser system performance.

The major transmitting and receiving components of the VIL are installed in two heavy steel frames that can be connected to each other to form one very rigid piece during operation (see fig. 2.2) or disconnected for shipping. The larger of these two sections contains the laser and its power supply and computer control, beam-expander, beam-splitter, energy monitor, and digitizer. The smaller of these two sections contains the telescope, detector, and log-amplifier. The BSU, shown in fig. 2.3, attaches to the

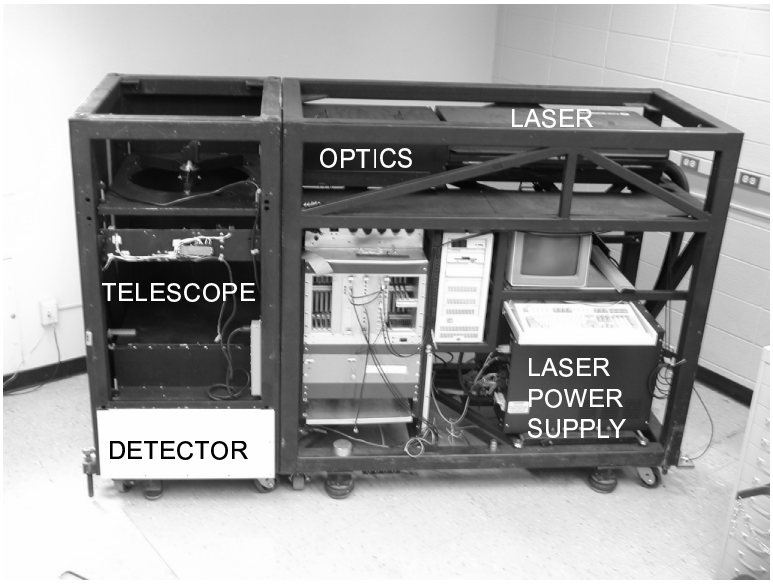

Figure 2.2: This photograph shows VIL in the lab. The vertically pointing telescope on the left side was located directly beneath the beam steering unit shown in fig. 2.3.

frame containing the telescope via a small frame which raises it above the roof of the trailer. A small crane is required to lift the BSU overhead the trailer and lower it on to the spacer frame above the telescope (see fig. 2.4). The SGI computer and optical disk (not shown) sit on a table inside the VIL trailer and are connected to the data acquisition system by Ethernet. A complete system schematic is shown in fig. 2.5.

Unfortunately, the VIL is not "eye-safe". This means that direct viewing of the laser beam can cause eye-damage. To prevent accidents, the VIL is always operated with an outdoor observer watching the direction that the beam-steering unit points. The observer holds a switch which permits transmission of the laser whenever the button on the switch is depressed. The observer watches the sky for any air traffic and releases the switch if any is sighted. When the button is released a mechanical shutter inside the VIL trailer blocks the laser beam. Because of the lack of eye-safety, the VIL laser beam is never pointed toward the ground. For this reason, VIL observations upwind of the lake were never collected during Lake-ICE.

2.2 Lidar equation

The light incident on the lidars receiver can be described by the lidar equation

$$P(r) = \frac{E}{r^2} K \beta_s(r) \frac{P'(180°, r)}{4\pi} \exp[-2 \int_0^r \beta_e(r')dr'] \tag{2.1}$$

where

E = transmitted laser pulse energy, $P(r)$ = power received by the detector, r =

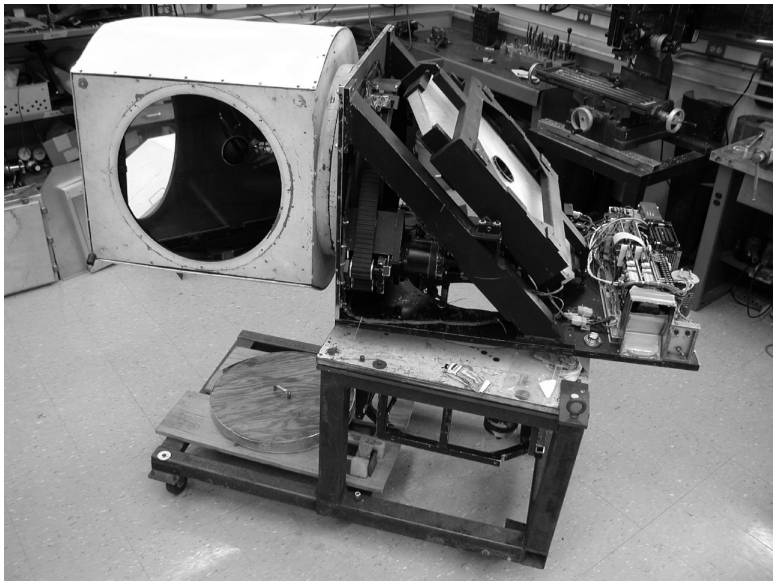

Figure 2.3: VIL beam steering unit with part of the cover removed in lab.

Figure 2.4: Ralph Kuehn, Patrick Ponsardin and Jim Hedrick installing the VIL beam steering unit in Wanakee, Wisconsin, in September 1997 for testing before Lake-ICE.

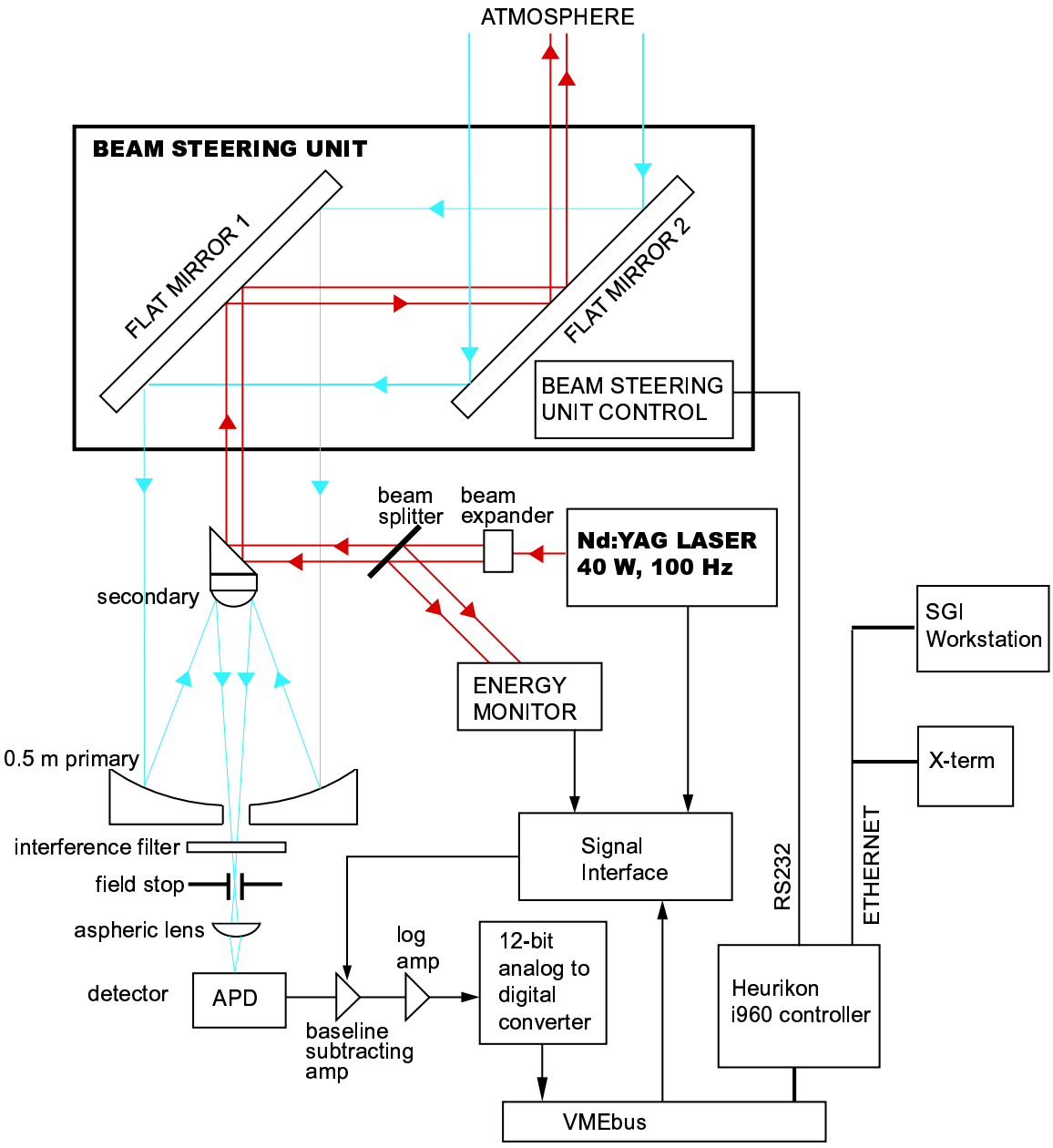

Figure 2.5: Schematic of the UW Volume Imaging Lidar.

Figure 2.6: UW-VIL as set-up for Lake-ICE in Sheboygan, WI, during the winter of 97-98. The car shown was the author's much loved 1983 Toyota Camry. This photo, taken just before sunrise with the moon setting to the west, was looking SW.

Figure 2.7: The author standing below the VILs beam-steering unit.

distance along the path, K = system constant= $Ac/2$, A = area of the receiver, c = speed of light, $\beta_s(r)$ = scattering cross-section per unit volume, $P'(180°, r)$ = aerosol backscatter phase function, and $\beta(r')$ = extinction cross section per unit volume. This equation does not include the effect resulting from differing transmit and receive fields of view.

In the VIL, the signal from the detector is input to a log amplifier and normalized for small fluctuations in the laser power E. All lidar returns at full range resolution are permanently recorded on a write once optical disk at this point. The log amplifier has two interesting benefits. First, it causes the causes the one over range-squared dependence and any effects of attenuation of the return to appear as a linear trend which can be removed easily. Second, the log amplifier increases the weaker signals more than the strong signals allowing users to see inhomogenities in the aerosol structure that may have gone unnoticed with aerosol lidars using linear amplifiers.

2.3 Scan strategies

The VIL's beam-steering unit is able to direct the laser beam anywhere in the sky. Elevation angles range from 90° (directly overhead, zenith) to slightly below 0° (i.e. slightly below the horizon). The azimuth range is 360°. Repeated systematic motions of the azimuth and/or elevation angles are called scans. Holding the elevation angle constant and varying the azimuth angle with a constant rate is called a *plan-position indicator* (PPI) scan. The result is a backscatter intensity on a conic surface. The actual PPI image is a plan view of the backscatter intensity on the surface. When the elevation angle (i.e. pointing toward the horizon) is near zero, the PPI scan is a horizontal map of aerosol scattering just above the surface of the earth.

When the azimuth angle is held constant and the elevation is changed, images of atmospheric structure on vertical slices can be obtained. This type of scan is called a *range-height indicator* (RHI) scan. The terms PPI and RHI have their origins in radar meteorology when cathode ray tubes were used to present the data in the natural spherical coordinate system of radars (and lidars).

To obtain the three-dimensional structure of the atmosphere, a series of RHI scans are made, each with an incremented azimuth angle. This is called an *RHI volume scan*. PPI volume scans are also possible, but it is better to collect RHI volume scans because of the distortion correction that needs to be applied due to the advection of structures across the volume over the duration of a volume scan.

The 3D RHI volume scan data, in its original spherical coordinate system can be interpolated to a horizontal or vertical 2D plane The 3D spherical data can also be interpolated to a 3D Cartesian grid. By interpolating the spherical coordinate RHI volume scan data to horizontal planes through the volume scan, *constant altitude PPI* (CAPPI) images are obtained which show aerosol backscatter on horizontal planes.

2.4 Distortion correction

The time required to make an RHI volume scan (composed of perhaps 100 RHI scans) is usually 2–3 minutes. During this time, if a mean horizontal wind existed, an aerosol structure will be advected horizontally a distance $\mathbf{d}$ that is proportional to the time difference δt between the time of the RHI it was collected in and the last RHI scan in the sequence for that volume. For example, the aerosol structures in the first RHI scan of a two-minute volume scan will move 1200 m in the time it takes to complete the entire volume scan if the mean flow is moving at 10 m s^{-1}. Because the RHI volume scans will be used to infer spatial information, such as eddy shape, correction for the distortion due to the mean wind is required.

The correction is performed using a procedure described by Sasano et al. (1982) and again by Schols and Eloranta (1992) . It requires an estimate of the mean horizontal wind vector $\mathbf{v}$. Given that, each individual aerosol backscatter profile is moved to its corrected position by adding a distance $\mathbf{d} = \mathbf{v} \cdot \delta t$.

2.5 High-pass median filtering

Bright scattering features such as the densest wisps of steam-fog cause harsh and distracting shadows in the lidar data. Often, useful aerosol structure information exists in the shadows but cannot be seen in images because the shadow places it beyond the limits of the color scaling which is usually selected to show structures in the brighter parts of the image. Furthermore, strong shadows will interfere with the cross-correlation method's ability to infer aerosol structure motion. Therefore, for a large part of the lidar data presented here, a high-pass median filter was applied to each lidar return array after being corrected for the one-over-range-squared dependence. The high-pass median filter works as follows: for each point in the array to be filtered, its nearest neighbors within one filter length (half a length on each side) are sorted. The center value of the sort is subtracted from the data value in the array being filtered. Effects of the high-pass median filter on the data are discussed in sections 4.1 and 4.5.

2.6 Systematic errors in the data

The lidar uses a sensitive silicon avalanche photodiode as a detector to measure light backscattered from the atmosphere. As the laser pulse leaves the lidar, some of the intense transmitted laser light is scattered by dust in the air and on optical surfaces in the lidar. The intense stray light is received by the detector as the transmitted pulse leaves the lidar. The result is an overload on the detector which (1) blinds the lidar from seeing atmospheric structures at ranges less than about 750 m and (2) causes a low amplitude, ringing that can be seen in the absense of atmosphere signal all the way out to the farthest ranges (i.e. 18 km). These systematic errors can be seen in fig. 2.8. The ringing has a frequency of about 0.3 MHz, which shows up in the data as sinusoidal waves with a wavelength of about 1 km. Fortunately, the ringing is usually

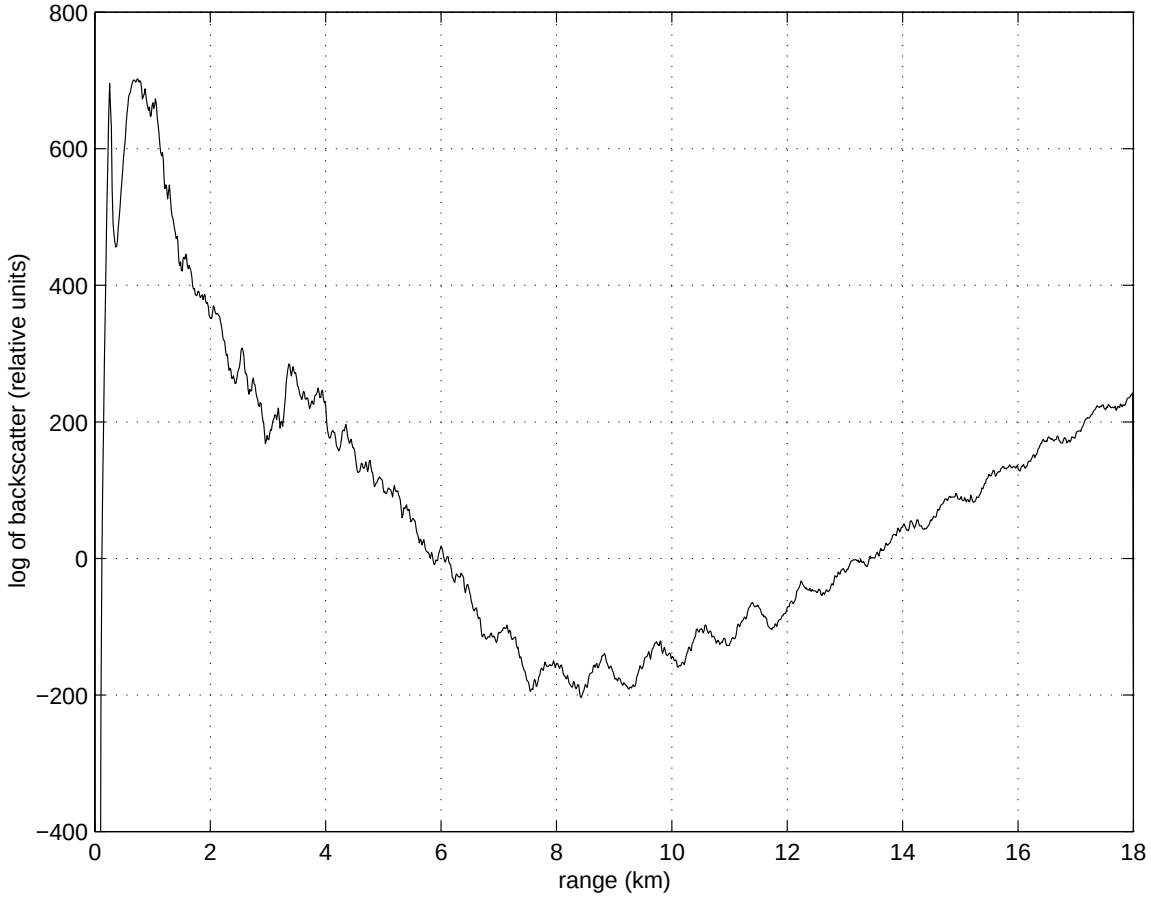

Figure 2.8: Range-corrected log of power received by the lidar as averaged over about 15 minutes on 13 January during PPI scanning. The increasing trend of the return beyond 9 km is caused by range-correction of the constant background.

easily distinguished from atmospheric waves because (1) it is exceptionally regular, (2) it is apparent low signal conditions, and (3) it appears as concentric rings around the lidar location in PPI and RHI scans.

Chapter 3

Lake-Induced Convection Experiment (Lake-ICE)

The Lake-Induced Convection Experiment (Lake-ICE, Kristovich et al. 2000) took place during December 1996 and January 1997. The VIL was just one of many observational facilities deployed in the experiment which was aimed to study the development of convection over Lake Michigan during cold air outbreaks. During the experiment, there were 11 intensive operation periods (IOPs) designed to coordinate and focus a variety of observing techniques on the lower atmosphere over the lake. All of the cold-air outbreak data presented in this dissertation occurred during IOP#6, with the exception of the land-breeze observations which occurred during IOP#4.

Other instruments used during Lake-ICE included the NCAR Electra aircraft with in situ sensors and the ELDORA radar on board; the University of Wyoming's King Air aircraft with in situ sensors; the Penn State University (PSU) Cloud Observing System, and NCAR's Integrated Sounding Systems (ISS) and mobile Cross-chain LORAN Atmospheric Sounding Systems (CLASS). The aircraft flew through and above the boundary layer across the lake. The PSU site was located in Michigan on the downwind side of the lake.

As can be seen in fig. 3.1, the shoreline near Sheboygan is aligned roughly north-south. The lidar was located in an industrialized part of the city approximately 2 km south of Sheboygan Point. Lake Michigan is ≈100 km wide at this latitude. The terrain west of Sheboygan is rolling hills covered by forests, farmlands, and small towns. The elevation varies less than 200-m within a 150 km distance from Sheboygan.

If an air-parcel in Sheboygan followed a constant reverse-trajectory, it would not have passed over any major bodies of liquid water for distances much greater than 500 km if the wind direction was less than about 313°. The closest bodies of open water to the northwest are Green Bay which is located at 343° at 100 km and Lake Superior at 313° at 500 km. The surface wind direction at Sheboygan during the days discussed here ranged from 250-300°.

The UW-VIL operated on nine days during the approximately two-month deployment in Sheboygan. Of the nine days, offshore flow with air temperatures near –20°C at the surface only occurred on three days: 10, 11, and 13 January 1998. It was hoped that the intense temperature contrast of the air and lake water would create

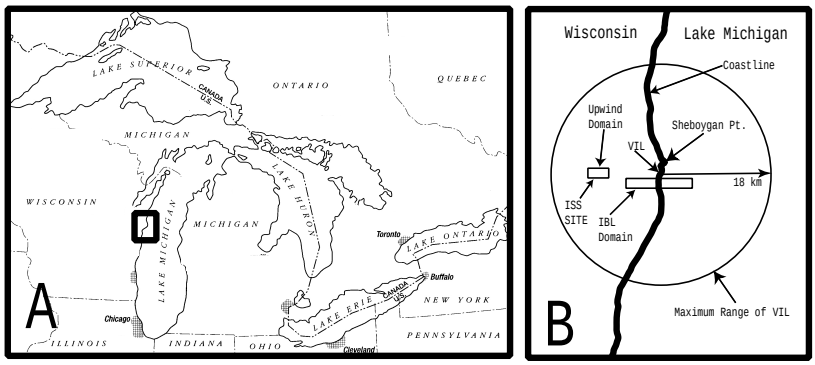

Figure 3.1: Location of the UW-VIL during the Lake-ICE.

Date	Time (UT)	Scan Type	Elevation	Azimuth	Frames
10 Jan	12:37-13:12	Vol 1	0-15	85-135	13
10 Jan	13:22-14:57	PPI	0	85-180	474
10 Jan	15:39-16:53	Vol 2	0-15	85-100	28
10 Jan	16:55-18:05	Vol 3	0-15	70-110	25
11 Jan	11:51-12:16	Vol 1	0-15	70-110	9
11 Jan	13:47-14:30	Vol 2	0-15	70-110	16
11 Jan	15:29-16:23	Vol 3	0-15	70-110	20
13 Jan	12:47-13:37	Vol 1	0-15	90-130	17
13 Jan	15:48-16:23	Vol 2	0-15	100-120	23
13 Jan	16:28-16:32	PPI	0	70-176	40
13 Jan	16:41-17:08	RHI	0-15	120	1620
13 Jan	17:19-18:37	Vol 3	0-15	90-130	27

Table 3.1: List of the times and types of VIL scans.

a strong IBL that could be seen in the lidar data. Furthermore, extremely cold days were of particular interest to other Lake-ICE investigators who were interested in the lake-effect snow along the lake's eastern-shore. There was concern before the experiment that the air upwind of the lake during such cold-air outbreaks (CAO) would be too clean (devoid of aerosol particles) to obtain useful lidar data. Fortunately, this was not the case. In fact, the lidar crew found abundant boundary layer aerosol scattering and very interesting atmospheric structure on most days. In many cases, gravity waves were observed above the boundary layer, and there were several cases where it appeared that waves were strongly affecting the organization of boundary layer eddy structure. Other interesting patterns were observed when light precipitation fell through horizontal scan planes. Although very interesting, these more complex situations are not presented in this work. (Examples can be found in Mayor et al., 1998.) This dissertation focuses on observed and simulated boundary layer structure during the three extreme cold air outbreak events during the experiment. Fig. 3.2 and table 3.1 show the periods of VIL data collection during the three CAO days presented here. In table 3.1, a *frame* is either a complete volume during a volume scanning period, or an individual RHI or PPI during a sequence of RHIs or PPIs.

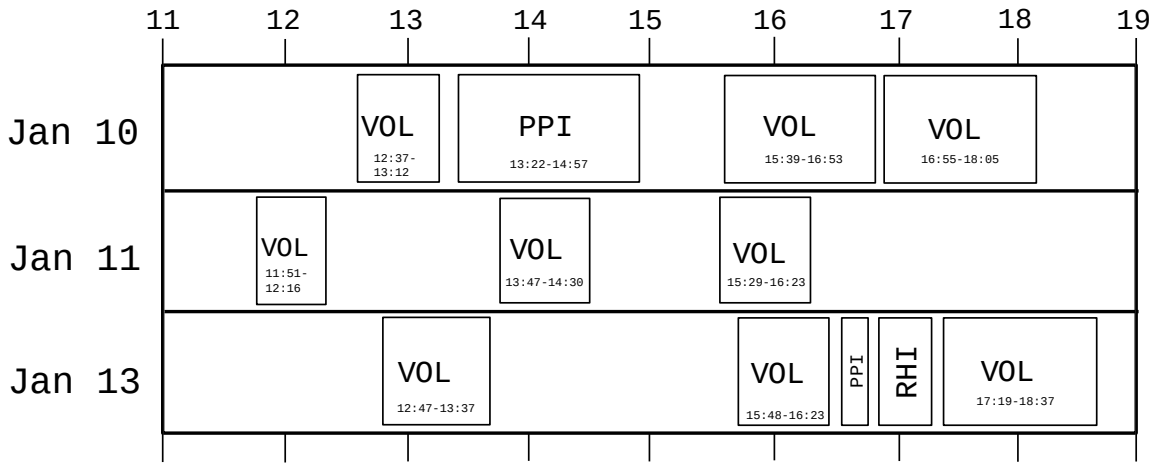

Figure 3.2: VIL operation times (in UT) on 10, 11 and 13 January 1998 shown graphically.

3.1 Mixing fog (Steam fog)

The physical process that causes a thin cloud to rise from a hot cup of coffee, or enables one to see his or her breath on a cold morning, is the same process that causes steam-fog (or sea-smoke) to form over open bodies of water during cold conditions. However, the name *steam-fog* is a misnomer because *steam* is vapor above the boiling point. A more appropriate name is *mixing fog*. An example of a classic paper on steam-fog is Saunders (1964) and a more recent one is Okland and Gotaas (1995).

Fig. 3.3 is provided to assist the reader in the following explanation of mixing fog formation (Bohren and Albrecht, 1998). When two air parcels of differing temperatures and water vapor content mix together isobarically and adiabatically, supersaturation will occur if the straight line connecting the points representing two parcels on an vapor pressure versus temperature diagram intersects the equilibrium saturation curve. In this case, if condensation nuclei are present, cloud droplets will form. In fig. 3.3, the point A represents the air with temperature and vapor pressure very near that of the water it lies over. Point C represents the temperature and vapor pressure of air advecting offshore. One can see by the line connecting points A and B that if warmer or drier air advects offshore, mixing fog may not form.

Other types of fogs, such as radiation or advection fog, involve cooling the air from below. Therefore, these fogs usually form in stable conditions with little or no vertical mixing. The result is that radiation and advection fogs tend to form in homogeneous layers. In contrast, mixing fog occurs only in the presence strong convection and the convective currents cause the fog to be concentrated in some regions and absent in others.

Figs. 3.4 and 3.5 are photographs of the mixing fog taken by Dr. David Rogers

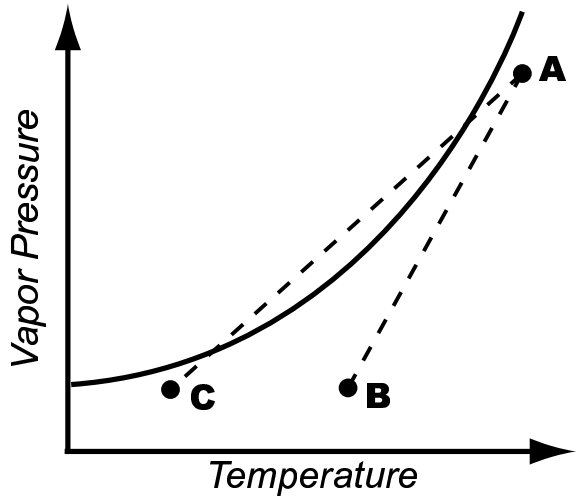

Figure 3.3: Diagram showing saturation vapor pressure as function of temperature.

from the NCAR Electra when it was near the Wisconsin coast north of the lidar site on 13 January. These photos show the heterogeneity of mixing fog. In some places, there is almost no fog and in others dense walls of fog. Fig. 3.6 is a photograph taken by the author while standing near the VIL in Sheboygan.

Under these extremely cold and convective conditions, steam devils often form (Lyons and Pease, 1972; Bluestein, 1990). Steam-devils are relatively narrow rotating columns of mixing-fog. Both airborne observers and lidar crew members observed many steam devils over the lake on the three days discussed in this chapter.

3.2 Effect of refraction

The VIL's beam-steering unit was located 5 m above the surface of the lake. If the atmosphere was not present, or there was no vertical gradient of atmospheric density, the laser beam would rise an additional 7.8 m over 10 km range due to the curvature of the earth. The effect of the atmosphere with a negative vertical density gradient is to reduce the rate of rise through refraction and result in a scan-plane slightly more parallel to the surface of the earth. Given an adiabatic lapse rate, we estimate the laser beam to be 11.4 m above the surface at 10 km range (beam-steering unit elevation plus refraction and curvature effects). Superadiabatic lapse rates, up to the autoconvective lapse rate of 34.1° km^{-1}, will place the beam between 11.4 and 12.8 m above the surface at 10 km. For lapse rates greater than the autoconvective lapse rate the laser beam would rise higher than 12.8 m in 10 km range. Fig. 3.7 is a depiction of these scenerios.

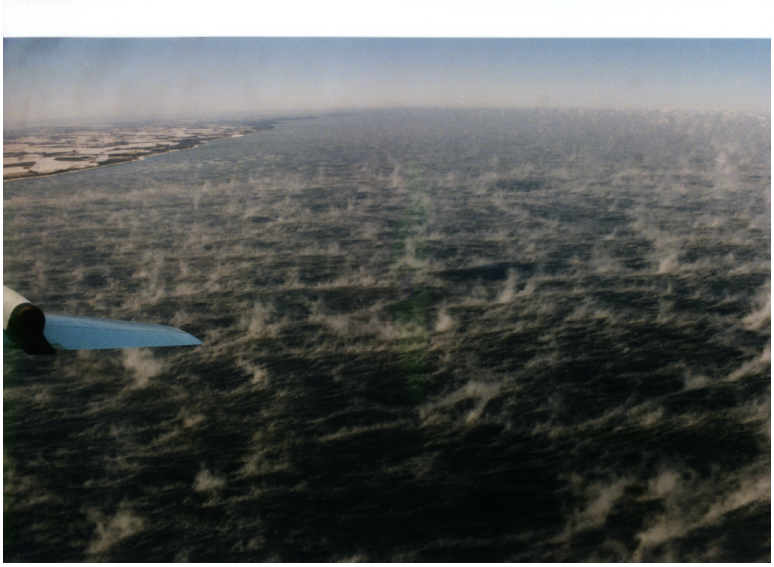

Figure 3.4: Photograph of steam-fog north of the lidar site on 13 January 1998 taken from the NCAR Electra. Photo courtesy Dr. David C. Rogers (NCAR).

Figure 3.5: Photograph of steam-fog north of the lidar site on 13 January 1998 taken from the NCAR Electra. Photo courtesy Dr. David C. Rogers (NCAR).

Figure 3.6: Photograph looking east from the lidar site near sunrise. Notice steam-fog just above the surface of the lake and deeper clouds on the horizon. Photo by S. Mayor.

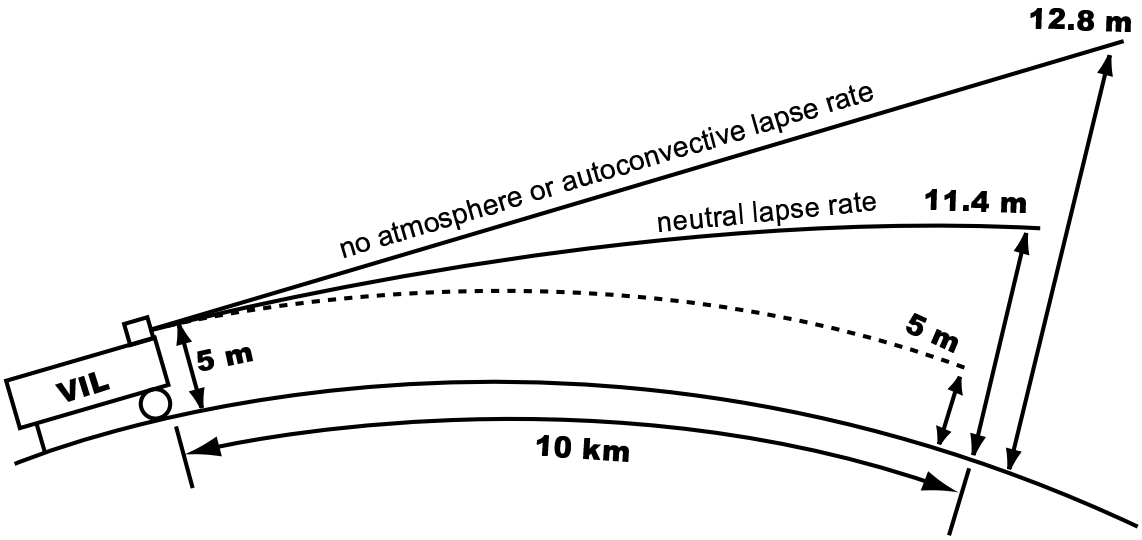

Figure 3.7: Diagram showing how curvature of surface of earth and lapse rate effect height of laser beam above surface.

3.3 10 January 1998

During the night of 10 January 1998, a cold-front passed over Wisconsin and Lake Michigan. At 12 UTC (6 AM CST) the front was located over eastern Michigan and the Ohio Valley with a 999-mb low-pressure system located over James Bay and a high-pressure ridge extending from Alberta, Canada, to Missouri. Winds at the surface in eastern Wisconsin were from the west-south-west at 5-10 m s^{-1}. At the lidar site, the lowest air temperature was -16.5°C at 14 Z. Observations at the lidar site indicated clear skies overhead and to the west. Steam-fog was present over the lake and stratocumulus clouds could be seen offshore. Steam-devils were spotted by lidar crew members during data collection. Surface water temperature measurements along the western edge of Lake Michigan from the NOAA-14 satellite overpasses range from 0° to 5° C. Visible satellite imagery (see fig. 3.8) from this day show a mostly solid deck of clouds over the lake with interesting wind parallel and shore-parallel enhancements. The wind parallel enhancements are most likely horizontal convective rolls (Kelly 1984) while the shore-parallel features are most likely enhancement of boundary layer clouds due to gravity waves in the capping inversion layer. The satellite pictures confirm clear skies over Wisconsin and for the first 10 or fewer kilometers of the western edge of the lake. Surface and 850 hPa analyses at 12 UTC for the western Great Lakes region show strong cold air advection over the entire region (see figs. 3.9 and 3.10).

VIL observations began on 10 January at 12:37 UTC with an RHI volume scan from 0-15° elevation to 85-135° azimuth. The sun rose above the offshore clouds at 13:12 UTC and corrupted those lidar shots that pointed toward it most directly. Therefore, the RHI volume scans were stopped and PPI scans started at 13:22 UTC. PPI scans were continued until 15:00 UTC.

Individual RHI scans (from the RHI Volume scans) as shown in fig. 3.14, indicate high aerosol scattering from the surface up to approximately 1 km AGL. From the first volume scan on this day, we see a layer of especially high aerosol scattering from 500-1000 m AGL, but not optically dense enough to cause shadows. Subsequent volume scans contain shadows which indicate the presence of clouds.

Six radiosonde soundings, collected at intervals of 1.5 hours between 13:30 and 21:00 UT, from the NCAR ISS site 10 km west of the lidar site all confirm a mixed layer that is approximately 1 km deep on this day (see Fig. 3.11).

CAPPIs from volume scan #1 (see upper left panel in fig. 3.13) show remarkable structure of aerosol and steam-fog below about 50 m. The cellular patterns observed near the surface by the lidar show strong resemblance to patterns documented by Willis and Deardorff (1979) in laboratory tank experiments of convection. They also resemble patterns generated in some large-eddy simulations of convective boundary layers (see Schmidt and Schumann, 1989; Mason, 1989). One important difference, however, is that the VIL observations were collected when a mean horizontal flow was

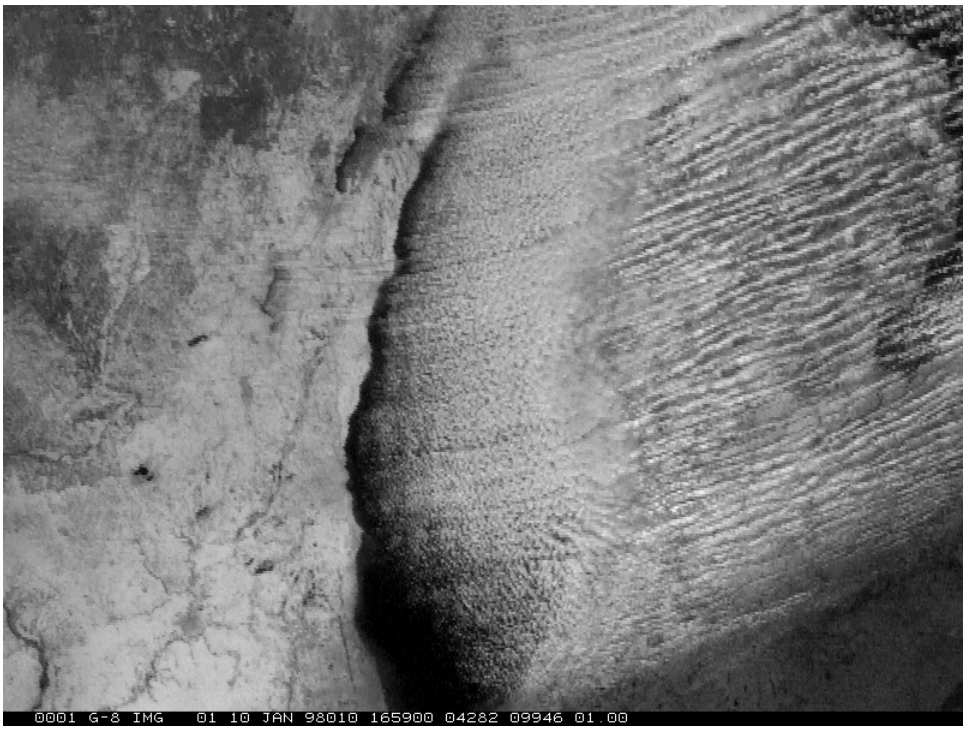

Figure 3.8: Visible satellite image showing Wisconsin, Lake Michigan and Michigan at 16:30 UT on 10 January 1998.

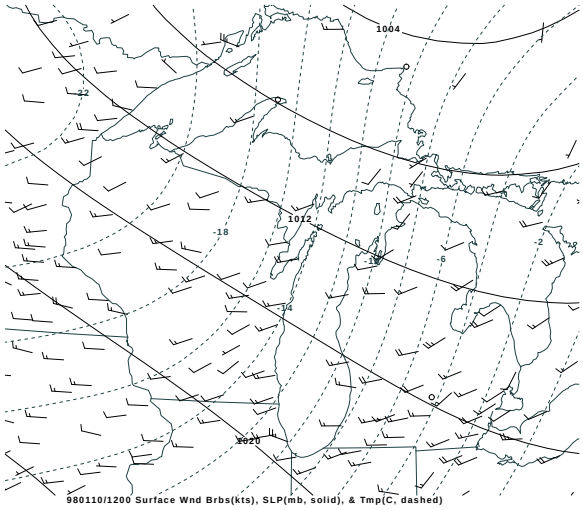

Figure 3.9: Sea-level pressure (solid), surface temperature (dashed), and wind observations at 12 UT on 10 January 1998.

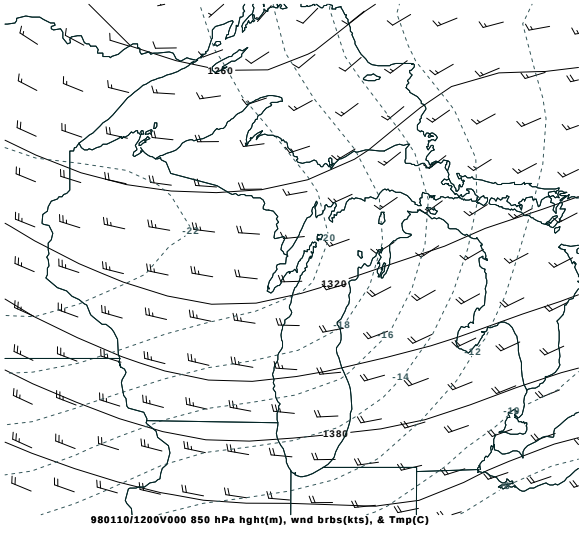

Figure 3.10: 850 hPa height surface (solid), temperature (dashed), and gridded winds at 12 UT on 10 January 1998.

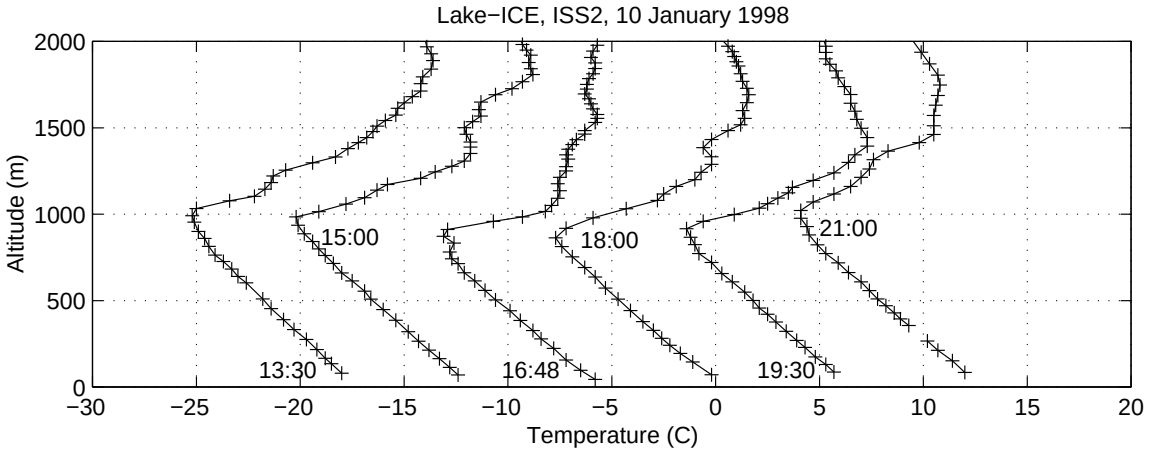

Figure 3.11: Six temperature profiles from radiosondes launched 10 km west of the VIL site on 10 January 1998.

present. The effect of this is that the patterns in the tank or LES experiments do not appear to have a preferred orientation while the patterns observed by the lidar do appear to be stretched, or elongated, in a direction parallel to the mean flow.

The PPI scans through the surface layer on this morning were the first during this field campaign to measure such interesting patterns with high temporal resolution ($\approx$24 s). Because the objective was to measure the *3-D* structure of the boundary layer, RHI volume scans were resumed from 15:39–16:53 UT and from 16:55–18:05 UT. These later volume scans are not presented here because they occurred during light snow-fall which greatly complicates interpretation.

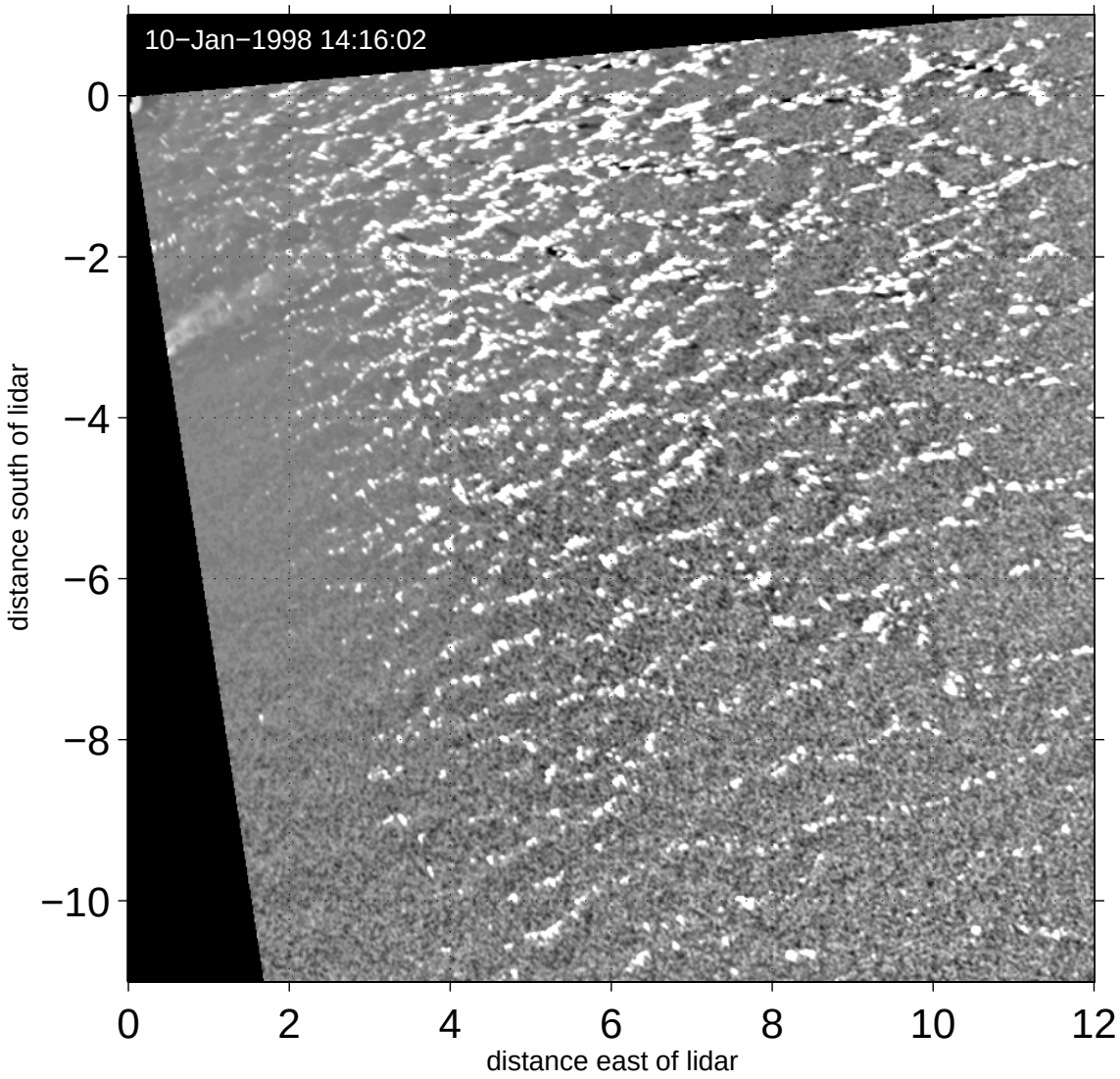

Figure 3.12: One PPI scan from the VIL on 10 January 1998.

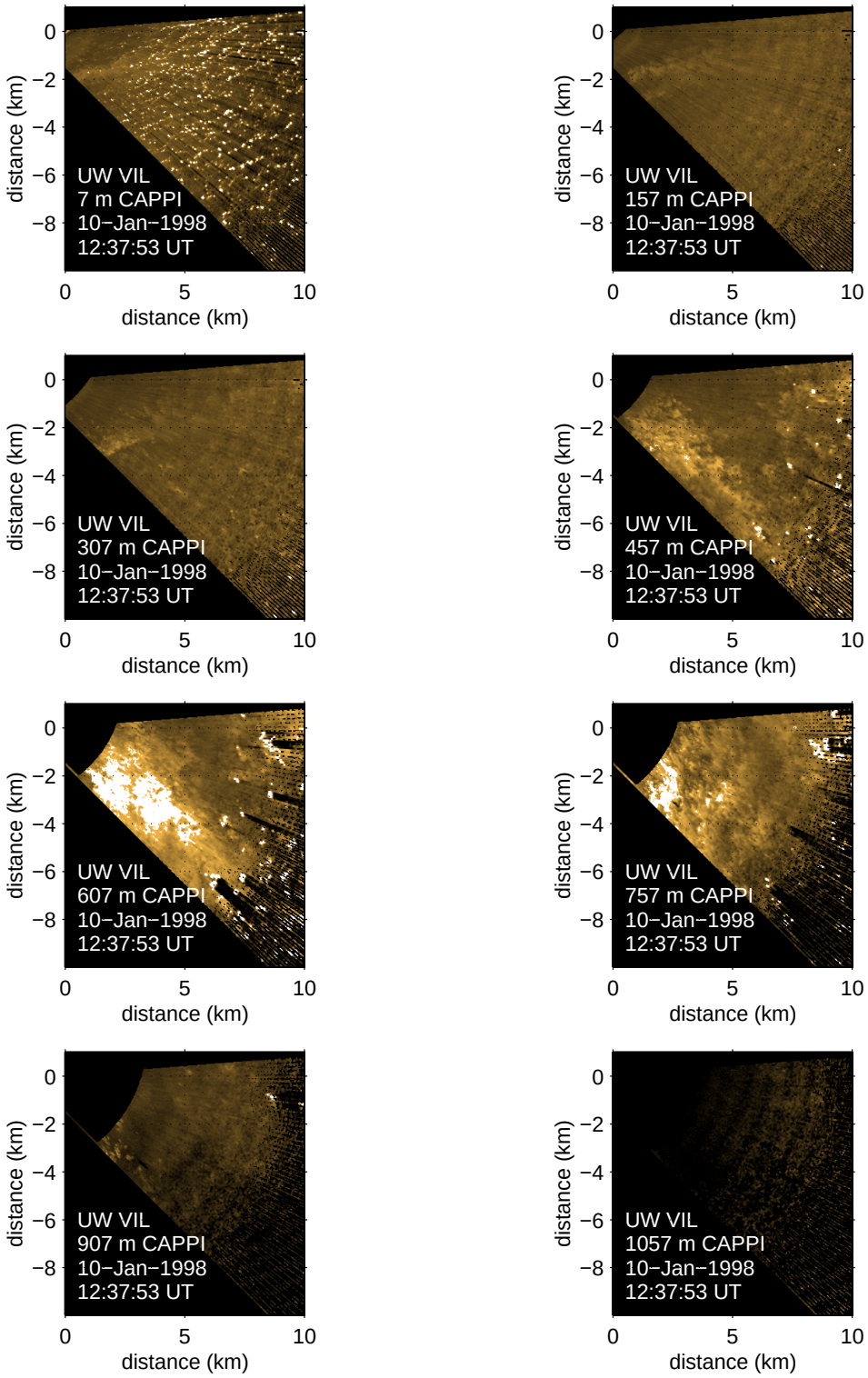

Figure 3.13: CAPPIs from one volume scan on 10 January 1998. (High-pass median filter not applied. Notice shadows to the right of brightest structures.)

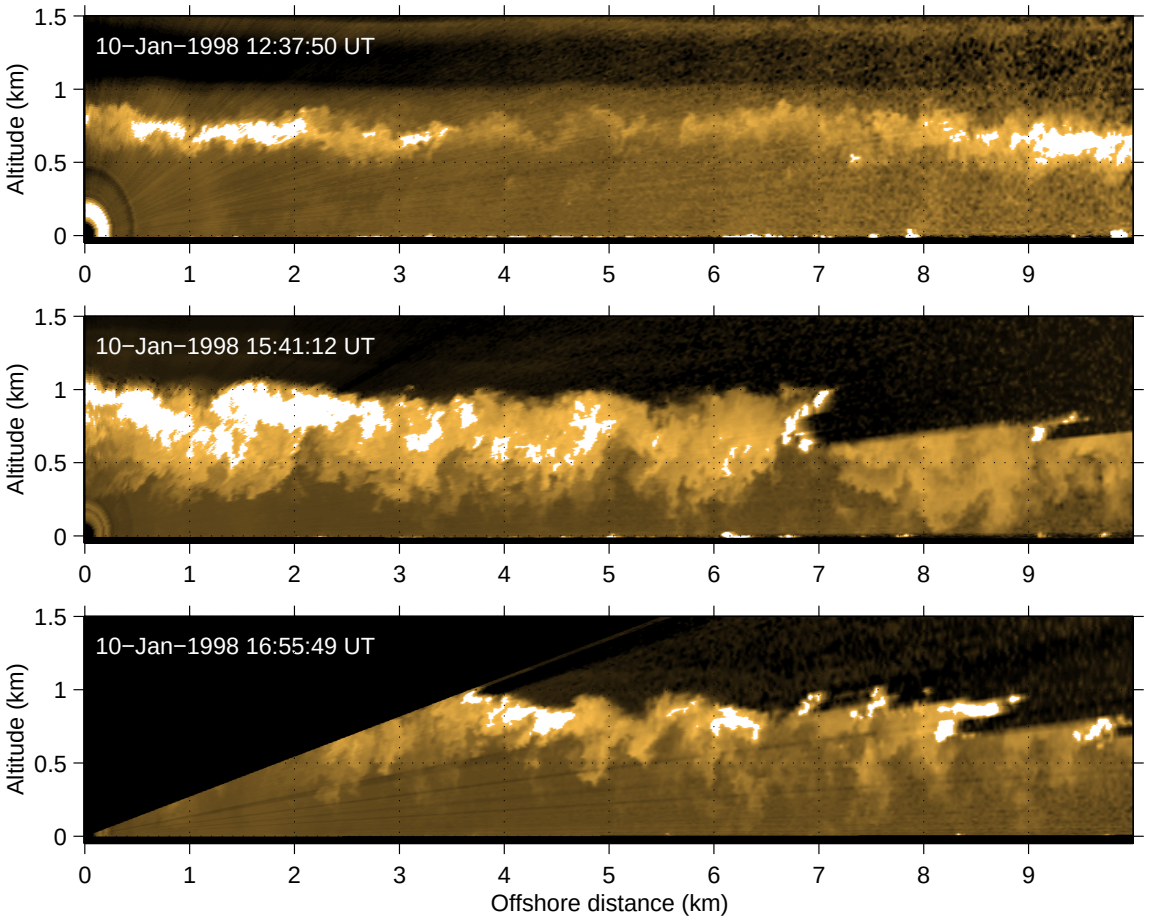

Figure 3.14: Three eastward pointing RHIs each from the beginning of RHI-volume scan period on 10 January 1998.

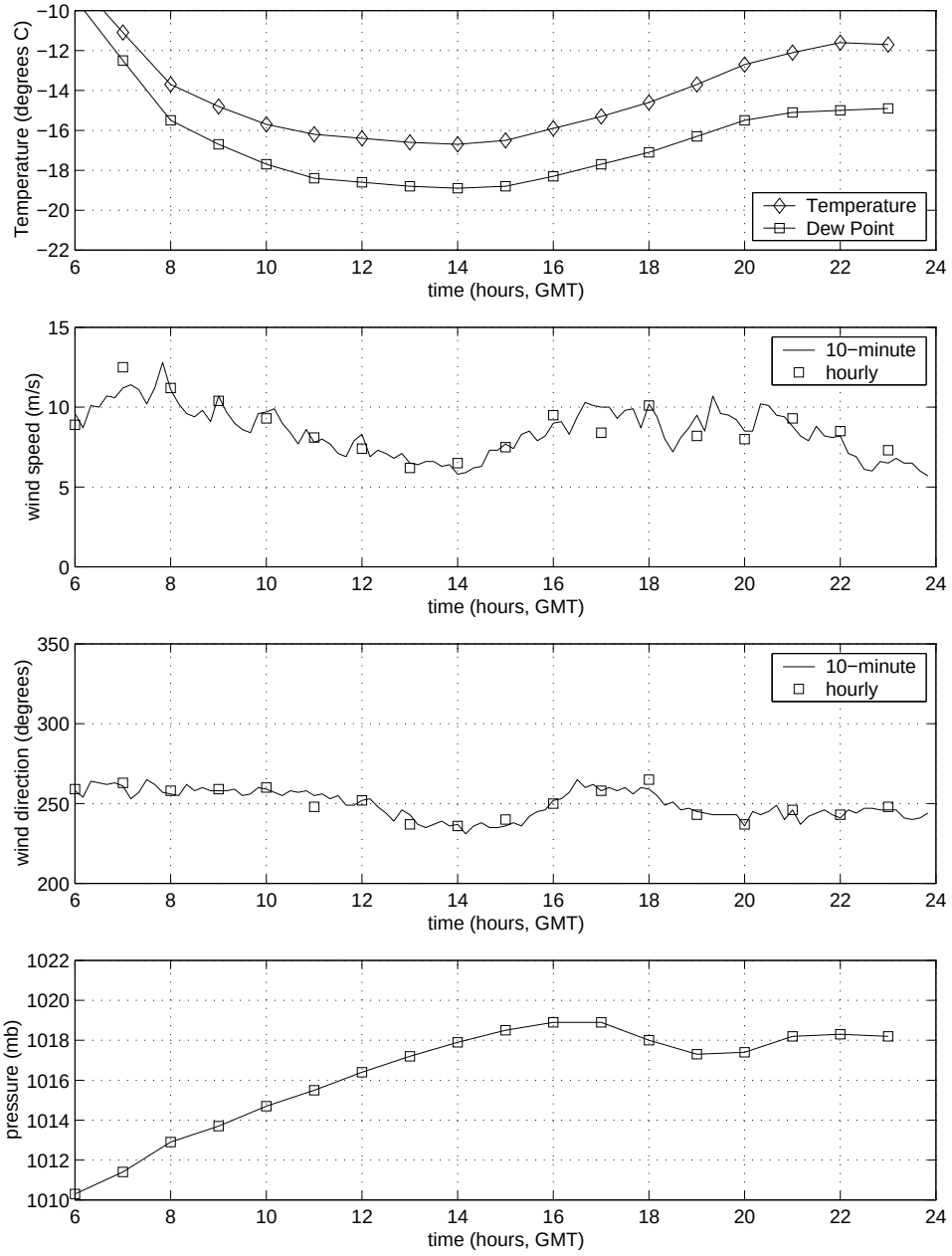

Figure 3.15: Traces of temperature and dew-point, wind-speed, wind-direction, and barometric pressure from the Coast Guard station near the VIL site on 10 January 1998.

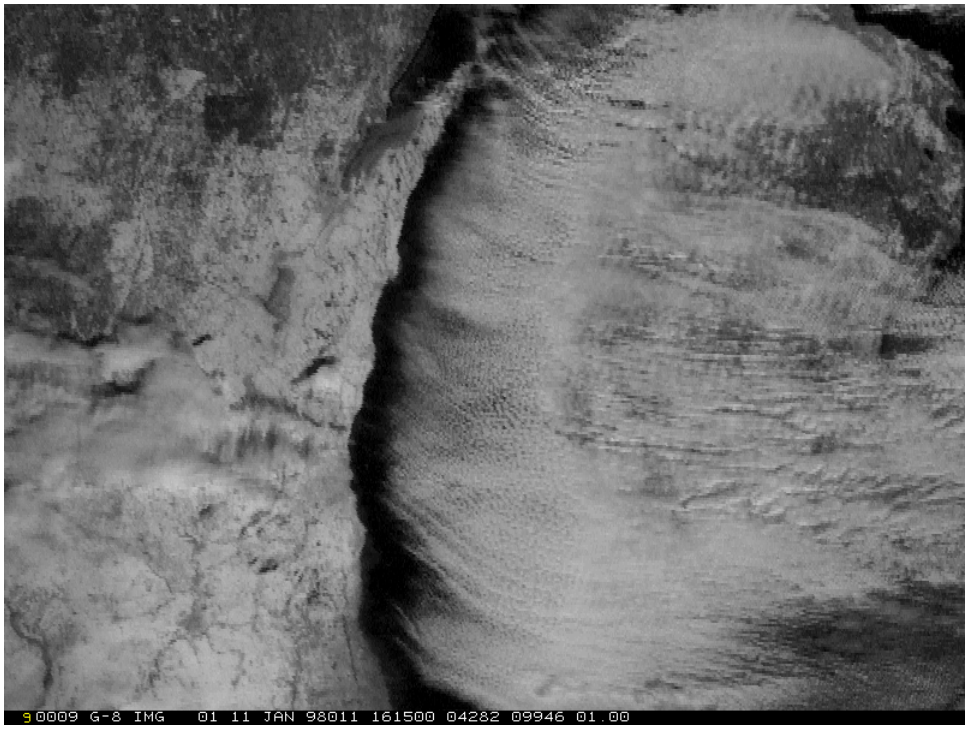

Figure 3.16: Visible satellite image showing Wisconsin, Lake Michigan and Michigan at 16:15 UT on 11 January 1998.

3.4 11 January 1998

By 18 Z on 11 January, the low pressure system over James Bay on 10 January weakened and moved to New Foundland. The surface pressure gradient over Wisconsin relaxed and the cold air advection weakened substantially as a ridge axis moved over the experiment region (see figs. 3.17 and 3.18). Fig. 3.16 shows the visible satellite image from 16:15 UT on this day. Wind parallel cloud structures are not as homogeneously located in the north-south direction and shore-parallel structures are not observed as in fig. 3.8.

On 11 January, the VIL only collected RHI volume scans. The first series of RHI volume scans was from 11:51–12:16 UTC and was stopped because of a failure of the water pump on the laser. The second series of RHI volume scan was collected from 13:47–14:30 and was stopped again due to the laser cooling system failure. The third set of RHI volume scan was from 15:29–16:23 and was stopped before the laser cooling system failed.

Three radiosonde soundings from the ISS site on this day confirm observations of a substantially shallower mixed layer. The sounding from 12 UT indicates the base of the inversion at 400 m. By 15 UT, the base of the inversion had dropped to 250 m.

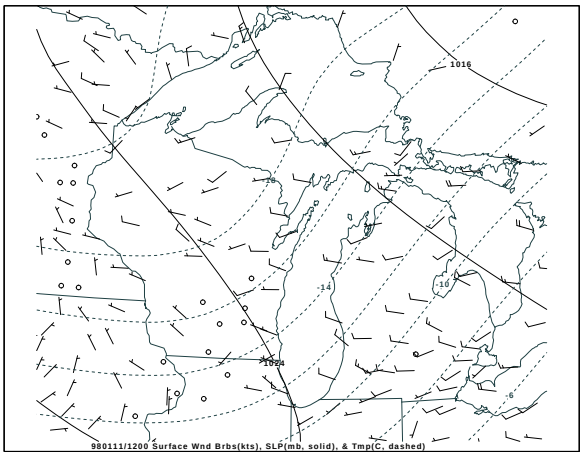

Figure 3.17: Surface pressure (solid), temperature (dashed), and wind observations at 12 UT on 11 January 1998.

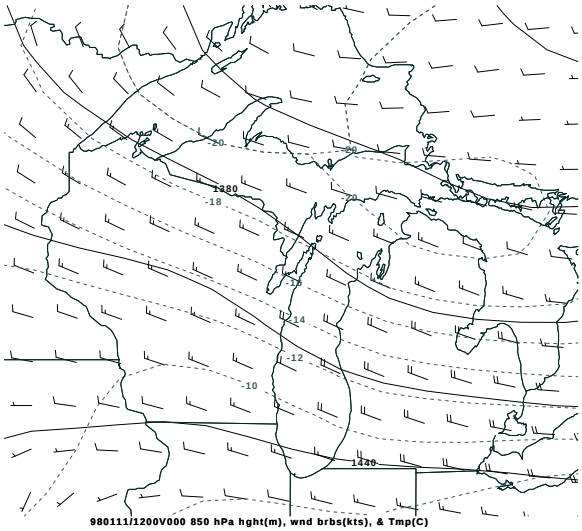

Figure 3.18: 850 hPa surface (solid), temperature (dashed), and gridded winds at 12 UT on 11 January 1998.

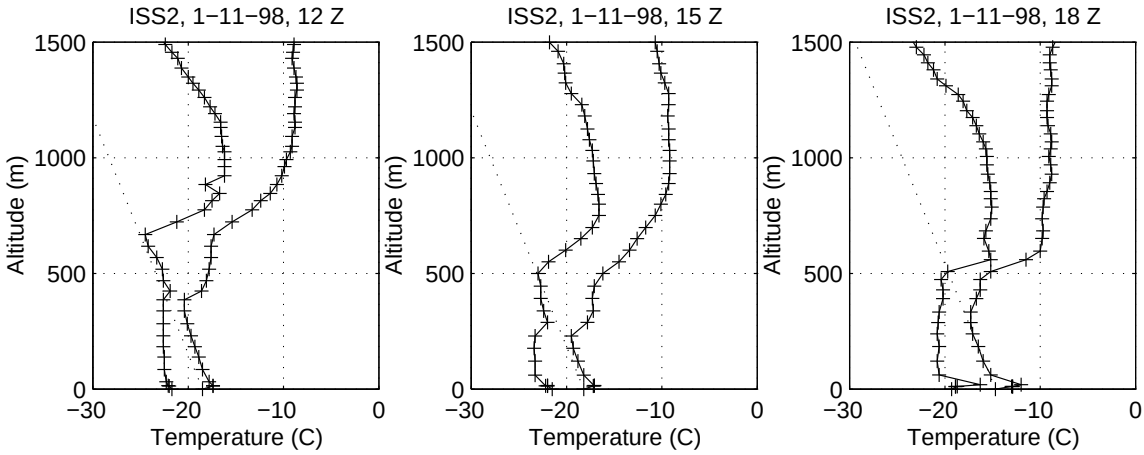

Figure 3.19: Temperature and dew-point soundings from NCAR's ISS site in Sheboygan, WI, on 11 January 1998.

The synoptic situation suggests subsidence as the cause. In contrast to some of the CAPPIs from 10 January, CAPPIs at all altitudes on 11 January have strong aerosol scattering structure. At low altitudes, the pattern is similar to that observed near the surface on 10 January. This pattern near the surface can be described as "cellular" where the walls of the cells are narrow and contain high aerosol scattering relative to the much broader and low scattering centers of the cells. At altitudes above about 100 m, the brightest spots on the CAPPIs are circular plumes rather than narrow walls. The size of these plumes increases as we approach the upper part of the boundary layer. At these altitudes we also see evidence of inhomogeneity. For example, in the CAPPIs above 300 m in Fig. 3.21 the variability of aerosol scattering is much larger on the right side of the image. This is evidence of stronger convection in the growing internal boundary layer over the lake.

The names *open-cell* and *closed-cell* are often used to describe mesoscale shallow convection patterns observed in satellite imagery. The mesoscale shallow convection cells have much larger diameters and aspect ratios (sometimes 30:1) in comparison to those cells observed in the lidar data. This assumes that the altitude of the top of the boundary layer is the vertical dimension of both type of cells. In both cases, open-cells have broad clear centers with relatively narrow walls outlined by convective clouds or high-aerosol scattering. Closed-cells have broad cloudy, or high aerosol-scattering, centers with narrow walls that are absent of clouds (Atkinson and Zhang, 1996) or high aerosol-scattering. Celluar patterns with aspect ratios close to one (i.e. the width of the cell is approximately the height of the ABL) have been observed many times with radars and lidar (see for example Konrad 1970 and Eloranta and Forrest 1992).

Fig. 3.25 shows the mean and standard deviation of aerosol backscatter on east-west oriented vertical planes. For each pixel on one of these images, the north-south oriented rows of aerosol backscatter from multiple times from gridded volume scans

were used. The left panels show the mean aerosol backscatter and the right panels show the standard deviation. These images show no obvious signature of the edge of the CIBL, such as the parabolic curves in the idealized diagrams in the introduction. Instead, the obvious features are the top of the boundary layer advecting offshore which can be seen by the strong vertical gradient in the mean and a local maximum in the standard deviation. Very close to the surface in the mean, the effect of the mixing fog is evident by the wedge shaped shadow which becomes taller to the right. In the standard deviation panels this shows up as an increase. Most interesting perhaps is what appears to be the formation of cumulus clouds at the top of the mixed layer beyond approximately 6 km offshore. Clouds cause strong shadows which cause the standard deviation to increase sharply in this region. All of these panels confirm a mixed layer that is about 400 m during the first volume scan and decreases to approximately 200-250 m deep before the second set of volume scans. Because the boundary layer height doesn't change that much as a function of offshore distance in these images, it appears that the capping inversion is very effective at limiting its depth over the lake in this near-shore region.

No lidar observations were collected on 12 January.

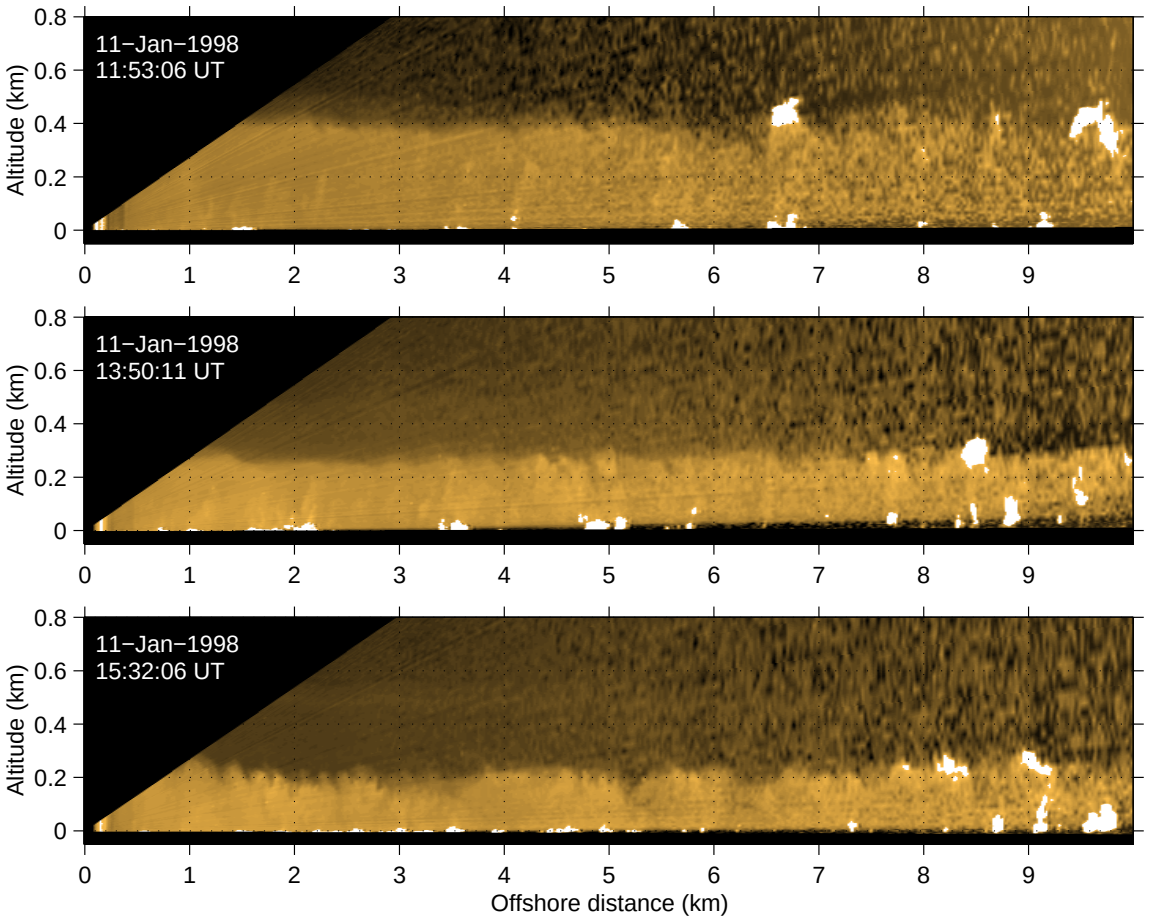

Figure 3.20: Three RHI scans at different times all pointing due east on 11 January 1998.

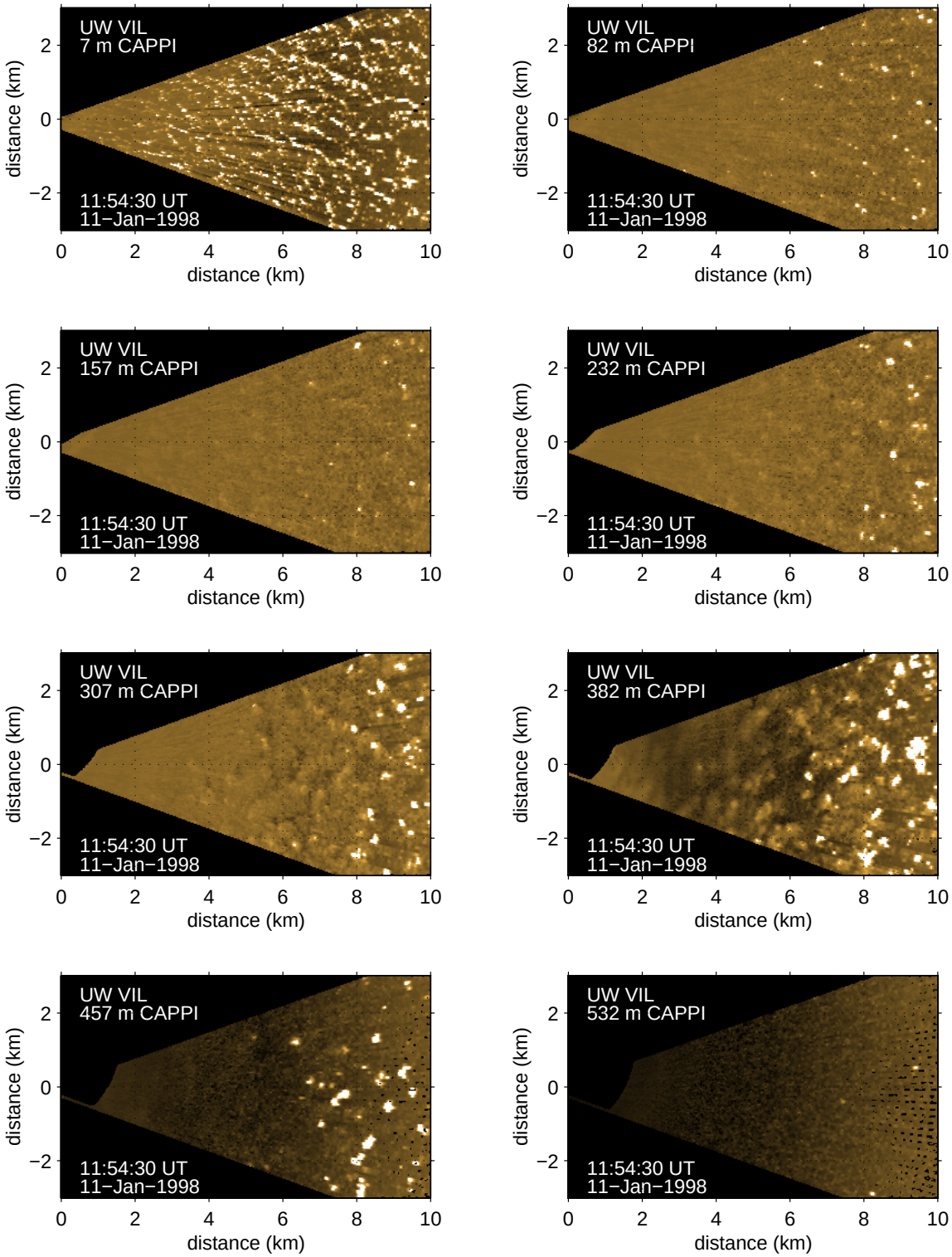

Figure 3.21: CAPPIs from first set of RHI volume scans on 11 January 1998.

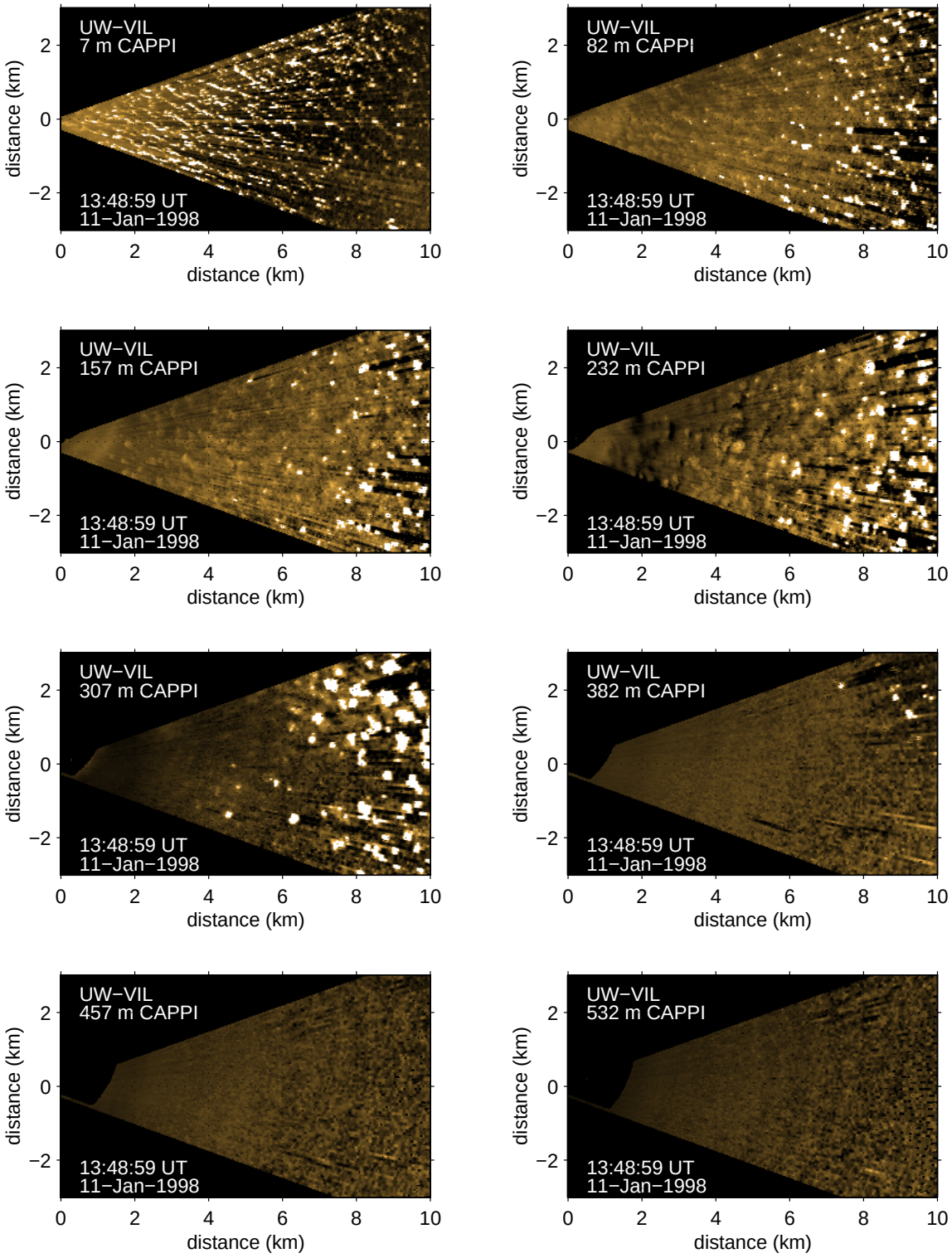

Figure 3.22: CAPPIs from second set of RHI volume scans on 11 January 1998.

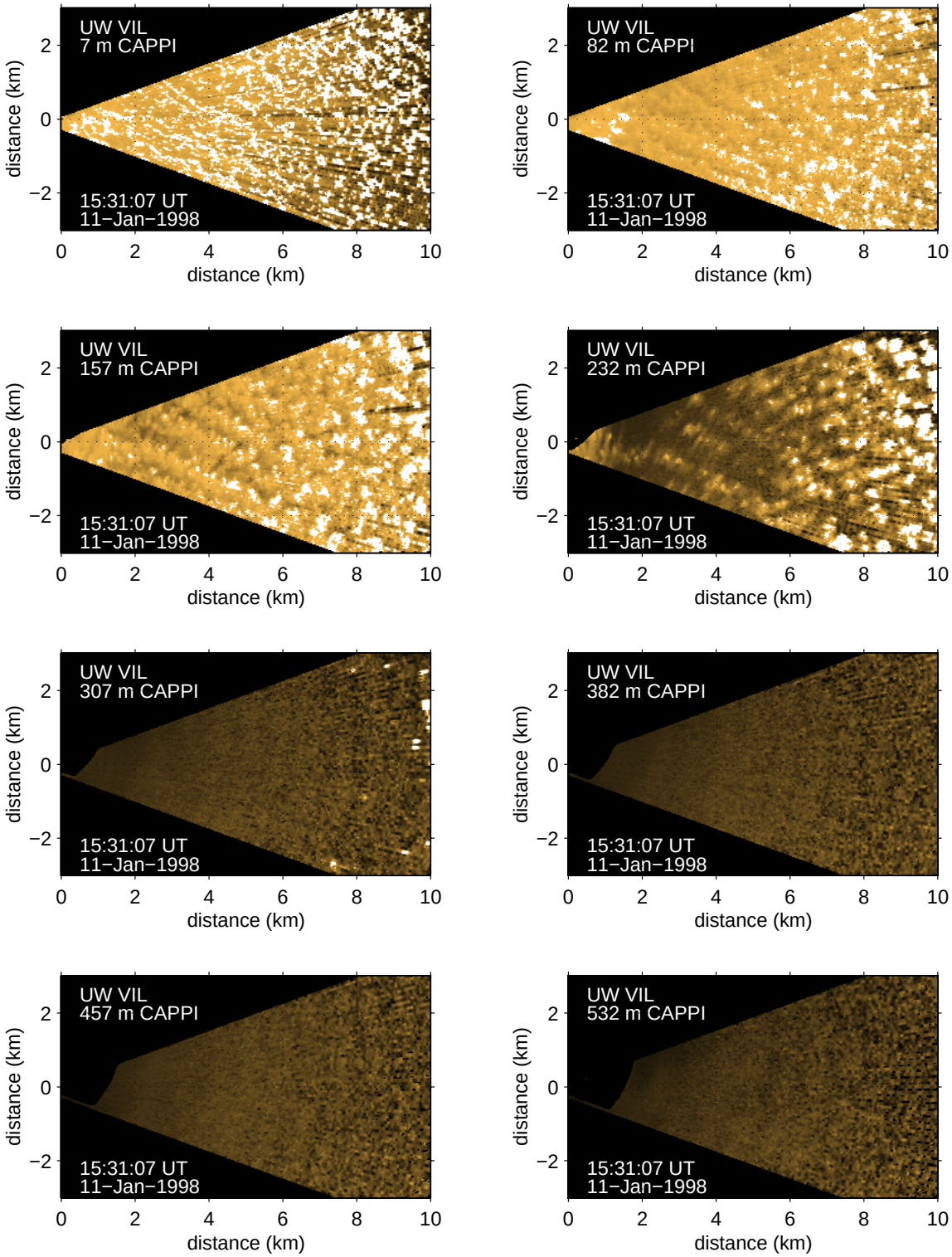

Figure 3.23: CAPPIs from third set of RHI volume scans on 11 January 1998.

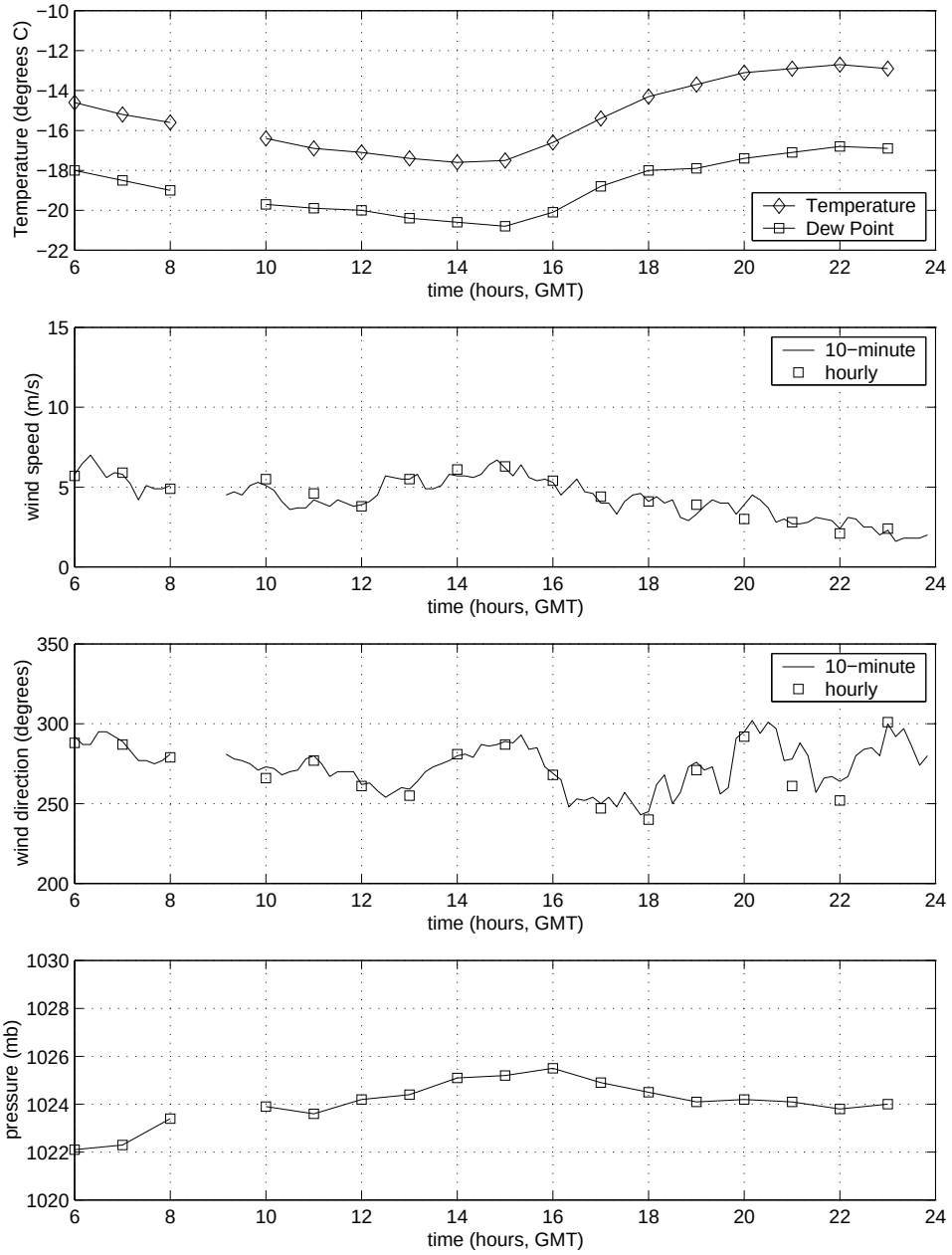

Figure 3.24: Traces of temperature and dew-point, wind-speed, wind-direction, and barometric pressure from the Coast Guard station near the VIL site on 11 January 1998.

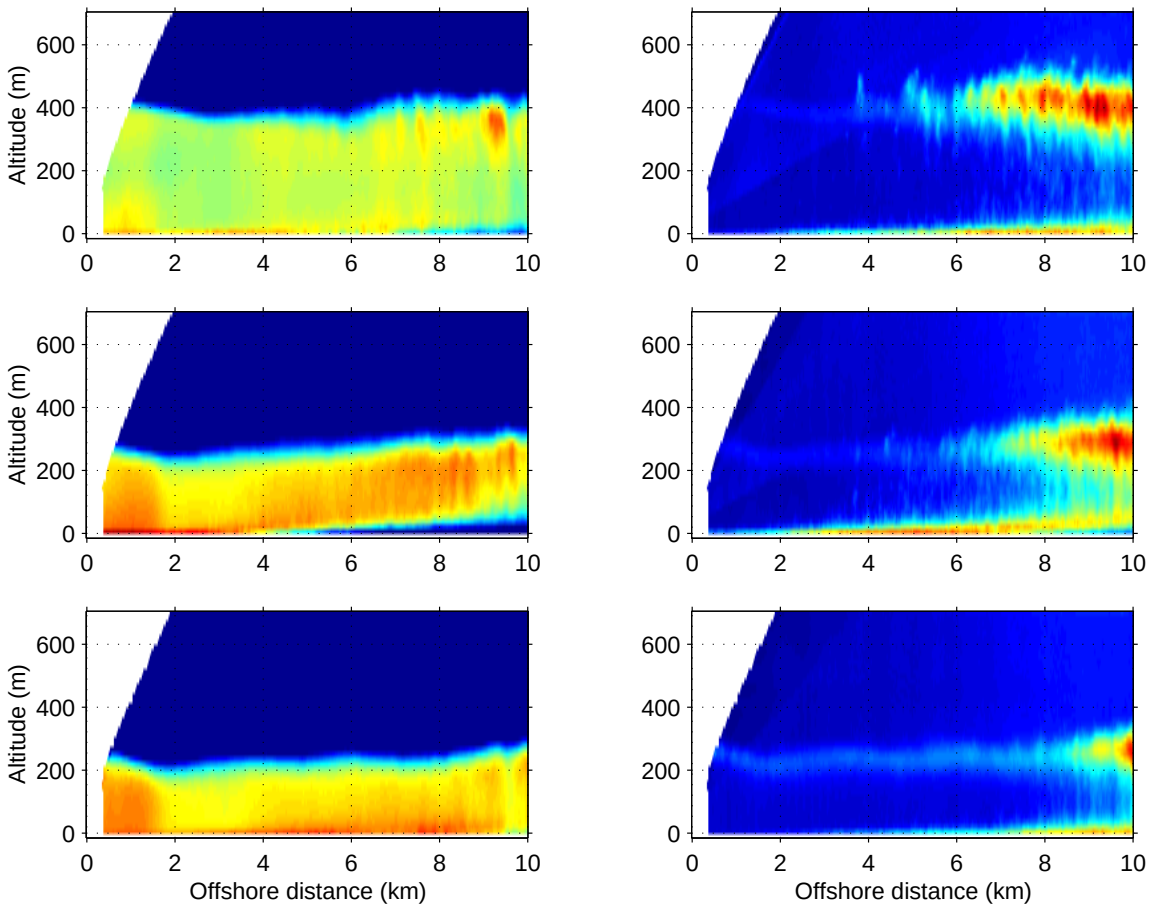

Figure 3.25: Mean (left panels) and standard-deviation (right panels) of relative aerosol backscatter from three volume scanning periods on 11 January. The periods were from 11:51-12:16 UT, 13:47-14:30 UT, and 15:29-16:23 UT.

3.5 13 January 1998

On 13 January 1998, a cold-front was located over New York State, western Pennsylvania, and the Appalachain Mountains. A high-pressure system was located over western Iowa and the surface winds across Wisconsin were from the west-northwest at 5-10 m s^{-1}. Strong cold air advection spanned the entire region again (See figs. 3.28 and 3.27). Air temperatures dropped to -22°C at 14 Z near the lidar site. Clear skies were observed overhead and to the west of the lidar site. Steam-fog was present over the lake and offshore clouds were observed. The smooth curve of solar radiation near the surface as a function of time in the second panel of fig. 3.30 supports this. If clouds had been present the curve would not have the smooth sinusoidal shape. Fig. 3.26 shows a visible satellite image of the western Great Lakes region on 13 January at 16:30 UT. This image confirms clear skies over Wisconsin and the formation of boundary layer clouds over the lake. Fig. 3.30 shows traces of temperature, solar radiation, net-radiation, wind-speed, wind-direction, and pressure versus time from surface sensors at the NCAR ISS site near Sheboygan on 13 January. Fig. 3.31 show traces of temperature, wind-speed, wind-direction, and pressure at the NOAA weather station SGNW3 located near the lidar site in Sheboygan. This site was located about 750 m from the VIL and it confirms that the conditions 10 km west of the lidar site were not that much different from those at the shore.

VIL data on 13 January indicated that 400–500 m deep mixed layer was advecting offshore (see figs 3.32 and 3.34). Radiosonde soundings, shown in fig. 3.29 at the NCAR ISS site confirm the presence of the inversion base at about 400 m. PPI scans such as the one shown in 3.33 show open cell patterns, like the ones also observed on 10 and 11 January, near the surface. On the 13th however, the cellular patterns are not observed beyond approximately 10 km offshore.

A strong effect of the shadowing caused by the mixing fog can be see in the top and center panels of fig. 3.37. The formation of clouds near the top of the ML is also evident beyond about 5 km.

Figure 3.26: Visible satellite image showing Wisconsin, Lake Michigan and Michigan at 16:30 UT on 13 January 1998.

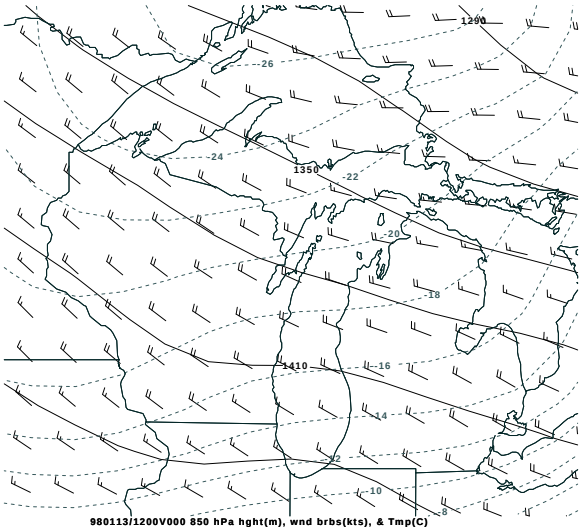

Figure 3.27: 850 hPa surface (solid), temperature (dashed), and gridded winds at 12 UT on 13 January 1998.

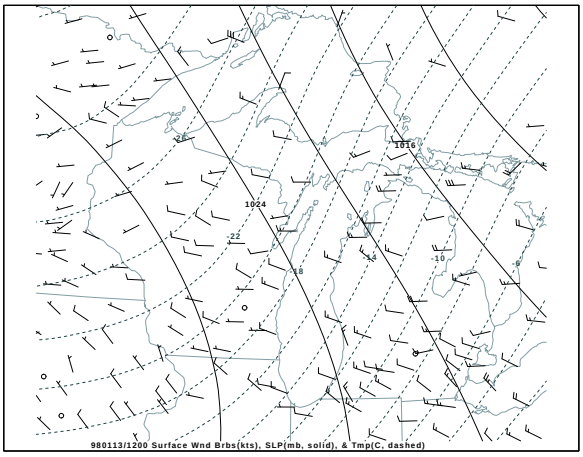

Figure 3.28: Surface pressure (solid), temperature (dashed), and wind observations at 12 UT on 13 January 1998.

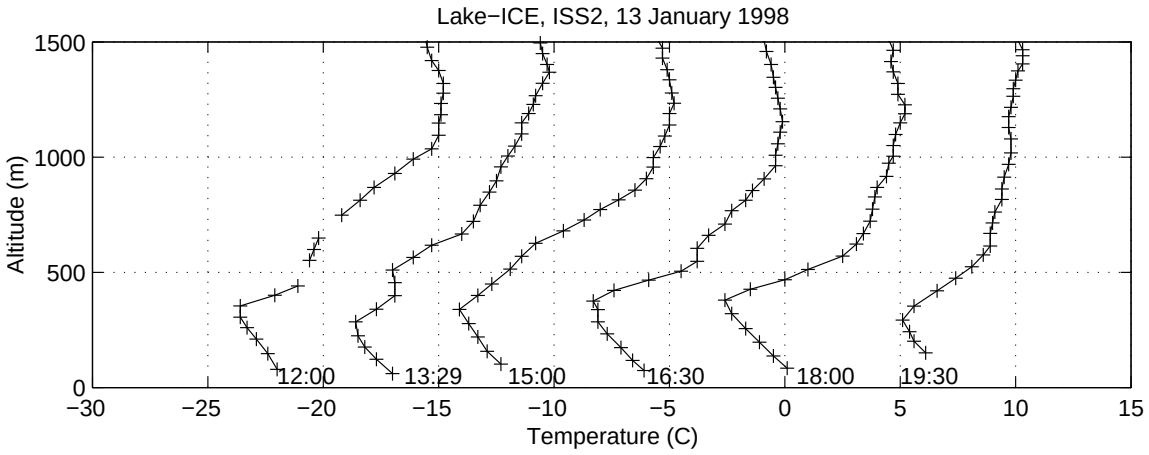

Figure 3.29: Temperature profiles from six soundings taken on 13 January 1998 at the NCAR ISS site.

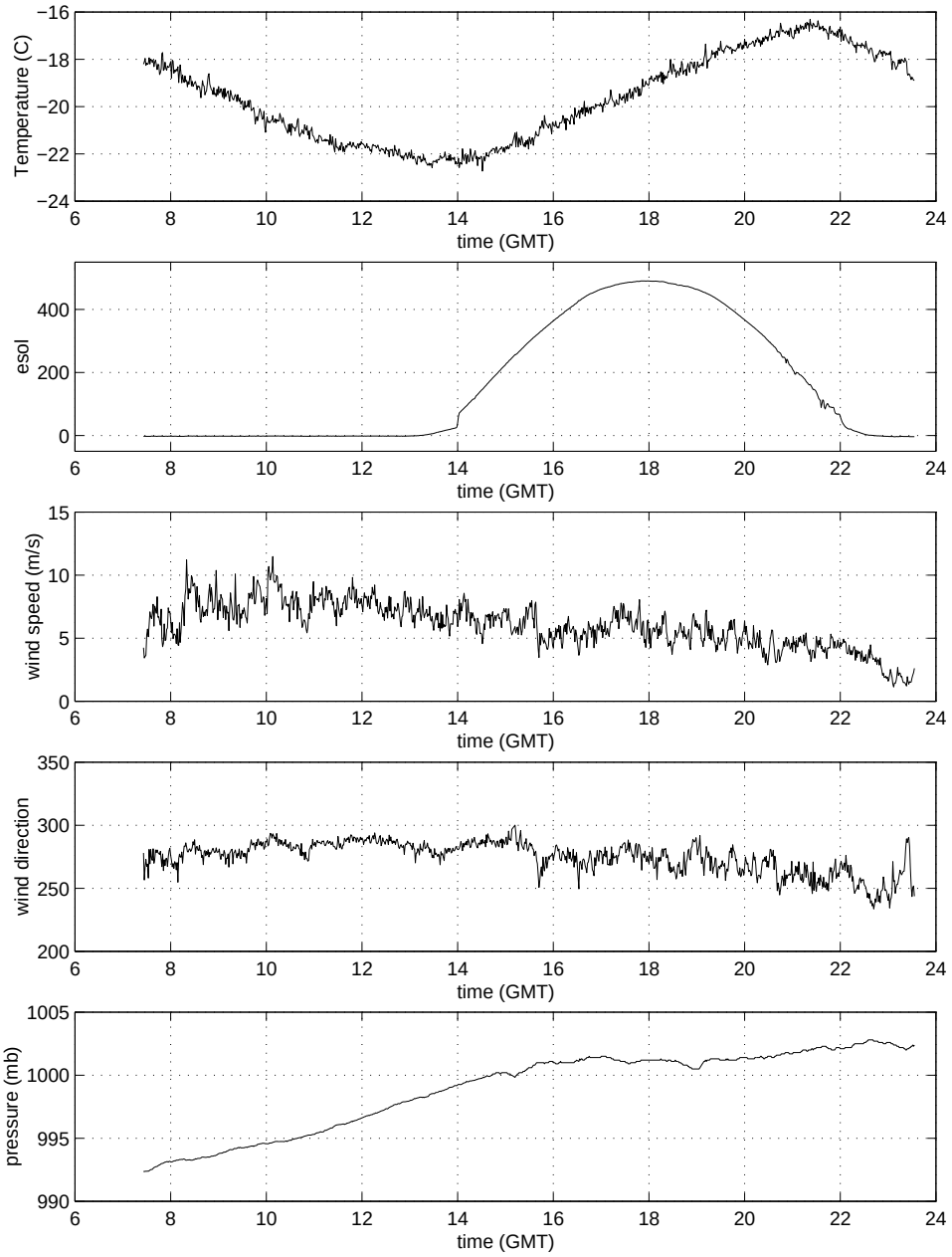

Figure 3.30: Surface variables measured as a function of time on 13 January 1998 at the NCAR ISS site near Sheboygan.

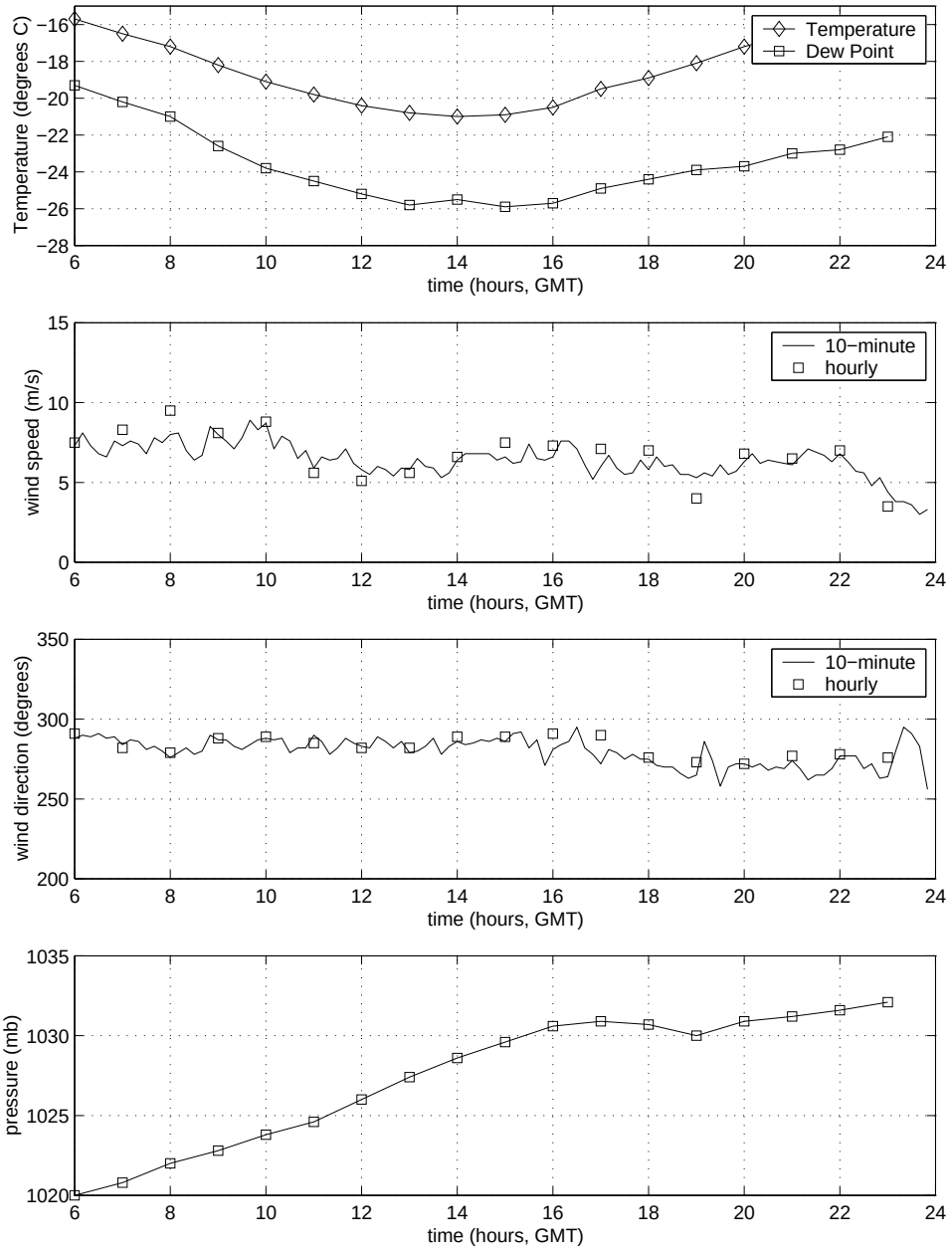

Figure 3.31: Temperature and dew-point, wind-speed, wind-direction and barometric pressure measured at the Coast Guard Station near the lidar site on 13 January 1998.

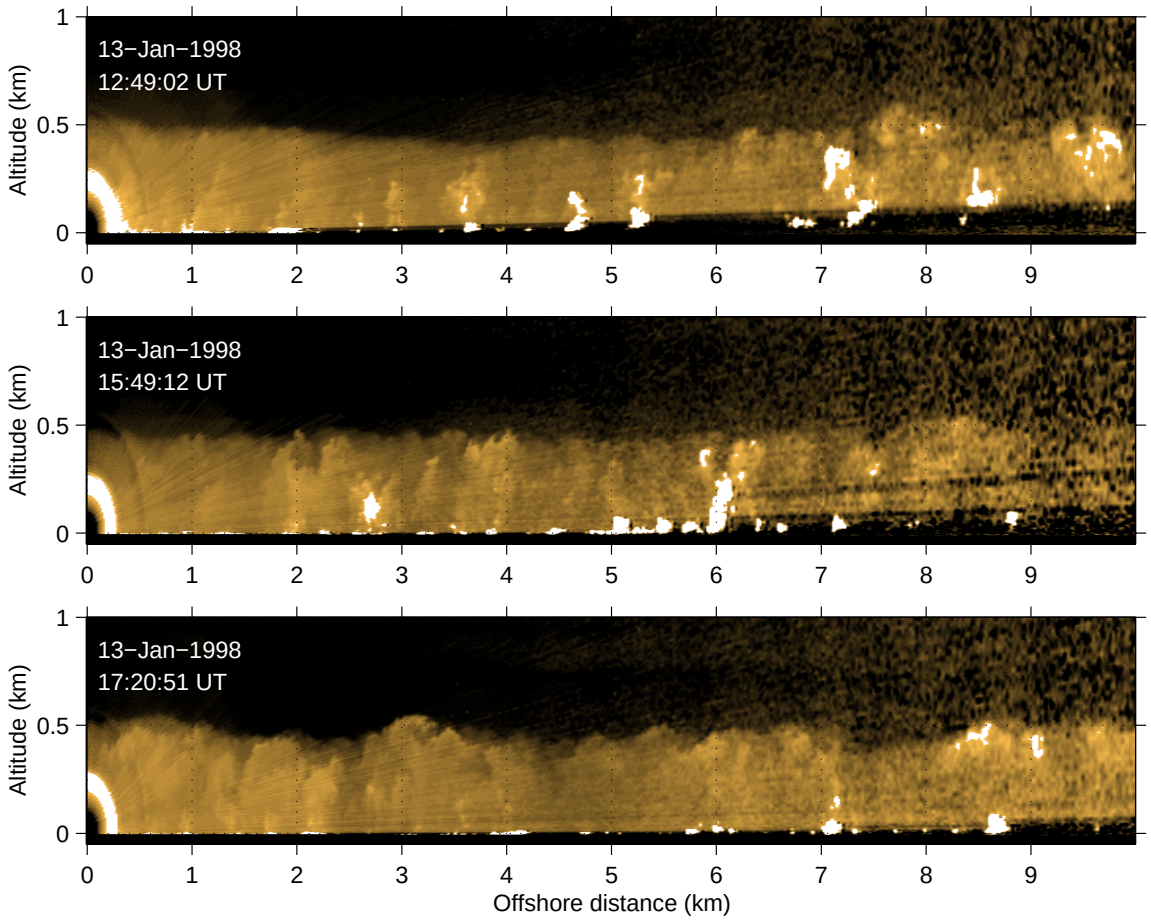

Figure 3.32: Three eastward pointing RHIs each from RHI-volume scans on 13 January 1998.

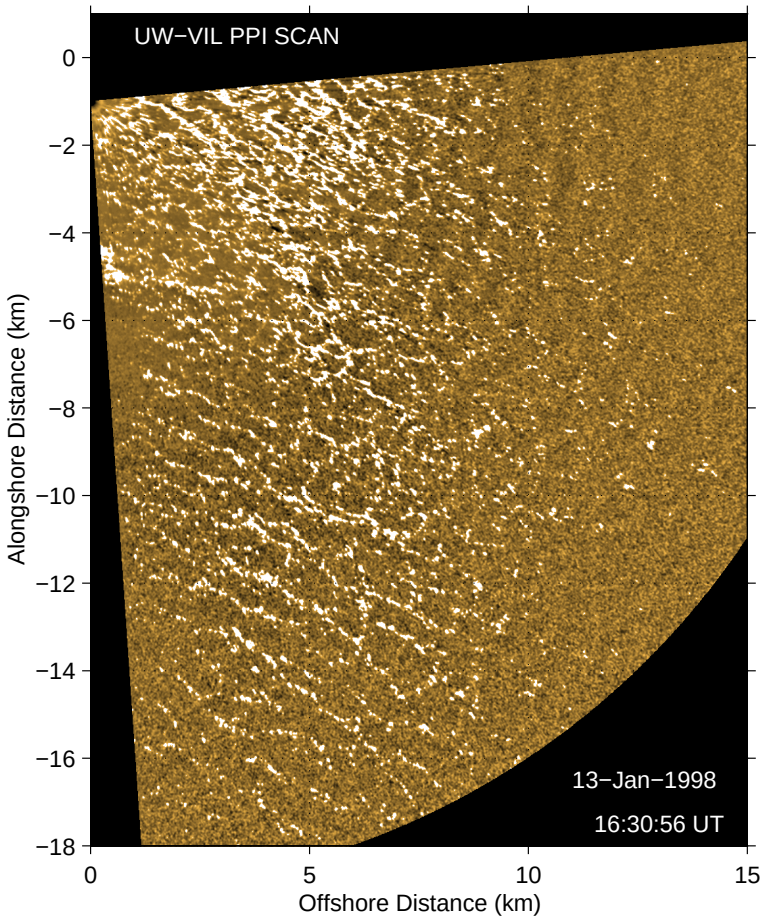

Figure 3.33: One PPI scan from the VIL on 13 January 1998. A 60-point high-pass median filter has been applied to these data to remove distracting shadows.

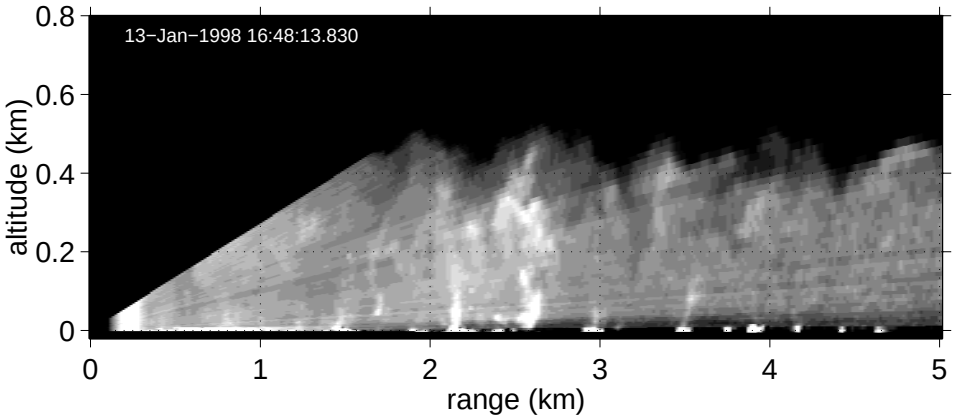

Figure 3.34: One RHI scan from the VIL on 13 January 1998. (High-pass median filter not applied.)

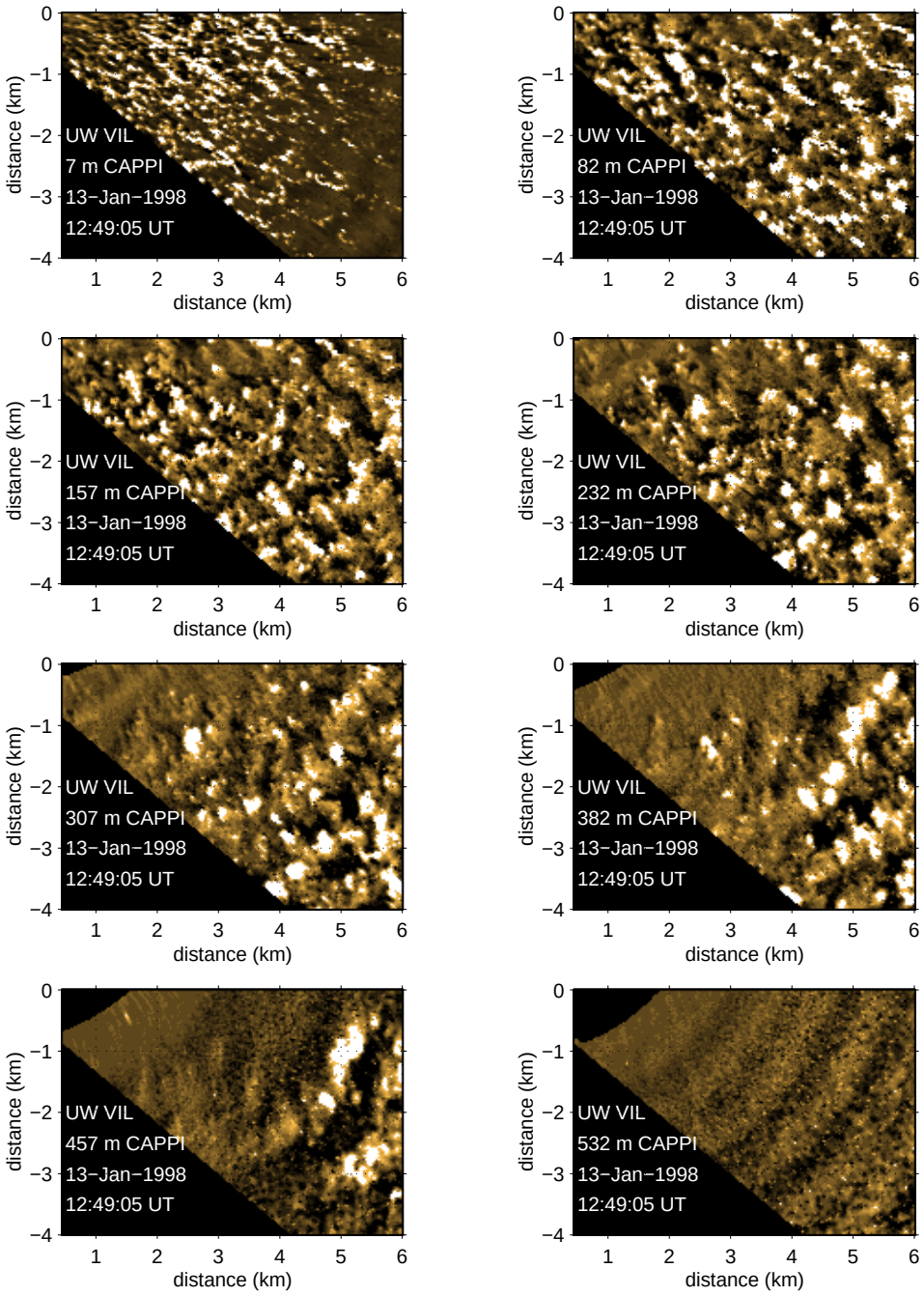

Figure 3.35: CAPPIs from an RHI volume scan at 12:49 UT on 13 January.

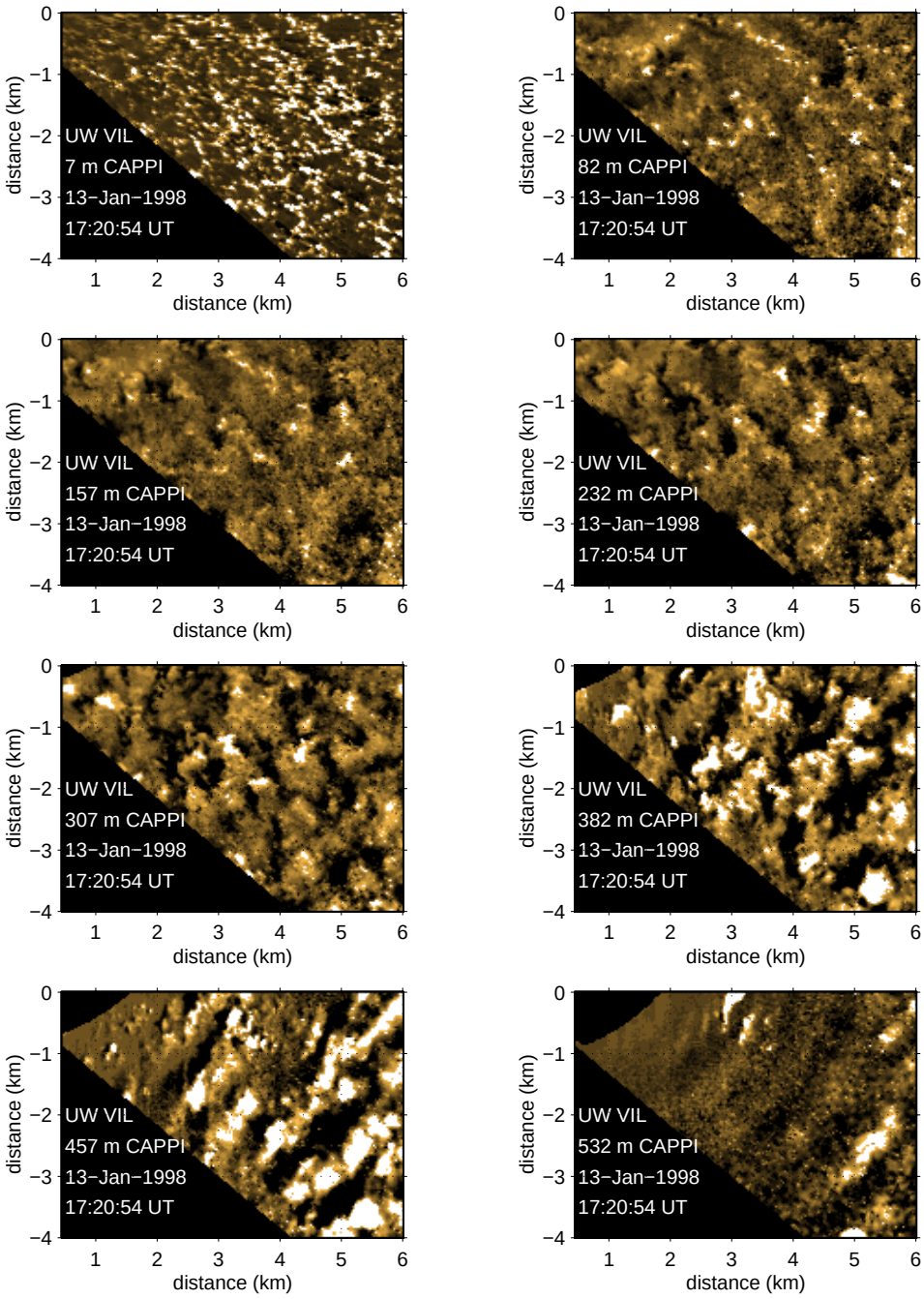

Figure 3.36: CAPPIs from an RHI volume scan at 17:20 UT on 13 January.

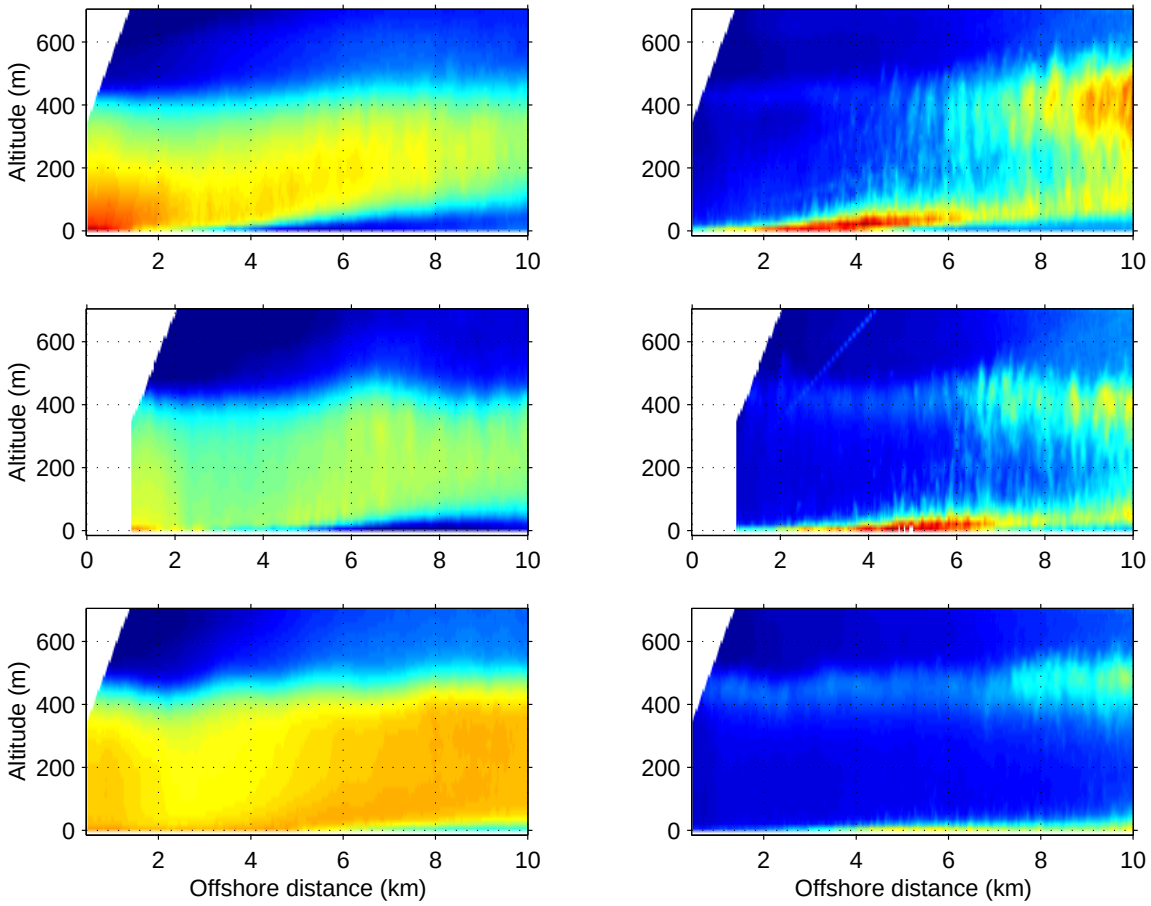

Figure 3.37: Mean (left panels) and standard-deviation (right panels) of relative aerosol backscatter from three volume scanning periods on 13 January.

Date	Low	High	Warming Rate	Speed	Direction	ML Depth
Jan 10	-16.5	-11.5	5 ° /8 hr	8-10 m/s	250°	1 km
Jan 11	-17.5	-13	4.5° /8 hr	4-6 m/s	250-300°	200-400 m
Jan 13	-21	-16.5	4.5° /8 hr	5-8 m/s	260-300°	400 m

Table 3.2: Upwind meteorological conditions on the three cold air outbreak days examined. Temperature and wind information was measured at the surface.

3.6 Chapter Summary

This chapter presented lidar and conventional weather observations from three days when very cold air was advecting offshore at the lidar site. In each case, westerly flow was present ranging from 250–300° and morning low temperatures ranged from -16.5°C to -21°C. Also common to each day were surface air temperature warming rates ranging from 4.5°C to 5°C over 8 hours. Because these dates occurred within the same week, the mean land surface albedo and the surface temperature of the lake probably didn't change that much. Cellular structure of steam fog was observed on each day.

The largest difference of the three cases presented was the height of the boundary layer advecting offshore which ranged from 1 km on the 10th to 200 m on the 11th. The surface wind speeds ranged from 4–10 m s^{-1}. Synoptic weather maps showed that cold air advection was strongest on the 10th and the 13th, and weak on the 11th.

The *average* lidar backscatter data does not show a well-defined parabolic edge of a convective internal boundary layer such as the one drawn in fig 1.1. The *average* lidar backscatter data does not show a gradual increase in intensity with increasing offshore distance either. This is somewhat suprising since optical aerosol scattering should increase exponentially with increasing relative humidity (see section 5.3 and fig. 5.1) and the mean relative humidity probably increases with increasing offshore distance. However, steam-fog does cause the mean and standard deviation of lidar backscatter to be large in the surface layer and the formation of clouds at distances beyond about 6 km increase the mean and standard deviation of backscatter in that region also.

The top of the boundary layer as a function of offshore distance does not change very much. There does however appear to be a systematic local minimum, though only 25–50 m lower than the surrounding BL top, at about 2 km offshore. This can be attributed to acceleration of boundary layer flow and will discussed more in section 4.4.

Lastly, the soundings and VIL observations from 13 January suggest that fig. 1 in Young et al. (2000) should be modified to include a 400-m deep mixed-layer advecting offshore on the western end of the lake. The diagram incorrectly shows a traditional IBL starting from the surface at the upwind shore.

Chapter 4

Aerosol Structure Motion

This chapter is reprinted from (Mayor and Eloranta, 2001) with permission of the American Meteorological Society.

Many problems in boundary layer meteorology require knowledge of two- and three-dimensional wind vectors in clear conditions with microscale resolution over a mesoscale area. Examples include determining the flow-field over complex terrain, resolving the eddies responsible for turbulent transport, predicting the dispersion of a pollutant, and verifying numerical models. Because of the difficulty and cost of deploying arrays of in situ wind sensors, remote sensors such as radars and lidars are are well-suited to measure the wind-field.

To measure the wind, Doppler radars and lidars rely on individual scatterers being tracers of air motion and only measure the radial component of motion of scatterers along the transmission path. To obtain both the u and v components of the wind-field using ground-based Doppler sensors, at least two instruments with overlapping scan volumes are required (Kropfli and Hildebrand, 1980), or a computationally intensive numerical technique such as single Doppler adjoint-methods (Xu and Qiu, 1995). Radars offer excellent coverage ($\approx 10^4$ km^2), and can penetrate clouds and precipitation, but they require insects, Bragg scattering, or chaff in order to image the clear atmosphere (Gossard and Strauch, 1983).

Lidars are able to image the visually clear atmosphere by scattering from naturally occurring aerosol particles. However, they are limited in range by severe attenuation from clouds and can typically map regions on the order of 100 km^2. Airborne Doppler lidars can map the wind-field over much larger areas by alternating the pointing direction or scanning the beam during flight. The translation of forward and aft directed beams while moving produces a grid of points where the beams intersect allowing the extraction of 2 and 3-D wind vectors (Bilbro *et al.* 1984 , Rothermel *et al.* 1998). Down-looking velocity-azimuth-display (VAD) scans from an airborne lidar can also provide spatially resolved wind fields (Werner *et al.*, 2001).

Non-Doppler, ground-based, scanning aerosol backscatter lidars can measure the wind speed and direction by cross-correlation of coherent aerosol structures (Eloranta *et al.* 1975 , Sasano *et al.* 1982). The cross-correlation technique has also been

successfully applied to radar data (Smythe and Zrnic 1983 , Tuttle and Foote 1990). To obtain the wind-field the approach relies on the assumption that coherent structures in the backscattering field are advected by the wind at that location. The technique relies on inhomogeneities in the scattering field. Both horizontal components of the wind vector can be obtained from the scans of a single instrument.

Non-Doppler incoherent lidars do not require coherent detection which removes limitations of telescope diameter and relaxes requirements for high spectral purity lasers. This lack of restriction becomes more attractive as large lightweight mirrors and small powerful lasers become more affordable and commercially available. The higher signal-to-noise ratio of incoherent systems allows faster imaging of the aerosol field. In addition to the wind-field, these measurements can also be used to compute mean dimensions and lifetimes of the turbulent eddies.

Unfortunately, the cross-correlation technique does not measure the wind velocity in all conditions. Coherent structures may not be advected with the wind in the scan-plane or scan-volume. Consider, for the simplest example, a non-scanning aerosol backscatter lidar intended to only measure the radial motion of coherent structures along the beam. Motion in any direction other than parallel to the beam from any structures not oriented perpendicular to the beam will result in a false velocity (see top of Fig. 4.1). By scanning in azimuth or elevation, non-radial motion of structures not aligned in the orthogonal directions as defined by the scan-plane will lead to false radial velocities. Three-dimensional scans strategies are able to eliminate this possibility, but are still susceptible to false velocities from wave-like motions.

Fortunately, irregularities in the aerosol scattering field within turbulent regions are usually oriented in all directions (see bottom of Fig. 4.1) and by averaging in space and time, the motion of the coherent structures advecting with the wind dominates the correlation functions. Previous work which compares the technique with observations from tower-mounted anemometers, radar-tracked pilot balloons, radiosondes, kytoons and aircraft shows agreement to within the uncertainty imposed by differing sample volumes or averaging times (Eloranta *et al.* 1975 , Kunkel *et al.* 1980 , Sroga *et al.* 1980 , Hooper and Eloranta 1986 , and Piironen and Eloranta 1995).

In previous work (Schols and Eloranta 1992 , Pirronen and Eloranta 1995) algorithms were developed to measure vertical profiles of the horizontal wind from volumetric lidar images of aerosol structure. These algorithms derived a single wind vector for each altitude representing the mean wind averaged over the approximately 100-km^2 area of a typical lidar scan. In this work, these algorithms were applied to allow computation of the spatially-resolved time-averaged wind field from successive near-zero-degree-elevation azimuthal-scans (plan-position indicator, PPI) and constant-azimuth elevation-scans (range-height indicator, RHI).

4.1 The Cross-correlation Technique

Extracting wind vectors from the backscatter data follows the basic approach described by Schols and Eloranta (1992) . The only difference in the initial processing

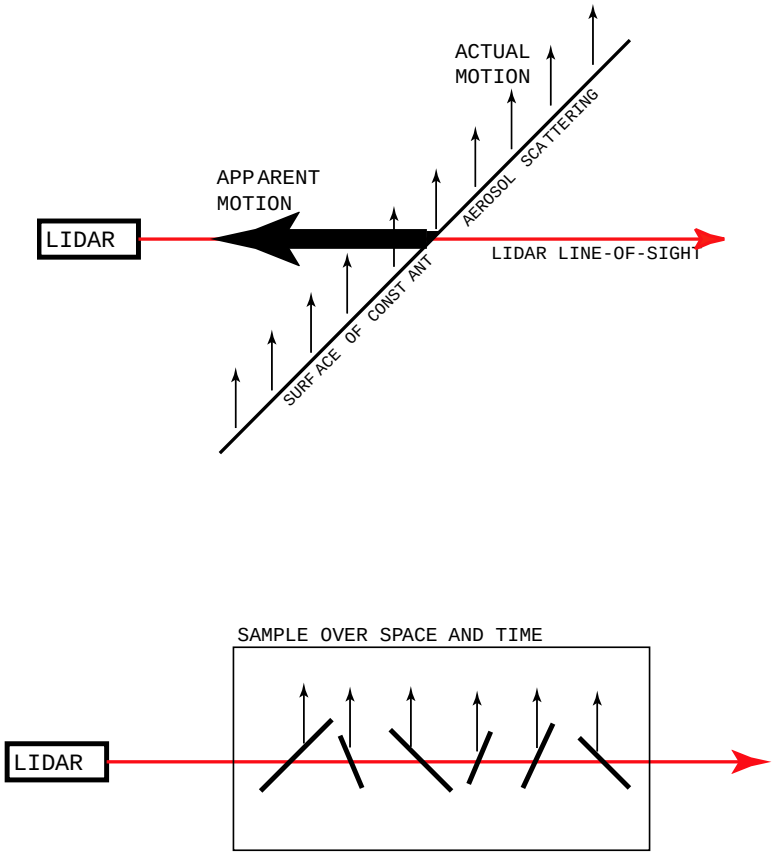

Figure 4.1: Top: example of how an aerosol gradient moving perpendicular to the lidar beam can produce an apparent velocity toward the lidar. Bottom: Fortunately, turbulence usually orients aerosol gradients in different directions eliminating this problem. In the bottom panel, the structures are moving perpendular to the laser beam but there is no apparent radial motion from lidar because of averaging many structures over space or time.

occurs because the scan consists of a single horizontal plane instead of a volume scan. The initial processing steps proceed as follows:

1. Individual lidar shots are corrected for the one-over-range-squared dependence of the returned signal and then filtered with a running median high-pass filter. The filter length was set to 450 m for the results presented here. The high-pass median filter works as follows: for each point in the array to be filtered, its nearest neighbors within one filter length (half a filter length on each side) are sorted. The center value of the sort is subtracted from the data value in the array being filtered.

2. The lidar data are mapped to a Cartesian grid with a uniform spatial resolution of 15 m. Data points on the Cartesian grid are computed from a linear interpolation between the 4 nearest points in the polar coordinates of the raw lidar-profiles. To correct for the distortion of the lidar image caused by the wind and a finite scan-duration, the position of data points in the lidar profiles are adjusted to the position they occupied at the time the first profile of the scan was acquired. The wind vector needed for this adjustment is estimated from a trial solution.

3. A temporal-median image is then formed from the complete set of Cartesian scan-images. In order to remove stationary features and artifacts caused by attenuation, this median image is subtracted from each of the scan images.

4. Finally, to prevent individual bright features in the image from dominating the cross correlation function, the resulting images are subjected to histogram normalization.

Up to this point, the wind processing is nearly identical to the scheme for computing winds averaged over the entire scan area as described in Pirronen and Eloranta (1995) . However, in order to compute the spatial variation of the wind field, the scan area must now be divided into sub-areas. For the PPI scans collected on 10 and 13 January 1998, we first computed the wind-vector field from adjacent square areas that were 500-m on each side. The resulting 500-m resolution wind field is used to initialize calculation of 250-m resolution winds.

For each sub-area two-dimensional correlation functions are computed between every other scan so that left-right/right-left scans are always paired with the same scan direction and thus the time interval between laser profiles in each part of successive images is approximately the same. For the 90° PPI scans shown here, this results in an approximately 24-s time separation between scans. Because the winds were as large as 9 m s^{-1}, the wind advected structures by up to 216 m between scans. Thus, for boxes smaller than about 500-m on a side, the cross-correlation suffers because most of the structure seen in a sub-area in one scan has advected out of the sub-area by the time of the next scan. This creates small correlation maxima contaminated by random correlations between unrelated structures.

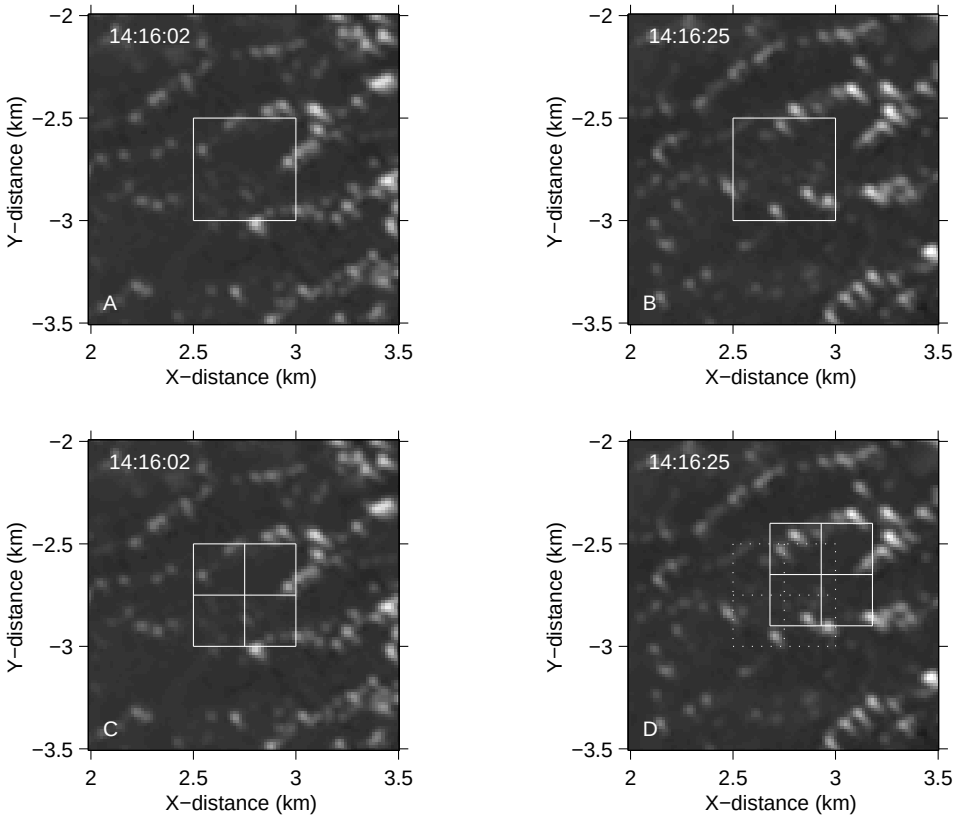

Figure 4.2: Subset of data for two PPI scans on 10 January 1998. The left two images are from 14:16:02 and the right two images are from 14:16:25. compute a single 500-m resolution wind vector, data from inside the white solid squares in the top two frames, which are located in the same place, are used for cross-correlation. The resulting vector is then used to displace 250-m resolution boxes as shown in the lower right frame.

To increase the correlation for smaller boxes, the procedure is modified. The location of the sub-area in the second frame of each pair is displaced downwind by the distance the structure is expected to move between frames. The wind vector obtained from cross-correlation of larger boxes is used to compute the displacement of the smaller boxes. This allows the correlation to take place with approximately the same features that were present in the first frame. The position of the correlation maximum is then corrected for the displacement of the box to compute the wind vector. Fig. 4.2 shows an example of 500 m and 250 m sub-areas for two scans.

4.2 10 January 1998

The top panel in Fig. 4.3 shows the average wind field computed for data acquired between 14:16 and 14:57 UT (8:16 and 8:57 AM CDT). The wind shadow in the lee

of the coastline is clearly visible. The wind shadow length varies with position. This probably reflects variations in the topography and surface roughness along the shore. The acceleration and veering of the wind as it leaves the shore is clearly seen in fig. 4.4. This presents a north-south average of the wind speeds and directions along with a crude estimate of errors. The length of the error bars were computed from the variance of the values contributing to each north-south average. The plotted length of the error bar is equal to the variance divided by the square root of the number of points (square-root of 24 in this case) contributing to the average. While these error bars provide an estimated upper bound for the random fluctuations in the wind, they are not true error estimates. They tend to underestimate the true error by failing to include systematic errors while at the same time tending to overestimate the errors because the true geophysical variability is included in the calculated variance.

The divergence and vorticity of the wind field can be computed from

$$\nabla \cdot \vec{V}_{i,j} = \frac{u_{i+1,j} - u_{i-1,j}}{x_{i+1} - x_{i-1}} + \frac{v_{i,j+1} - v_{i,j-1}}{y_{j+1} - y_{j-1}} \tag{4.1}$$

and

$$\nabla \times \vec{V}_{i,j} = \frac{v_{i+1,j} - v_{i-1,j}}{x_{i+1} - x_{i-1}} - \frac{u_{i,j+1} - u_{i,j-1}}{y_{j+1} - y_{j-1}}, \tag{4.2}$$

respectively. These divergence and vorticity fields are shown in the middle and bottom panels of Fig. 4.3, respectively, and were derived from the wind vectors which are also plotted on them.

In fig. 4.3b notice the strong divergence along the shoreline caused by the acceleration of the wind as it adjusts to the lower surface roughness lengths presented by the water relative to the land. Several linear structures, aligned approximately with the mean wind direction near the surface, can be seen. A narrow band of divergence extends downwind from a point ≈3.2 km south of the lidar. The Edgewater power plant, which consists of a very large building complex, is located at this point on the shore. We estimate the building to be ≈60 m wide and tall.

Fig. 4.5 presents the mean divergence as a function of distance from shore calculated from the data presented in fig. 4.3b. Random variations in the smoothed curve between 3.5 and 5.5 km from shore appear to be less than 10^{-4} s^{-1}.

Fig. 4.3c shows the vorticity field computed from the wind vectors. Fig. 4.6 shows the mean vorticity as a function of distance from the shore. Strong negative vorticity appears along the shoreline as the wind veers in response to the smaller friction over water. In Fig. 4.3, the possible wake feature shown in the divergence field appears as a strong negative vorticity wake. At distances greater than ≈3 km from the shore there is evidence of a coupled band of positive vorticity north of the negative band. Our preliminary large-eddy simulations of turbulent flow around a building of similar size support the hypothesis that this pattern is due to the presence of the building. We speculate that the wake is amplified by convective instability.

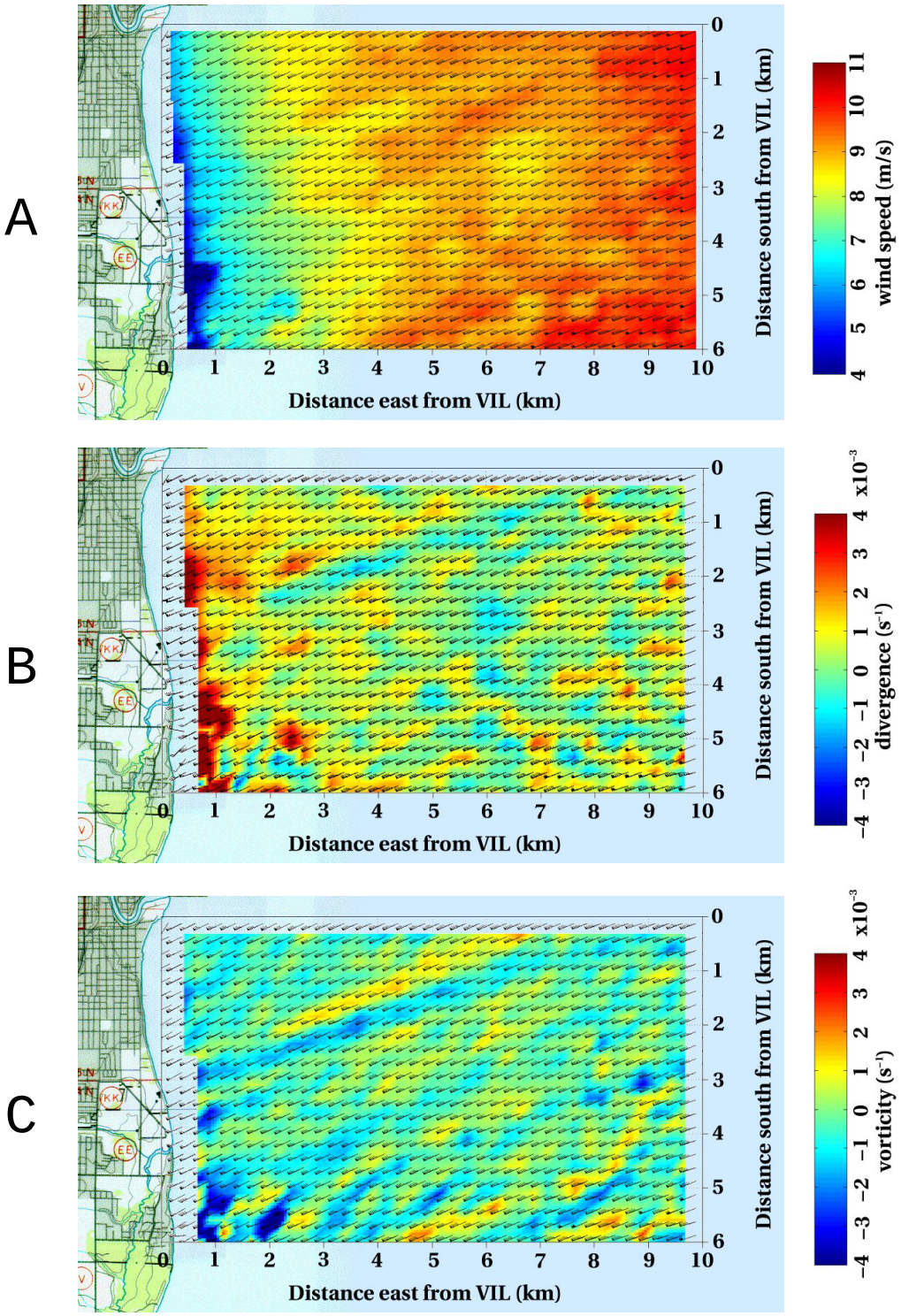

Figure 4.3: Aerosol structure speed, divergence and vorticity on 10 Jan 1998.

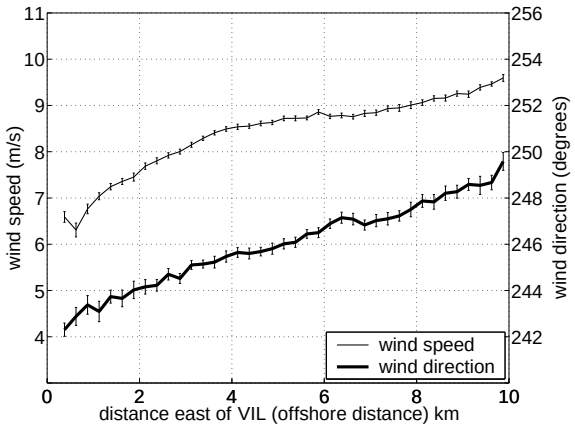

Figure 4.4: Mean wind speed and direction as a function of offshore distance on 10 Jan 1998.

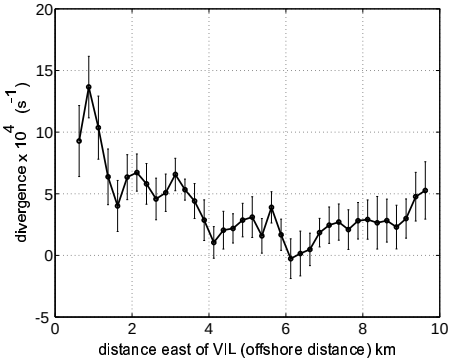

Figure 4.5: Mean divergence as a function of offshore distance on 10 Jan 1998.

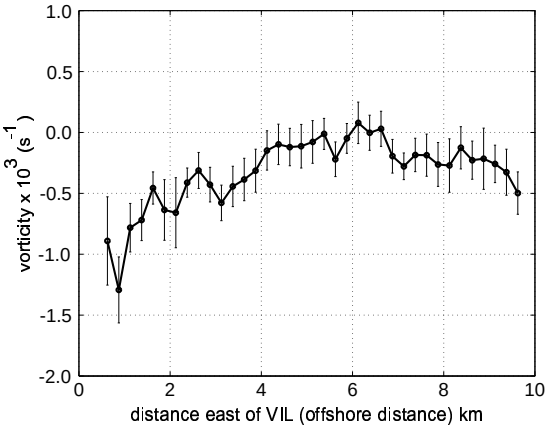

Figure 4.6: Mean vorticity as a function of offshore distance on 10 Jan 1998.

4.3 13 January 1998

Fig. 4.7 shows the 250-m resolution winds over a 36 km^2 area derived from approximately 5-minutes of 0° elevation PPI scans on 13 January. The speed is indicated on each wind-direction shaft with barbs and pennants. Each barb and pennant represents 1 m s^{-1} and 5 m s^{-1}, respectively. Fig. 4.7 (top panel) shows the wind speed in color of this vector field. A wind-speed maximum exists in the upper-right corner of the image. The shear-line points to Sheboygan Point which apparently generates this flow feature. Figs. 4.7b and 4.7c show the divergence and vorticity field, respectively. A band of negative divergence and vorticity is located along the shear-line.

4.4 Horizontal Winds from RHI-scans

To obtain horizontal winds from RHI scans, the individual range-corrected lidar returns are high-pass median filtered in range to correct for attenuation. The filtered backscatter-intensity data is then converted using linear interpolations from spherical to a Cartesian grid with 15-m resolution in both altitude and downwind distance. At each point in this vertical plane, we compute the spatially lagged cross-correlation function between a value at one time and the value 20-s later. Each value of the correlation function is obtained by shifting the later frame by one pixel upwind. Correlation functions are accumulated for successive pairs of scans and the position of the peak proportional to velocity. Second degree polynomials are fitted to the peak to improve velocity resolution.

The derived horizontal wind speeds for the surface-direction component, shown in fig. 4.8, reveal a vertical gradient of speed near the shore that diminishes by ≈6 km downstream distance. Fig. 4.9 shows that the 30-m wind increases from ≈5 m s^{-1} to almost 8 m s^{-1} over 5.5 km while the 480-m wind decreases from almost 10 m s^{-1} to less than 8 m s^{-1} over the same interval. Intense convection over the lake is responsible for vertically mixing the momentum. A reduction in surface roughness (from land to lake) is also partly responsible for acceleration of the flow at the lower altitudes. By assuming $\partial v/\partial y = 0$ and vertically integrating the incompressible continuity equation with the RHI wind data, we estimate the average vertical velocity between 2 and 5 km offshore at 330 m altitude to be -4.6 cm s^{-1}.

4.5 21 December 1997

In this section, in striking contrast to the relatively homogeneous conditions on 10 and 13 January, we present VIL observations of a shallow density current advecting aerosol rich air offshore at ≈1 m s^{-1} in the presence of a 3–4 m s^{-1} larger-scale onshore flow. A land-breeze front became remarkably sharp and quasi-stationary during our observations. Passarelli and Brahm (1981) and Schoenberger (1986) have shown using surface, radar, and aircraft observations that shoreline parallel snowbands over Lake Michigan can be the result of rising motion generated by such confluence lines over the lake. Although clouds were present, light precipitation was not observed until after

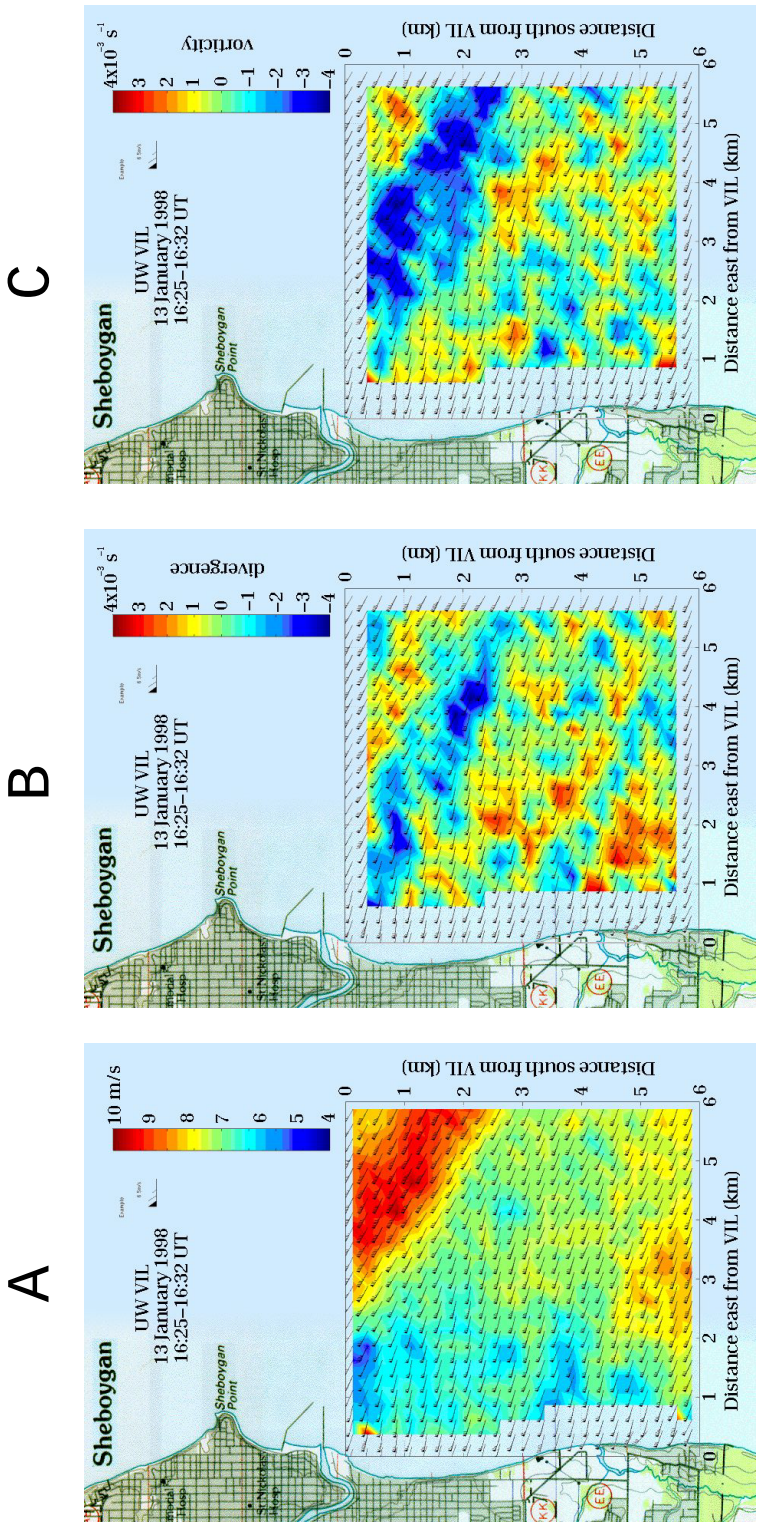

Figure 4.7: Aerosol structure speed, divergence and vorticity on 13 Jan 1998.

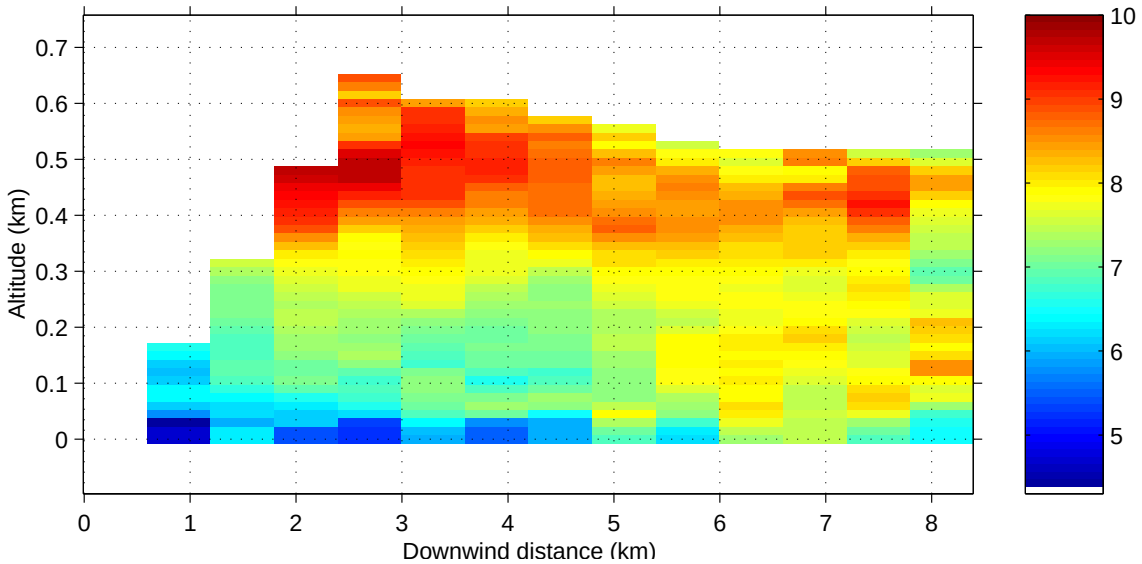

Figure 4.8: Wind speed derived from cross-correlation method of RHI scans.

we collected the data used to compute winds. It was not apparent that the clouds and precipitation were caused by the land-breeze front. Other lidar observations of land-breezes include those by Kolev *et al.* (1998) .

On the morning of 21 December 1997, a 1028-mb high-pressure system was located over southeastern Ontario resulting in a very weak pressure gradient across lower Michigan, Lake Michigan, and Wisconsin. At the NOAA Weather Station (SGNW3) located ≈0.5 km north of the lidar site in Sheboygan, and at the NCAR Integrated Sounding System 10-km west of the lidar, tower wind measurements indicated weak ($<$ 1–3 m s^{-1}) westerly flow throughout the night with air temperatures dropping to -7°C at 7 AM CST.

RHI volume scans over the lake collected between 12:44-15:19 UTC show a diffuse, north-south oriented boundary near the surface that gradually became sharper with time and moved toward the lidar. East of the boundary, the backscatter intensity was lower indicating cleaner air. Constant altitude PPIs (CAPPIs; horizontal slices interpolated from RHI volume scans) at 10-m above the surface show the diffuse boundary approximately 10-km offshore at 12:44 UTC. Fig. 4.10 shows one RHI from a volume scan at 14:04 UTC when the front was sharper. By 15:18 UTC the front is sharply defined and stationary near the surface ($<$20-m AGL) and is located approximately 2-km offshore. The volume scans during this period also show the boundary-layer advecting onshore is ≈1-km deep and that clouds with bases above 750-m began advecting into the scan volumes from the south-south-west around 14:30 UTC.

From 15:24 to 16:46 UTC, we collected PPI scans, like the one shown in fig. 4.11, with an elevation angle near 0°. This enabled high-temporal resolution horizontal slices

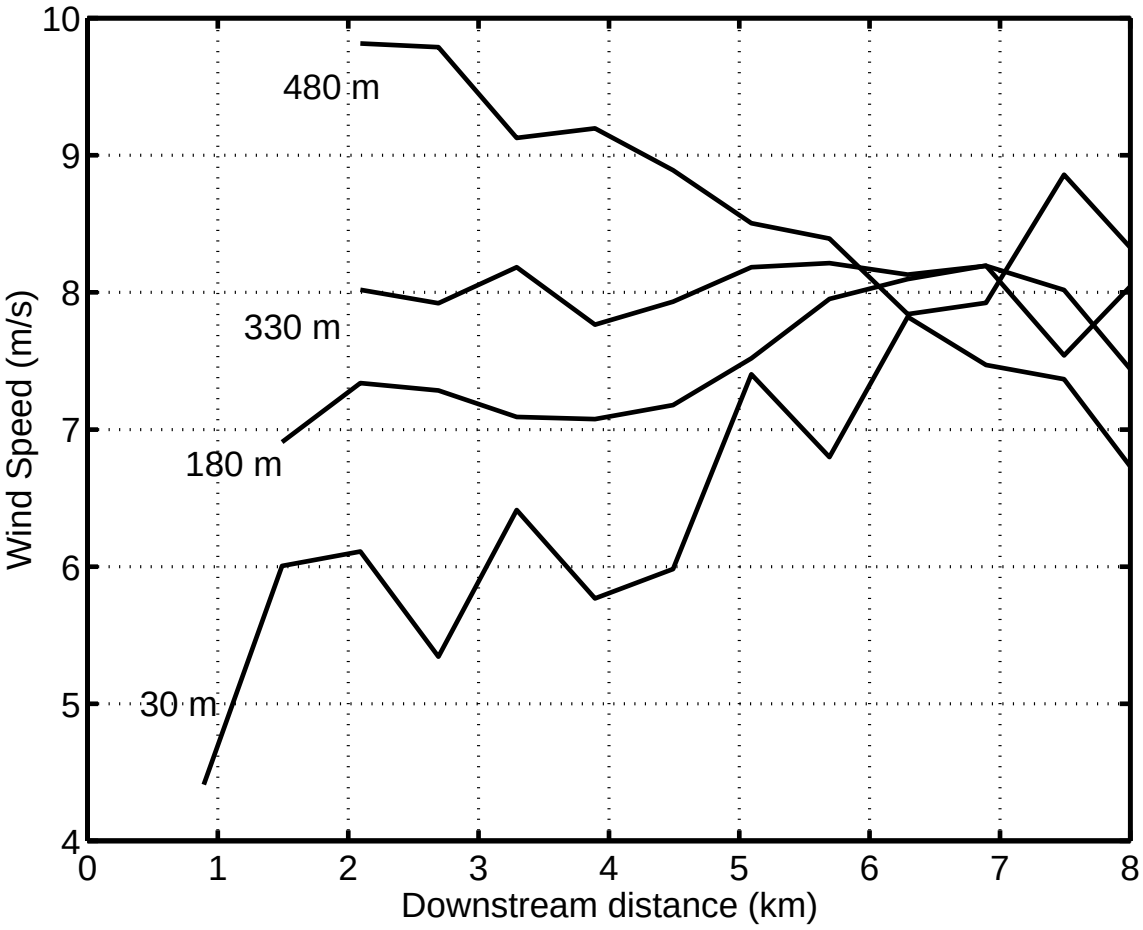

Figure 4.9: Wind speed derived from cross-correlation method of RHI scans.

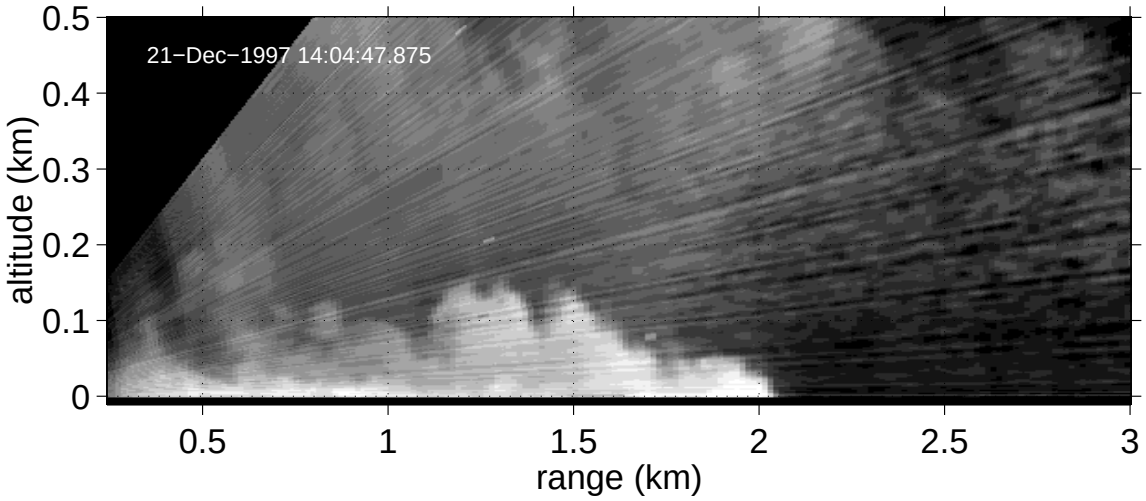

Figure 4.10: One RHI scan on 21 December 1997 at 14:04 UTC. The nose of the density current can be seen at the surface at $\approx$ 2 km range. The bright specs at 1.25 km range and 200 m altitude and at 1.7 km range and 80 m altitude are believed to be seagulls soaring on updrafts produced by the onshore flow rising over the head of the density current.

through the land-breeze 5 m above the surface of the lake. Animations of the PPI-scans reveal wave-like perturbations in the east-west position of the frontal boundary propagating to the north. Cross-correlation of the aerosol backscatter field from these scans indicate westerly flow in the aerosol rich airmass west of the boundary and southeasterly flow in the cleaner air east of the boundary. Despite the relatively low scattering of the onshore flow, the algorithm is still able to determine wind vectors in this region. Fig. 4.12 shows the average wind vector field using PPI scans from 15:24 to 15:56 UTC. Wind vectors were first obtained in 1-km square boxes and were used to initialize the algorithm for boxes that were 250-m by 1-km on the west side of the front and 500 m by 1-km east of the front. At 16:00 UTC precipitation began falling through the PPI-scan plane. The wind-vectors presented in fig. 4.12 are from data obtained before the precipitation arrived.

At 16:51 UTC, we began collecting RHI scans, like the one shown in fig. 4.13, that were pointed at 165° azimuth (into the larger scale wind direction). At this time and azimuth the head of the land-breeze was located at approximately 5.6 km range. Animations of the RHI scans show an extremely thin and high-scattering layer near the surface, moving toward the east. Large-eddies from the prevailing onshore boundary layer lift up and push back the nose of the density current. The RHIs also show precipitation falling from clouds that are advecting onshore. VIL observations were stopped at 17:12 UTC.

The PPI scans through the well-defined land-breeze on 21 December offer a unique opportunity to witness the effects of the high-pass median filter on the data.

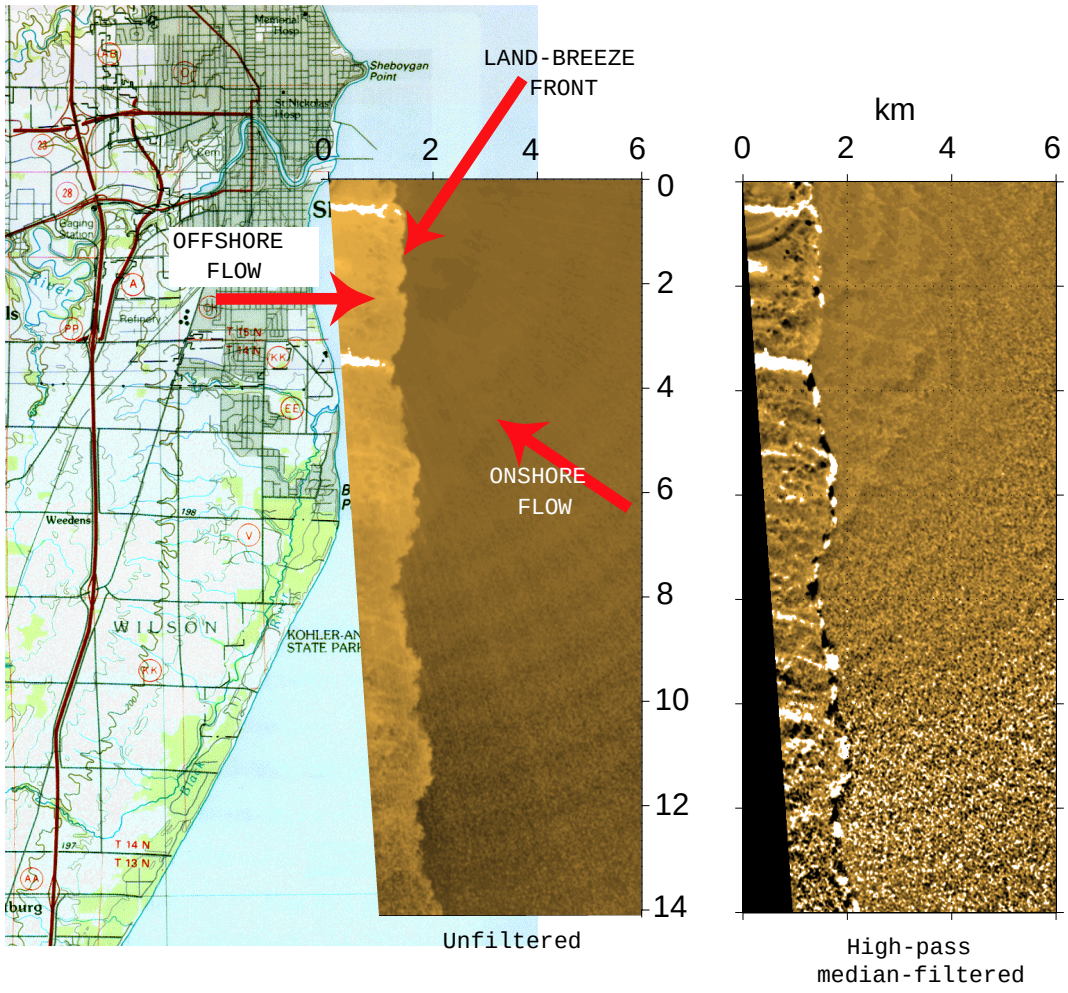

Figure 4.11: PPI scan at 0° elevation angle through the density current observed at 15:24:58 UTC on 21 December 1997. The image on the left is unfiltered data and relative to the map is it superimposed on. The high scattering on the left side of the left image corresponds to the cold offshore flow. The brightest areas ≈0.5 km and ≈3.5 km south of the lidar are from atmospheric effluents associated with industrial sites along the shore. The image on the right is the high-pass median filtered version of the image on the left and is not relative to the map.

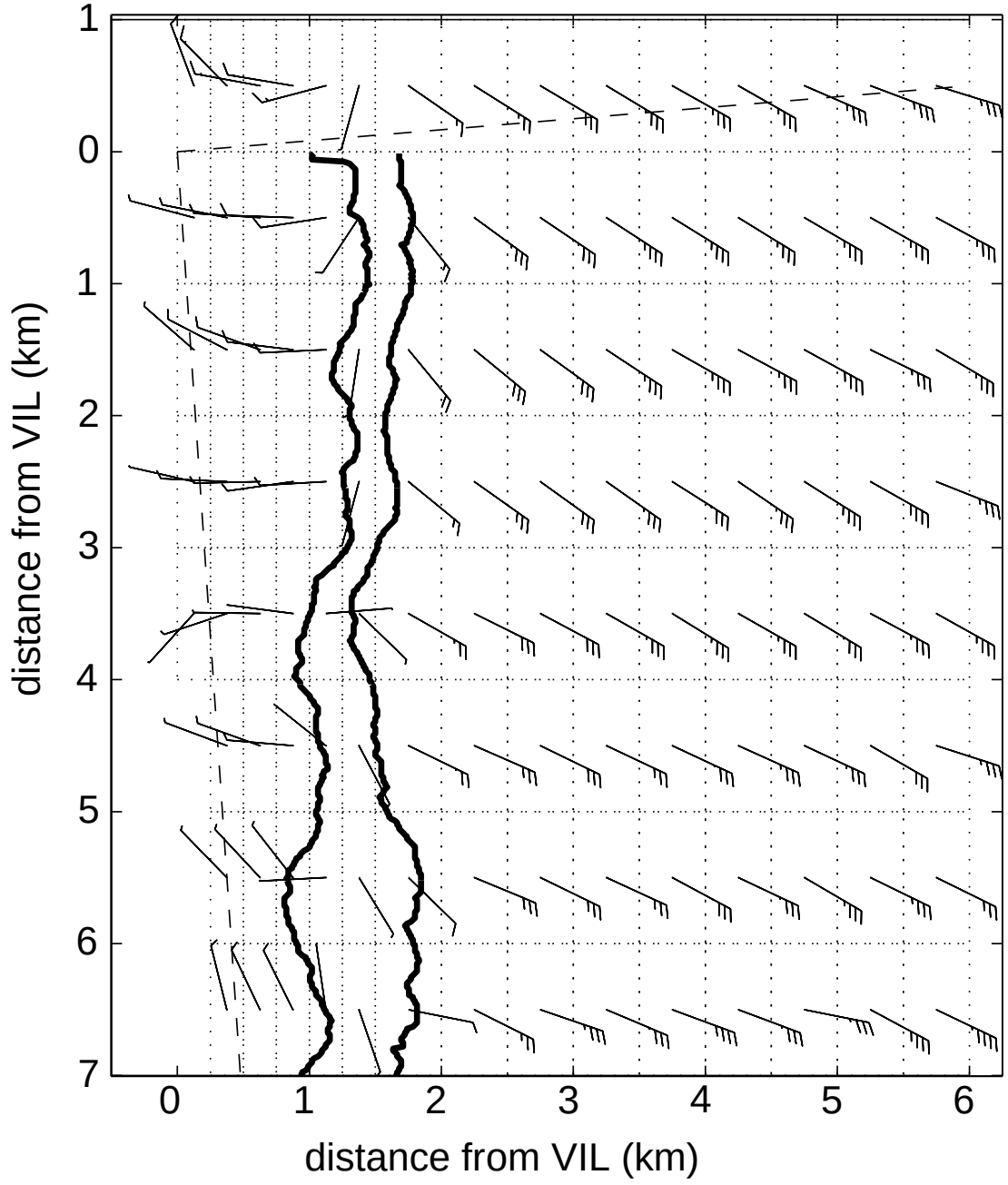

Figure 4.12: Wind-vectors derived from 155 PPI scans on during the period 15:24 to 15:56 UTC on 21 December 1997. The scan plane was divided into sub-areas shown by the dotted lines. The maximum and minimum eastward position of the land-breeze front is shown by the bold lines. The azimuthal range of the lidar scan is shown by the dashed lines.

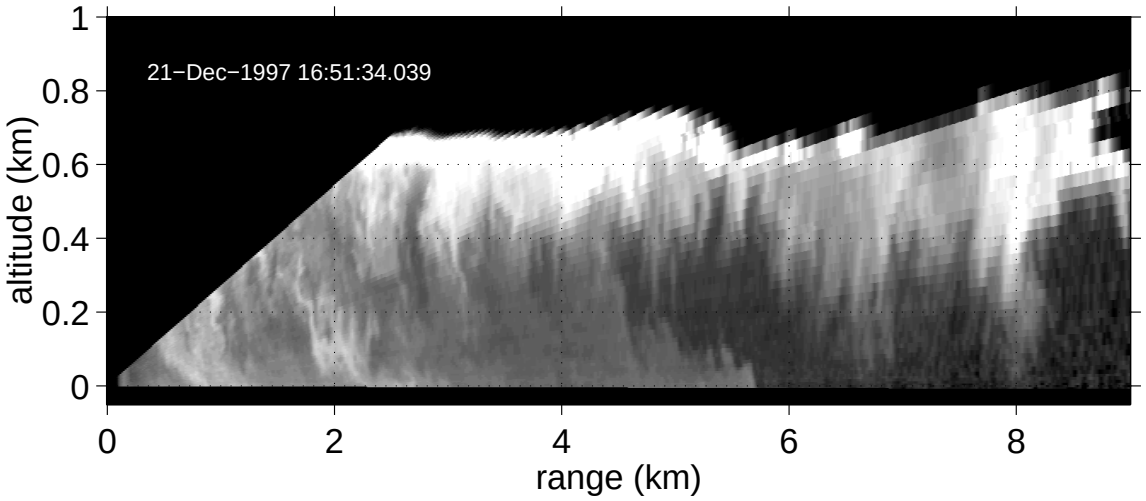

Figure 4.13: One RHI-scan at 16:51 UTC at 165° azimuth. The white areas above ≈500 m are cloud-base. High-scattering in vertical streaks below the cloud is precipitation. The nose of the land-breeze is at ≈ 5.5 km range.

The right image in fig. 4.11 is the median filtered version of the image on the left. A 30-point (450 m) median filter was applied to the lidar returns. The scattering intensity of the relatively clean onshore flow is now about the same as that in the aerosol-rich offshore flow. The step-like change in scattering intensity, a feature much larger than the filter-length, and caused by differing aerosol content of the two airmasses, has been removed. Aerosol structure can now be seen in the clean onshore flow.

The high-pass median filter is a required step in the wind calculation. It removes features in the data that are larger than the filter length such as the radial shadows from the brightest steam-fog elements. It also reduces the effect of less severe attenuation and normalizes the data for fluctuations in laser power. For these reasons, it should be applied to the individual lidar returns.

Therefore, the boxes which contain the land-breeze front (the sharp discontinuity between airmasses) are examples of where the cross-correlation technique may produce an apparent motion not equal to the mean wind over that area. Wind determinations in boxes along the boundary are ill-determined even in cases where median filter artifacts are absent, because some fraction of the area is composed of coherent structures moving east while the remaining area contains coherent structures moving west. In fig. 4.12, the bold lines indicate the range of position of the front. The vectors between these lines indicate southerly winds. These seem to relate to the northward propagation of wave-like perturbations in the front as seen in animations of the PPI scan data. It is not clear how these velocities relate to the vector average winds in the boxes along the front.

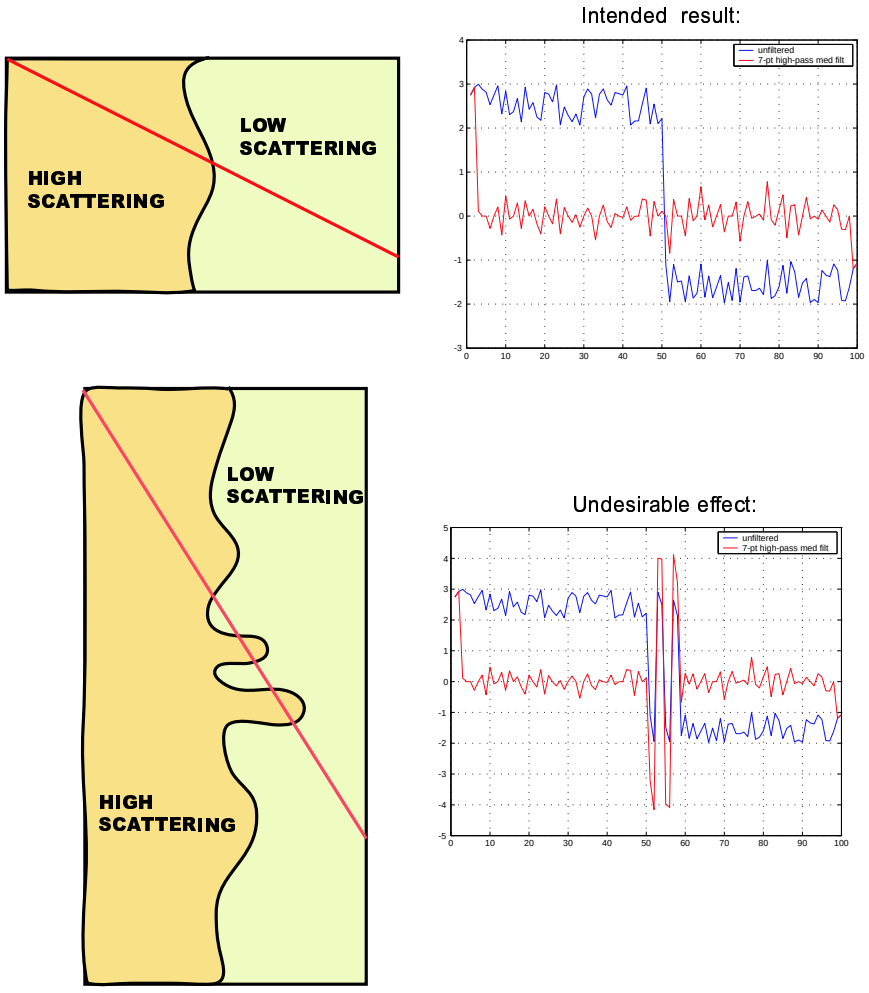

Figure 4.14: Top panels: sketch of intended result. Bottom panels: sketch of what actually happens.

Chapter 5

Large eddy simulation

Permission has been requested from the American Meteorological Society to reprint of Mayor et al. (2001) as part of this chapter.

5.1 Introduction

The University of Wisconsin Nonhydrostatic Modeling System (UW-NMS), developed by Professor Greg Tripoli, is used as the LES code in this research. The model is *scalable*, which means that the grid-spacing and time-step can be changed to match the requirements for the simulation. The model can be run in either a real data configuration (i.e., initializing from assimilated gridded data for weather forecasting) or in an idealized horizontally-homogeneous initial condition, employing wall, radiative or periodic lateral boundaries and initialized from prescribed profiles. It is formulated to simulate a wide variety of atmospheric phenomena ranging from global scales of thousands of kilometers to micro-scales of single meters with only minor changes. A full range of physical processes are available to the model as options including vegetation, precipitation processes, radiative processes, convective parameterization, and turbulence schemes. Two-way grid nesting is available to locally enhance resolution. In this work, topography, vegetation, precipitation and convection parameterizations were not used.

Because of the wide range of spatial scales that are interacting simultaneously in a turbulent flow and the desire to resolve as many of those scales as possible, LES tends to be a computationally expensive endeavor. The largest eddies in the boundary layer are restricted to the boundary layer depth, and the smallest are at the Kolmogorov microscale, which is typically on the order of 1 mm. On 13 January, the boundary layer advecting offshore was about 400 m deep. Furthermore, the spin-up process (i.e., the generation of turbulence from a horizontally homogeneous initial condition) adds to the computational cost.

For this study, it was also desirable to simulate the spatial scales observable by the lidar. The VIL has 15 m range resolution and records data out to ranges of 18 km. The best quality (high signal to noise ratio) lidar data lay within approximately the first 6 km offshore on 13 January.

Ideally the simulations would resolve all scales, but even the most state-of-the-art supercomputers do not make that possible. In this work, simulations were performed on an 8-processor IBM model J50 running the AIX operating system. This symmetric multiprocessor (SMP) computer had 2-GB of RAM and eight 200-MHz Power-PC 604e microprocessors. Given this facility and the model code with a core framework that was constructed prior to this study, it was found that about 6.6 million grid points could run without swapping to hard disk during execution. SMP directives were installed in the UW-NMS source code, and major parts of it were rewritten by Professor Tripoli so that one executable would use all eight processors simultaneously.

Therefore, 15 m horizontal and vertical grid-spacing was used to simulate the internal boundary layer. The grid was set in the vertical so that the lowest velocity point in the atmosphere was 7.5 m above the surface, an ideal altitude for comparison with data from the VIL's 0° elevation PPI scans. VIL CAPPIs were also constructed starting at 7.5 m AGL to facilitate comparison with model output. Numerical filters and eddy viscosity limit the effective resolving capability of the model to approximately 5 to 6 times the grid spacing. This means that eddies smaller than about 90 m are not entirely explicitly simulated. The filters and eddy viscosity have a larger effect on the smallest scales ($2\Delta x$) and become less effective for larger scales ($5–6\Delta x$). For scales greater than about 90 m the features are almost entirely resolved. The size of the model domains used will be discussed in section 5.5.

Hundreds of LES experiments were run over the several years required to complete this research. For example, there were many simulations to test the new ideas for boundary conditions, effect of numerical filters, grid-spacing, and initial conditions. Each simulation was assigned a number so that model output could easily be linked to the information about the model parameters used and the purpose of the simulation. In the remaining chapters a simulation will usually be referred to with a number, such as LES#260. Table 5.1 lists the experiments with output used in this dissertation.

5.2 Model issues

Although based on the Navier-Stokes equations, like all other LESs, the method in which UW-NMS solves the equations is quite different. The model formulation is presented in the Appendix. Other differences, when compared to other popular LES codes, include:

1. The formulation is quasi-compressible rather than anelastic as in many LES codes. Benchmark comparisons do show that there can be substantial differences (Straka et al., 1993) resulting from the anelastic approximation. These differences are most apparent in regions of strong acceleration where the elastic formulation is less restrictive and plumes tend to be more penetrative.

2. A Boussinesq approximation is not made for scalability purposes. This has little effect on the LES scale.

Run Number	Purpose
47	Nieuwstadt, horizontally homogeneous CBL
181	CIBL with restoring zones, Sadourney
195	CIBL with restoring zones, Arakawa
212	CIBL, no restoring zones, DKR=0.20
215	CIBL, no restoring zones, DKR=0.10
216	CIBL, no restoring zones, DKR=0.15
222	CIBL, no restoring zones, DKR=0.05
223	CIBL, no restoring zones, DKR=0.00
252	Upwind for #260, enstrophy conserving, DKR=0.05
260	CIBL with recycler, enstrophy conserving, DKR=0.05
263	Upwind for #264, enstrophy non-conserving, DKR=0.05
264	CIBL with recycler, enstrophy non-conserving, DKR=0.05
266	Upwind for #267, enstrophy non-conserving, DKR=0.15
267	CIBL with recycler, enstrophy non-conserving, DKR=0.15
269	Same as #266 except moving grid
274	CIBL, Continuation of #260 with flux output

Table 5.1: List of simulations presented.

3. The 1st law of thermodynamics used is based on the conservation of moist entropy, (Tripoli and Cotton, 1981). As a result, condensation is implicit to the system and no formal saturation adjustment approximation is necessary as it is in other models.

4. A finite difference scheme is used for the calculation of advection and pressure gradient acceleration. This is different from LES codes that employ horizontal spectral techniques (Moeng, 1984). Although inferior to spectral techniques in accuracy, finite difference techniques allow for the use of arbitrary lateral boundary conditions necessary for this study. In addition, it makes some sense to treat horizontal and vertical advections in the same way numerically, especially on the LES scale where motions are more three-dimensional than in geostrophic flows.

5. Advection of wind is handled using either of two 2nd order centered-in-space-and-time techniques including:

   (a) Modified (Arakawa and Lamb, 1981) 2nd order enstrophy conserving form applied to vorticity components in all three dimensions.

   (b) 2nd order vorticity conserving form.

   (c) 2nd order flux-conservative Crowley (forward up-winding technique) is used for scalar quantities.

6. A simple turbulence 1.5 level closure described by Tripoli (2001) and originally based on Redelsperger and Sommeria (1982) is employed. Unlike mesoscale models, the turbulence levels are based on the full three dimensional deformation fields. This is similar to the simple closures used by other LES models except

that it includes the possibility of using different levels of turbulence in the vertical compared to horizontal when the resolutions differ. Since these simulations used equal grid-spacing in each direction, our turbulence was similar to other LES codes.

7. The large-scale pressure gradient is represented by the method described by Tripoli and Cotton (1981) whereby a geostrophic velocity is specified and the pressure gradient acceleration associated with that velocity is determined by the pressure gradient acceleration that balances that velocity. In doing so, the reasonable assumption is made to neglect the horizontal thermal gradients of the synoptic scale flows that are associated with the mean geostrophic winds. Of course, retaining the mean thermal gradients would be inconsistent with the imposition of periodic conditions, anyway, and is implicit to all large-eddy models. The geostrophic velocity is determined from the observed sounding by extrapolating the linear trends of winds above the boundary layer to the surface. As a result, both the observed boundary layer wind and the geostrophic wind must be specified initially.

8. The surface layer fluxes are based on the Louis (1979) scheme. This is similar to other LES codes except for the way it is applied. The Louis scheme is used to derive a locally defined surface mixing constant in the form:

$$\overline{w'A'} = C(A - A_s) \tag{5.1}$$

where A is any scalar, w is vertical motion, and C is the mixing constant. The formula is then solved implicitly holding the surface quantity and mixing constant fixed over the time step rather than the flux. In this form we can insure that the flux stays down-gradient regardless of the timestep. A roughness length of 0.2 m was used over land and 0.0001 m over water.

5.2.1 Boundary conditions

Boundary conditions are the required specification of all predictive variables on the grid points at the edges of a model domain in order to find the solution on the grid points between them. In the two lateral (horizontal) directions, the easiest method is to simply copy the information from the opposing end. This periodic, or cyclic, condition in LES is useful for horizontally homogeneous boundary layers. It also facilitates spectral methods. Periodic lateral boundaries are one of several boundary condition options the user can select in UW-NMS. Furthermore, it is possible to make the domain periodic in one or both of the lateral directions.

There are also three other types of non-periodic boundary conditions the user can select from: closed, absorbing, and open. Closed boundaries hold the flow constant, reflecting outward moving waves and perturbations. Absorbing boundaries hold

the flow constant according to the initial conditions and damp the amplitude of perturbations moving toward them so that reflections do not occur. Open boundaries allow waves and perturbations to pass out of, but not into, the domain.

Several methods for open lateral boundary conditions have been proposed and are routinely used in limited area models. They are based on the Sommerfeld radiation condition (Orlanski, 1976; Klemp and Wilhelmson, 1978; Klemp and Lilly, 1980; Hack and Schubert, 1981) whereby both waves and advected phenomena are allowed to pass out of the domain while no wave or perturbation can advect into the domain. It is set up by having one variable, usually the normal component of velocity, specified by a radiative wave tendency equation given by Orlanski (1976) on the inflow boundary while all other variables except one (usually pressure) are specified by the assumption of zero normal gradient. This condition allows for some, often unchecked, evolution of the structure in the tangential direction to the boundary and for (sometimes destructive) trends in net mass inflow or outflow. To preserve the original inflowing mean thermodynamic and wind flow structure, it is necessary to hold the inflow constant. This choice results in unfortunate problems including not only the reflection of upstream propagating waves from the boundary, but also the continued movement of laminar flow from the inflow boundary.

Surface boundary conditions are closed. In the IBL domain, the left half of the surface is parameterized as snow-covered land and the right half is 279 K water. The domain is periodic in the north-south direction. The western boundary condition is closed and the variables on it are held constant according the mean vertical profile of upwind conditions. This results in an inflow on the western boundary. The eastern boundary condition is open.

All simulations presented here used a Rayleigh damping zone in the top of the domain to absorb vertically-propagating gravity waves. In this user-defined region, the time tendencies of θ_{il}, u, v, and q_r are given by:

$$\frac{\partial A}{\partial t} = \frac{A - A_B}{\tau_z(z_{top} - z)} \tag{5.2}$$

where A is the predicted variable, A_B is the value of the predicted variable at the top of the domain and τ_x is a damping timescale that is a maximum at the top of the domain and decreases linearly to zero at a height defined by the user. In the IBL simulations, the eight top points were assigned as the absorbing layer with a dissipation time scale of 10 s.

5.3 Simulated lidar aerosol scattering

Lidar backscatter intensity to first order is dependent upon the concentration of aerosol particles and their size. Aerosol particles swell as the relative humidity increases. To enable the comparison of model output with lidar backscatter data, lidar scattering was simulated by computing optical scattering α from a function that uses the LES relative humidity as the independent variable (see fig. 5.1). The function

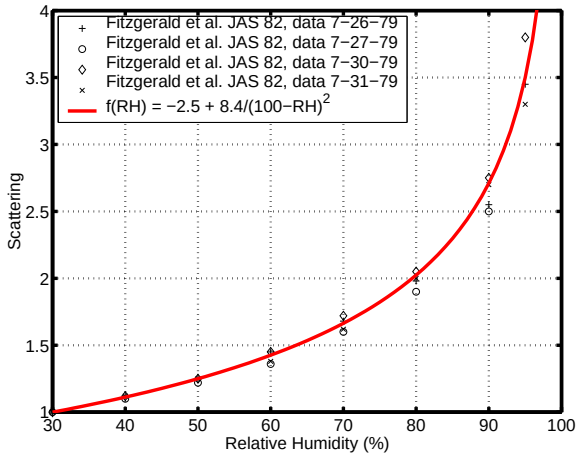

Figure 5.1: Function used to convert model relative humidity to optical scattering.

was determined from a best fit to data obtained by Fitzgerald et al. (1982) and is given by

$$\alpha = -2.5 + \frac{8.4}{(100 - RH)^2} \tag{5.3}$$

where RH is the relative humidity in percent and α is the optical scattering. To avoid the very unrealistic infinite scattering when the relative humidity is at or above 100%, all occurrrences of model relative humidity greater than 99.99% are set to 99.99%. Optical scattering from eqn. 5.3 is multiplied by a model passive tracer. The passive tracer is initialized as one below 400 m and zero above 400 m. Furthermore, if any liquid water is found at the grid-cell, the simulated lidar scattering at the location is assigned a value of optical scattering for a relative humidity of 99.99% which is equal to 18.53. This is because even a few cloud droplets produce tremendous scattering.

This is an extremely crude method for estimating relative lidar scattering. The function is based on data collected during the summer in Washington, D.C., and, therefore, the aerosol type is probably very different from that found in Sheboygan, Wisconsin, during the middle of January. The function also unrealistically goes to infinity as the relative humidity approaches 100%. It does not account for variations in the amount of liquid water present, which probably has a very large effect on the variance of the lidar data, especially in the surface layer where steam fog is common.

5.4 LES of Homogeneous CBL

The atmospheric boundary layer is driven by two main forcings: 1) wind-shear[1] and/or 2) heat from the surface of the earth. Sometimes these driving forces act

[1]An entirely shear-driven and neutral, Ekman, boundary layer was also simulated to test UW-NMS's ability to generate a mechanical boundary layer. Those results are summarized by Tripoli and Mayor (2000) but not presented in this dissertation.

simultaneously and sometimes alone. Turbulence structures from these two types of forcings are quite different (for examples see Moeng and Sullivan, 1994). Buoyancy in the convective boundary layer tends to form deep thermal plumes which connect the surface-layer to the top of the boundary layer. Therefore, since this type of mixing is very important in the CIBL, as a first step in testing UW-NMS as an LES, a horizontally-homogeneous convective boundary layer was simulated. This thermal instability, when occurring simultaneously some wind-shear and a capping inversion, appears to be the cause of horizontal convective rolls (Weckwerth et al., 1997).

To test UW-NMS's ability to simulate convective boundary layer (CBL) simulations were run for comparison with the statistical results of Nieuwstadt et al. (1993). That paper compares turbulence statistics from four different LES codes of very similar grid-resolutions and domain sizes with identical forcing. The results, which are in general agreement among themselves (and agree with some in situ observations), appear to set a first-order test for other codes that might be considered capable of simulating boundary layer turbulence.

In this case of an entirely heat-driven, or convective boundary layer, there is no mean horizontal motion. The surface of the earth is heated by the sun and through conduction warms the bottom of the atmosphere causing it to be thermally unstable and convection to mix the air vertically. Convective currents transport the heat vertically in the atmosphere as a response to the heat-input at the surface. As a result, the boundary layer becomes deeper with time.

For comparison with the results in the Nieuwstadt paper, a model domain of 40 x 40 x 60 grid-points is used. The dimensions of the domain are 6.4 km x 6.4 km wide (160 m horizontal resolution) and 3-km tall (50 m vertical resolution). These dimensions and resolutions match those of grids run in Nieuwstadt et al. Furthermore, 0.06 K m s^{-1} ($\approx$ 72 W m^{-2}) sensible heat-flux is supplied at the surface. Normally, this heat comes from solar radiation warming the ground, but, to keep it constant, an artificial heat flux is coded into the surface, and the radiation package is turned off. For this experiment the model contains no moisture and the soil model is also turned off. The model is initialized with a neutral temperature sounding from the surface to approximately 1500 m altitude. The temperature and w-component of velocity are randomly perturbed in this neutral layer at initialization to help speed the development of large-eddies. The time-step for this simulation was 5 s.

Fig. 5.2 shows the total turbulent kinetic energy in the model domain as a function of dimensionless time. Here the mean eddy turnover time t_* is 1096 s. A sharp increase and overshoot in the total-TKE occurs for all the codes between $2 < t/t_* < 4$. This corresponds to about 36 to 73 minutes after initialization. During this time, many convective cells, each approximately 1-km in diameter, form in a very organized arrangement in the lower part of the domain to quickly convect the heat that builds up there. The initial absence of large eddies and the presence of a surface-sensible heat flux causes this to happen. The cells are shown in fig. 5.3 which is a snapshot of the vertical velocity on a horizontal plane 37 minutes after initialization.

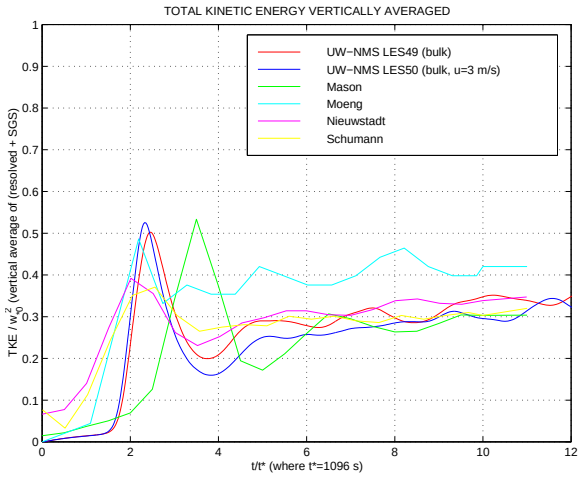

Figure 5.2: Total turbulent kinetic energy in entire model domain as function of time for UW-NMS and other LESs. This graph shows the simulations becoming approximately steady state after an initial overshoot around 2200 s.

Fig. 5.2 also shows that the simulation becomes quasi-stationary after $4 < t/t_* < 6$. The term *quasi*-stationary is used because, while the boundary layer continues to slowly deepen with time the character of the turbulence during one large-eddy turnover time, doesn't change significantly. Fig. 5.3 shows the typical pattern of the convective cells at 75 m above the ground at t/t_*=10.5 (3.2 hours after initialization). At this time, one can see that the arrangement is less organized and the cells range in size from less than 1-km to approximately 3-km in diameter. The vertical velocities at this altitude and time range from approximately -1 to +1 m s^{-1}.

At higher altitudes different patterns are seen. For example, at 850 m, about mid-way up in the CBL, one sees the outlines of the largest cells shown in the previous image with areas of stronger, more concentrated updrafts in the walls of these large cells. At this altitude, vertical velocities range from about -1.5 m s^{-1} to +3.5 m s^{-1}. Fig. 5.3D shows the vertical velocity on a horizontal plane through the entrainment zone. Here the plumes of the strongest thermals penetrate the stable capping inversion.

Fig. 5.4 shows two vertical slices of vertical velocity at 37 minutes (top) and 3.2 hours (bottom) after initialization. In both panels one sees thermals, or plumes, which extend from near the surface to the entrainment zone. This is consistent with glider pilot observations and other lidar measurements: the CBL has a high vertical coherence of vertical velocity. All of these qualitative patterns agree with those presented by (Schmidt and Schumann, 1989) and (Mason, 1989).

Fig. 5.5 shows vertical profiles of turbulence statistics computed during one large-eddy turnover time. The mean potential temperature profile is show in panel A and the mean sensible heat flux in panel B. The potential temperature profile is slightly unstable near the surface, neutral (constant) through the boundary layer, and stable

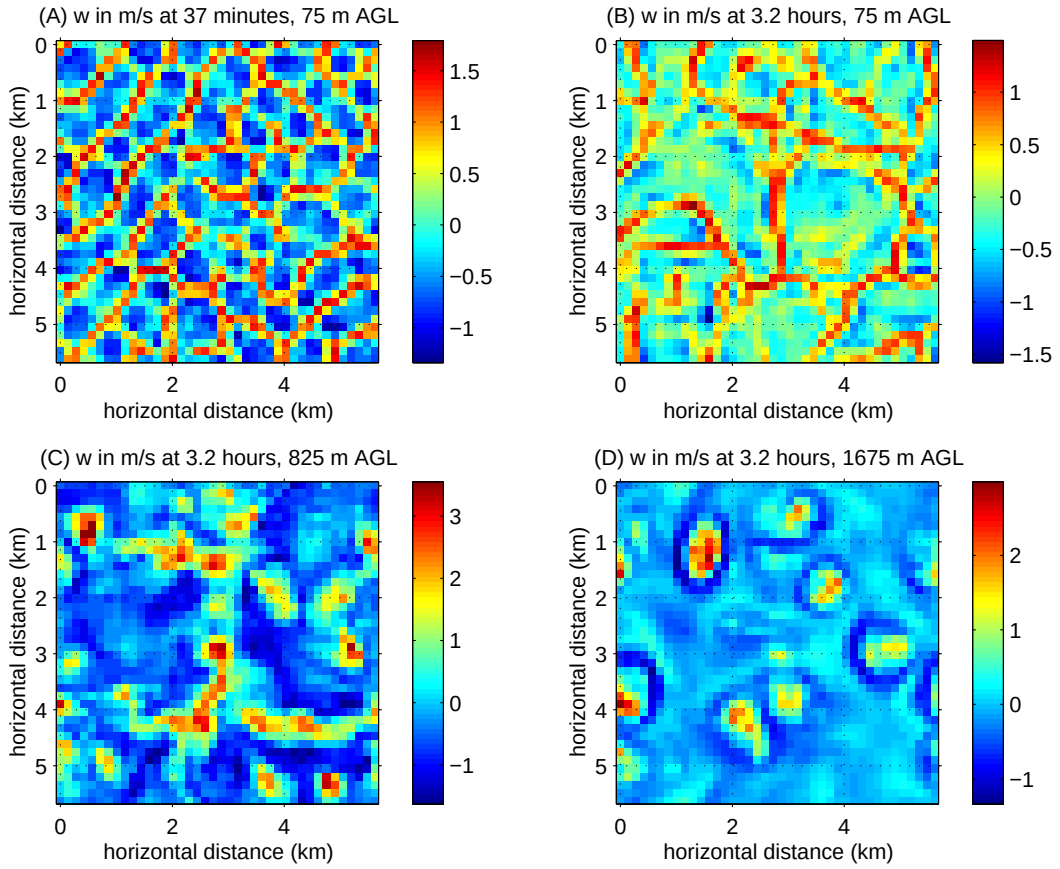

Figure 5.3: Vertical velocity in m/s on horizontal slices from the large-eddy simulation of a convective boundary layer. (A) at 37 minutes after initialization many small convective cells form (75 m AGL). (B) Same altitude as A except at 3.2 hours after initialization when the cells have become much larger and steady-state. (C) Same time as B except for an altitude in the middle of the boundary layer. Here the outline of the convective cells can still be seen. (D) Same time as B and C except at an altitude in the entrainment zone where only the most energetic plumes can penetrate into the capping inversion.

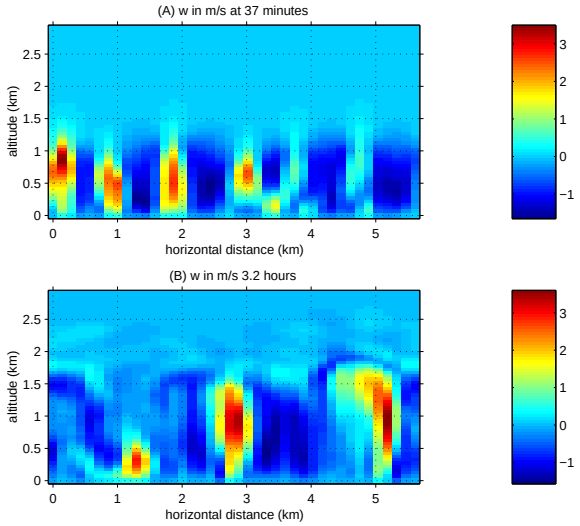

Figure 5.4: Top panel: vertical velocity on vertical slice at 37 minutes after initialization. Bottom: same as top except at 3.2 hours after initialization.

in the capping inversion. The heat flux profile decreases linearly from it's surface value of 0.06 K m s^{-1} to a slightly negative value in the entrainment zone. Both of these plots (figs. 5.5A and B) match those constructed from observations of many convective boundary layers (Stull, 1988).

The axes of the plots in panels C through F in Fig. 5.5 are scaled according to mixed-layer similarity theory (Deardorff, 1972; Deardorff, 1980). The two most important scales in a boundary layer in a state of free convection are the altitude of the stable inversion which caps the convective layer (z_i) and the buoyancy flux at the surface $\left((\overline{w'\theta'_v})_s\right)$. The convective velocity scale (w_*) combines buoyancy flux and inversion height to form an important scaling variable:

$$w_* = \left[\frac{g z_i}{\overline{\theta_v}}(\overline{w'\theta'_v})_s\right]^{1/3}. \tag{5.4}$$

Fig. 5.5C shows the normalized variance of vertical velocity (w) as a function of scaled altitude. The w variance profile matches that of the other codes and aircraft observations (Lenschow et al., 1980).

Fig. 5.5 also shows vertical profiles of the third-moment (D) and normalized third-moment (skewness, E) of vertical velocity. These profiles also match those from other codes and are consistent with the observation that narrow updrafts contain stronger velocities while the broad areas in between them contain more gentle compensating sinking motion. The UW-NMS has 50% higher third moment in the middle of the CBL compared to the other model results. Fig. 5.5F shows vertical profiles of variance of the horizontal components (u and v). These curves are approximately constant through the mixed layer with local maximum near the entrainment zone and

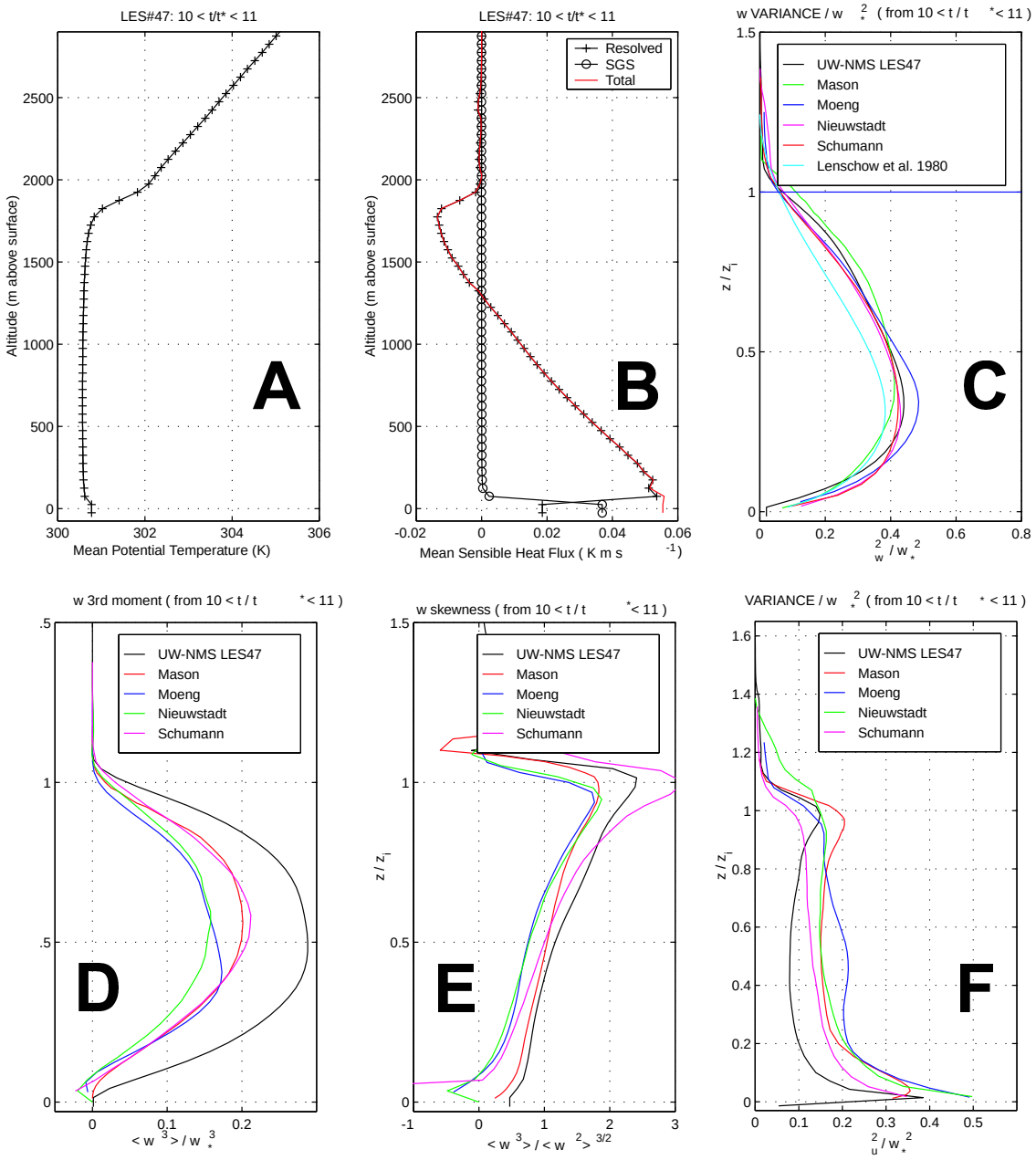

Figure 5.5: Turbulence statistics as a function of altitude from LES of a horizontally homogeneous CBL. A) Mean potential temperature, B) Sensible heat flux, C) vertical velocity variance, D) third moment of vertical velocity, E) skewness of vertical velocity, and F) variance of horizontal velocities. In figures C-F results from other LES codes are shown for comparison.

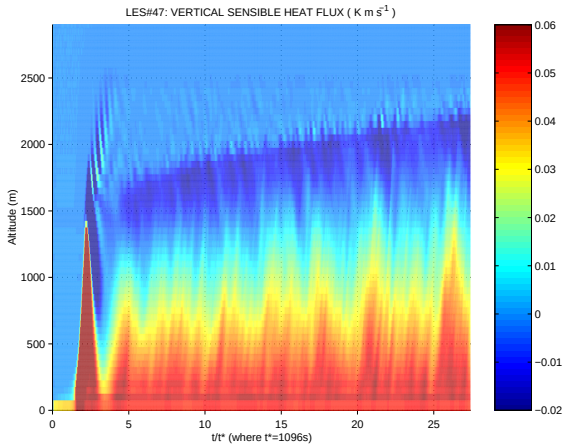

Figure 5.6: Mean sensible heat flux as function of time and altitude for the convective boundary layer simulation.

in the surface layer, where shear is the strongest.

Because heat is being added to the model at a constant rate, the boundary layer becomes deeper with time. Fig. 5.6 shows mean sensible heat flux as a function of time and altitude. This figure shows the same variable as shown in the right panel of fig. 5.5B except here it is displayed as a function of time. The dark blue band, representing slightly negative heat flux, is the entrainment zone and the minimum value in any vertical profile is a good measure of boundary layer depth. Fig. 5.6 tells us that, after the initial overshoot, the boundary layer is about 1600 m deep and it grows to $\approx$ 1800 m by 10 t/t_*. Note that this plot contains data out to over 25 t/t_*.

The Nieuwstadt simulation showed that the UW-NMS can simulate a homogeneous CBL as well as any other LES code. It produced turbulence statistics, celluar convection patterns, and temporal boundary layer growth rates that are in agreement with results from other LESs and observations. It also showed that an accumulation of potential energy near the surface, which occurs during spin-up, causes an overshoot of vertical sensible heat flux in the beginning of the simulation.

5.5 LES of CIBL

Internal boundary layers (IBLs) were observed on several dates during Lake-ICE; however, only 13 January was chosen for simulation because the weakly convective boundary layer upwind of the lake was limited to 400-m depth and the VIL data obtained was of excellent quality and contained PPI and RHI scans. Excellent PPI scans were also collected on 10 January; however, the boundary layer upwind of the lake was 1-km deep, and, thus, the domain size and number of grid-points required for simulation at 15-m spacing was too large for the computer resources available. The upwind boundary layer on 11 January was less than 400 m deep and also presents another case for the comparison of lidar data with simulations; however, no PPI

scans were collected on that day. The PPI scans reveal high spatial and temporal resolution aerosol scattering structure on an almost horizontal plane in the surface layer. RHI volume scans were collected on all days in order to create 3-D images of aerosol scattering structure; however, they lack the temporal resolution which allows us to calculate the eddy lifetime in relatively shallow boundary layers where the eddy lifetime is short.

The first attempts of simulating the 13 January CIBL are presented in Mayor et al. (1999). The domains used 140 x 70 x 80 grid points where only the western most 40 grid points were located over land. These early simulations, which experimented with a variety of grid spacings, produced a stationary, homogeneous, shore-parallel band of steam-fog immediately downsteam of the shoreline because of the lack of eddies advecting offshore. As convection developed over the water, elongated convection cells emerged from the downsteam edge of this stationary band. These simulations, when compared with the lidar observations, clearly demonstrated the need to have turbulent flow occuring over the land to simulate a more natural transition at the upwind edge of the lake. It also required a substantially larger domain.

Eventually, a three-dimensional rectangular domain consisting of 800 x 120 x 69 grid points with 15 m spacing in all three directions was chosen. The western 400 grid-points were over land and the eastern 400 grid-points over water. This provided a modest, but inadequate, region upsteam of the lake for eddies to develop. A time-step of 0.5 s was used.

5.5.1 Restoring zones

In a few simulations such as #181 and #195, a periodic boundary condition was implemented in the east-west (shore-perpendicular) direction (see also Mayor et al. 2000). In these, 900 m wide *restoring zones* were used to return the outflow properties to the mean before they could flow through the end of the domain. The restoring zone applies the same numerical method as the Rayleigh damping layer in the top of the model. Figs. 5.8 and 5.9 show output from simulations that used this method.

A disadvantage of this method is that a valuable portion of the grid at the east and west ends of the model domain is used for restoring the flow therefore reducing the area which can used to obtain IBL turbulence statistics. In the simulation output shown in figs. 5.8 and 5.9, nine hundred meters of domain were used on each end. Perhaps more importantly, the use of restoring zones causes laminar inflow, thereby requiring a longer domain for the spatial development of turbulence.

5.5.2 Perturbation recycler

The idea of taking perturbations from a downstream north-south vertical slice and adding them to the inflow wall was arrived at after reading about a technique devised by Lund et al. (1998) and partly inspired by the work of Spalart (1988). Spalart's work was developed for a spectral model and difficult to implement. Lund modified the technique for finite difference models. However, both techniques com-

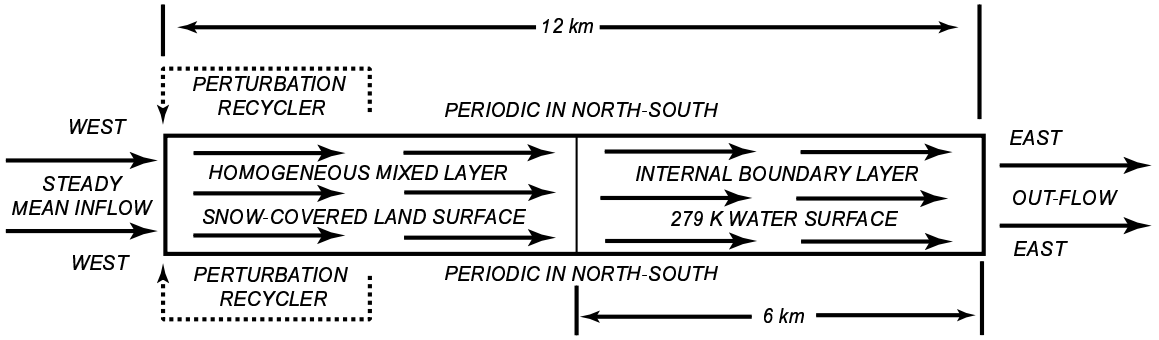

Figure 5.7: Plan view of model domain and boundary conditions for simulation of internal boundary layer.

press the vertical plane of perturbations before adding them to the mean inflow. Their application is simulation of shear-driven boundary layers over flat surfaces in mechanical engineering. For the atmospheric application in this work, the perturbations can simply be added to the inflow wall without scaling since the upwind portion of the IBL domain (i.e., the half over land) is approximately horizontally homogeneous. The capping temperature inversion that begins at 400 m AGL prevents rapid growth of the boundary layer in the upwind section of the IBL domain. Fig. 5.7 shows a plan view of the IBL model domain used for the simulations.

This technique eliminates the need to use large amounts of computer memory for a section of the domain for the spatial development of turbulence upwind of the beginning of the IBL. A test simulation (not shown) indicated that at least 8 km of domain were required to develop the boundary layer turbulence from a laminar inflow prescribed by the observations of mean vertical structure on 13 January.

Examples of the spatial development of the mainly shear-driven (weakly heated) boundary layer are shown in 5.8 and 5.9. These figures show vertical velocity on horizontal and vertical slices from simulations with restoring zones at the eastern and western ends of the domain. Laminar flow comes out of the eastern restoring zone. Within two km of the western wall, many closely-spaced linear structures can be seen which merge together and form more widely spaced and stronger amplitude linear structures by a distance of 6 km from the west wall. The linear structures quickly break up into patterns more like convection cells within the first two kilometers over the water. Unfortunately, these linear features over the land are not mature turbulent eddies and, therefore, this approach was abandoned.

5.5.3 Initialization

The CIBL simulation was initialized by replicating the turbulent solution of a LES that is 25% of the east-west length of the CIBL domain. This smaller simulation is called the *precursor simulation* or sometimes the *upwind simulation* because it is run prior to the IBL simulation and its purpose is to simulate the boundary layer *upwind*

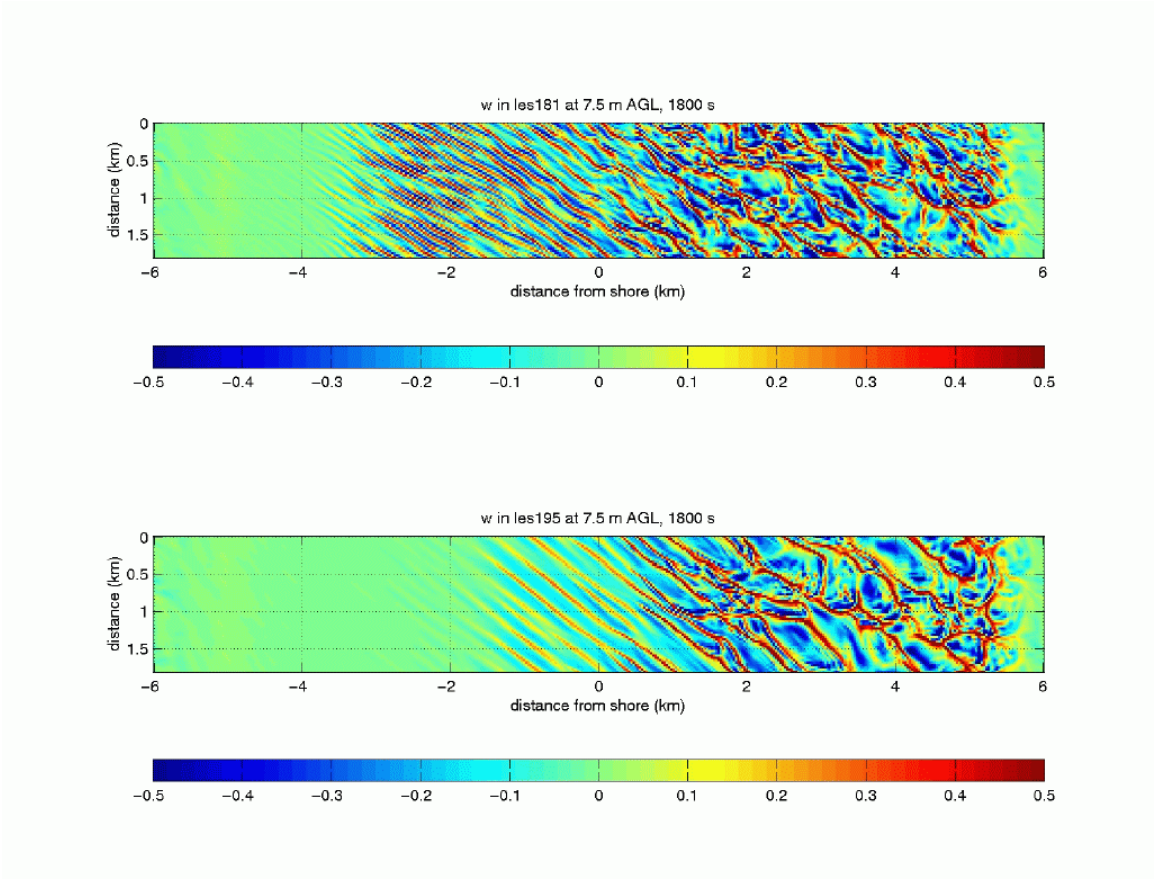

Figure 5.8: Vertical velocity at 7.5 m above the surface from two LES runs that used restoring zones: (top) #181 and (bottom) #195. These images were taken 30 minutes after initialization.

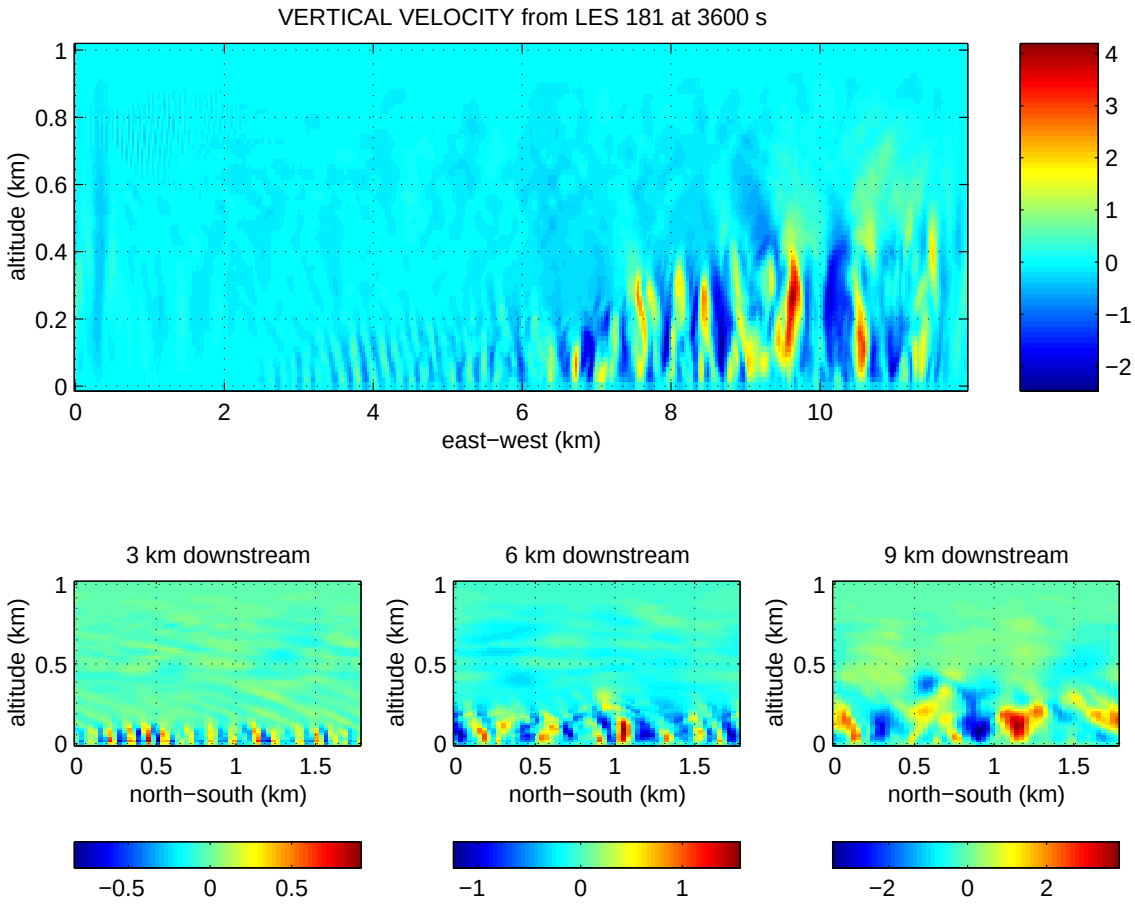

Figure 5.9: Snapshot of vertical velocity on vertical planes during simulation 181 showing boundary layer development that increases with increasing downstream distance across the entire domain.

of the lake. The precursor simulation was done in order to generate a mean inflow condition for the IBL simulation free of sampling errors in conventional measurements and for efficient development of explicit eddies that can be used to start the IBL simulation. The precursor simulation has the same grid-spacing, vertical, and north-south dimensions as the IBL domain. It has periodic lateral boundary conditions and the surface boundary condition is snow-covered land that has a temperature set equal to that of the lowest atmospheric grid-point.

The horizontally homogeneous initial conditions of the precursor simulation are based on observations collected at an NCAR Integrated Sounding System (ISS) that was located 10-km west of the lidar site. Random perturbations of ± 0.5 m s^{-1} were added to all three velocity components at all grid-points below 450 m to speed the development of eddies (a common practice among LES). Temperature, pressure and dewpoint data were obtained from a radiosonde launched at 16:30 UT and indicate that a well-mixed boundary layer existed up to about 350 m. A strong capping inversion exists above 400 m. Data from the radiosonde launched at 16:30 UT are plotted as circles in fig 5.10. The diamonds, at altitudes between 207 and 543 m AGL, in the left and center panels represent wind measurements from a 915-MHz boundary layer profiler. These winds, with 60 m vertical resolution, are a consensus of data collected between 16:35 and 16:51 UT. In addition to the radiosonde and profiler data, two observations of wind speed and direction are included on fig. 5.10. The first is from the NCAR ISS tower and is plotted as a square. The second is from the NOAA weather station SGNW3 that was located close to the lidar and is plotted as an upside-down triangle. The SGNW3 temperature and dewpoint observations at 16:30 UT match those from the ISS to within 1 degree. Because of the sampling errors in radiosonde and wind-profiler wind measurements, the wind-speed and direction profile used to initialize the model was obtained from a subjective (piecewise) linear fit among these data.

The wind-profile for initialization is constructed in three parts. Above 500-m, it is assumed that the observed wind profile is geostrophic. Therefore, a straight line is fit to the wind data above 500 m and used to extrapolate the pressure gradient at lower altitudes. Below 300 m, where the boundary layer is well mixed, we set the speed and direction constant. Between 300 and 500 m, where the sounding is weakly stable, we interpolate between the constant values below and the geostrophic values at 500 m. The sounding indicates the base of the strong capping inversion at 365 m. The increase of potential temperature in this capping inversion layer is 2.6° per 100 m. RHI scans from the lidar data confirm the presence of a boundary layer at the coast with an entrainment zone between approximately 300 and 500 m above the surface. The exact initial wind profile for the horizontally homogeneous initial condition is not important because the model will adjust to a quasi-equilibrium with unique mean properties after large-eddies are formed.

The air temperature at shelter height at the NCAR ISS site on 13 January rose steadily at a rate of 0.8°C per hour after sunrise. This local temperature change

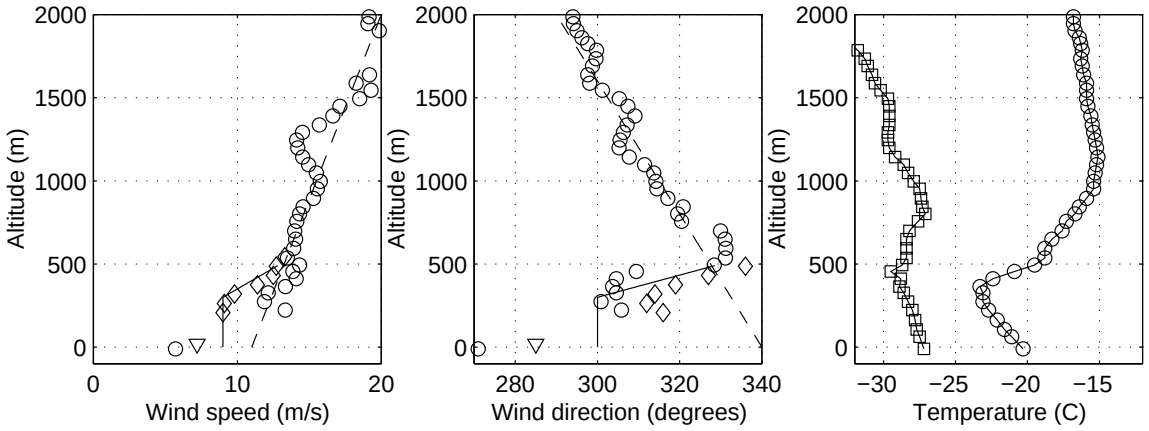

Figure 5.10: Vertical profiles of wind speed (left), wind direction (center) and temperature and dewpoint (right) from observations. Circles from radiosonde and diamonds from profiler.

must have been the result of heating the surface by the sun as cold air advection was certainly happening at this time. Flux measurements were not recorded. To match the surface heat flux over the land in our simulation, a series of precursor simulations were run, each with a different surface albedo. It was determined that an albedo of 0.66 in the model causes the mean temperature at the lowest grid point (7.5 m) to warm at the observed rate after explicit eddies have formed.

Fig. 5.11 shows traces of total TKE (entire domain), and mean temperature, dew-point, wind-speed, wind-direction and pressure for lowest grid-point in the precursor domain (7.5 m) as a function of time after initialization. The total TKE plot shows that the simulation requires about 30 minutes to become turbulent and is approximately steady state after that. The dew-point, shown as the lower line in the second plot, indicates a rapid increase within the first couple minutes and may indicate an error in the near surface dew-point measurements used to initialize the model. The wind speed decreases rapidly during this spin-up and the wind direction shifts after the spin-up. Fig. 5.12 was computed from 516 s of model output starting at 30 minutes past initialization. It shows potential temperature approximately constant and the sensible heat-flux profile decreasing linearly in the boundary layer. These profiles are consistent with those from other LESs of convective boundary layers and indicate a surface sensible heat flux of about 0.03 K m s^{-1}. Fig. 5.15 shows vertical and horizontal slices of vertical velocity at 30 minutes past initialization of this precursor domain. These images confirm a turbulent boundary layer with coherent structures aligned with the mean wind direction.

Extrapolating along the linear sensible heat flux profile to the surface tells us that the surface sensible heat flux should have been about 0.03 K m s^{-1} during this period. The radiosonde sounding tells us inversion height z_i is about 400 m. We

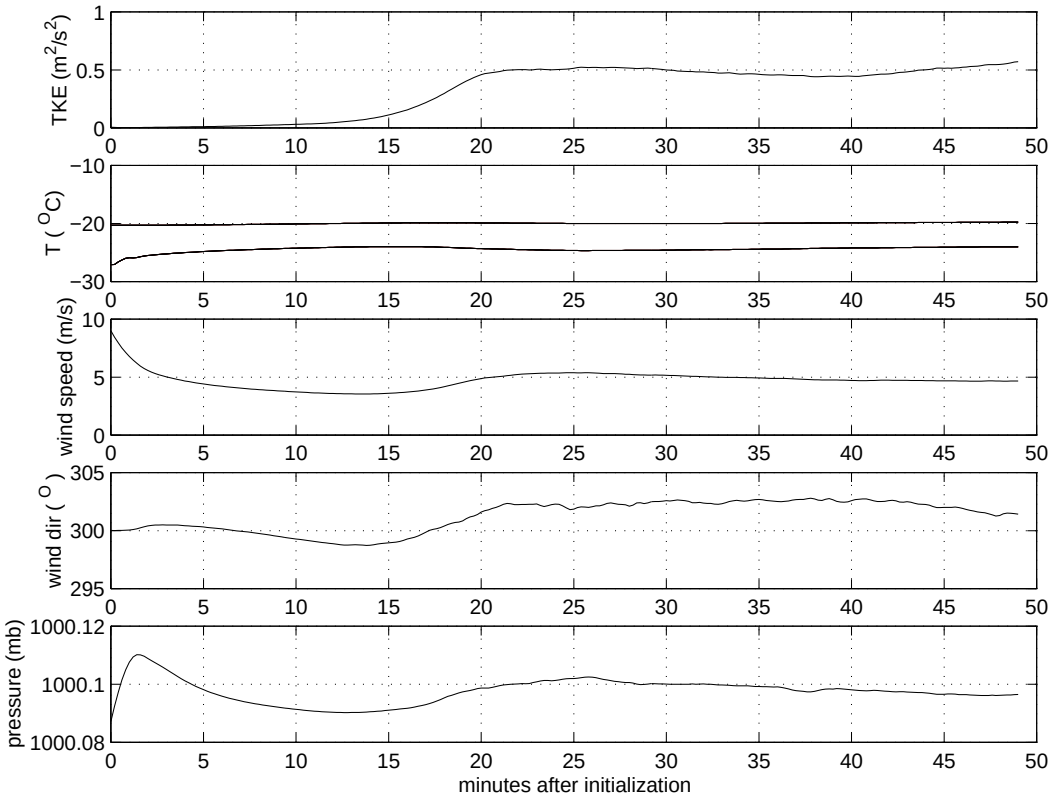

Figure 5.11: Traces of total TKE (entire domain), and mean temperature, dew-point, wind-speed, wind-direction and pressure for lowest grid-point in the precursor domain (7.5 m) as a function of time after initialization.

can use this information to estimate a convective velocity scale (see eqn. 5.4) which can then be used to compute a large-eddy convective timescale. For $\theta_v = 253$ K, $t* = Q_s/w* = 516$ s (8.6 minutes). As expected, this is approximately 50% of the large-eddy turnover time for the Nieuwstadt simulations.

The precursor simulation tends to produce linear structures that are aligned with the mean wind direction. During spin-up, their horizontal spacing is small and, after spin-up, approximately 400–500 m apart (see figs. 5.13 and 5.14). To make sure these linear structures were not a numerical artifact due to truncation error, the precursor simulation was run again with the grid advecting with the mean boundary layer wind. In this Lagrangian (moving) domain, the same linear coherent structures developed, supporting the idea that they are the result of boundary layer organization. Other LES studies which support the existence of linear structures include Moeng and Sullivan (1994), Glendening (1996), Lin et al. (1996), and Khanna and Brasseur (1998). Notice at 397.5 m in figs. 5.13 and 5.14 the linear patterns are oriented perpendicular to the mean flow, suggesting that, the structure there is being influenced strongly by gravity waves in the inversion layer or by Kelvin-Helmholz instability type circulations.

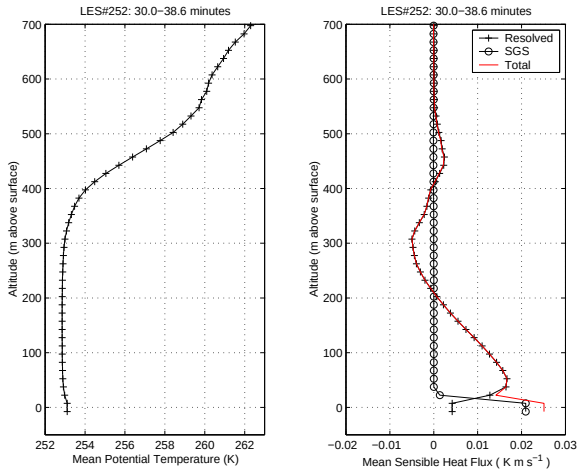

Figure 5.12: Profiles of mean potential temperature (left) and sensible heat flux (right) as a function of altitude for the precursor simulation.

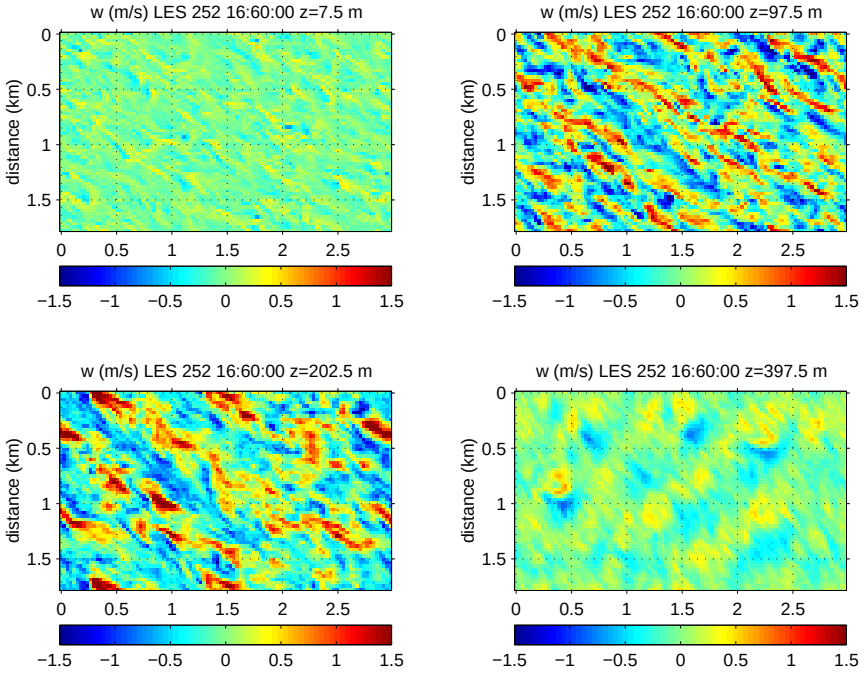

Figure 5.13: Vertical velocity on horizontal planes at different altitudes from LES #252 at 30 minutes after initialization. The altitude is listed above each panel.

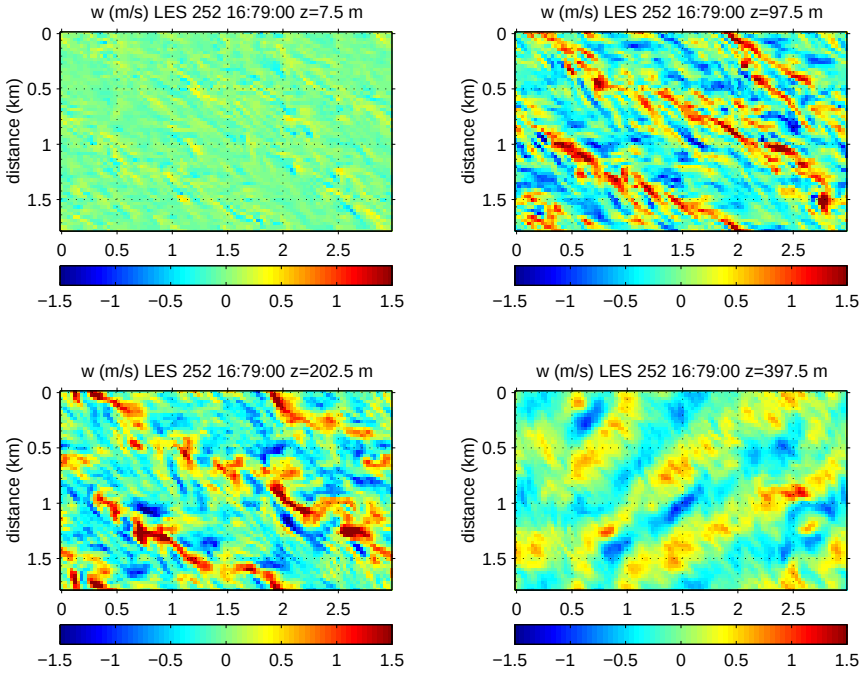

Figure 5.14: Vertical velocity on horizontal planes at different altitudes from LES #252 at 49-minutes after initialization. The altitude is listed above each panel.

Figs. 5.17 and 5.18 show vertical velocity and simulated lidar backscatter, respectively, on east-west oriented vertical slices at one instant from the LES. These images show the lack of a smooth IBL transition. For example, in fig. 5.17, a strong penetrative plume reaches to a 500 m altitude between 2 and 2.5 km offshore. At greater offshore distances, the boundary layer height, based on the altitude of maximum gradient, is lower. A short time later (not shown) the plumes will have changed substantially and a different snapshot would be seen.

5.6 Model sensitivity

The coherence of turbulence structures generated by the model is controlled by the nondimensional mixing coefficient, DKR. This parameter sets the magnitude of the subgrid turbulence parameterization, which is represented by eddy viscosity for mechanical mixing;

$$K_m = \mathrm{DKR}\, l\, \sqrt{e} \tag{5.5}$$

where l is the scale length, and e is the turbulent SGS kinetic energy which is predicted. The eddy viscosity for thermal mixing is $K_h = 3K_m$. For these experiments, the scale length is set to the grid spacing. When DKR is approximately equal to or above 0.20, we find an almost steady state solution after running the large IBL domain for times greater than approximately 2 hours (see Fig. 5.21). As DKR is decreased, we

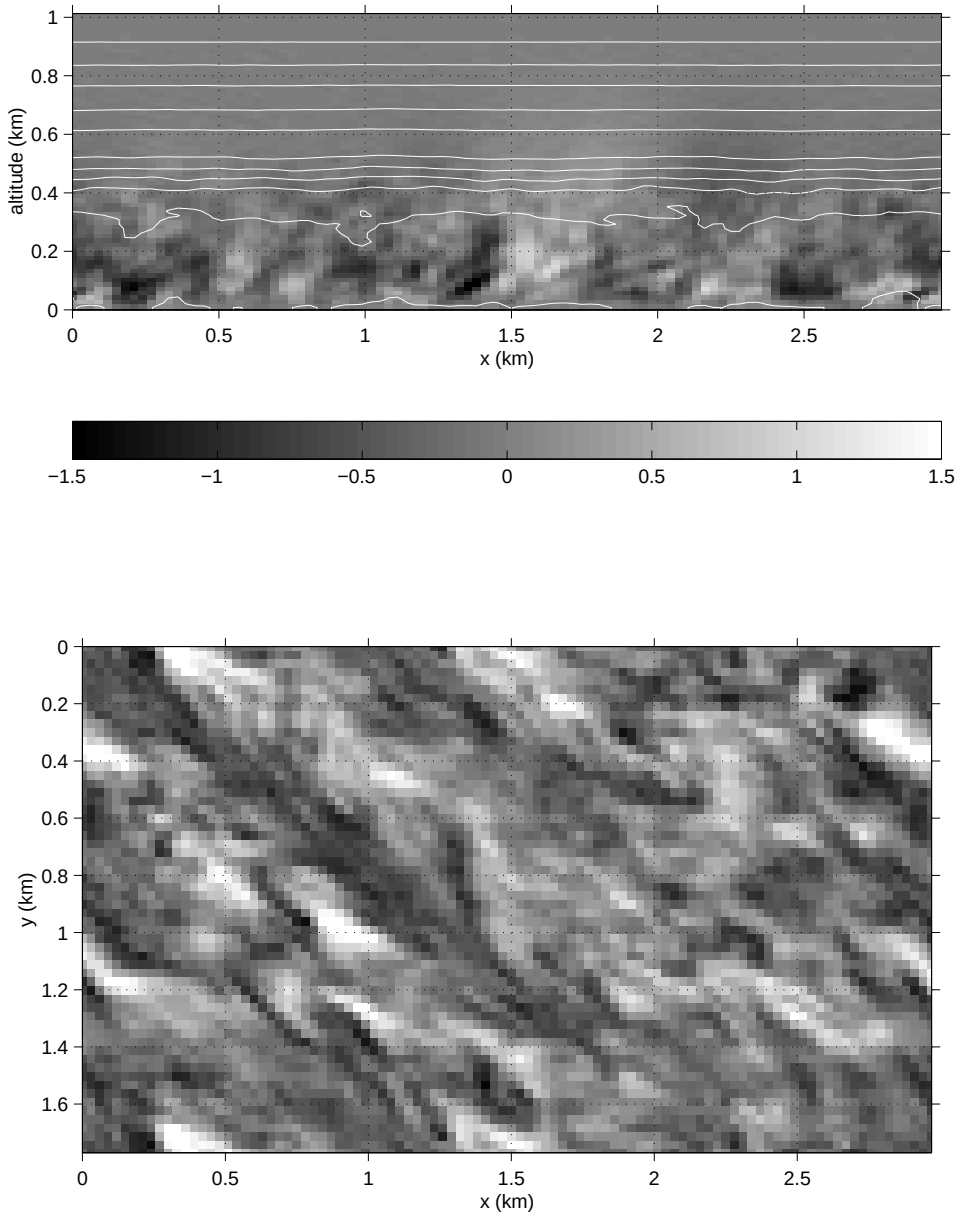

Figure 5.15: At 30 minutes in the precursor simulation. Top panel: vertical velocity (gray shades) and potential temperature (white contours) on a vertical plane. Bottom panel: vertical velocity (gray shades) on a horizontal plane at 200 m above the ground. Both images share the same color bar.

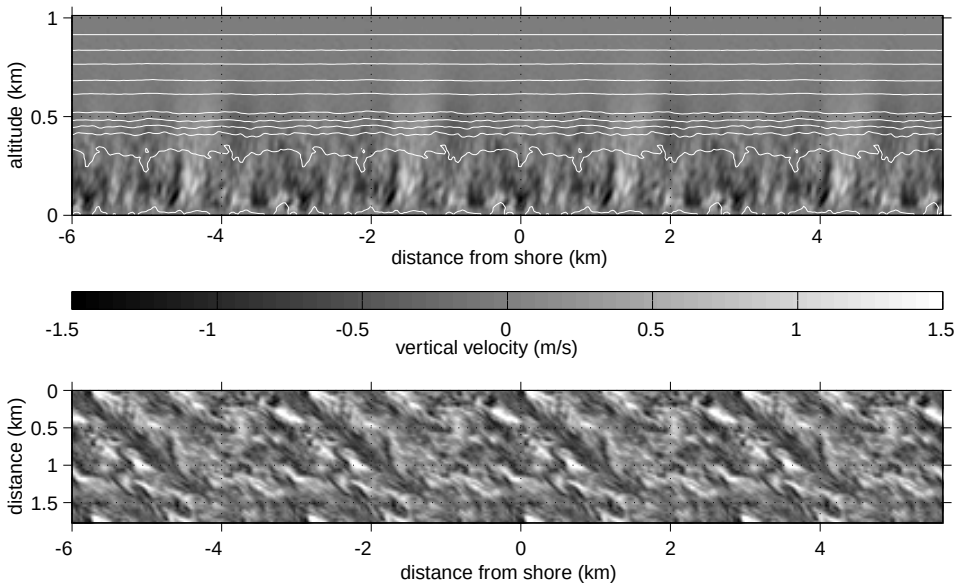

Figure 5.16: Vertical velocity on vertical (top) and horizontal at 200 m (bottom) slices at the initial condition of the IBL simulation. The initial condition of the IBL simulation is the 30-minute solution of the precursor simulation which has been replicated four times in the east-west direction.

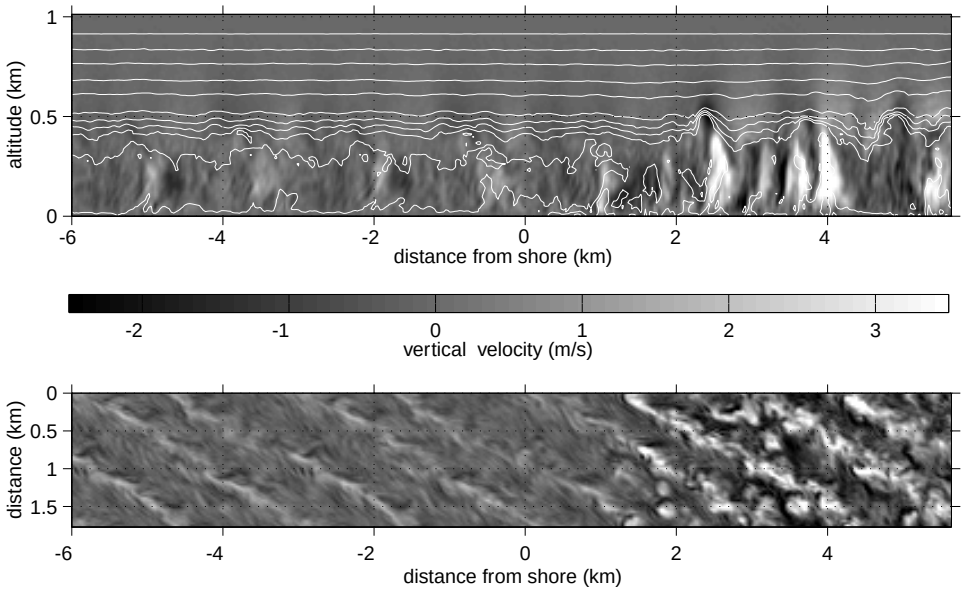

Figure 5.17: Vertical velocity on vertical (top) and horizontal at 200 m (bottom) slices at 30 minutes past initialization of the IBL simulation.

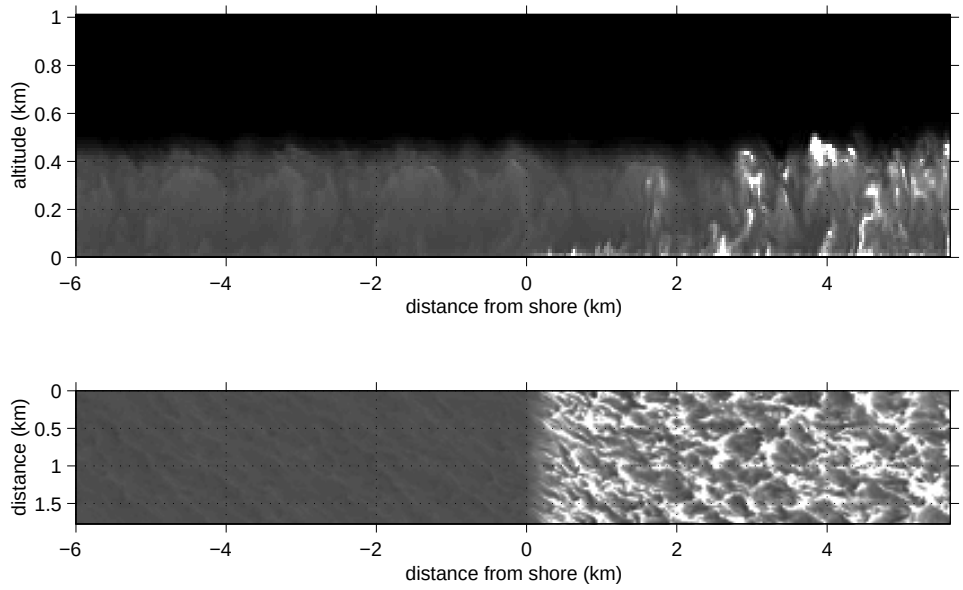

Figure 5.18: Simulated lidar backscatter at 30 minutes past initialization on vertical (top) and horizontal at 7.5 m (bottom) in the IBL simulation. Brightness is proportional aerosol scattering.

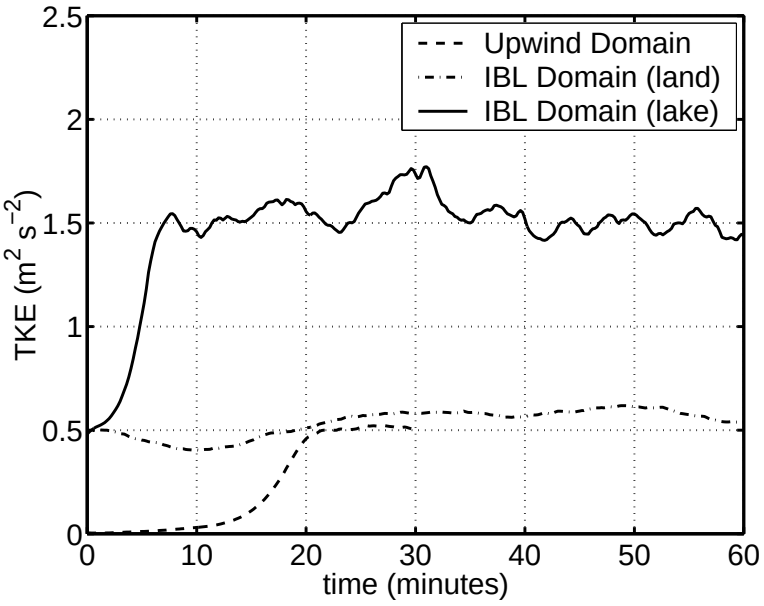

Figure 5.19: Resolved TKE as a function of time for the precursor simulation (dashed), and over the land (dash-dot) and over the lake (solid) in the IBL simulation #260.

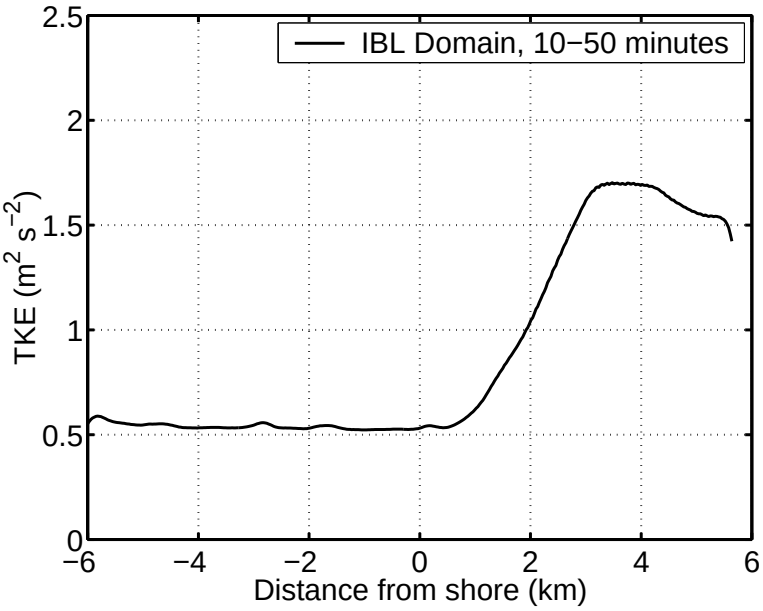

Figure 5.20: Resolved TKE as a function of distance from the shore for IBL simulation #260.

see more variation in the solution. With a DKR of zero, the simulation becomes very noisy and the noise generates very unrealistic values which prevent the simulation from continuing. Fig. 5.22 shows solutions for simulations with DKR set to 0.15, 0.10, 0.05 and 0.00. Each of these simulations was started with the final solution of #212 (see Fig. 5.21). Note that simulation numbers 216, 215, and 222 were intentionally terminated as they showed no signs of noise that lead to the unrealsitc values as in #223 which used a DKR=0.

5.7 Mean CIBL structure from LES

Fig. 5.26 shows the mean and standard deviation of simulated aerosol scattering on an east-west oriented vertical slice. This figure can be compared with fig. 3.37, which shows mean and standard deviation of the real lidar observations in the same dimensions. The model shows a gradual increase in aerosol backscattering in the middle of the boundary layer as the offshore distance increases. This increase in the mean is not observed in the lidar data. The smooth structure shown in fig. 5.26 is very different from the highly variable structure from a snapshot such as the ones shown in figs. 5.18, 3.32 and 3.34.

Vertical slices of mean wind speed, wind direction, potential temperature and relative humidity from the three IBL simulations appear very similar to each other when viewed as contour plots such as figs. 5.27, 5.28, and 5.29. Perhaps the most pronounced feature in these plots is the dip in the height of the boundary layer between 2 and 4 km offshore. This dip is the result of divergent flow which is also observed in

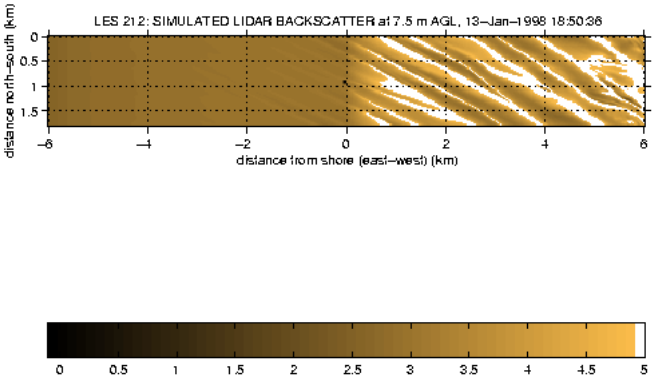

Figure 5.21: Simulated lidar aerosol scattering on a horizontal plane near the surface in LES #212. This simulation used DKR=0.20 and the solution converged to almost steady linear structures.

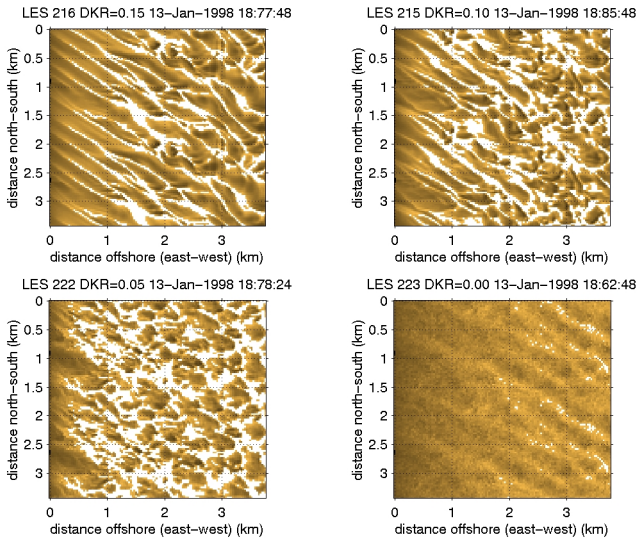

Figure 5.22: Simulated lidar backscatter near the surface from four different simulations. The only parameter changed was DKR coefficient.

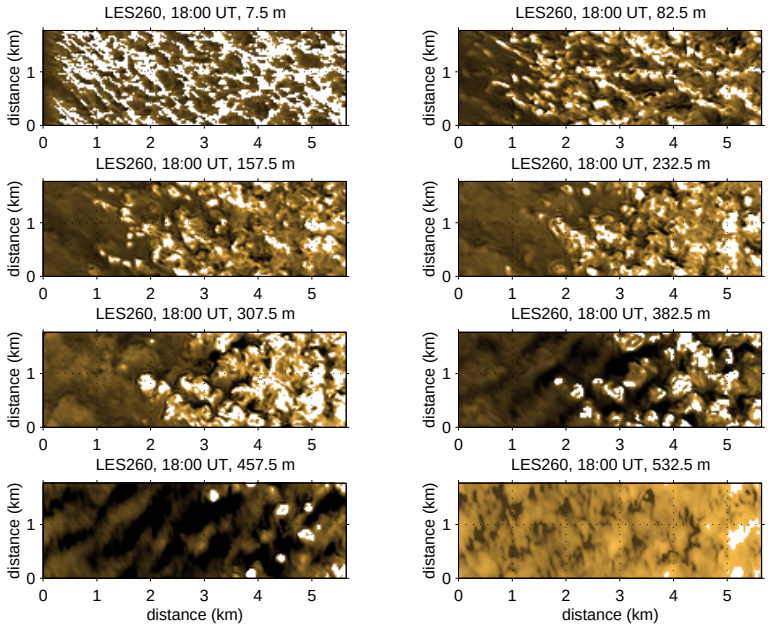

Figure 5.23: Simulated lidar aerosol scattering on horizontal planes in LES #260. The altitudes were chosen to match those in Fig. 3.36.

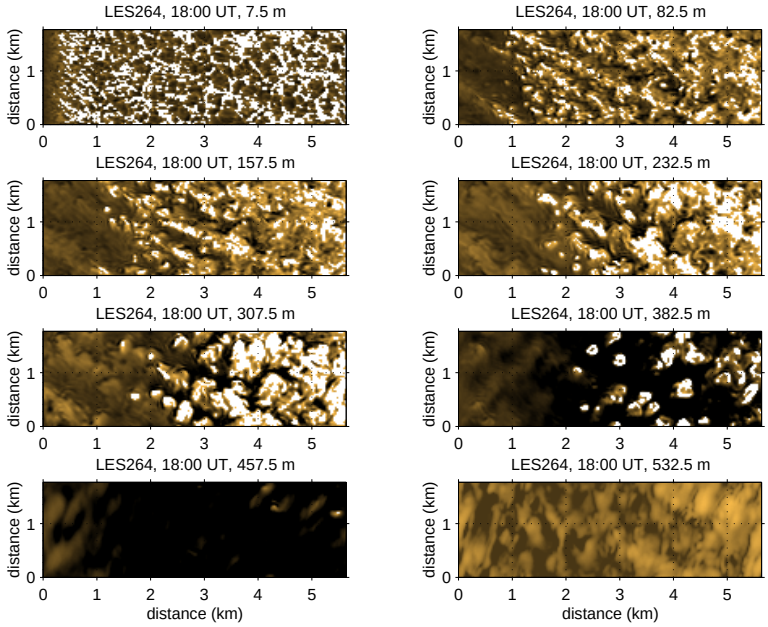

Figure 5.24: Simulated lidar aerosol scattering on horizontal planes in LES #264. The altitudes were chosen to match those in Fig. 3.36.

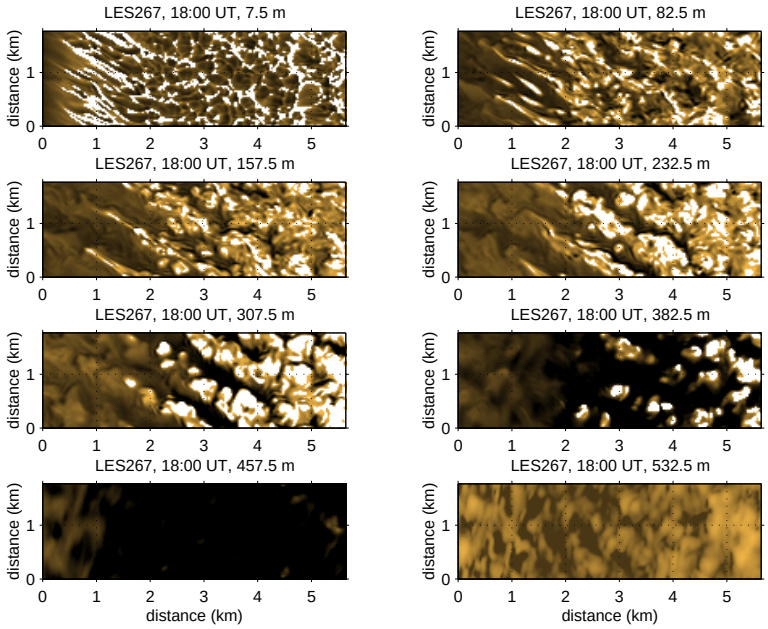

Figure 5.25: Simulated lidar aerosol scattering on horizontal planes in LES #267. The altitudes were chosen to match those in Fig. 3.36.

the lidar measurements of aerosol motion (see section 4.4).

All of the simulations produce a sharp increase in the near surface wind-speed with increasing offshore distance that is more similar to the mean lidar derived acceleration on January 10 than for January 13 (see top panel of fig. 5.30). The lidar-derived wind-speed increase for January 13 is much less probably because most of the lidar sample region appears to lie within a mesoscale eddy associated with Sheboygan point (see fig. 4.7). The lidar-derived wind field on 10 January (see Fig. 4.3) is much more homogeneous than 13 January, and the acceleration more similar to that of the model despite the fact that the mean flow is from a slightly different direction.

Upon closer inspection of the contour plots, however, and as shown in line plot in the bottom panel of fig. 5.30, we find that the LES surface layer winds for LES#260 turn clockwise with increasing offshore distance and counterclockwise in LES#264 and #267. The lidar-derived wind direction on January 10 and January 13 turn clockwise also, although at a smaller rate. This veering of the wind is consistent with the change that would occur to the resulting wind vector in a body force diagram if the friction vector were reduced.

Fig. 5.30 also provides clues regarding balances or imbalances in the model which govern the mean flow. For example, in LES#260, the mean wind speed at 7.5 m over the land remains constant and is equal to that in the final solution of the precursor run. This is an indication of a balance of forces. The other simulations, #264 and #267, which did not use the enstrophy conserving advection scheme, increased the speed by about 1 m s^{-1} in the first 500 m downstream of the inflow boundary condition. The

same two simulations show a backing trend of 5° over the 6 kilometers of domain over the land while the simulation using the enstrophy conservation scheme only backed about 2° over the same 6 km. This over-the-land difference between the two schemes appears only near the surface. At higher altitudes, differences between the two schemes is apparent in the mean wind over the lake. The cause of the discrepancy among the three model runs remained under investigation at the time of this writing.

The break in the LES#260 curve in fig. 5.30 is due to the presence of a four grid point cube at the shore in a few frames which was installed to simulate flow around a large building and attempt to study its wake-effect over the lake. This numerical experiment was never completely analyzed, which required comparing the simulated flow patterns with and without the cube. The presence of the cube probably has little effect on the mean properties of the flow and probably very small effects on turbulence statistics.

One of the powers of LES is to estimate fluxes with sampling errors much less than traditional observations. The model can also be used to show the distribution of fluxes over a region. Fig. 5.31 shows mean sensible heat, latent heat, and momentum fluxes at the surface as a function of distance from shore during a continuation of simulation #260. (Fluxes were not output correctly for #260, so the simulation was resumed with repairs as #274.) This shows that over land the mean sensible and latent heat fluxes were about 40 W m^{-2} and 32 W m^{-2} respectively. Those fluxes increased to 900 W m^{-2} and 450 W m^{-2}, respectively, over the water. The total (resolved plus subgrid-scale) momentum flux decreased from 0.46 kg m^{-1} s^{-2} to 0.26 kg m^{-1} s^{-2}. Unfortunately, there are no observations to confirm these fluxes, but they do appear to be within reason. Fig. 5.32 shows north-south averaged fluxes on east-west vertical slices. These average fluxes contain systematic high-frequency oscillations (they do not cancel out with averaging) and the cause of this was still under investigation at the time of this writing.

5.8 Chapter Conclusions

In the case of 13 January, and probably in most others, it is important to have mature turbulent offshore flow in order to simulate realistic convection patterns near the shore. This is because the accumulation of potential energy near the surface in the premixed boundary layer causes a subsequent overshoot in the vertical heat flux. The lagged formation of explicit eddies during spin-up was also observed in the simulation designed to duplicate the Nieuwstadt experiment. A similar phenomena occurs in the LES when laminar flow advects offshore; there are no explicit eddies to transport the potential energy that accumulates near the surface over the water. The explicit eddies require time and, hence, downstream distance to develop.

To overcome this problem, turbulence is generated in a small, laterally periodic, domain with surface properties equal to that of the surface upwind of the lake. Spin-up occurs in this small *precursor* domain. The turbulent solution to the small domain is replicated in the IBL domain. To maintain a turbulent boundary layer over the upwind

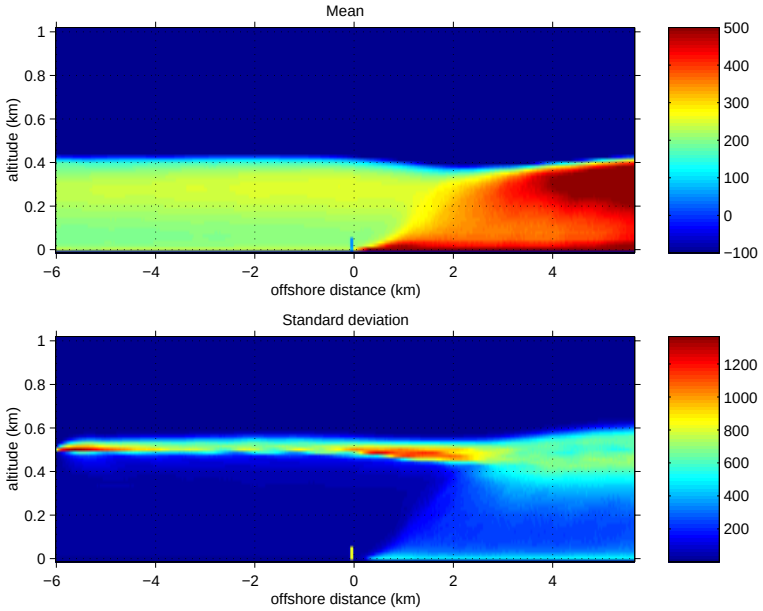

Figure 5.26: Mean (top) and standard deviation (bottom) of simulated lidar backscatter from LES#264.

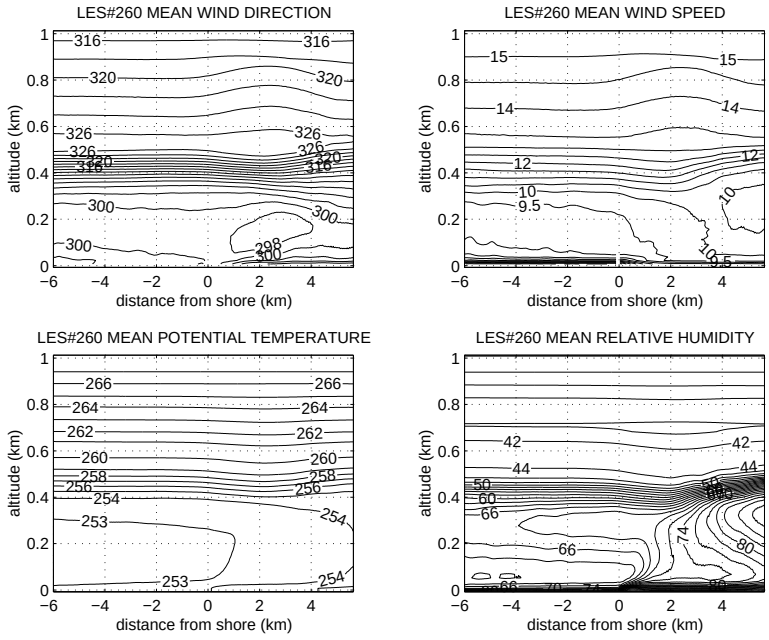

Figure 5.27: Mean wind, temperature and moisture for LES#260.

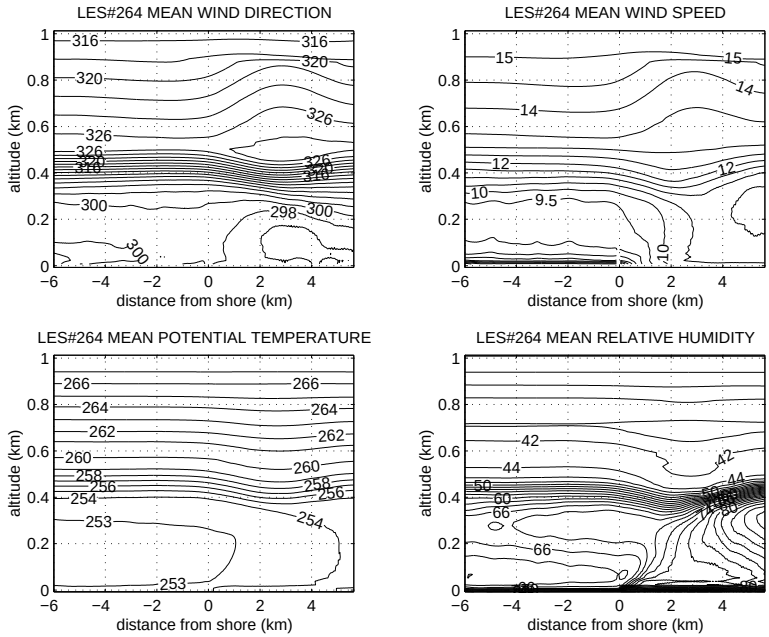

Figure 5.28: Mean wind, temperature and moisture for LES#264.

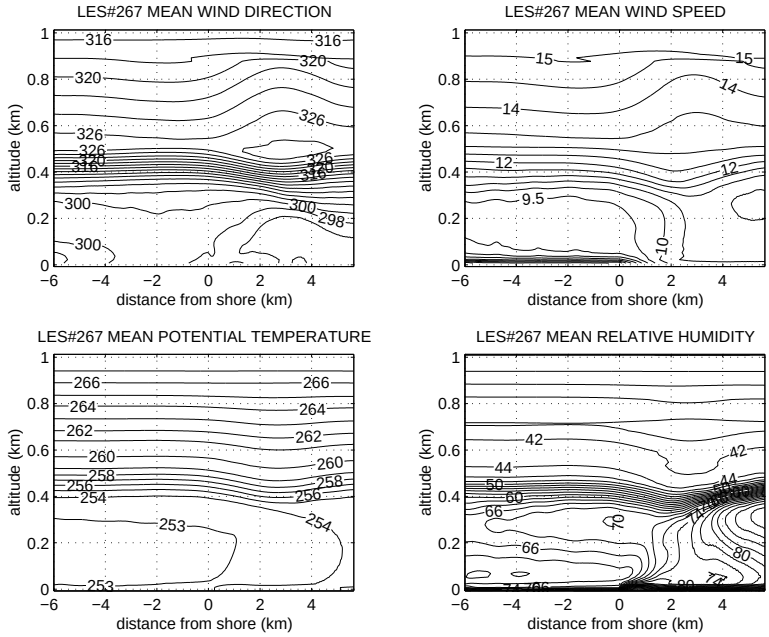

Figure 5.29: Mean wind, temperature and moisture for LES#267.

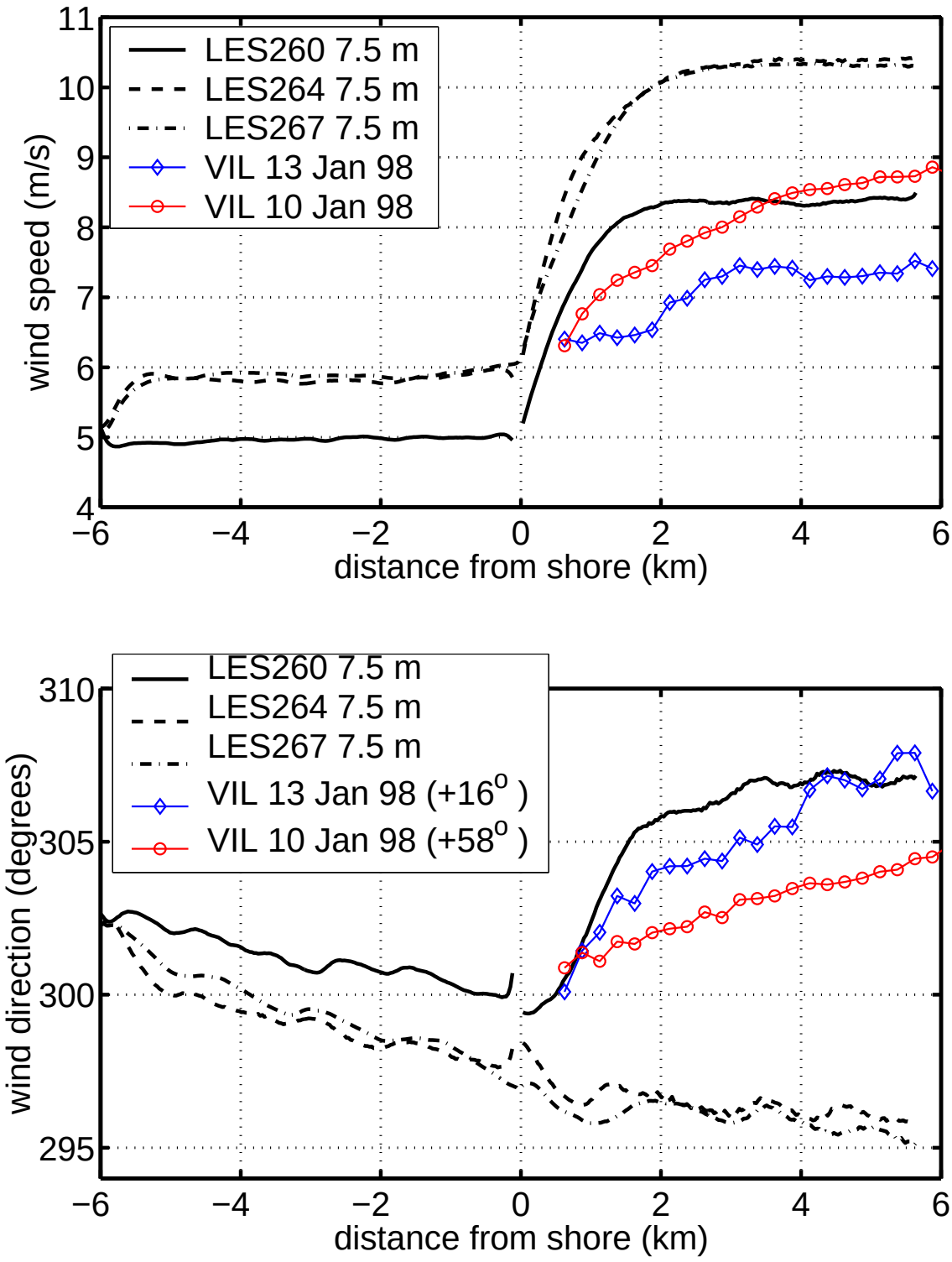

Figure 5.30: Mean wind speed (top) and direction (bottom) at 7.5 m above the surface from the three LESs and lidar observations on 10 and 13 January 1998.

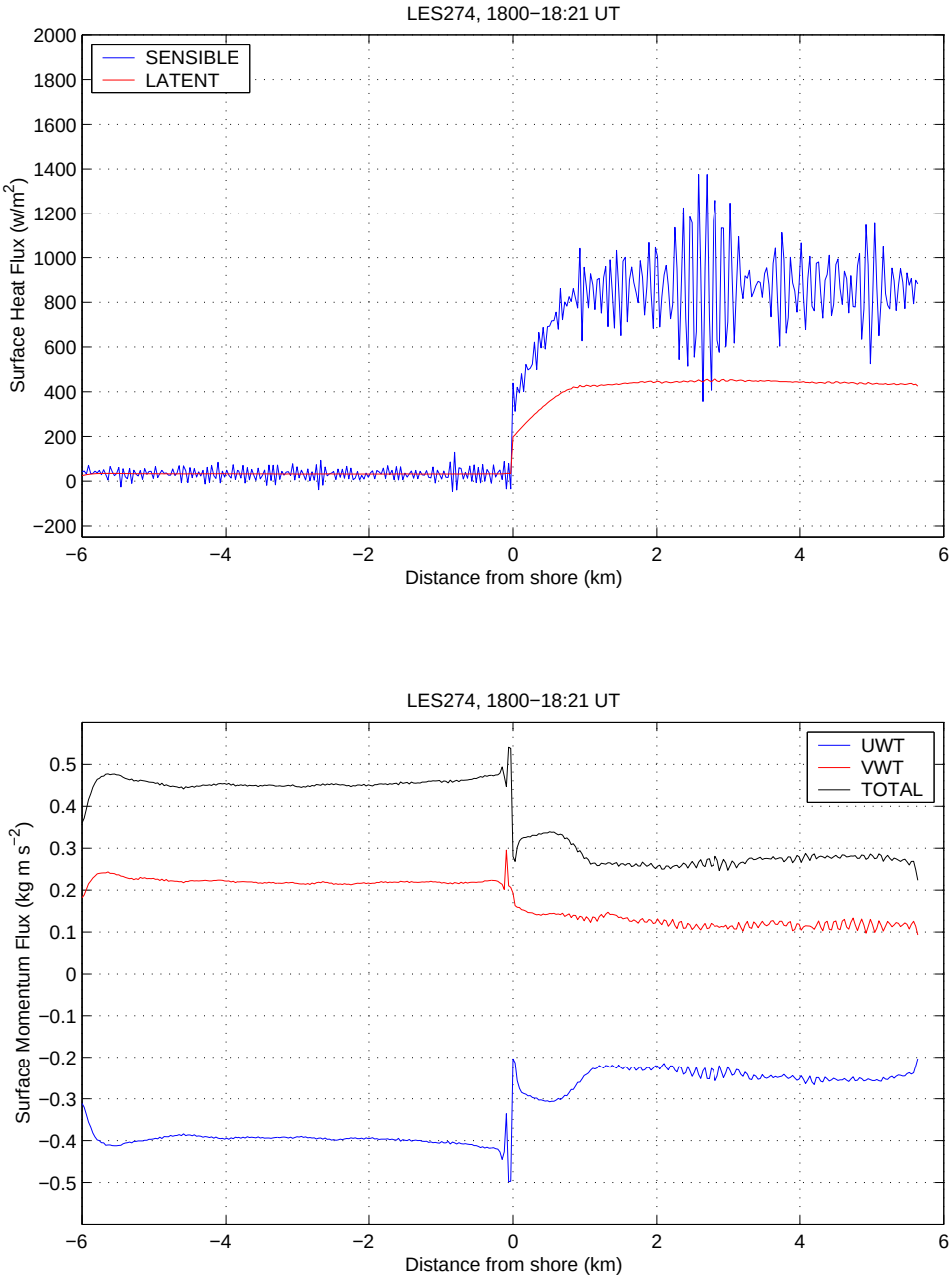

Figure 5.31: Mean sensible, latent, and momentum fluxes at the surface from LES#274.

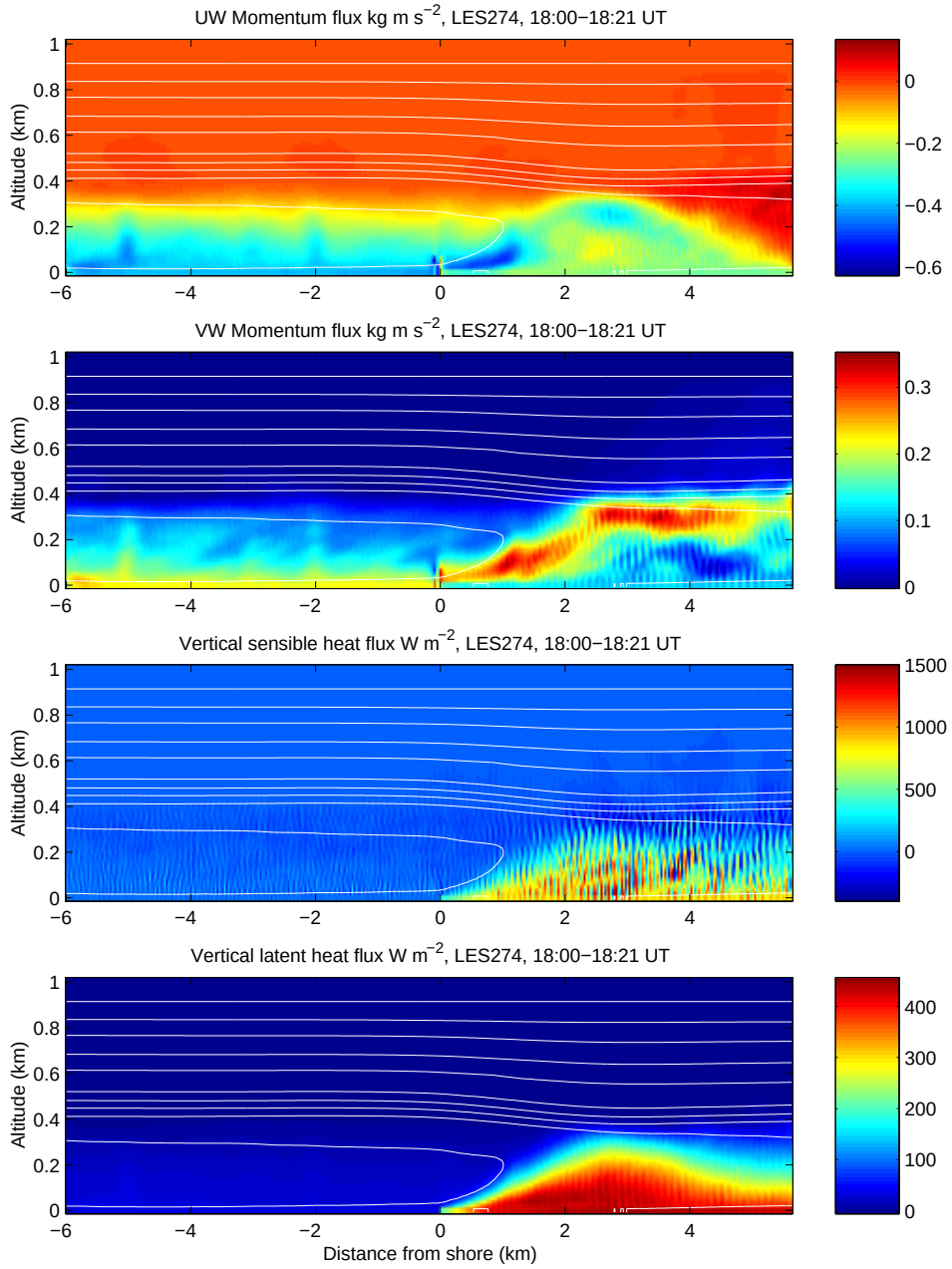

Figure 5.32: Mean u-momentum (top), v-momentum (second down), sensible-heat (third down), and latent-heat (bottom) vertical fluxes as a function of distance from the shore and altitude for LES#274. White contours are of potential temperature at 1.5 K intervals.

part of the IBL domain, perturbations are recycled or added to the mean state of the precursor solution on the western wall. Turbulence statistics can be computed from LES output after about 30 minutes of simulation. During the first 30 minutes, the IBL grows and reaches a steady state.

The LES produces cellular, or braided, coherent structures near the surface. These patterns are similar to those seen in the lidar data on all three cold-air outbreak days. Except for their elongation in the mean wind direction, they resemble convection cell patterns near the bottom surface in a laboratory tank experiment (Willis and Deardorff, 1979) and in other LES experiments of homogeneous convective boundary layers (Schmidt and Schumann, 1989; Mason, 1989). The observation is convincing evidence that the turbulence structure in the convective surface layer is strongly controlled by convection cells that span the depth of the boundary layer.

The enstrophy conserving advection scheme appears to change the wind direction as a function of offshore direction in a manner that makes physical sense and is in agreement with lidar observations. The acceleration of the simulated flow also happens within a shorter distance when compared to the lidar derived accelerations.

It is important to note that for these simulations to be successful, the height of the domain was restricted to 1 km. Gravity waves became trapped in the inversion layer when the simulations were run with deeper domains. These waves amplified over time, and, in simulations over several hours, the waves eventually dominated the turbulent structures in the boundary layer. It is likely that gravity waves play a role in the organization of boundary layer structure (Carruthers and Moeng, 1987; Kuettner et al., 1987; Hauf and Clark, 1989). It is also important to keep in mind that the constant inflow boundary condition does not allow gravity waves to propagate upstream, and, as a result, it places a restriction on the direction of wave propagation. Therefore, the technique may not work for some atmospheric simulations where the modeling of upstream propagating waves are important.

Chapter 6

Horizontal eddy structure

6.1 Introduction

Prior to this chapter, comparisons of patterns in the lidar data with patterns in the simulated lidar backscattering from LES output were very subjective. This chapter presents and applies a technique that identifies the patterns in the flow fields more quantitatively, thereby allowing less subjective comparisons.

In other observational turbulence research, measurements of a variable such as a velocity component are commonly obtained at a single point as a function of *time*. This is probably because of the dearth of instruments that can provide spatial information. An example of a traditional turbulence measurement is a time-series of wind-speed measurements obtained from an anemometer on a tower. Eddies advecting past the sensor cause the measurement to fluctuate about a mean over time. To explore the characteristics of the turbulence at that point location, the time-series of measurements can be used to compute descriptive statistics such as the mean and higher-order moments (i.e. variance, skewness and kurtosis) which describe the distribution of that variable. For example, it has been confirmed that the positive skewness of vertical velocity in a convective boundary layer is a result of narrow intense updrafts and broader regions of weaker subsidence (Lemone 1990, Moeng and Rotunno, 1990).

Another popular and traditional use of time-series data is to compute autocorrelation functions (ACFs). An ACF indicates the amount of common variation between a variable at one time and the same variable at a later time (Stull, 1988). Therefore, ACFs of time-series are a function of time-shift, or time-lag. ACFs are always equal to one at zero time-lag, and, for turbulent flow, typically decrease with increasing time-lag. Quantities which can be derived from the ACF include the Taylor microscale (Tennekes and Lumley 1972) and the integral length scale, which will be discussed in section 6.7.

By continuously moving a single point sensor at a steady rate, invoking Taylor's frozen-turbulence hypothesis, and converting time to distance by multiplying by the speed of the sensor, one can infer the spatial characteristics of turbulence. This is commonly done with aircraft data (Lenschow and Stankov, 1986), but it only pro-

vides one-dimensional information (i.e. along the flight path). The one-, two-, and three-dimensional spatial imaging capability of the lidar permits much improved spatial sampling compared to traditional probes. Because the VIL can obtain spatial information on regular intervals of time, it is really capable of providing 4-D data.

Of course, the LES also produces 4-D output therefore, the VIL is ideally suited for LES verification. This chapter presents spatial correlation functions of both lidar and LES output in order to see differences in the data that might have otherwise gone unnoticed by subjective visual comparison of the images.

6.2 Technique Description

For two-dimensional (2D) data that are homogeneous in both directions, 2D ACFs can be computed using fast-Fourier Transforms (FFTs) or by incrementally shifting an image with respect to itself and computing a correlation coefficient for each pair of lags. For horizontally homogeneous data, the resulting ACF is representative of the mean properties at any position on the images used to compute it. In this work, because of the inhomogeneity of the boundary layer in the east-west direction, a slightly different procedure was used. Here, correlation coefficients are calculated only for north-south oriented one-dimensional rows. It is assumed that the turbulence statistics are homogeneous in this shore-parallel direction at any altitude. The 2D CCF, therefore, was computed using the linear-correlation coefficient for shifted north-south oriented rows of data at the same altitude. The amount of east-west shift is called *x-lag* and the amount of north-south shift is called *y-lag*. Lags to the east and north are positive lags. Fig. 6.1 illustrates how the shifted arrays, a and b, are extracted from a 2-D grid of data points for a given set of lags. 2-D cross-correlation functions (CCFs) were computed from data on horizontal planes at a series of offshore distances. The RHI volume scan data enabled this to be done at multiple altitudes.

The formula for the linear correlation coefficient (Bevington, 1969) is:

$$R = \frac{N \sum a_i b_i - \sum a_i \sum b_i}{[N \sum a_i^2 - (\sum a_i)^2]^{1/2} [N \sum b_i^2 - (\sum b_i)^2]^{1/2}} \tag{6.1}$$

Here, a and b are the shifted north-south oriented arrays and i is the index into either array. N is the number of points in either the a or b array. Because the azimuthal limits of the lidar scans usually do not line up with the cardinal directions, large parts of the gridded data are usually filled with values to indicate absence of data. If a "no data flag" is present in either a or b, the companion value is changed to a "no data flag" and that pair is not used in the calculation of the correlation coefficient. Correlation coefficients were only calculated if at least 20 data pairs were available for any lag. If 20 pairs were not available, the 2D CCF was marked with the "no data flag" at that particular x-lag and y-lag location.

It should be noted that eqn. 6.1 produces an illegal arithmetic operation when the denominator is zero. This occurs if either the a or b array is filled with a constant value. Unfortunately, the lidar data and LES output occasionally have short segments

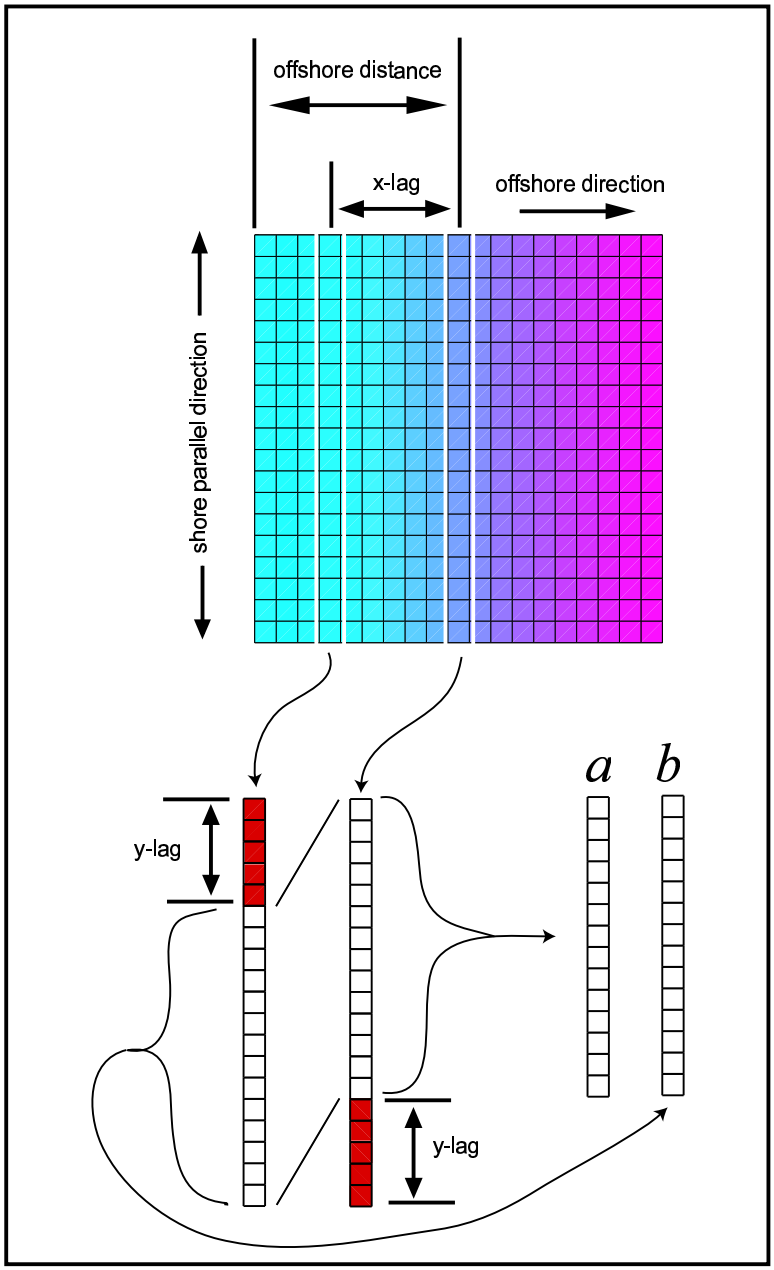

Figure 6.1: Illustration showing how shifted arrays are extracted from gridded data that are inhomogeneous in the x-direction. The linear correlation coefficient will be computed from a and b for the given x- and y-lag.

of constant values. In the lidar data, it is caused by inadequate dynamic range in digitization of the signal, and it occurs when the aerosol scattering is homogeneous at close ranges. Constant values occur in the simulated lidar backscatter because the crude algorithm used to compute simulated lidar backscatter from model output sets the scattering to a constant value when any amount of liquid water is present at a grid point. The solution to this problem in the present work was to check every a and b array for constant values before using them in eqn. 6.1. If either a or b contained a majority of constant values, then the correlation function was marked with a "no data flag" for that particular set of lags. The checking procedure increased the CPU time requirements substantially for an already CPU intensive process.

6.3 Technique Application

The technique described above was applied to both lidar aerosol backscatter data and the simulated aerosol scattering from large-eddy simulations. Range-corrected RHI volume scan data was high-pass median filtered, corrected for distortion, and then interpolated to a 3D Cartesian grid so that the technique could be applied to data on horizontal planes at multiple altitudes. The LES output is on a Cartesian grid also.

2D CCFs were computed for a series of offshore distances and altitudes. For lidar data and model output the horizontal spacing of the zero lags of the CCFs was chosen to be 360 m. The vertical spacing of the CCFs was chosen to be 15 m for the lidar data and 30 m for the LES output. The CCFs were computed using 30-m lags in both directions and used lags up to 1-km in both directions. Therefore, one CCF is a two-dimensional array containing 5041 points (71 by 71).

The CCFs were averaged over time to reduce noise. For the lidar data, this means averaging CCFs that were computed from a sequence of RHI volume scans separated in time by 2–3 minutes. The volume scans were grouped into data collection periods that lasted between 25–78 minutes and contained from 9 to 28 volume scans each. (See table 3.1 and fig. 3.2 for a complete list of the data collection periods.) CCFs of LES output at 12 s intervals were averaged over 30 minute periods. It was assumed that the turbulence statistics are stationary over these periods of time.

For all lidar CCFs, the closest offshore distance of the zero-lag was 1.77 km. For data collected on 10 and 11 January, CCFs were computed for offshore distances out to 8.6 km. For data from 13 January, CCFs were computed only out to 4.65 km. The CCFs were also computed for a series of altitudes between 7 and 577 m above the surface of the lake. In this chapter, CCFs from 13 January are focused on for comparison with the LES CCFs. CCFs from 11 January are presented in appendix C. Figs. 6.2, 6.3 and 6.4 show every other CCF in the horizontal and vertical as a small square tile. The range of lags on the edge of each tile is 2 km ($\pm$1 km) and the zero-lag, or origin, is located at the center of each tile. This form of presentation tends to emphasize the structure at longer lags, which takes up more area on each CCF and shows how the CCFs change as a function of offshore distance and altitude.

Figs. 6.2 and 6.3 show the CCFs for lidar RHI volume scans that were collected during the periods 12:47–13:37 UT and 17:19–18:37 UT, respectively. Fig. 6.4 shows the CCFs for LES#260 (18:00–18:30 UT), which should be compared with the CCFs in fig. 6.3. Perhaps the most interesting difference between figs. 6.2 and 6.3 is the presence of ridges that run through the origin from the lower-left to the upper-right in the tiles located within 3 kilometers of the shore and below 200 m altitude in fig. 6.3. Those ridges do not appear in fig. 6.2 or, more importantly, in fig. 6.4. A closer look at fig. 6.3 shows the correlation functions are positive in the extreme upper-left and lower-right corners of those tiles. This feature is an indication of lineal structures in the lidar data that are oriented 90° to the direction of the mean flow and have a wavelength of over 1 km. This organization of convection in the boundary layer is most likely caused by gravity waves in the capping inversion layer which influence the development of convective plumes beneath them. This may happen by gravity waves changing the height of the capping inversion slightly and, thereby, affecting mean vertical motion and convergence/divergence patterns in the boundary layer with the same spacing as the waves. Animations of PPI scans from 14 December 1997 and 19 January 1998 provide additional observational evidence that waves strongly influence boundary layer turbulence structure. Fig. 6.4 also shows the strong tendency for the LES to generate lineal structures which are aligned with the mean flow.

The absence of the effect of waves at this location in the earlier volume scan data (12:47–13:37 UT) and their absence at farther ranges is convincing evidence that they are not systematic errors as discussed in section 2.6. The absence of the effect of waves at that location in the LES suggests that the waves in the capping inversion layer are not being simulated correctly. This is most likely a problem with the boundary conditions. For example, perhaps the model domain is not tall enough and the absorbing layer too low. Another possibility is that the inflow boundary condition interferes with proper wave development.

Fig. 6.4 shows the tendency for the LES to generate linear structures that are oriented with the wind direction throughout most of the boundary layer. Particularly between 50 and 250 m altitude and from the shore to about 1.5 km offshore, strong flow parallel bands with 1 km spacing are observed. The effect of increased convective forcing from the lake can be seen in a layer that rapidly deepens to about 200 m altitude at 2 km offshore. In this region, the band spacing is about 250 m. Some evidence for gravity wave activity exists in the CCFs above about 300 m. These CCFs have flow perpendicular bands with spacing of about 250 m.

6.4 The two parts of a CCF

Based on the inspection of many CCFs in this and previous studies it appears that there are two particularly interesting regions on each CCF: a steeply sloped region near the origin and a broad, unsloped region outside the steeply-sloped region. The origin of a correlation function is always equal to one, and the CCF decreases rapidly as the lag (the distance from the origin) increases slightly. For the CCFs

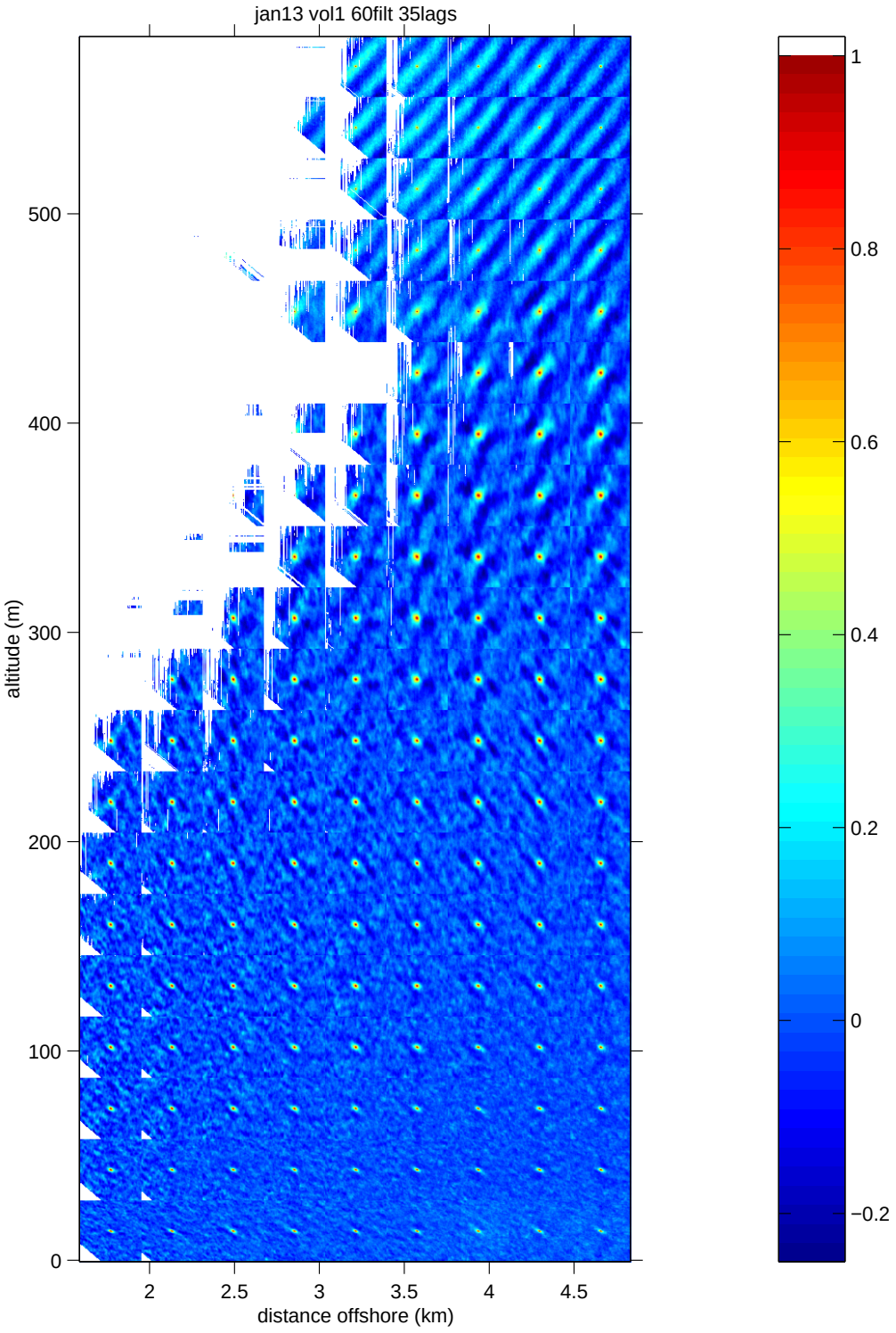

Figure 6.2: 2D CCFs for many offshore distances and altitudes as computed from the VIL data between 12:47 and 13:37 UT on 13 January.

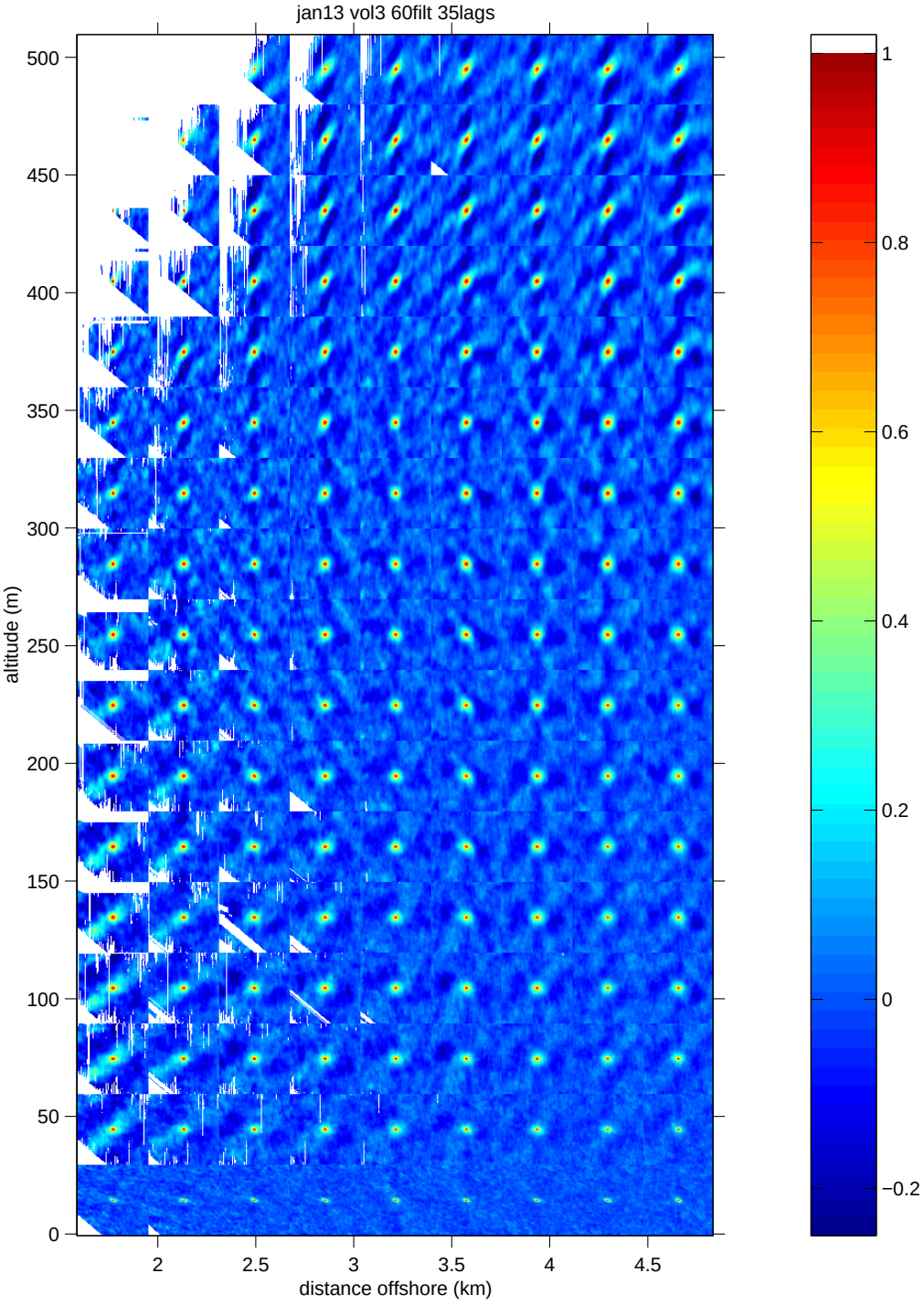

Figure 6.3: 2D CCFs for many offshore distances and altitudes as computed from the VIL data between 17:19 and 18:37 UT on 13 January.

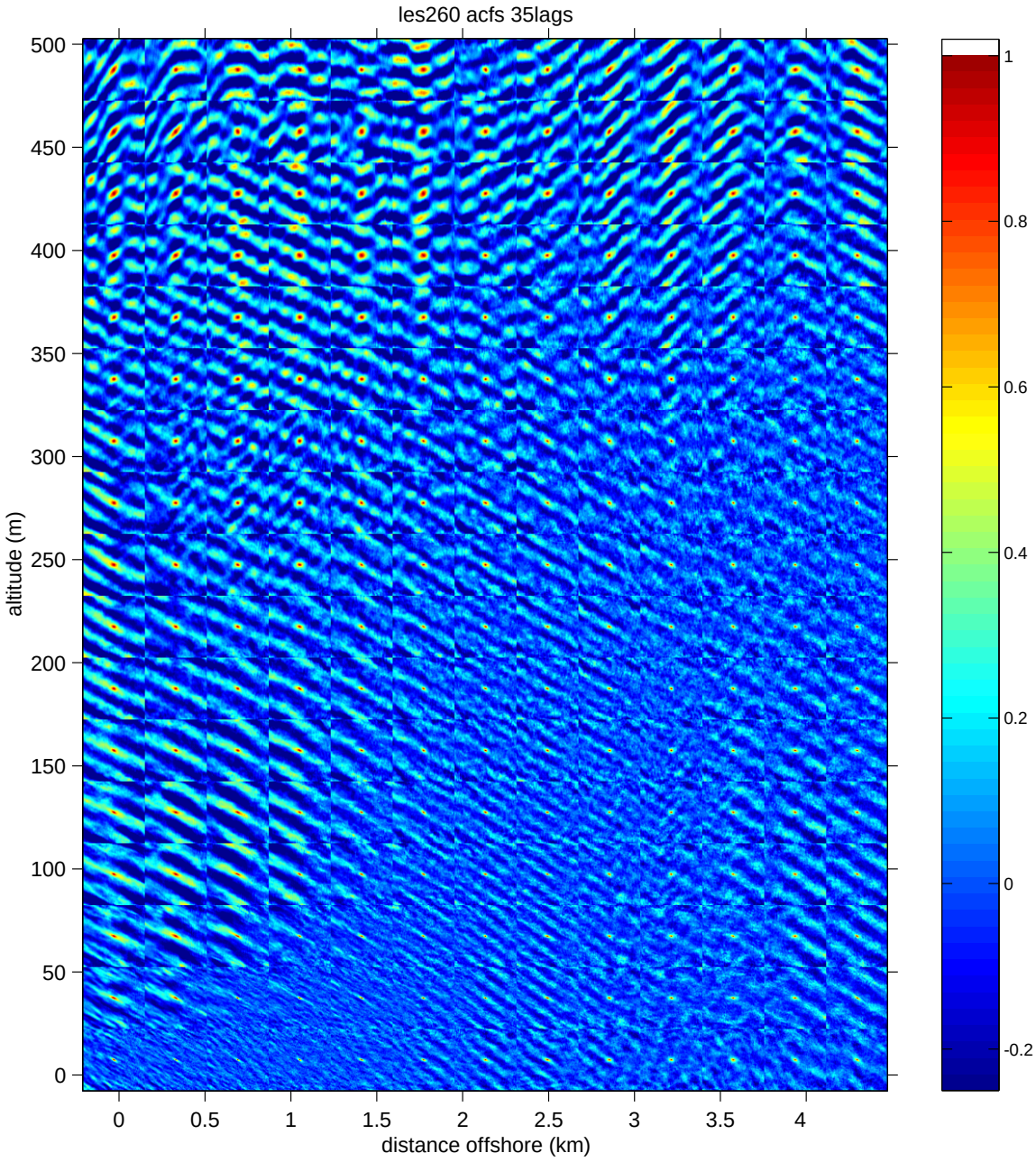

Figure 6.4: 2D CCFs for many offshore distances and altitudes as computed from LES#260.

computed from data on 13 January, this rapid decrease occurs within a distance of about 400 m from the origin, which is the same as the depth of the boundary layer on that day. In this region, where the correlation function tends to be greater than about 0.1, a given isopleth of correlation tends to form closed circles and ellipses which change size, shape and orientation as the offshore distance and altitude change. Kunkel (1978) showed that power spectra of lidar aerosol backscatter at high frequency have a $f^{-5/3}$ dependence. Small lags on the correlation function correspond to high frequency in power spectra. Therefore, this steep inertial subrange region near the peak can be associated with the dissipative turbulent fluctuations of the flow. However, the region very near the origin is also sensitive to small scale correlation due to linear interpolation in the conversion of data from spherical to Cartesian coordinates. This effect will be discussed in section 6.9.

The second interesting region on the CCFs is the remaining broad and unsloped region. In this region, the isopleths of correlation tend not to form closed contours around the origin. The lags in this region correspond to scales larger than those in the inertial subrange. In this region, we can see the effects of mesoscale organization such as horizontal convective rolls. The spacing of lineal rolls can be obtained by determining the distance between the origin and the next local maximum associated with a ridge line that runs approximately parallel to the direction of the flow or the flow's mean shear vector.

6.5 Best-fit ellipses

Contour levels of 0.1 and above on the 2D CCFs tend to form circles or ellipses and lie within the steeply-sloped region. Ellipses can be completely described by three numbers: major axis, minor axis, and orientation. The ratio of the major to minor axes is the ellipticity. The ellipticity of a circle is one. As the length of the major axes increases, relative to the length of the minor axis, the ellipticity increases from one. Because the major axis is always longer than the minor axes, there are no ellipticities less than one. For example, near the surface it is common to see ellipticities ranging from 2 to 3. At higher altitudes, the ellipticities decrease, especially offshore where the convection is the strongest. Above the boundary layer, where there is no aerosol structure in the lidar data, the ellipses become very small as expected for noise.

The best fit ellipse from a least-squares solution to any closed contour encircling the origin of the cross-correlation function was obtained using functions developed by Gander et al. (1994). Other possible methods for ellipse fitting, although not used here, include Halir and Flusser (1998) and Halir (2000).

Features such as ellipticity of the contours in the steeply-sloped region and periodic linear structure of the broad and unsloped region were shown by Ferrare et al. (1991) using PPI scan data of homogeneous convective boundary layers collected in 1983. They found the orientation of the ellipses to be approximately parallel to the shear vector. Improvements in lidar scanning speed since that time have enabled RHI volume scans as described in Chapter 2. Therefore, the lidar data can now be used to

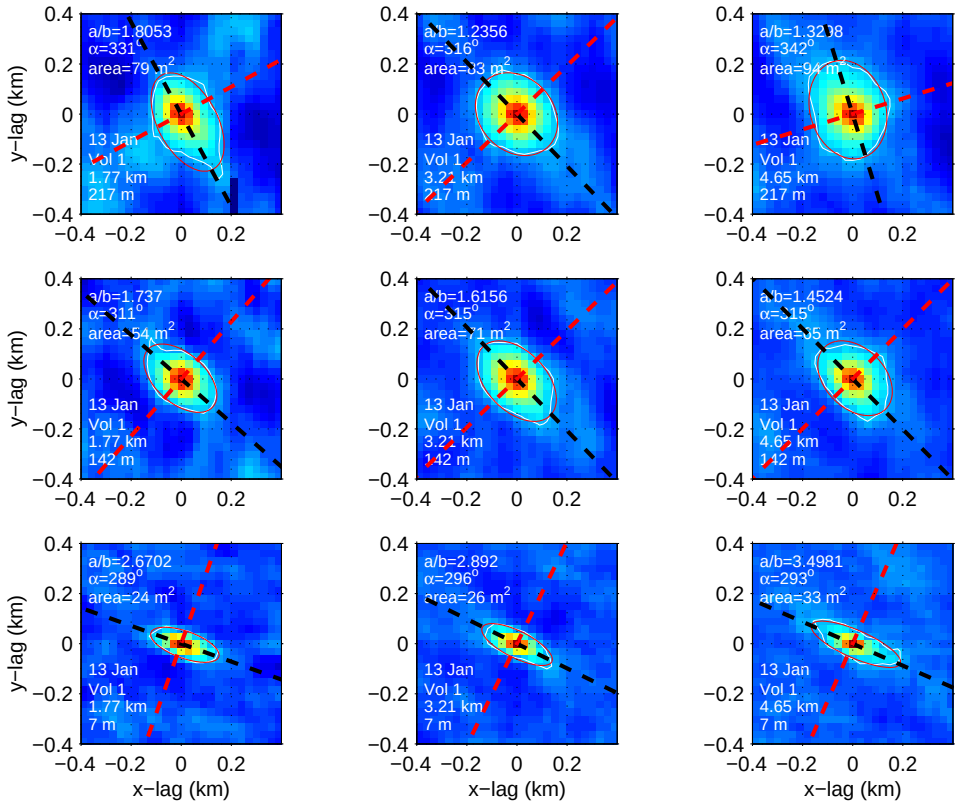

Figure 6.5: 2D CCFs for three altitudes and three offshore ranges on 13 January. The ellipse fitted to the 0.13 contour level and the ellipse's major and minor axes are shown.

search for changes in eddy structure as a function of altitude and offshore distance.

6.6 Variation and comparisons of CCFs

Fig. 6.5 is presented to show how the steeply-sloped region within ± 400 m of the CCF's origin changes with offshore distance and altitude. These six CCFs were computed from the series of RHI volume scans collected between 12:47 and 13:37 UT on 13 January. The white contours in fig. 6.5 are for the 0.13 isopleth of correlation (the lowest contour level that would form a closed loop around the origin for the chosen six CCFs), and the red lines are the best fit ellipses to the white contours. The black and red dashed lines run along the major and minor axes of the ellipses, respectively. The closed contours from CCFs near the surface tend to have smaller area and are elongated (bottom row) while the closed contours from CCFs in the middle of the mixed layer (top row) are larger and more circular. For all rows, there appears to be very little change in the shape with increasing offshore distance (right to left). The correlation functions with smaller area indicate greater spatial decorrelation of the turbulence structures when compared to those with larger areas.

The spatial variation of the closed contours of correlation at the 0.1, 0.2, and 0.3 levels on 13 January are shown in figs. 6.6 and 6.7. The closed contours from the volume scans on 11 January are shown in Appendix C as figs. B.1, B.2 and B.3. Some features common to all of these figures are (1) the gradual increase in size of circles with increase in altitude and a sudden decrease in size above the BL, (2) the absence of closed contours for some regions near the shore and at higher altitudes, and (3) the orientation of the major axes of the ellipses near the surface are aligned approximately parallel to the wind direction while the major axes of the ellipses near the top of the ML are perpendicular to the mean wind direction. Also, the lower the contour level chosen, the noisier looking the closed contours appear. The increase of area enclosed by a closed contour with altitude in the surface layer can be explained by surface layer similarity theory, which states that the size of eddies near the surface is restricted by their distance from the surface. The sudden decrease in area enclosed by the contours above the mixed-layer is caused by the lack of turbulence structure and the dominating noise at these altitudes. The regions with no contours indicate either a closed contour encircling the origin could not be located for the chosen level of correlation or because there was insufficient variability in the lidar data to compute correlation functions.

Figures 6.8 through 6.10 show quantities in image form as a function of offshore distance and altitude that were obtained from the best-fit ellipses. Here the focus is on lidar observations from 13 January since those will be the used for comparison with CCFs from the LES output. Figs. 6.8 and 6.9 are from observations and fig. 6.10 is from LES#260. The top two panels in each figure show the length of the minor and major axes. The middle two panels show the ellipticity and the orientation. Near the surface, where the ellipticity is much greater than 1, we see that the orientations are approximately aligned with the mean wind direction (290°). In the bottom two panels, one sees the area of the ellipses and the RMS, or goodness of fit, of the ellipse to the contour. The left middle panels in fig. 6.8 and 6.9 indicate that there is a slight increase in the depth of the shallow layer of high ellipticity near the surface with increasing offshore distance.

Fig. 6.12 indicates that simulation #260 produced smaller eddies than those observed by the lidar for a very broad range of altitudes in the middle of the CIBL. The sizes of the contours compare well near the surface and in the entrainment zone. This is also true for simulations #264 and 267. They show very slight changes in offshore distance and substantial changes with altitude. Therefore, the ellipse parameters between 2.85 and 4.29 km offshore were averaged and are shown as a function of altitude in fig. 6.13. The error bars represent one standard deviation in each direction for the ellipse parameters in the five offshore distances.

The top two panels in fig. 6.13 show the minor and major axis lengths as a function of altitude. They show that the observed minor axis lengths are at least a factor of two larger than those from the simulation in the middle of the mixed layer. The observed major axis lengths are approximately 50% larger than those from the

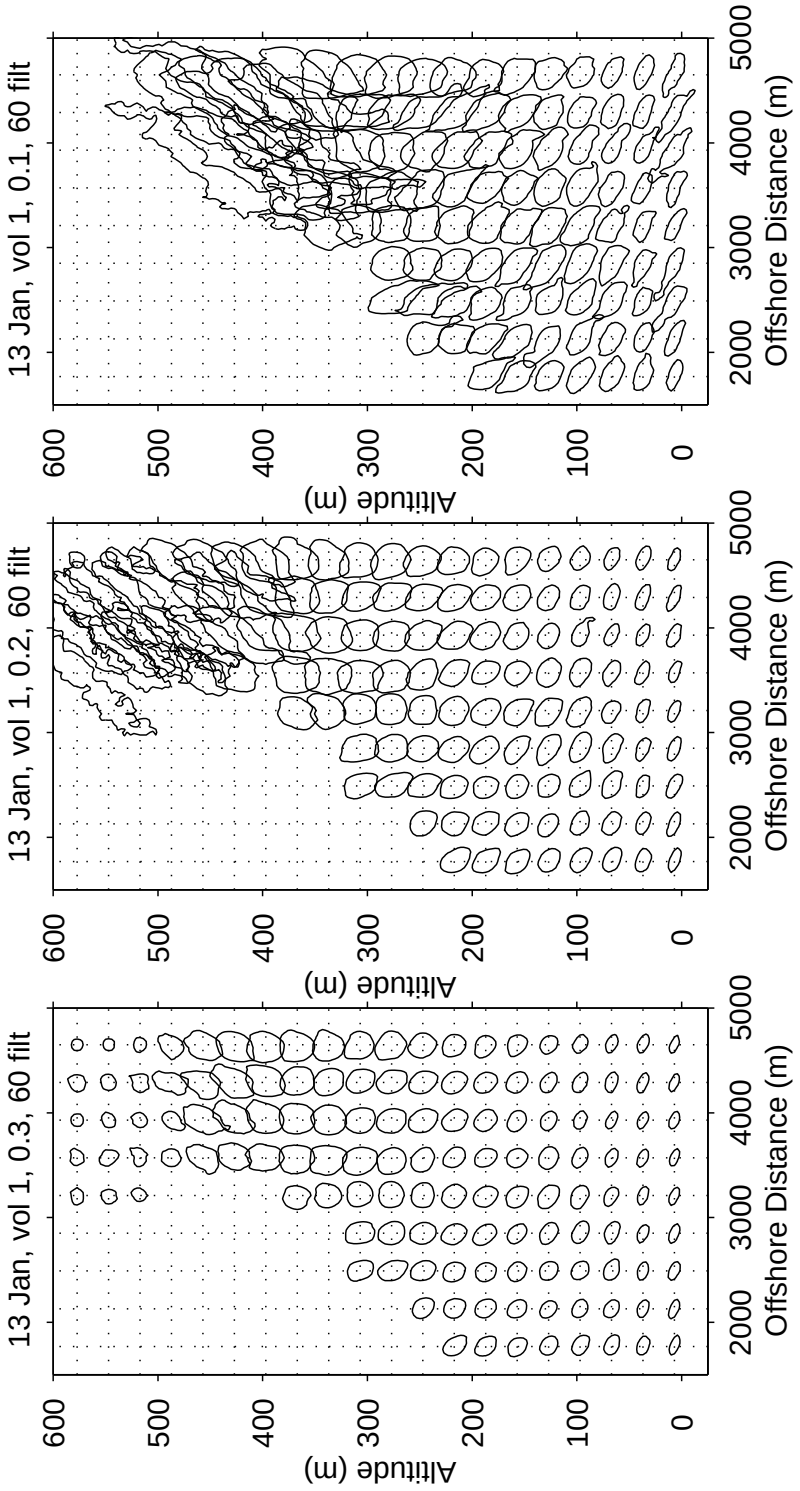

Figure 6.6: Contours of 0.3 (left), 0.2 (middle) and 0.1 (right) from cross-correlation functions of aerosol backscatter data collected from 12:47–13:37 UT on 13 January.

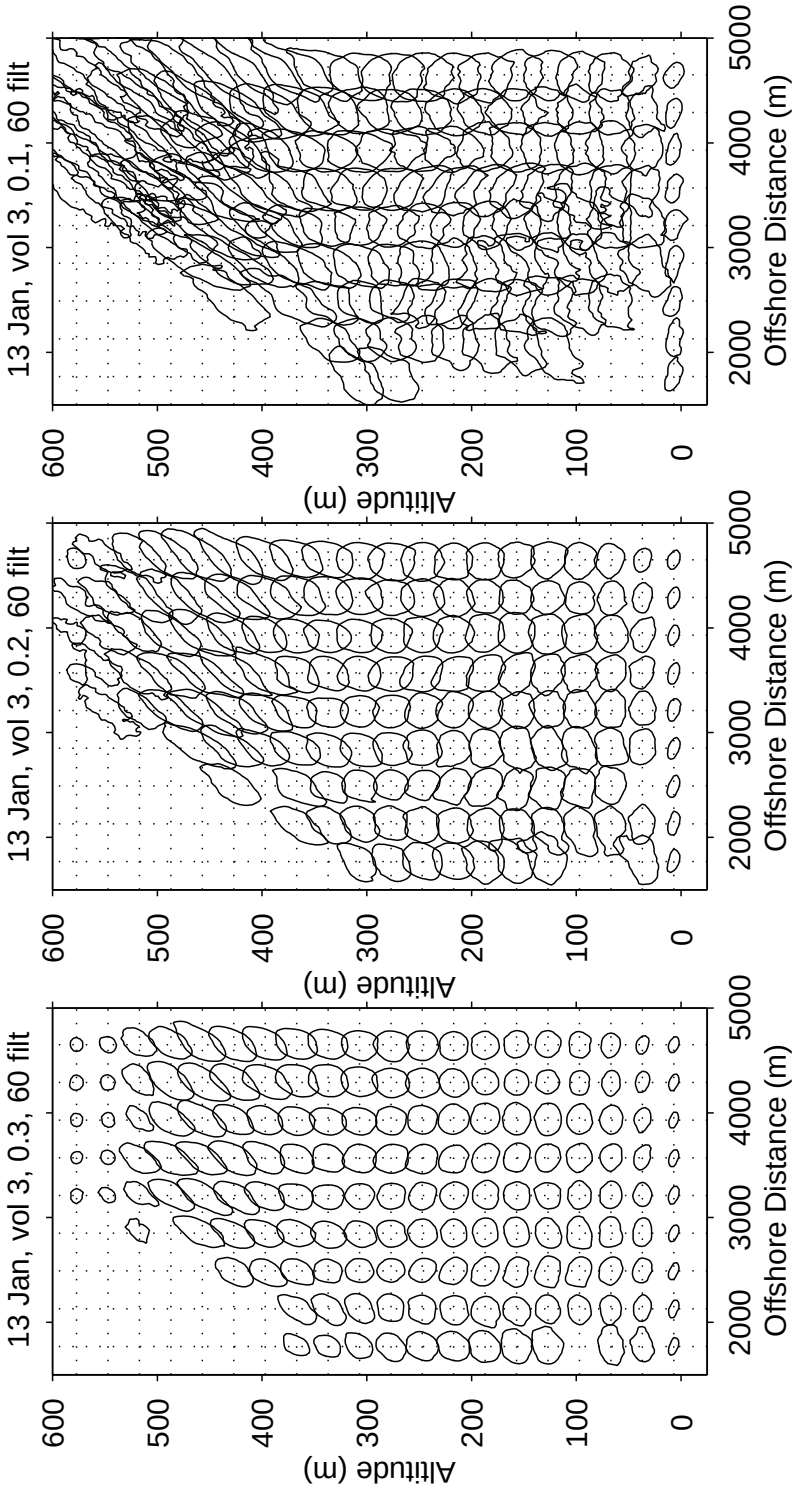

Figure 6.7: Contours of 0.3 (left), 0.2 (middle) and 0.1 (right) from cross-correlation functions of aerosol backscatter data collected from 17:19–18:37 UT on 13 January.

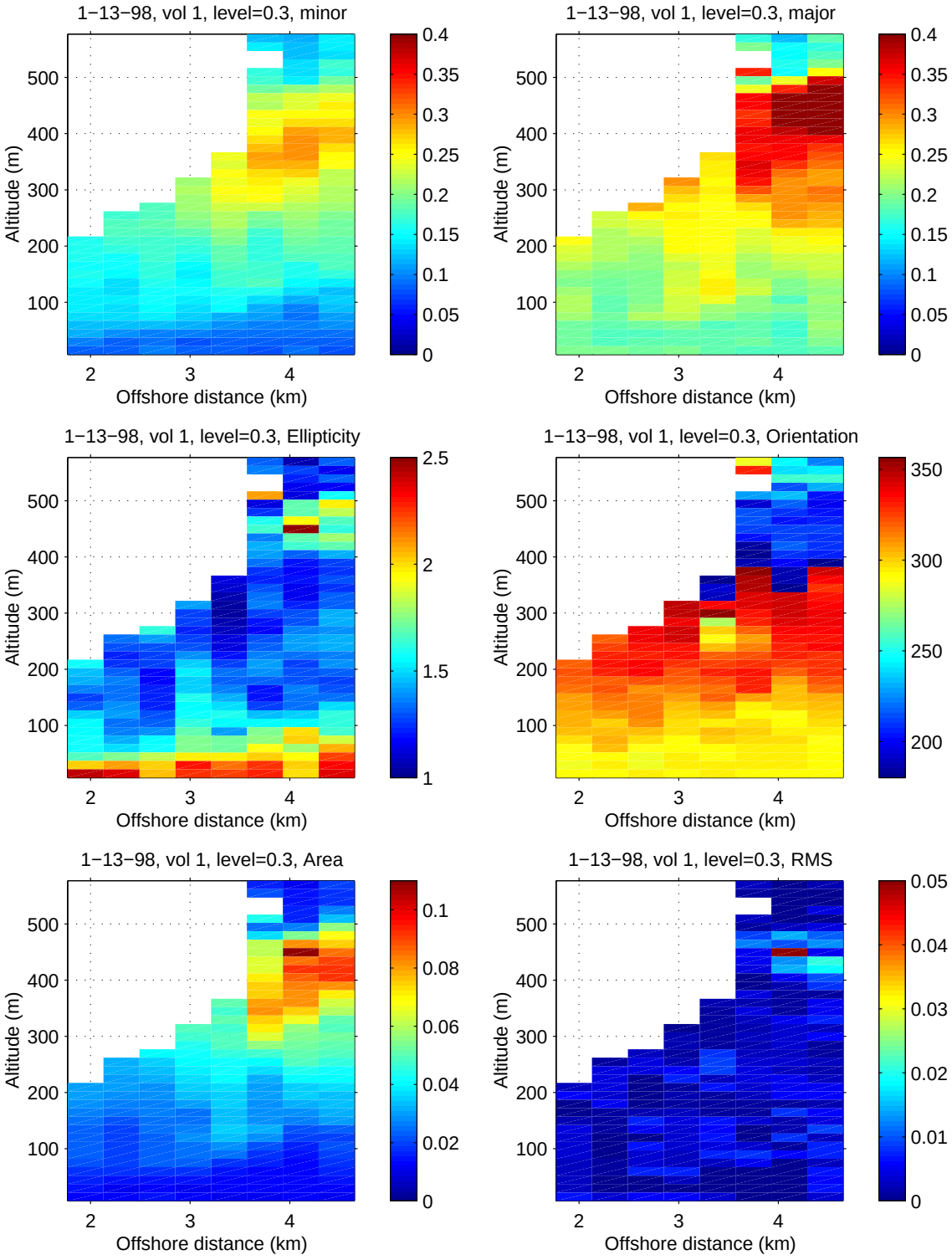

Figure 6.8: Quantities derived from ellipses fit to isopleths of 0.3 correlation from CAPPIs from 12:47-13:37 UT on 13 January.

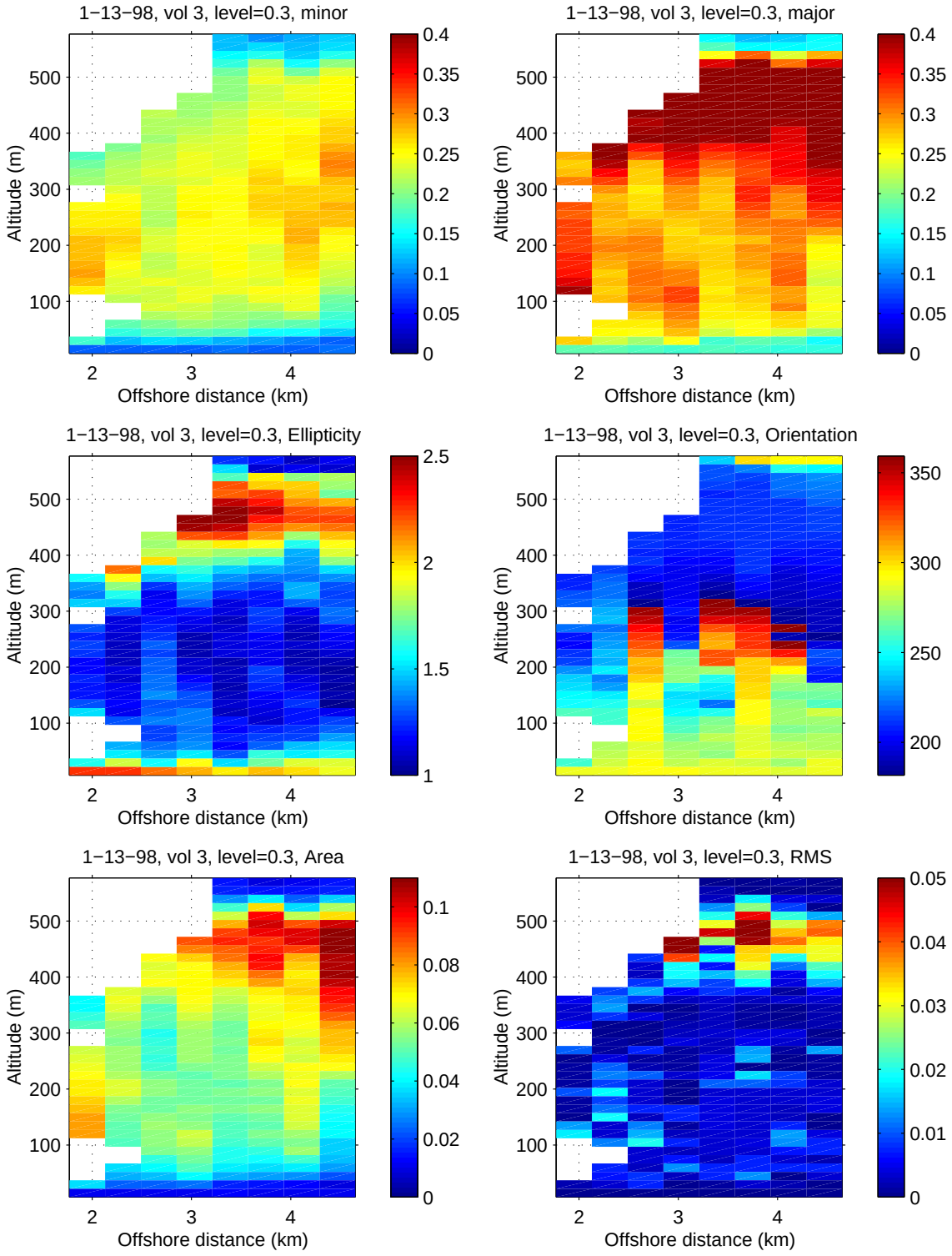

Figure 6.9: Quantities derived from ellipses fit to isopleths of 0.3 correlation from CAPPIs from 17:19-18:37 UT on 13 January.

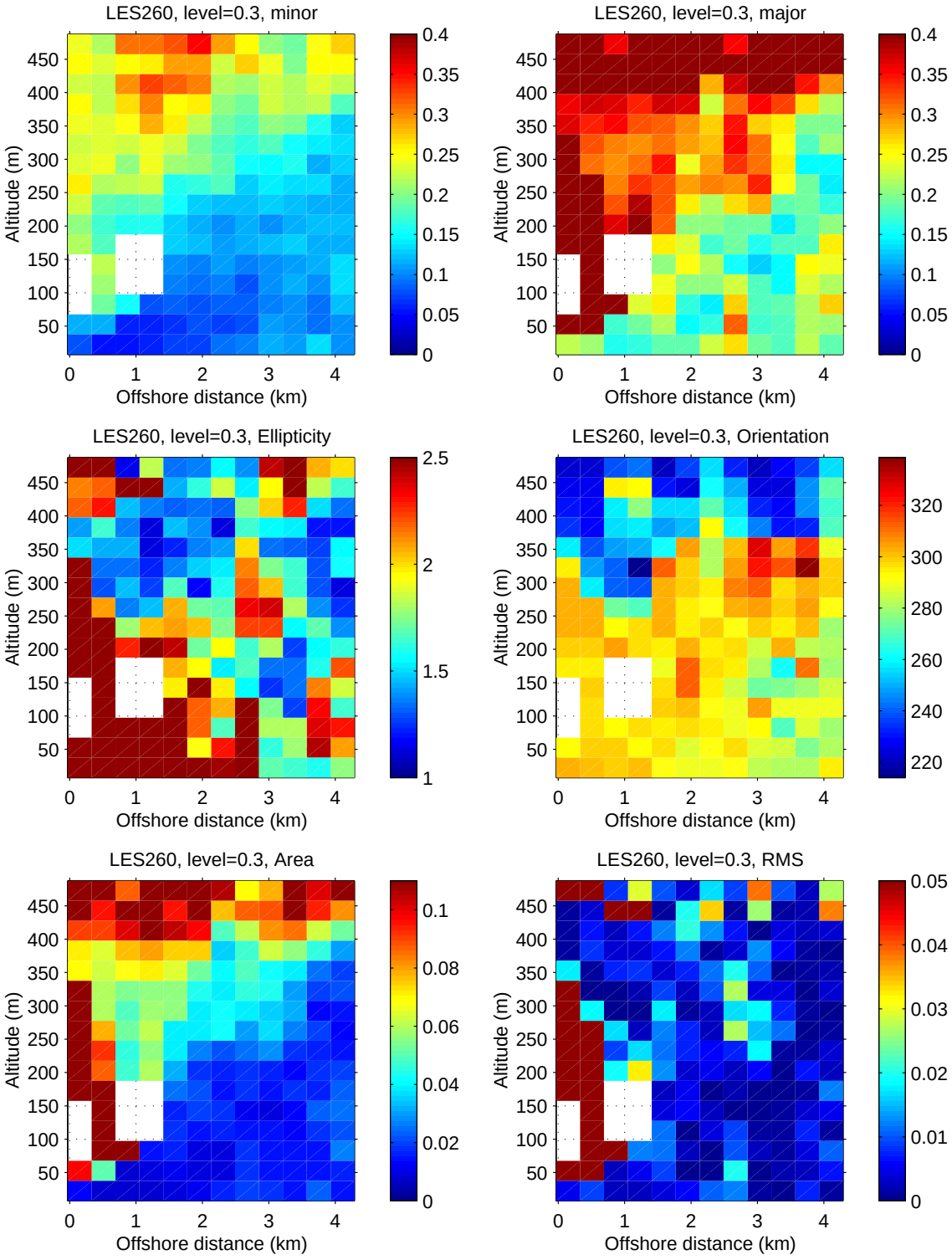

Figure 6.10: Quantities derived from ellipses fit to isopleths of 0.3 correlation from LES#260.

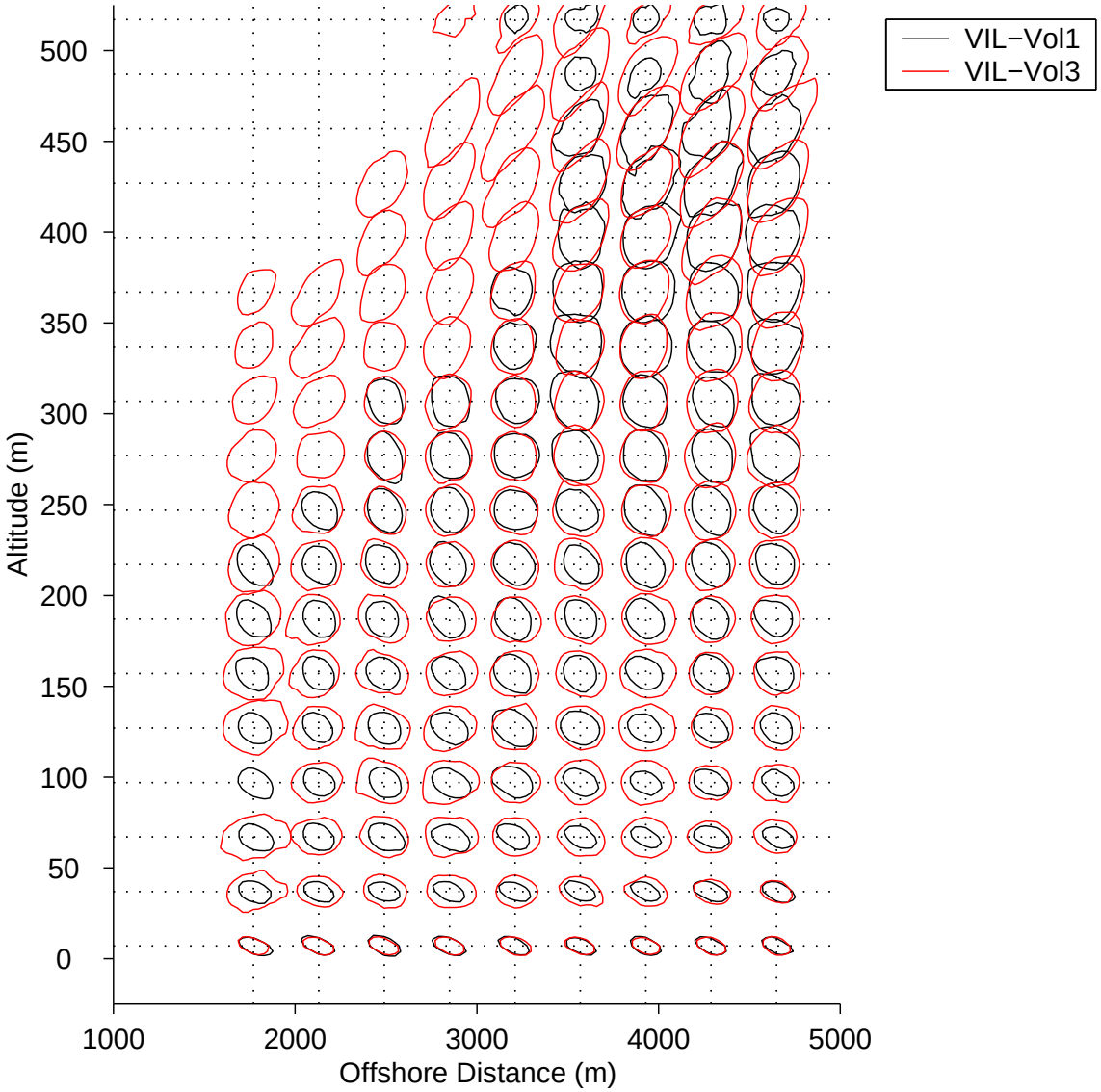

Figure 6.11: Comparison of 0.30 contours of CCFs from RHI volume scan data during two periods on 13 January. The black contours are from data collected between 12:47 and 13:37 UT and the red contours are from data collected between 17:19 and 18:37 UT.

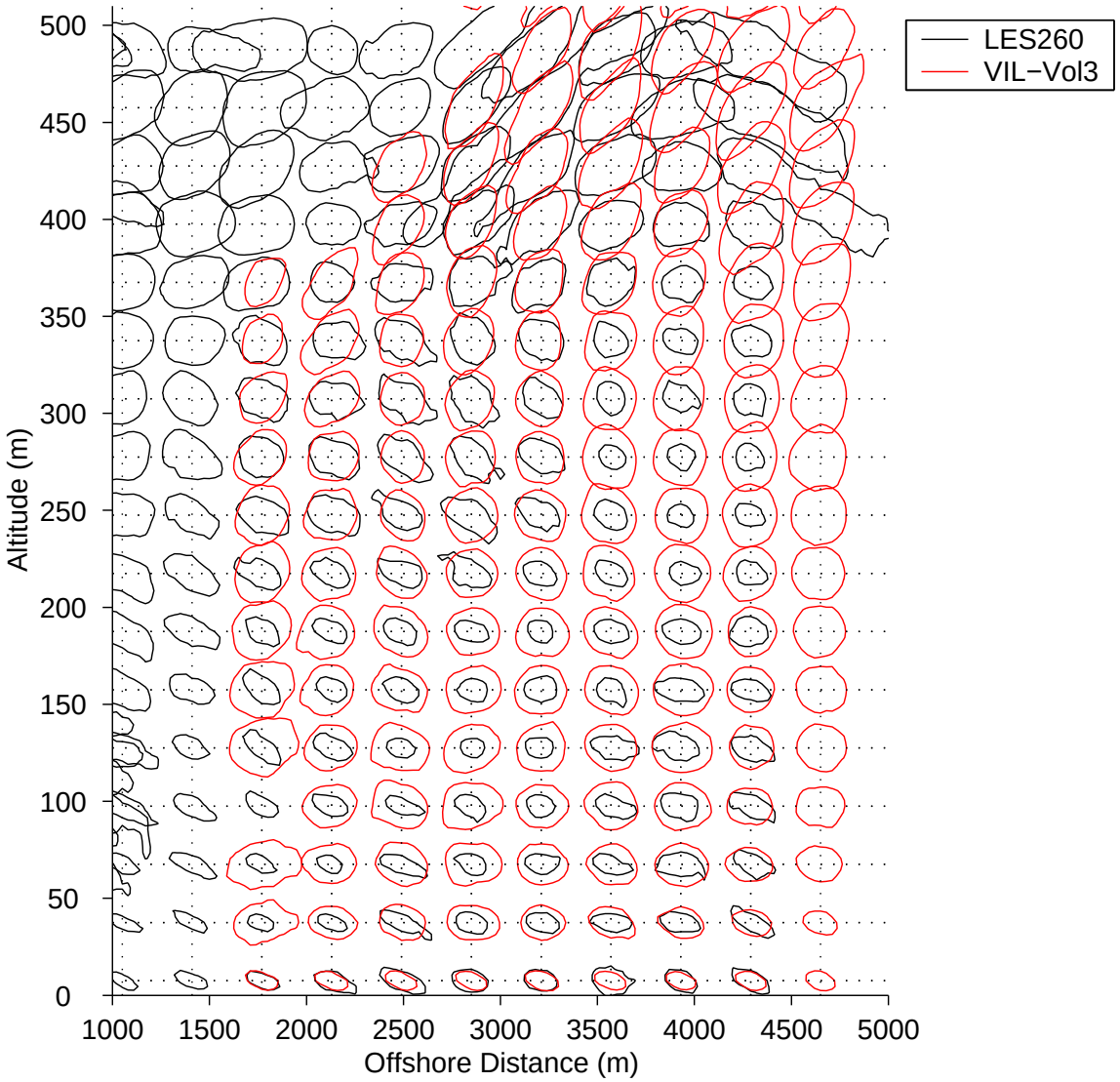

Figure 6.12: Comparison of 0.30 contours of CCFs from LES#260 and RHI volume scan data collected between 17:19 and 18:37 UT on 13 January.

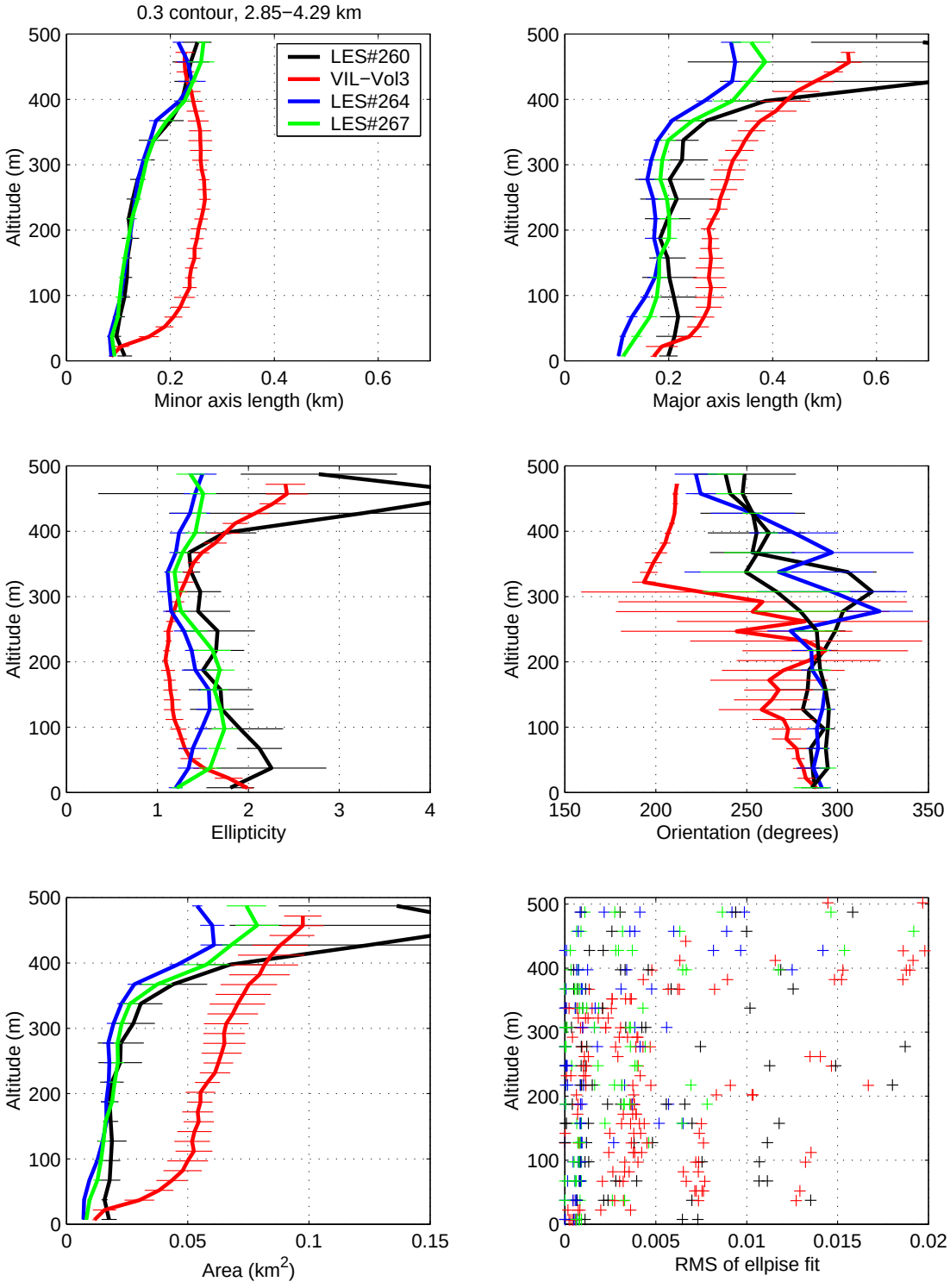

Figure 6.13: Comparison of ellipse parameters for LES#260, 264, 267 and CAPPIs collected between 17:19 and 18:37 UT on 13 January.

simulation. The ellipticities are plotted as a function of altitude in the middle left panel of fig. 6.13. They show that near the surface the correlation functions are elongated in the streamwise direction by a factor of two more than in the cross-stream direction. In the middle of the mixed layer, the observed ellipticities are near one. The ellipticities from the simulation are much larger that those from the observations at all altitudes except near the surface, where they appear to decrease slightly. The middle right panel in fig. 6.13 shows the orientation of the best-fit ellipses as a function of altitude. It shows that, near the surface and in the lower mixed-layer, the ellipses from both the observations and simulations are aligned with the wind direction. In the middle of the mixed layer, where the ellipticities are near one, subtle changes in the major and minor axis lengths can cause the orientations to change by 90°. Above the mixed-layer the observed orientations are clearly about 90° different than the orientations in the middle and lower mixed layer. The orientations from the simulations appear to change in this region but not as sharply as those from the observations. Last, the lower left panel in fig. 6.13 shows the area of the ellipses as a function of altitude. This confirms the most obvious difference between observed and simulated eddy structure shown in fig. 6.12: the observed eddies are in general larger than the simulated eddies by a factor of about 2 throughout most of the depth of the mixed layer.

Figures 6.14 through 6.22 are presented to show the correlation functions, and their differences, at three altitudes where the turbulence characteristics should be noticably different. The three regions are (1) in the middle of the boundary layer (figs. 6.14– 6.16), (2) the surface layer (figs. 6.17– 6.19), and (3) the entrainment zone (figs. 6.20– 6.22). Figures 6.14, 6.17 and 6.20 show the correlation functions within lags of ±400 m of the origin. Figures 6.15, 6.18 and 6.21 show the same correlation functions out to lags of ±1 km. Figures 6.16, 6.19 and 6.22 show the cross-sections of the correlation functions along major and minor axes.

In fig. 6.14 we see the region within ±400 of the origin of the correlation function for the middle of the mixed layer (217 m). The top panel is from lidar observations and the bottom from LES#260. The correlation function computed from lidar observations is more circular and larger than that from the large-eddy simulation. Furthermore, orientation of the ellipse fit to the 0.1 correlation contour is approximately 90° different from that of the LES. Fig. 6.15 reveals that the orientations fail to identify the orientations of the most significant features beyond the ±400 range of lags. For example, the lidar correlation function shows a ridge with positive correlations near 0.1 running about 210°. The LES correlation function shows a ridge with values greater than 0.2 in some places running across the origin at about 300°, which corresponds to the direction of the mean flow. More importantly, however, the images in fig. 6.15 reveal an interesting pattern consisting of ridges and minima. In the top panel, minima of -0.15 are located directly to the east and west of the origin at about ±500 m lag. Similar minima are located ESE, S, N and SW of the origin, also at about ±500 m lag, in the bottom panel.

Fig. 6.17 shows the correlation functions witin ±400 m of the origin for the

altitude=217 m

range=3.93 km

contour=0.1

minor length=211.6722 m

major length=281.6045 m

ellipticity=1.3304

orientation=187.1935^{o}

area=187263.5705 m^{2}

RMS of fit=0.031563

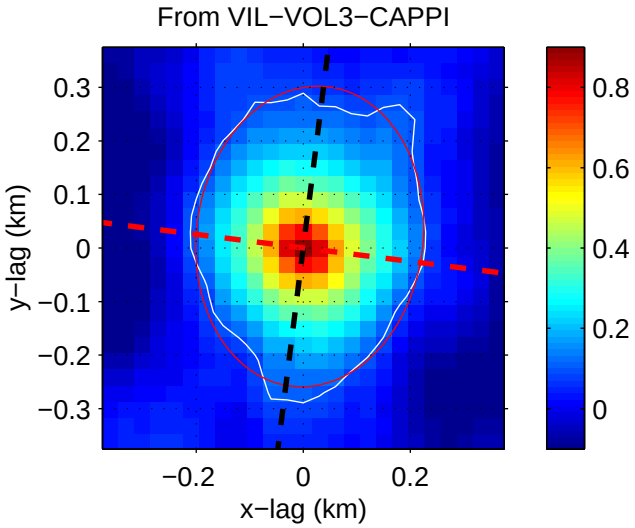

altitude=217.5 m

range=3.93 km

contour=0.1

minor length=282.4232 m

major length=99.0908 m

ellipticity=2.8501

orientation=269.8389^{o}

area=87919.1645 m^{2}

RMS of fit=0.044973

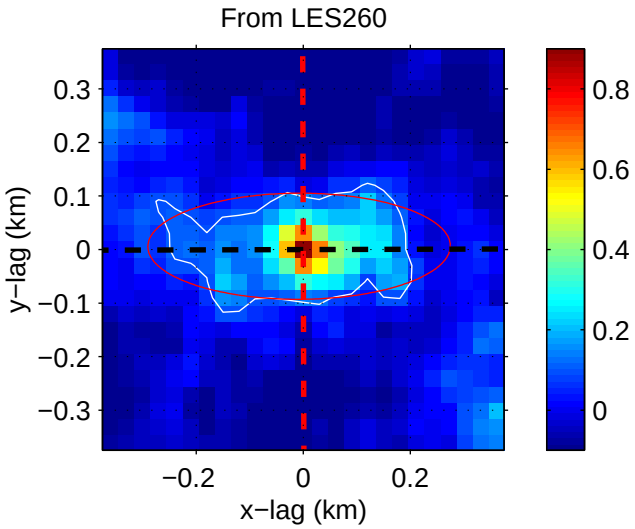

Figure 6.14: Comparison of 2D-CCFs from the lidar (top) and LES (bottom) in the middle of the convective internal boundary layer (217 m above surface and 3.93 km offshore).

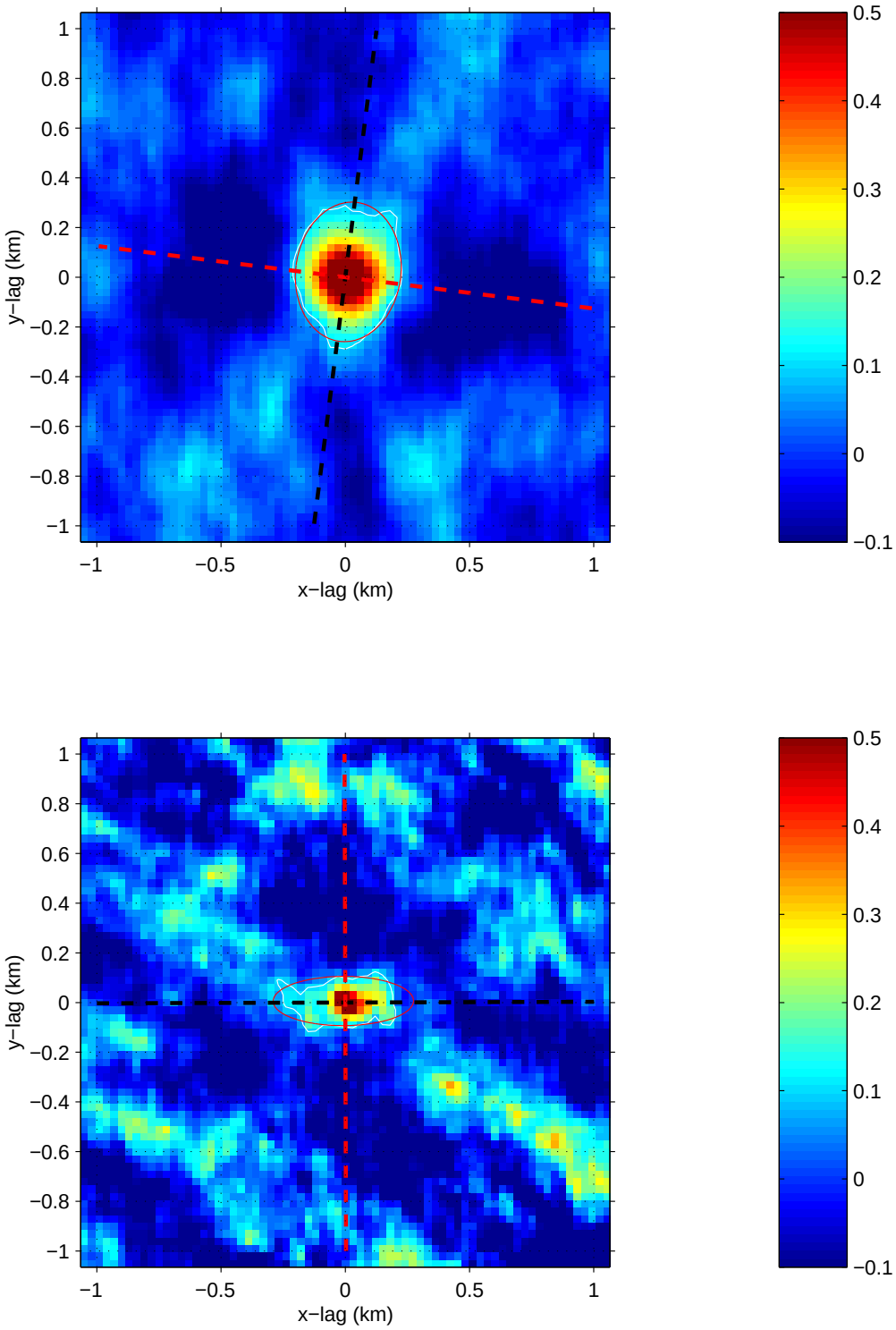

Figure 6.15: Same as Fig. 6.14 except for lags to ±1 km. (217 m above surface and 3.93 km offshore).

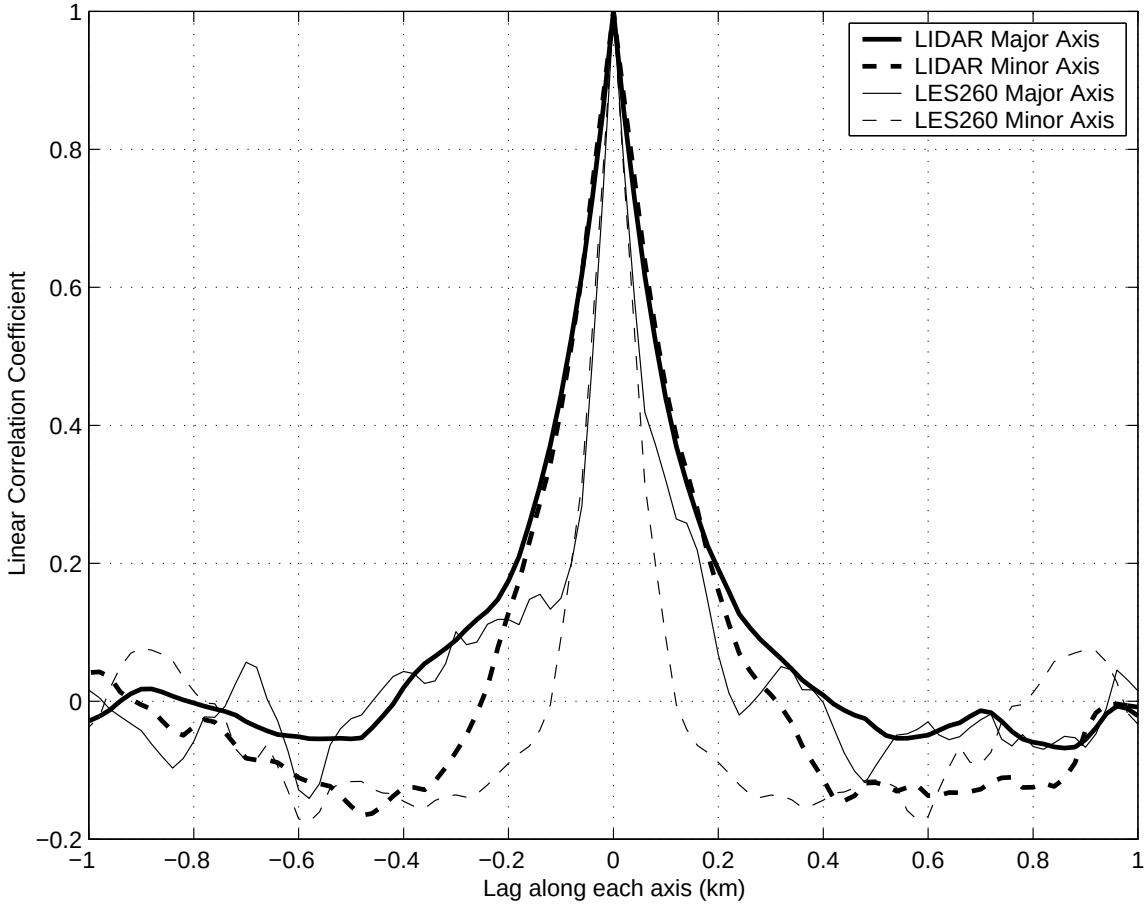

Figure 6.16: Comparison of slices through the origin of the two 2D-CCFs along the major and minor axis directions shown in fig 6.14.

surface layer (7 m altitude). The orientations of the 0.1 contours are different by 25°. The ellipticities are 2.58 and 3.77 for lidar data and LES output, respectively. The area enclosed by the ellipse from the LES output is over twice as large as that from the lidar data. Most importantly, however, the top panel of fig. 6.18 is very flat and devoid of strong correlations beyond lags of about ± 200 m. In fact, weak and broad minima (0 to -0.05) do exist north and south of the origin, and a weak ridge extends from the origin to its northwest. These weak features are consistent with convective cells which have very narrow, but high-intensity walls that are aligned with the wind direction. Furthermore, in the lidar data, bright spots of steam-fog in the cell walls often shadow structures immediately downwind of themselves, even in the presence of high-pass median filtering. Therefore, the weak ridge of correlation does not extend to the southeast of the origin. The most dramatic difference, however, between the top and bottom panels of fig. 6.18 is the lack of strong correlations at large lags. This is most likely caused by the very skewed distribution of backscatter intensities in the data and absence of broad correlating features such as horizontal convective rolls in the observations. The bottom panel of fig. 6.18, from LES output, shows more significant linear bands oriented in the direction of the mean with spacing of about 500–600 m. Regions of negative correlation near -0.1 are located ±400 m of the origin. This pattern is somewhat similar to that shown in the bottom panel of fig. 6.15 and shows the strong tendency for the model to generate linear structures.

In figs. 6.20 and 6.21 we see the vivid signature of the effect of gravity waves which influence the organization of turbulence in the entrainment zone. The pattern was also evident in the lower-right panels of figs. 5.13 and 5.14. The orientation of ellipses is about 15° different and approximately perpendicular to the mean flow. The orientation of the ellipses appears to be a good indicator of the orientation of the larger-scale linear features in this case. These functions show minima 300–400 m from the origin in the minor axis direction. The secondary maxima in the minor axis direction, however, occur at substantially longer lags (700-800 m) for the lidar data, which indicate larger wavelengths of the gravity waves in the observations than in the LES (600 m) (see fig. 6.22). Fig. 6.23 is presented to show another example of how the model tends to create flow-parallel linear structures with close band spacing near the surface.

We can conclude that it is dangerous to rely on orientations of the ellipses from the inertial subrange region to precisely determine orientations of linear structures at larger lags. This becomes quite important if we intend to find streamwise and cross-stream integral length scales from the correlation functions, which will be described in the next section.

altitude=7 m

range=3.93 km

contour=0.1

minor length=157.1666 m

major length=60.7413 m

ellipticity=2.5875

orientation=283.1281^{o}

area=29991.2155 m^{2}

RMS of fit=0.011022

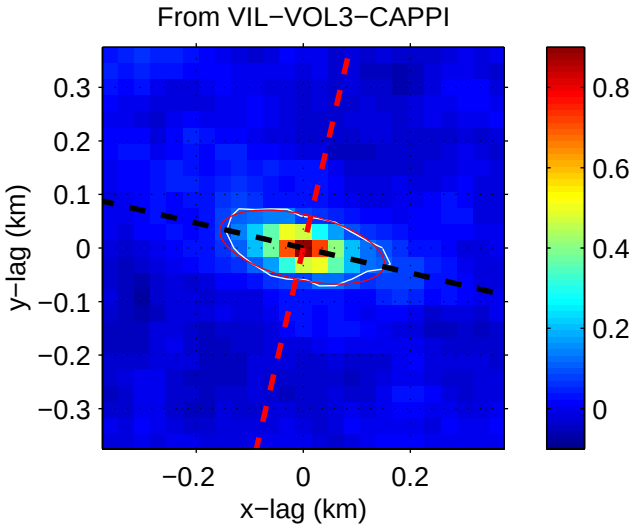

altitude=7.5 m

range=3.93 km

contour=0.1

minor length=318.6464 m

major length=84.4874 m

ellipticity=3.7715

orientation=313.1743^{o}

area=84576.7387 m^{2}

RMS of fit=0.092574

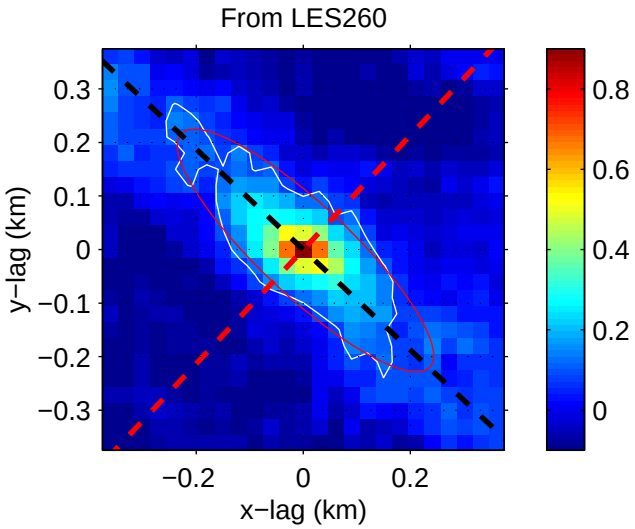

Figure 6.17: Comparison of two 2D-CCFs from the lidar (top) and LES (bottom) near the surface in the convective internal boundary layer (7 m above surface and 3.93 km offshore).

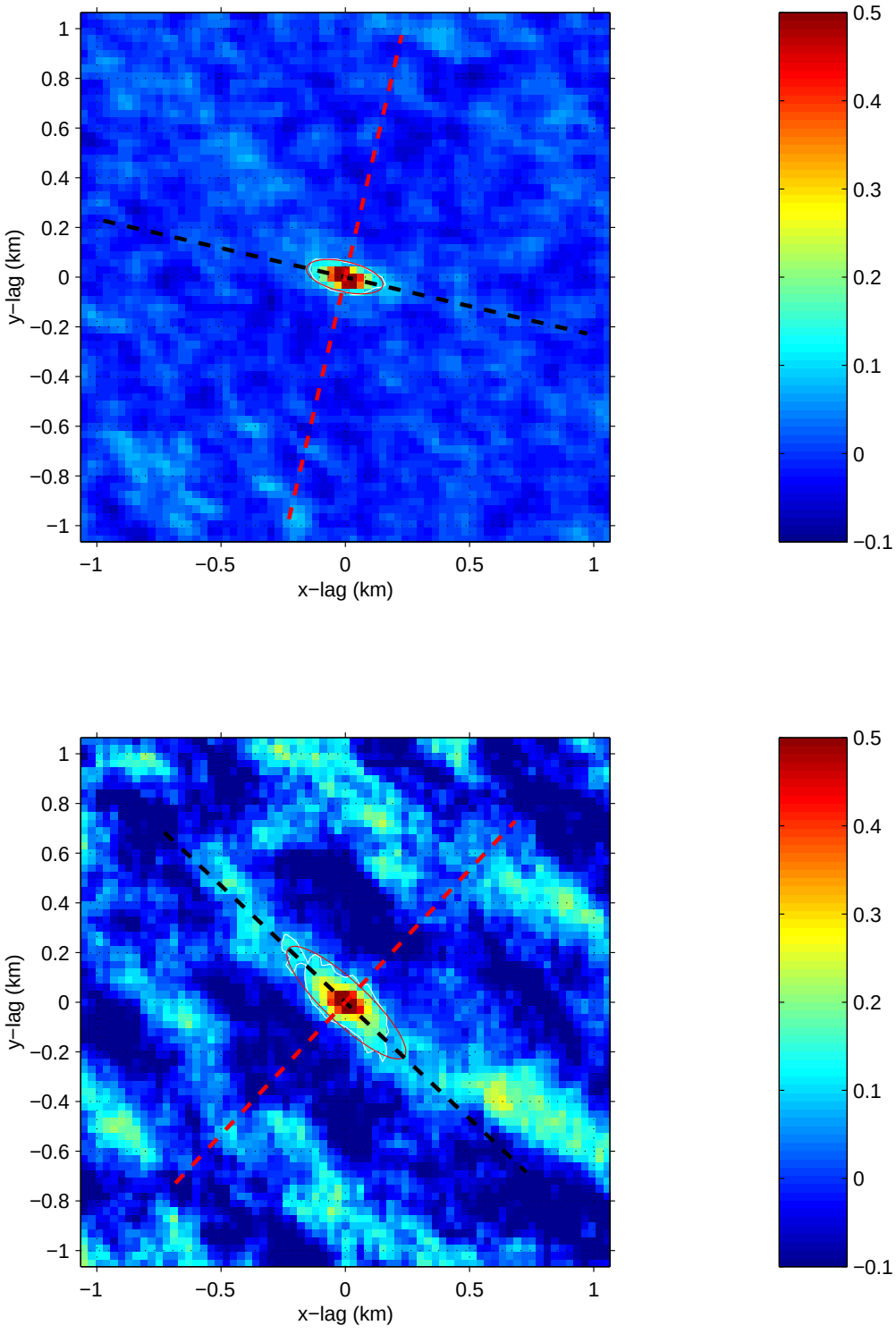

Figure 6.18: Same as Fig. 6.17 except for lags to ±1 km. (7 m above surface and 3.93 km offshore).

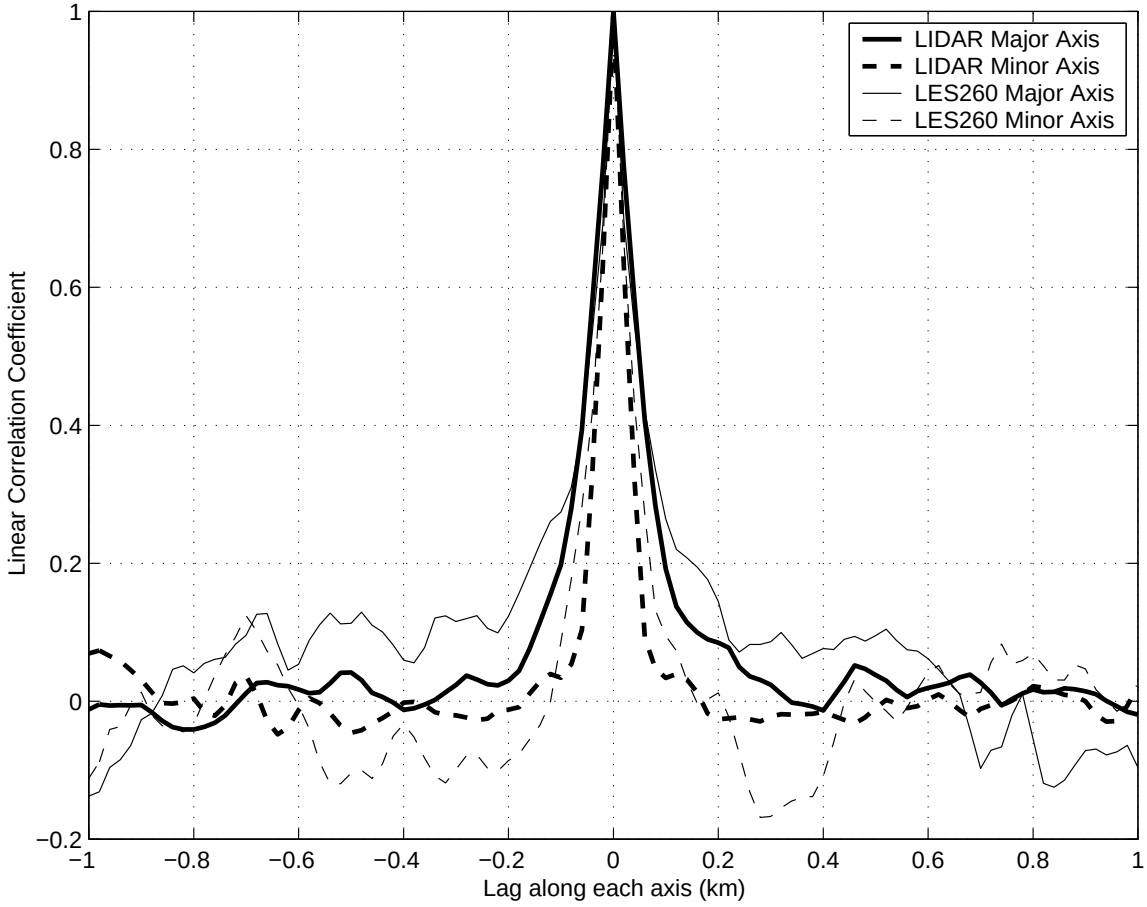

Figure 6.19: Comparison of slices through the origin of the two 2D-CCFs along the major and minor axis directions shown in fig 6.17.

altitude=427 m

range=3.21 km

contour=0.31

minor length=107.8648 m

major length=237.8077 m

ellipticity=2.2047

orientation=209.7282^{o}

area=80585.2524 m^{2}

RMS of fit=0.040174

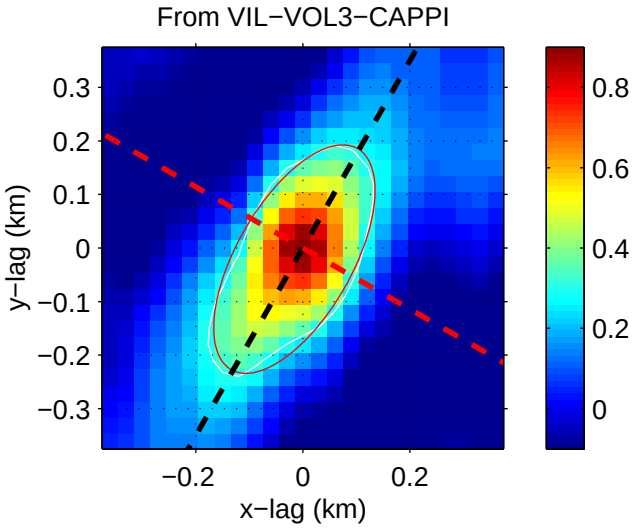

altitude=427.5 m

range=3.21 km

contour=0.31

minor length=292.1703 m

major length=103.6223 m

ellipticity=2.8196

orientation=225.306^{o}

area=95112.8603 m^{2}

RMS of fit=0.0043829

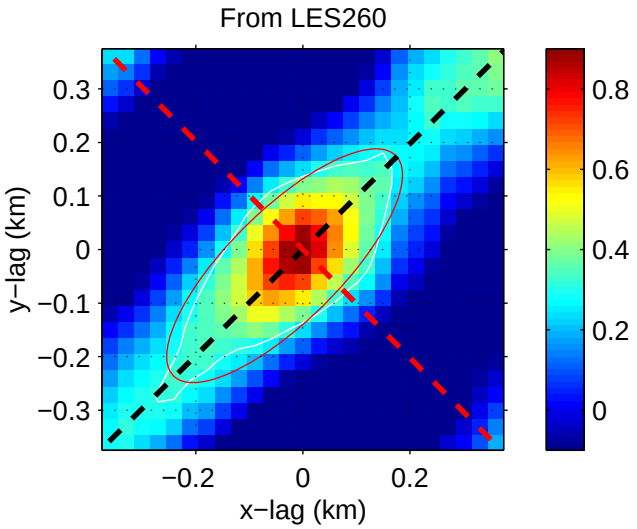

Figure 6.20: Comparison of 2D-CCFs from the lidar (top) and LES (bottom) near the surface in the entrainment zone of the convective internal boundary layer (427 m above surface and 3.21 km offshore).

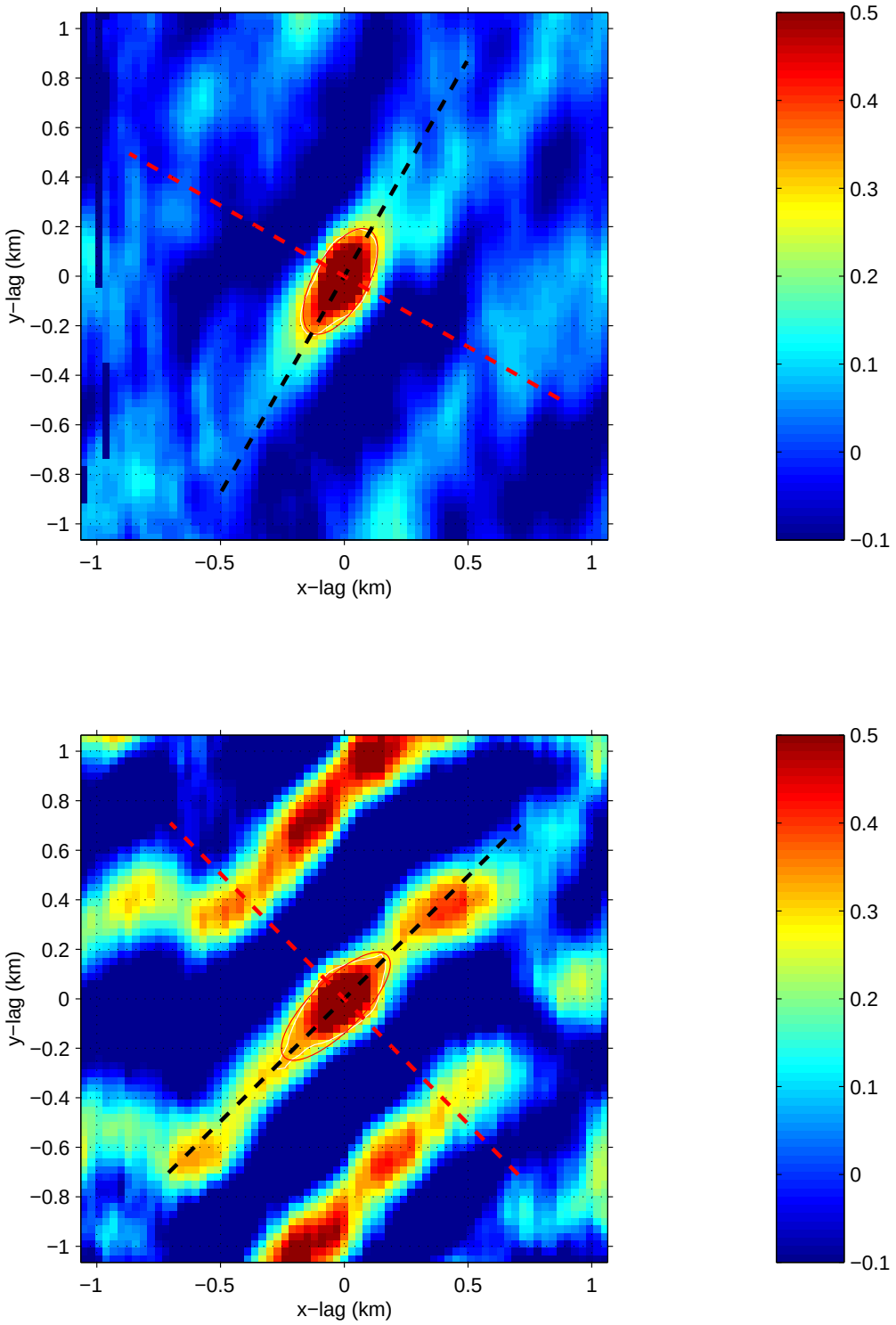

Figure 6.21: Same as Fig. 6.20 except for lags to ±1 km. (427 m above surface and 3.21 km offshore).

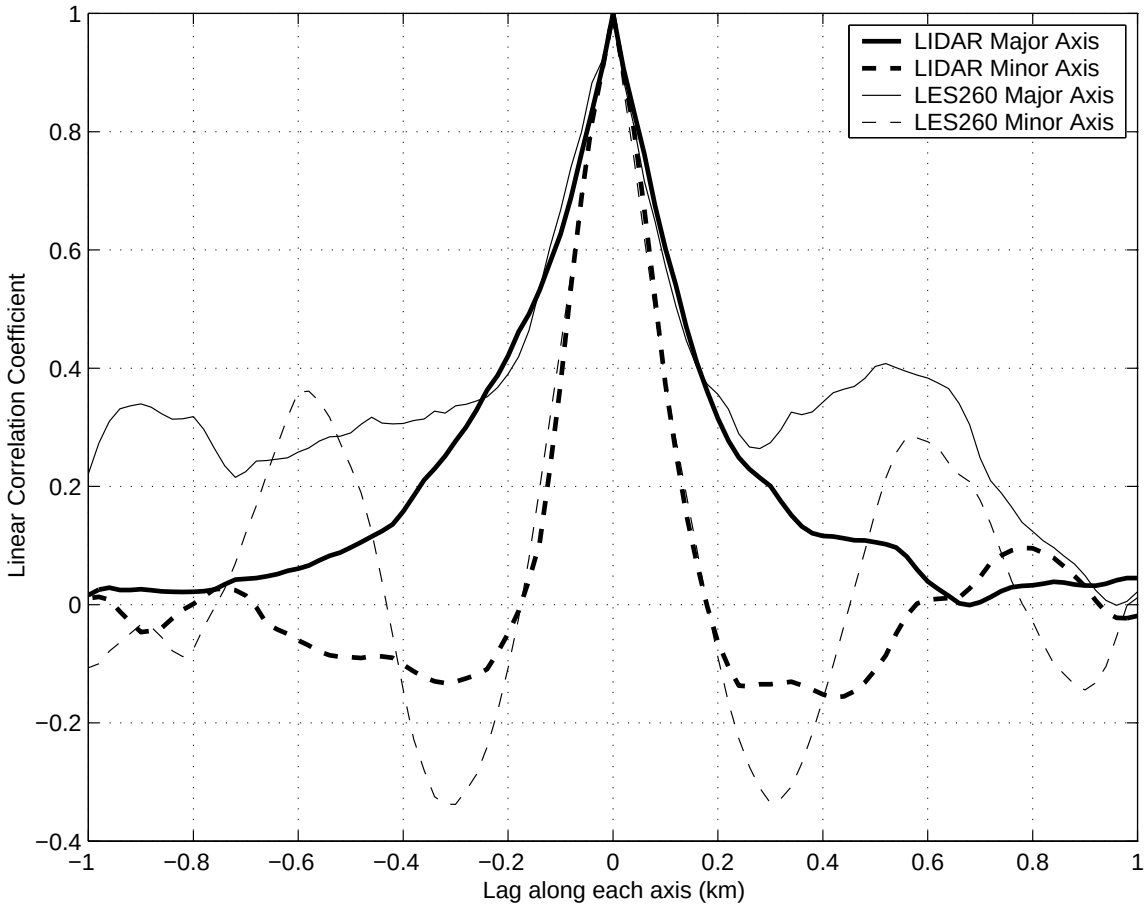

Figure 6.22: Comparison of slices through the origin of the two 2D-CCFs along the major and minor axis directions shown in fig 6.20.

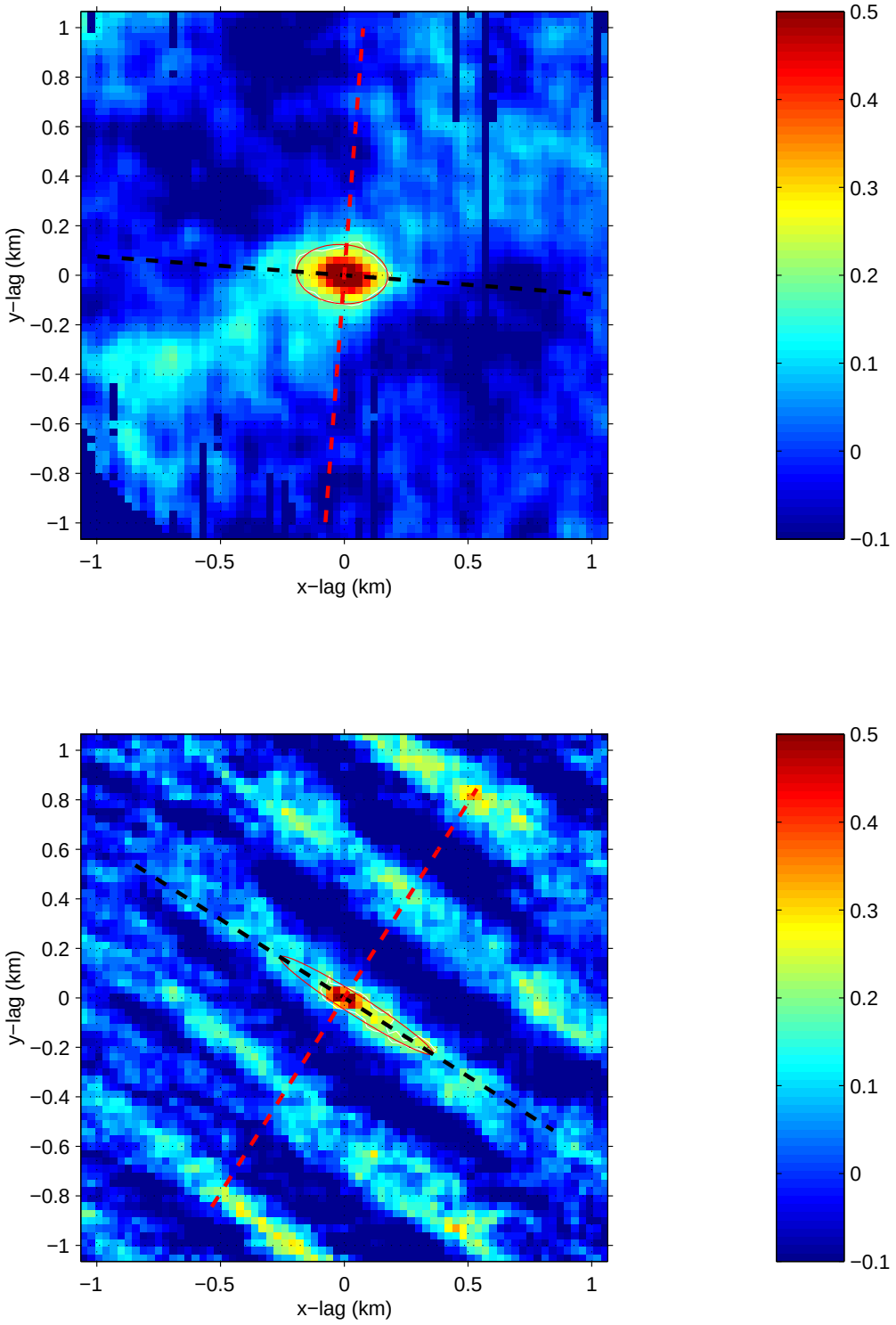

Figure 6.23: Comparison of CCFs from 37 m altitude and 2.13 km offshore showing the strong tendency of the LES to generate linear structures.

6.7 Integral length scales

The integral length scale (Lenschow and Stankov, 1986) is defined as

$$\lambda = \int_0^\infty R(r)dr/R(0) \tag{6.2}$$

where

$$R(r) = \langle f'(x)f'(x+r)\rangle. \tag{6.3}$$

In the equations above, $f(x)$ is space-series, a prime denotes departures from the ensemble average of $f(x)$, $R(r)$ is the autocovariance function, and $R(0)$ is the variance of $f(x)$. (By dividing $R(r)$ by $R(0)$ we obtain the autocorrelation function.) In turbulence research, it is most common to compute temporal statistics for components of flow that are streamwise and cross-stream or spatial statistics in directions that are streamwise and cross-stream. These directions are the easiest to identify and statistics from them differ the most. The spatial correlation functions computed from lidar data and LES offer the ability to compute the integral length scale in all directions. However, this work was not finished at the time of this writing.

By integrating the CCFs along the major and minor axes, multiplying that sum by the spacing of the points along the axes, and dividing by two, we obtain the integral length scales for the directions which are very roughly aligned in the downstream and cross-stream directions. However, an ellipse with ellipticity near one can easily produce orientations that are not aligned with the mean wind direction. Furthermore, near the surface the major axes are aligned in the steamwise direction, but in the entrainment zone the major axes are aligned approximately perpendicular to the mean flow. In future work, the integral length scales should be computed as a function orientation. Perhaps integral *area* scales could be computed using the entire CCF. The integral length scales for the major and minor orientation directions were averaged over the offshore distances and are presented as a function of altitude in fig. 6.24. They also indicate the lidar observed coherent structures are larger than any of the simulations.

6.8 Effect of high-pass filter length

To test the effect of the high-pass median filter length on the CCFs, five high-pass median filter lengths (60, 50, 40, 30, and 20 points) were applied to the last volume scan on Jan 13. No noticeable differences appear in the images with these various filter lengths. However, the median filter length does have an effect on the CCFs above the lowest levels as shown in fig. 6.26.

In fig. 6.26 contours for all median filter lengths are approximately the same size for the 7.5 m level. At all altitudes, the shape of the isopleths are approximately the same. This indicates that the variability occurs on scales smaller than the shortest median filter (300 m). At altitudes above 7.5 m, however, the smaller median filter lengths cause the area of the ellipses to be substantially smaller. This is because, as the

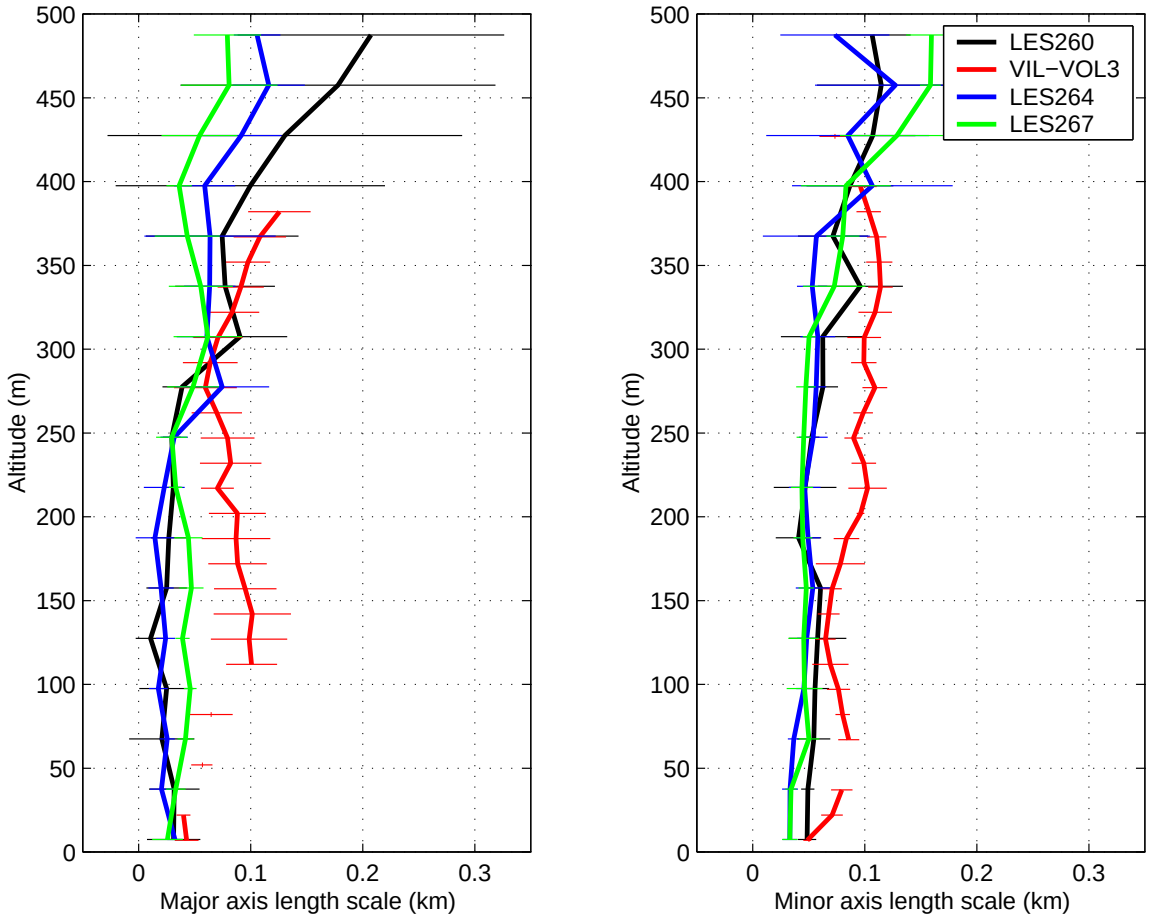

Figure 6.24: Comparison of integral scales of aerosol backscatter for lidar data and LESs. The left plot shows integral scales along the major axis of the CCF and the right plot shows integral scales along the minor axis.

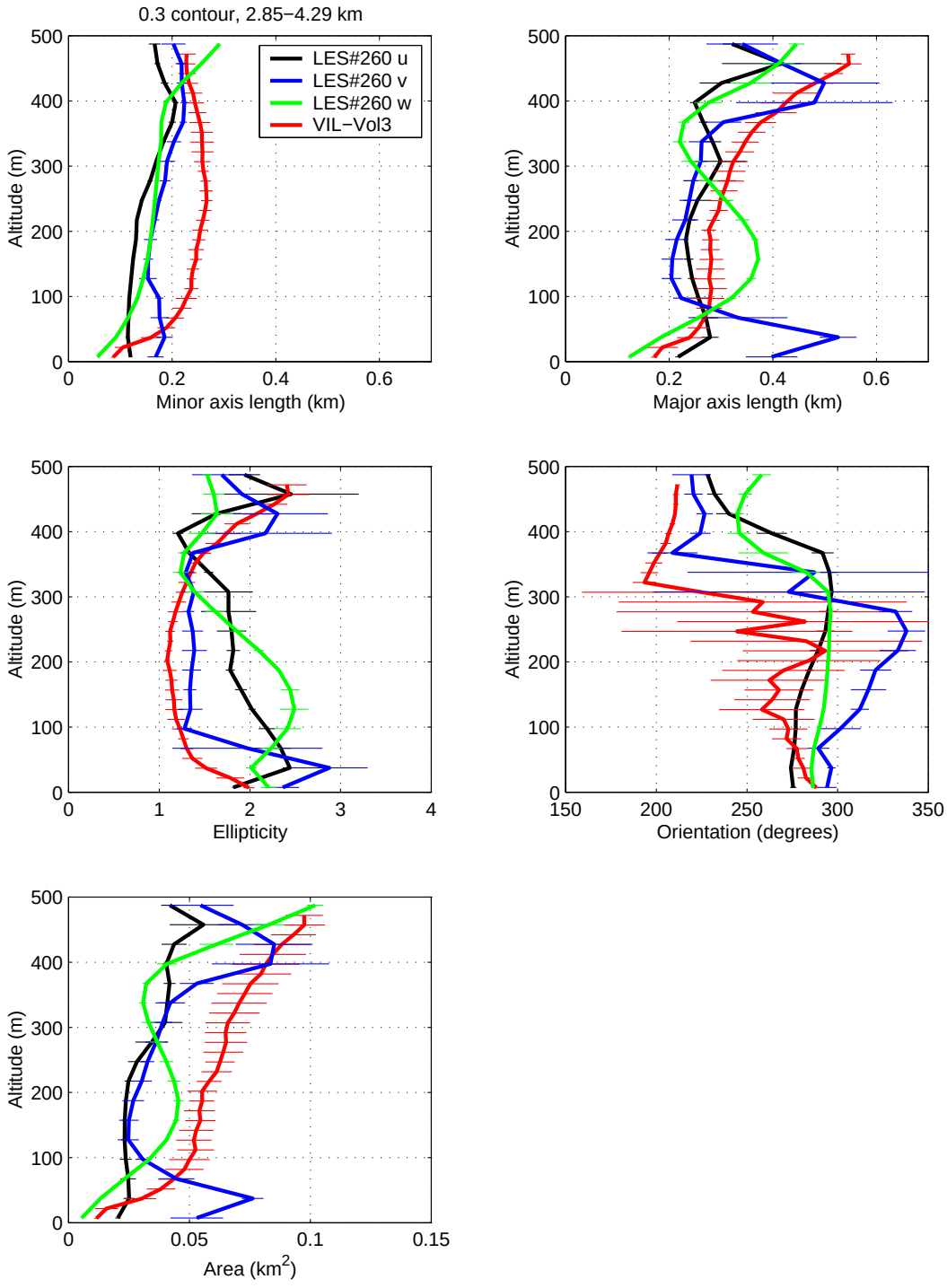

Figure 6.25: Comparison of ellipse parameters for the u, v and w velocity components in LES#260 and for the observed aerosol backscatter from 17:19–18:37 UT on 13 January.

length of the high-pass median filter decreases, more of the low-frequency variability is removed. Therefore, at altitudes above the surface layer, we see a substantial difference between the areas contained by isopleths of CCFs from data that had 20-point and 60-point high-pass median filters applied. However, only a very small difference is seen in the areas from data that had the 50-point and 60-point high-pass median filters applied. This indicates that most of the variability in the data occurs on scales smaller than about 50 points (750 m). Therefore, a 60-point (900 m) high-pass median filter was applied to the lidar data before CCFs were computed.

6.9 Effect of interpolation

For ease in data processing, all of the lidar data was converted from its original spherical coordinate system (azimuth, elevation and range) to a Cartesian coordinate system. Because the lidar beams are much farther apart at greater ranges, Cartesian grid-elements, which have uniform spacing, are influenced by the same data points and, therefore, cause correlation among the gridded data. For example, if there were no correlation between the gridded values (i.e. uncorrelated white noise) the CCF would be a delta function. That is, it would equal one at the origin and be near zero for all other lags.

To examine the correlating effect of the gridding, CCFs from lidar data above the boundary layer can be used. In this region, because of the absence of aerosol structures, the high frequency information should be white and the CCF should be a delta function. Fig. 6.27 shows cross-sections of CCFs for three offshore distances: 3.2, 6.1 and 8.6 km. The cross-sections broaden with increasing offshore distance, indicating that the interpolation does have an effect on the CCF for lags smaller than about 150 m. This correlating effect increases as a function of offshore distance and applies to all altitudes approximately equally for small (i.e. 0–15°) elevation angles.

6.10 CCF sensitivity to aerosol swelling curves

There are several papers which describe optical scattering as a function of relative humidity (for a recent example, see Wulfmeyer and Feingold, 2000). All the functions show an increase in optical scattering as the relative humidity increases. Unfortunately, the composition of atmospheric aerosols is quite variable, especially regionally, and, therefore, the exact shape of the scattering curves also change with time and location. For the results prior to this section, a curve was fit to optical scattering data from a very different time and location (Washington, D.C., in 1979). Therefore, it is likely that the optical scattering as a function of relative humidity for Sheboygan was quite different from the one used.

A different function was obtained later in the research. To test the sensitivity of the CCFs on a different optical scattering curve, 2D-CCFs were re-computed for LES#260 using a best-fit to data obtained by Covert et al. (1972) in Denver, Colorado,

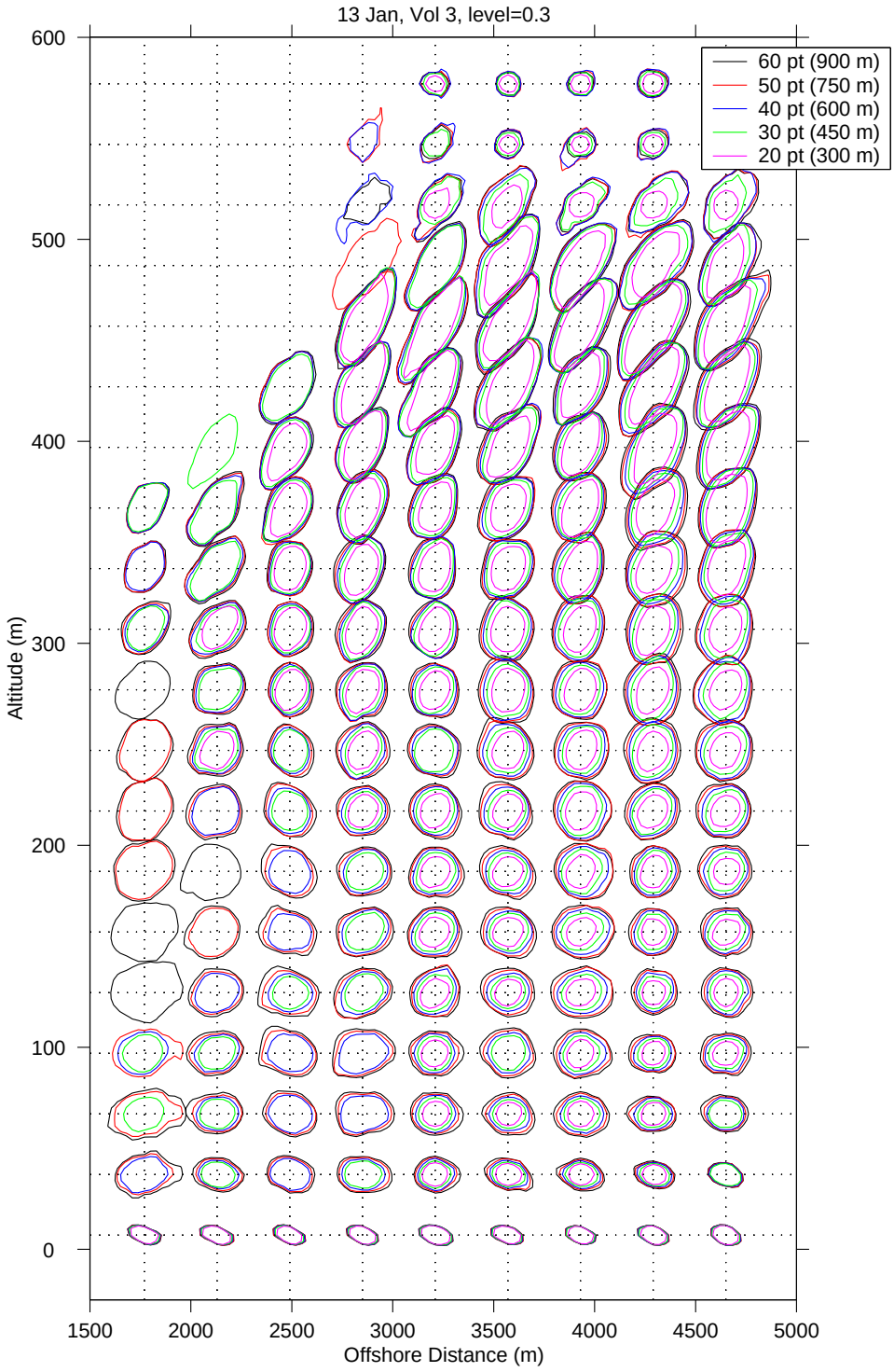

Figure 6.26: Comparison of the 0.3 contour for CCFs of data using five different high-pass median filter lengths.

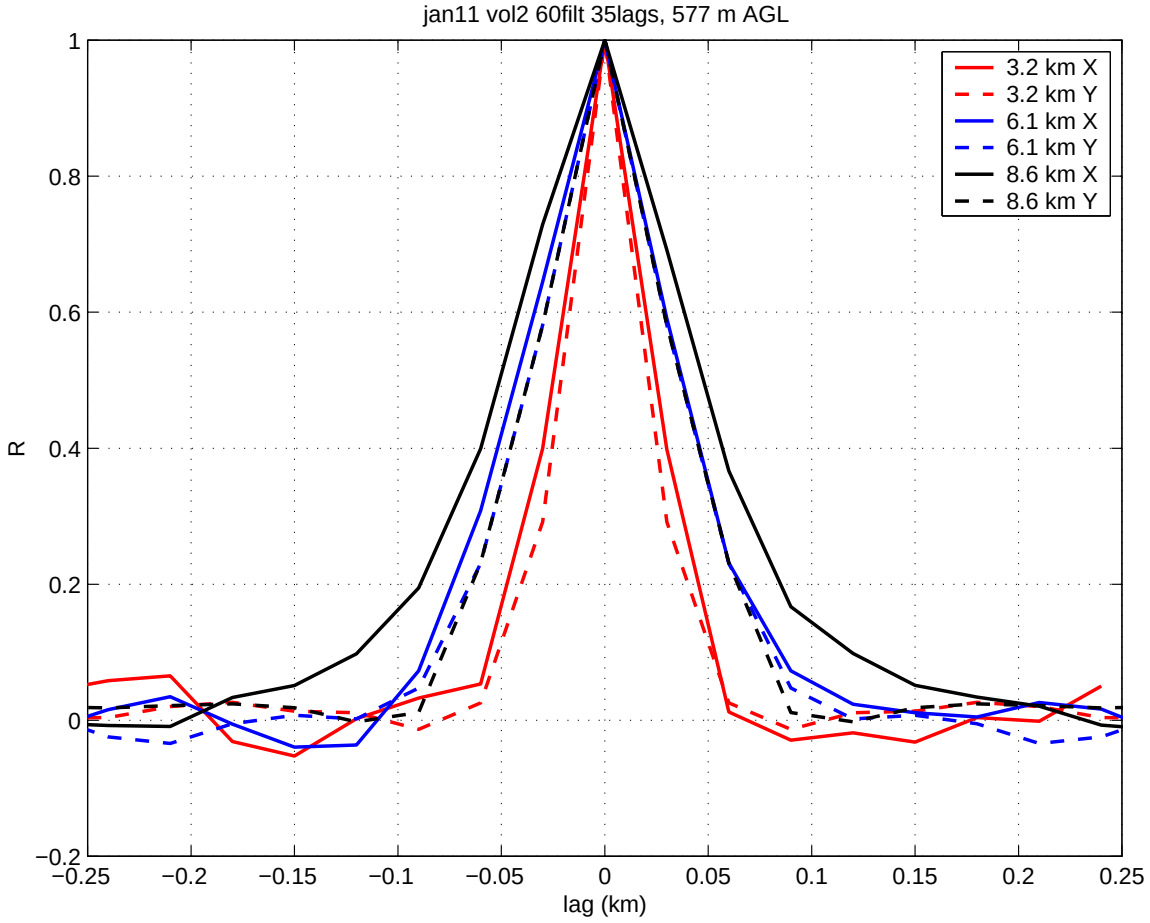

Figure 6.27: East-west (solid) and north-south (dashed) slices through the CCF at 3.2, 6.1 and 8.6 km offshore at 577 m altitude on 11 January showing the correlating effect of placing the spherical lidar data on a evenly spaced Cartesian grid.

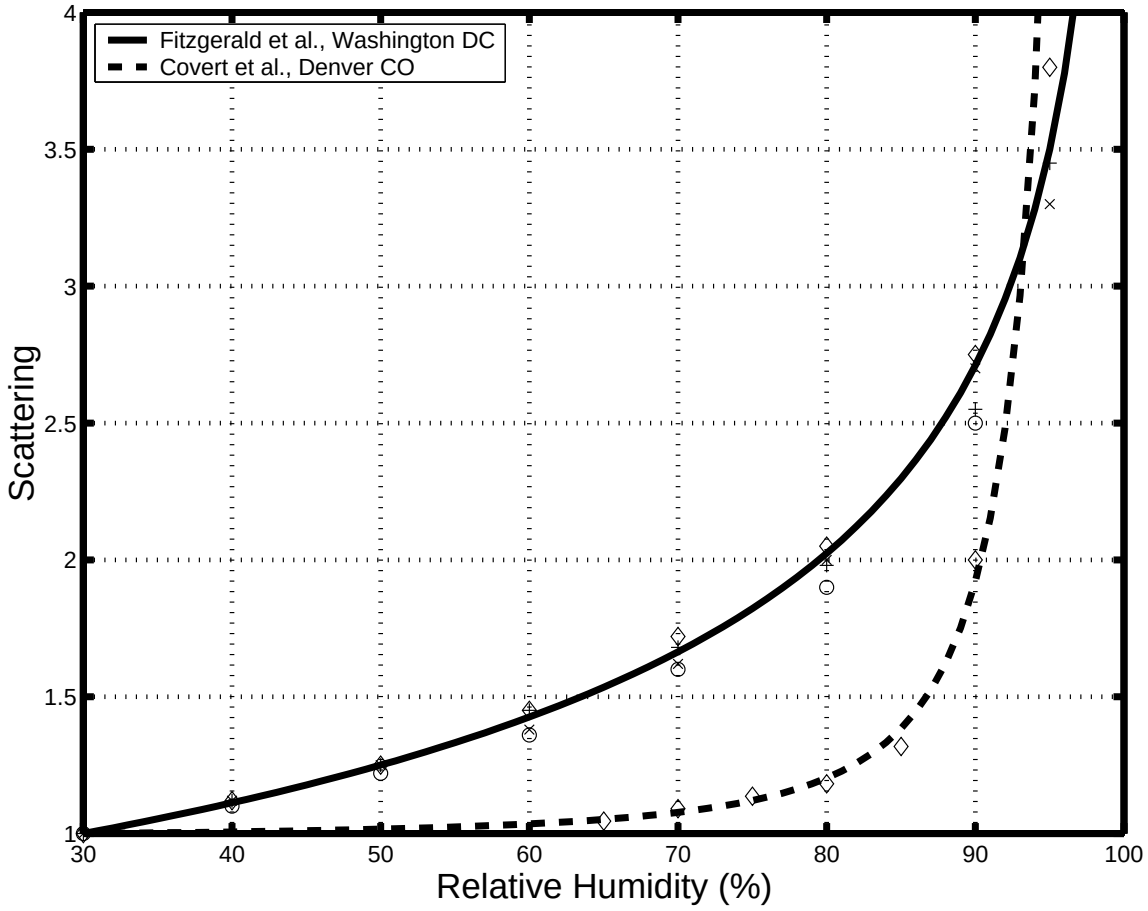

Figure 6.28: Comparison of two functions used to convert model relative humidity to optical scattering.

on 21 Oct. 1971. The function is described by

$$\alpha = -0.98 + \frac{117.92}{(100 - RH)^2} \tag{6.4}$$

and shown as the dashed line in fig. 6.28. Because of its mid-continental origin, this function probably closer to the scattering in Sheboygan over a broad range of relative humidities, but unfortunately, this fitted curve produces extremely high scattering at very high humidities. At 99.99%, this curve produces an unrealistic optical scattering of 1.87 x 10^6 times that which occurs at 30%. (The curve from the Washington, D.C., data was equal to 18.53 at 99.99%.)

The results show that over most altitudes the ellipses fit to the contours of correlation functions from the Covert et al. data are about 50% of the area of those that were fit to the contours of correlation functions from the Fitzgerald et al. data. The comparisons are shown in figs. 6.29 and 6.30. The ellipticities are approximately 10%

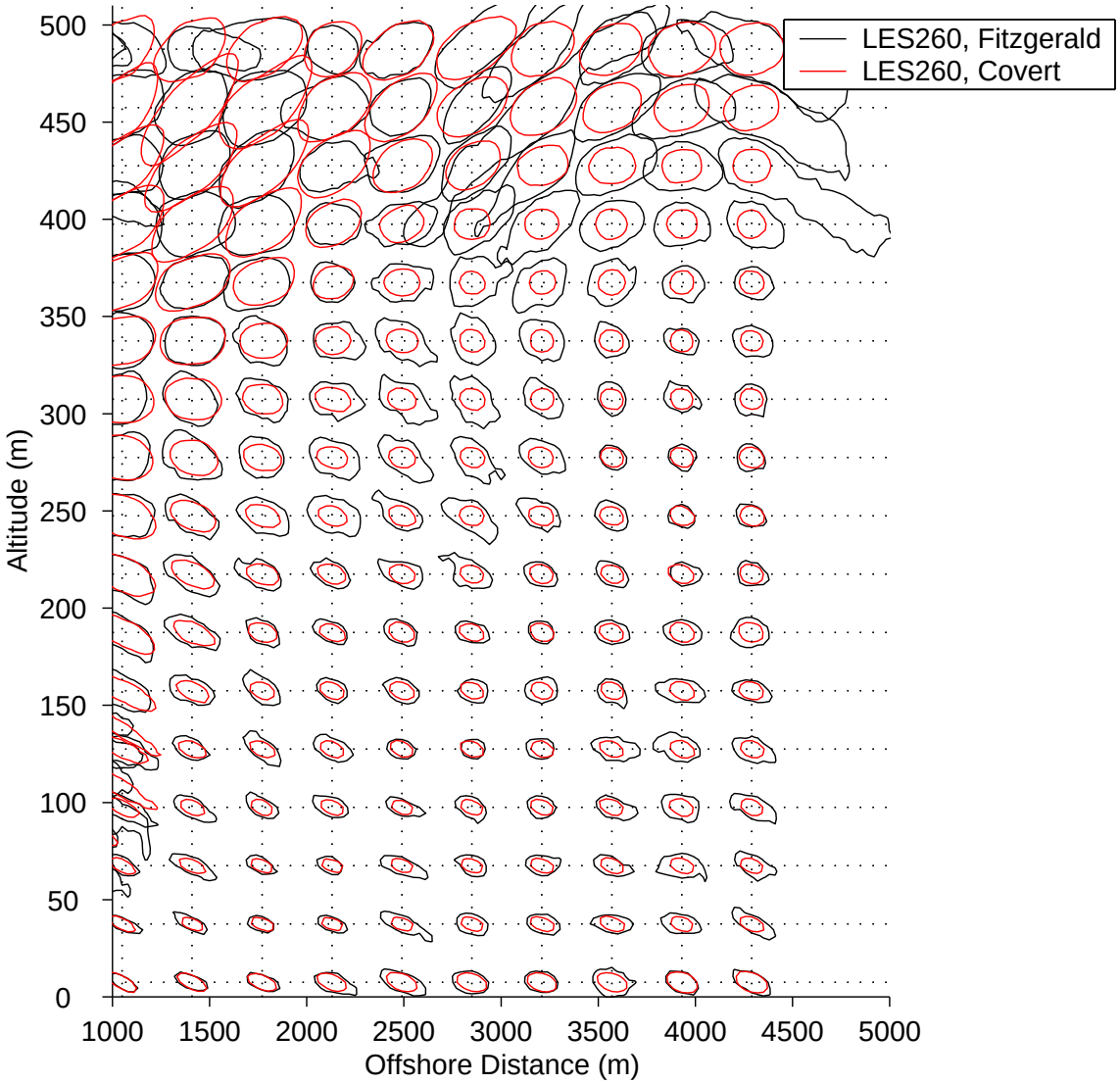

Figure 6.29: Comparison of 0.30 contours of CCFs from LES#260 using Fitzgerald (black) and Covert (red) optical scattering data.

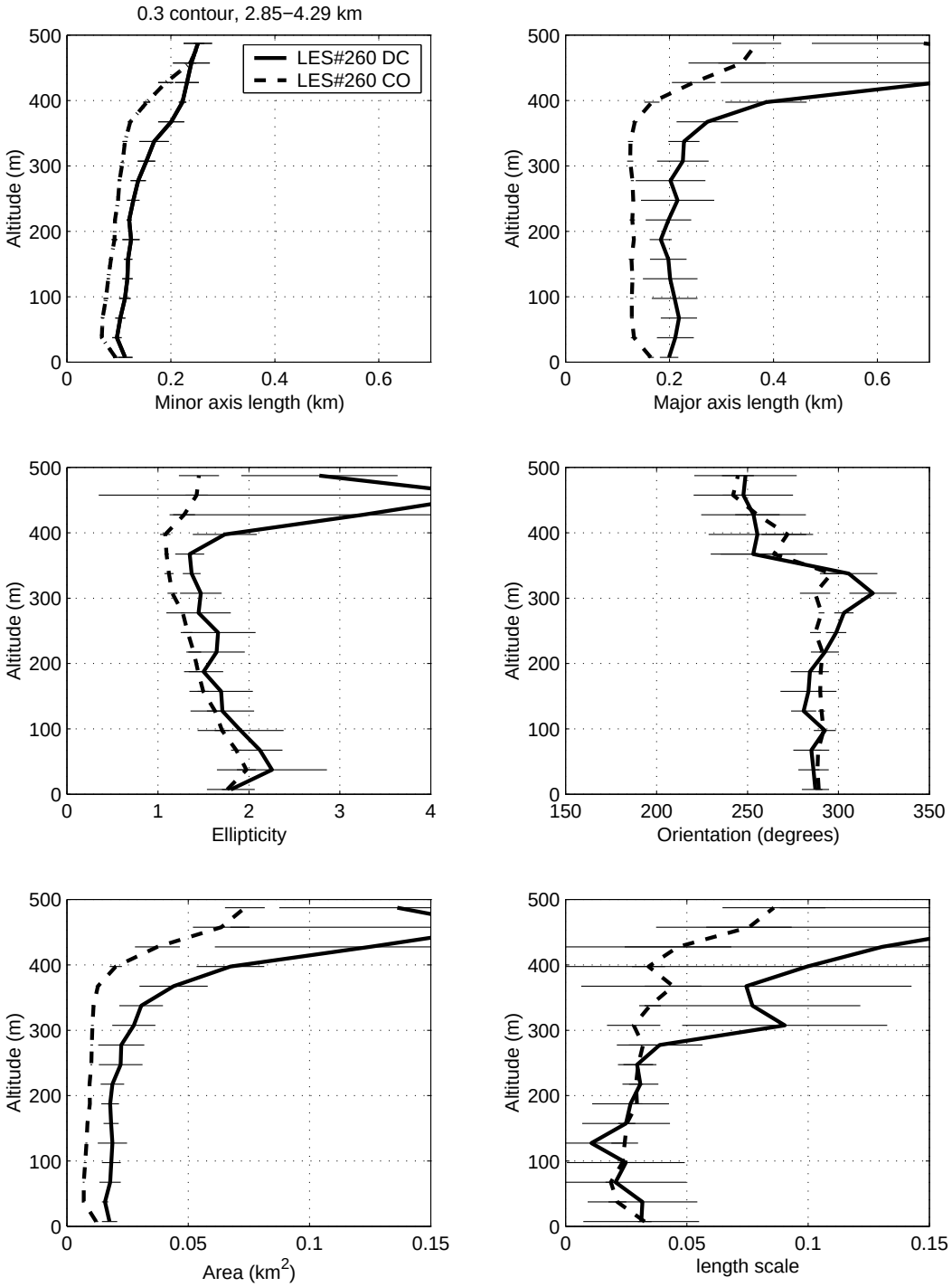

Figure 6.30: Comparison of ellipse parameters for LES#260 using the Fitzgerald et al. (DC) and Covert et al. (CO) optical scattering curves.

smaller over a broad range of altitudes. Fortunately, the orientations remain about the same. The reason for the smaller ellipses is probably because of the scatterings stronger sensitivity to small changes in relative humidity at relative humidities greater than about 80%.

6.11 Eddy lifetime from PPI scans

The unqiue spatial imaging capability of the volume imaging lidar has been emphasized in this Chapter, and others, thus far. However, the VIL is also capable of showing how the spatial patterns advect and decorrelate in with *time*. In fact, it is the VIL's ability to measure the aerosol structure with sufficient *temporal* resolution that allowed the determination of aerosol motion as described in Chapter 4.

The following results were computed before the LES perturbation-recycler was implemented. There was not enough time to recompute these statistics for the IBL simulations which did have the perturbation recycler. Therefore, the temporal decay of the surface layer coherent structures form VIL PPI scans will be compared with that from two simulations (#181 and #195) which used the restoring zones and resulted in immature turbulence at the coastline. The objective was to use the lidar data to judge which of the two simulations produced more realistic turbulence structures near the surface at 1800 m offshore. LES#181 used the Sadourny (1975) advection scheme and LES#195 used a modified Arakawa and Lamb (1981) advection scheme. A snapshot of the vertical velocity near the surface from these two simulations is show in fig. 5.8.

Fig. 6.31 shows examples of two-dimensional cross-correlation functions for aerosol backscatter images separated by increasing amounts of time. The top pair of panels shows the cross-correlation for zero time separation and so the peak is equal to one at the origin. The subsequent pairs of panels show the CCFs from images with 24, 48 and 72 s of time separation, respectively. The peak moves downstream (along the white dashed line in the images in the left hand column) due to the advection of coherent structures. The amplitude of the peak decreases with increasing time separation due to the decorrelating effect of turbulence.

Fig. 6.32a shows the downstream oriented cross-sections of the CCFs for lidar PPI scans on 13 Jan. Fig. 6.32b shows the same result for LES#181 which used the Sadourny advection scheme. Fig. 6.32c are from LES#195 which used a modified Arakawa and Lamb advection scheme. Comparison of the zero time-separation CCFs along a line in the downstream direction (fig. 6.32d) shows that LES#195 produced coherent structures which did not have the spatial decorrelation as seen in the lidar data and LES#181. The lidar data, however, indicates that the temporal decorrelation of the atmosphere on 13 Jan was stronger than either simulation (fig. 6.32e). The curves in fig. 6.32e were obtained by dividing the downwind position of their peaks by the mean wind-speed in order to obtain time as an abscissa.

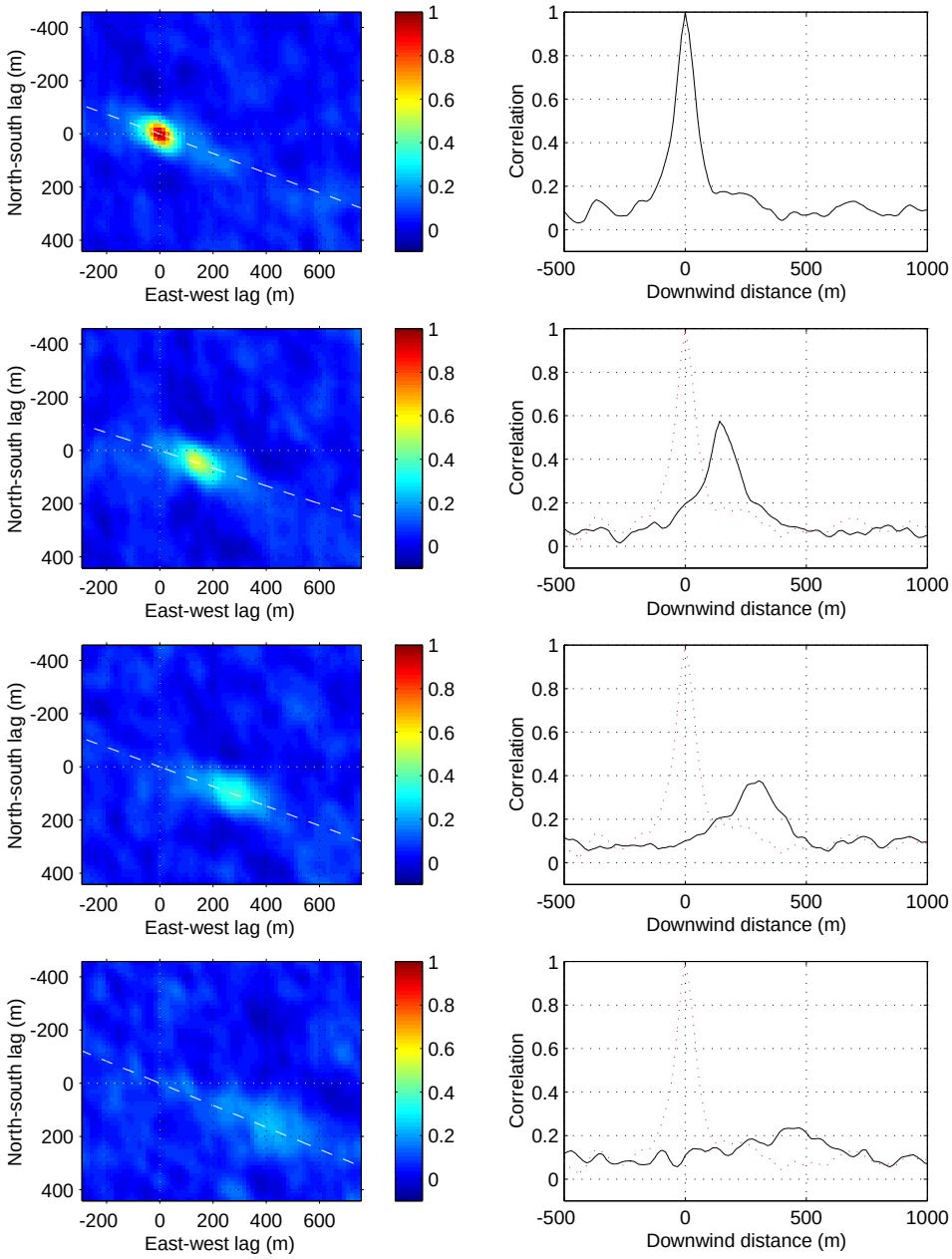

Figure 6.31: Examples of 2D CCFs from aerosol backscatter images separated in time. The peak of the CCF decreases in amplitude due to the decorrelating effect of turbulence and moves downsteam of the origin due to advection.

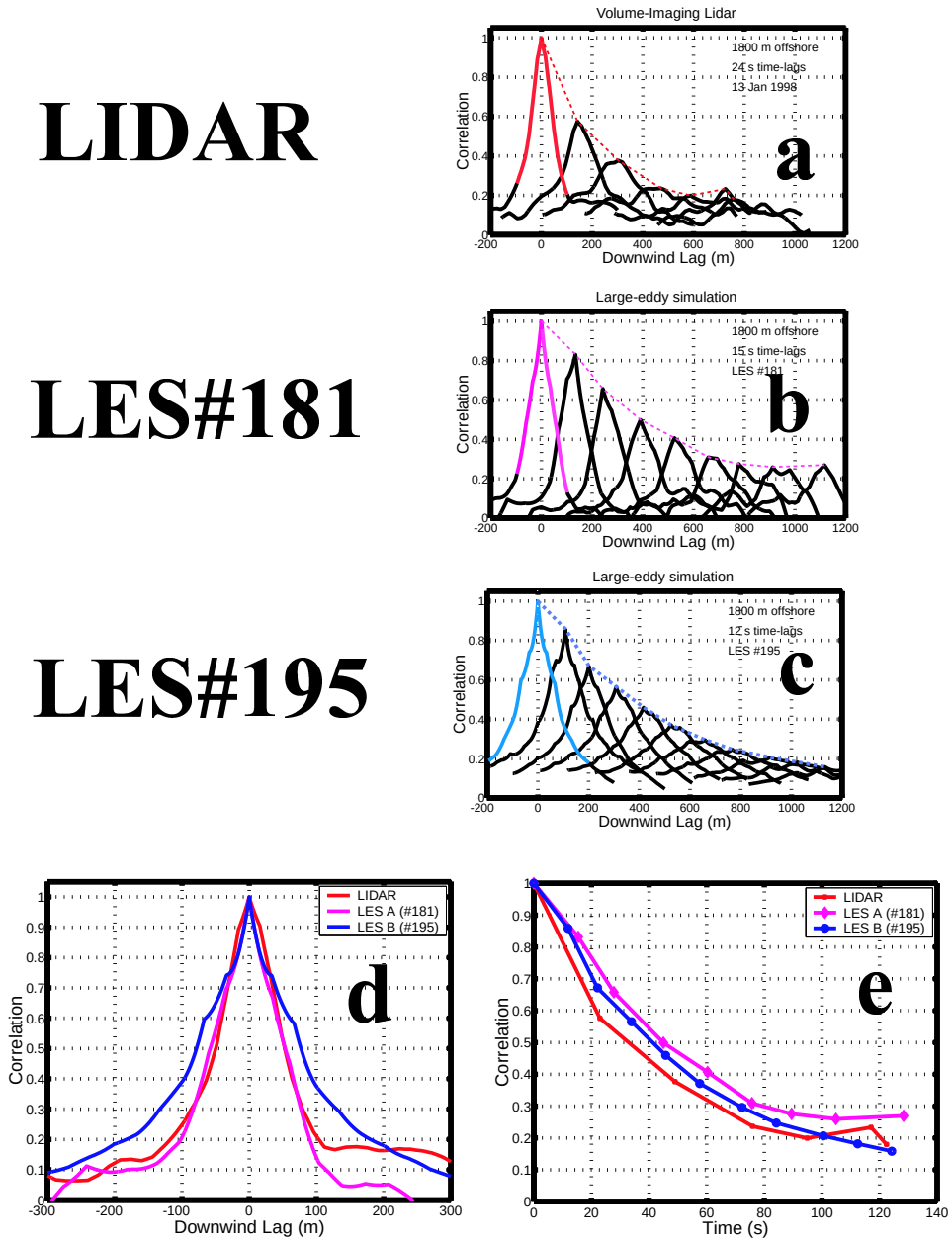

Figure 6.32: Cross-correlation functions for increasing amounts of time-separation for VIL data from PPI scans and from two LESs.

Chapter 7

LES aerosol motion compared to LES wind

Although all comparisons of VIL dervied aerosol motion match traditional observations of the wind within the limits of the sampling error (Eloranta *et al.* 1975 , Kunkel *et al.* 1980 , Sroga *et al.* 1980 , Hooper and Eloranta 1986 , and Piironen and Eloranta 1995), there may be times and places within the boundary layer when the two quantities are not the same. Certainly, because of wave motions, we know the two do not agree under stable conditions. Most of the experimental comparisons listed above have been made in the middle of deep convective boundary layers.

The LES offers the ability to reduce the sampling error on the mean wind to the same level as the coherent structure motion and therefore get closer to seeing if differences exist. Furthermore, it allows us to investigate the vector difference in regions such as the surface layer or the entrainment zone that may not have been focused upon previously. It also allows us to have controlled experiments by changing inversion height, and the buoyancy and shear forcing.

In this chapter the cross-correlation technique described in chapter four, is applied to the simulated aerosol backscatter from the simulations presented in chapter five. The resulting motion field is compared with the model winds. Differences in speed and direction are presented as a function of offshore distance and altitude.

At the time of this writing, coherent structure motion vectors were only computed for simulation number #181. This simulation of the internal boundary layer employed restoring zones (as discussed in section 5.5.1) and periodic boundary conditions. Although the eddies at the shoreline were not as mature as those from simulations employing the perturbation recycler, it still provides an interesting case to examine the difference between coherent structure motion and wind.

The coherent structure motion was obtained by averaging together cross-correlation functions for pairs of frames seperated by 30 s. The advection of coherent structures displaces the correlation peak downwind of the origin. The precise position of the peak of the correlation function was found by fitting a surface following Piironen and Eloranta (1995). The distance of the peak of the fitted surface from the origin divided by 30 s is the coherent structure speed. The angle of line connecting the origin with the displaced peak equals the coherent structure direction.

Fig. 7.1 shows the differences between coherent structure motion and wind for four different altitudes as a function of offshore distance. At 7.5 m above the surface (bottom row of plots), where the flow undergoes a strong acceleration from 5 to 10 m s^{-1} and veering of approximately 5° over 3 km, the differences are barely noticable. This indicates that the inhomogeneities in the simulated aerosol scattering field are traveling with the mean wind at that level. At 100 m altitude we begin to see that the speed of the coherent structures lags behind the wind speed by less than about 1 m s^{-1} at all offshore distances. The largest differences however occur within the first two kilometers offshore where the acceleration is strongest. It is within this region also that we see directional differences of up to about 3°. At 200 m altitude, which is approximately in the middle of the CBL, we see speed differences as much as 2.5 m s^{-1} within the first 2 km offshore. The first coherent structure speed point is an anomaly at this altitude probably because the coherent structures in this region are very lineal therefore making the mean cross-correlation functions very linear. The result is a ridge-line in the cross-correlation function instead of a well-defined peak. Finding the maximum on the ridge-line results in some noisy coherent structure motion vectors. At 400 m we are in the entrainment zone. The coherent structures have the same speed as the wind until convective plumes from the new internal boundary layer begin reaching this level at about 1 km offshore. Beyond this distance we see that the coherent structure are moving approximately 2 m s^{-1} slower and approximately 5-10° to the left of the actual wind. The differences in speed and direction as a function of offshore distance and altitude are summarized in fig 7.2.

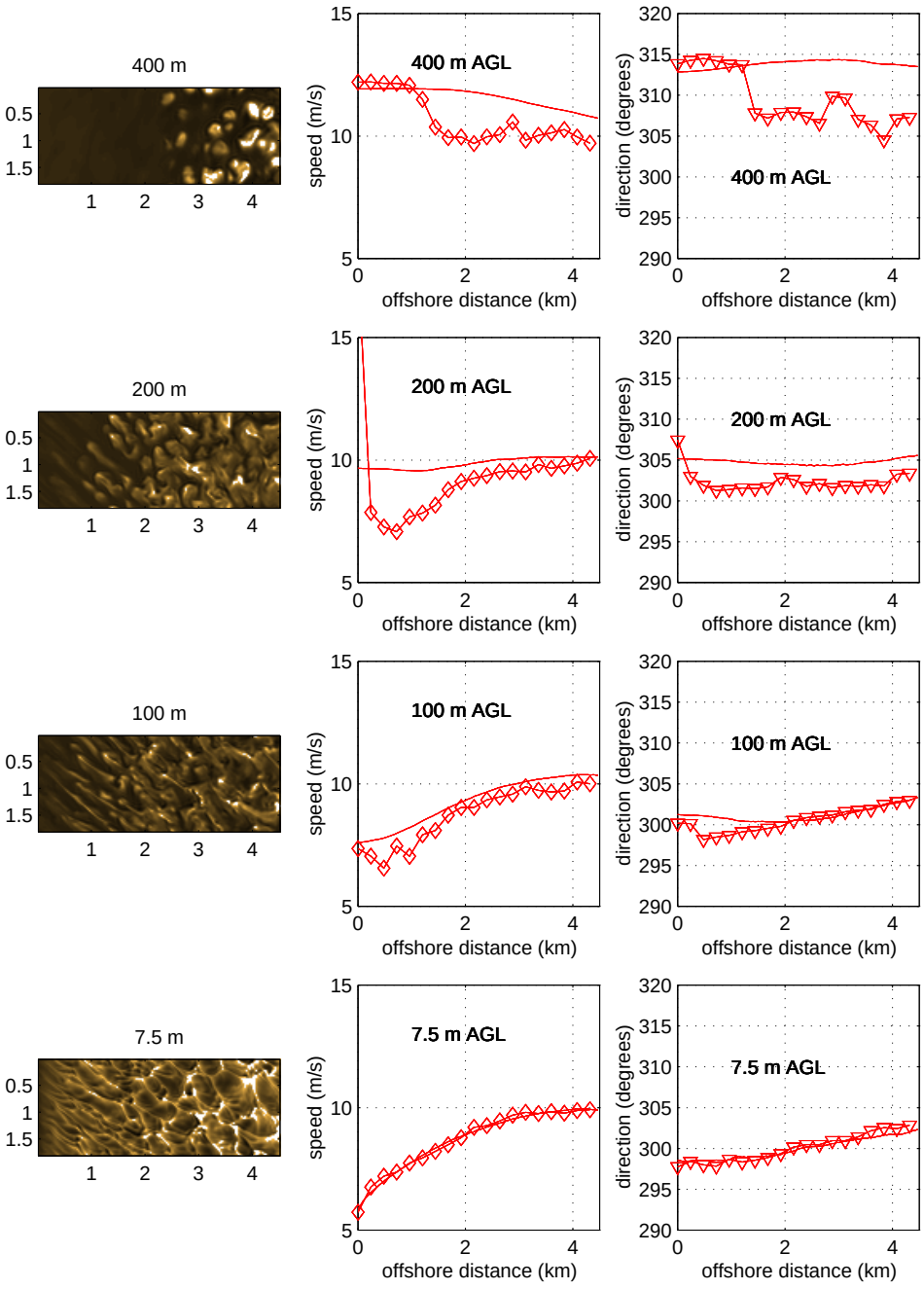

Figure 7.1: Left column: simulated aerosol backscatter from the LES#181 on horizontal slices at selected altitudes. Middle column: line plots of wind speed (line without symbols) and coherent structure speed (line with symbols). Right column: line plots of wind direction (line without symbols) and coherent structure direction (line with symbols).

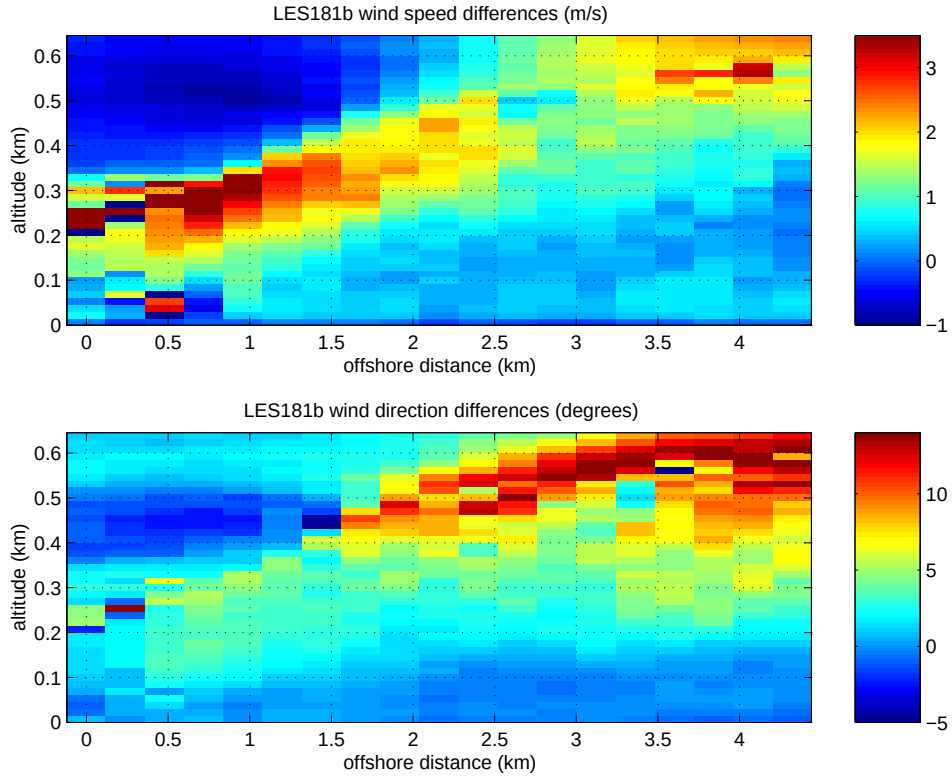

Figure 7.2: Top panel: actual wind speed minus coherent structure speed (in m s^{-1}) as a function of offshore distance and altitude. Bottom panel: actual wind direction minus coherent structure direction (in degrees). Both panels from the last 30-minutes of LES#181.

Chapter 8

Conclusions

8.1 From the Lidar Data

The lidar data was invaluable as a constant reminder of the real eddy structure while many LES experiments were run. An important lidar observation was that the boundary layer was continuously well-mixed at the shore on the three cold-air outbreak days. The lidar observations confirmed the ISS observations of a mixed layer over the land and eliminated the possibility that the upwind boundary layer was stable. This improved awareness drove the effort to develop a turbulent upwind boundary layer in the simulations.

The lidar observations show that near the surface under conditions of intense convection the organization of aerosol structures (including steam-fog) takes on an *open-cell* character. The patterns change to *closed-cell* structures above about 100 m altitude. These observations show that in highly convective boundary layers, the surface layer structure is strongly influenced by convective cells which have a depth comparable to the mixed layer depth.

On 13 January, the lidar data indicate that the convective plumes above the surface layer are organized into linear bands that are oriented *perpendicular* to the mean flow. This pattern was not observed in the LES output and confirms the importance of gravity waves in organizing convection as documented in other studies. Although gravity waves were simulated here, their strength was limited because of the chosen boundary conditions, the limited depth of the domain, and the closeness of the absorbing layer to the duct.

The lidar observations also show that the aerosol structures advect with the mean flow and change with time, thereby eliminating the LES solutions which contain very smooth linear structures such as those in LES#212. The averaged lidar backscatter data do not indicate a well defined edge to the internal boundary layer. However, some of the instantaneous images from the CAPPI, PPI and RHI scans do show inhomogeneity in the coherent structures in the offshore direction. This is reflected in the variance of the backscatter which does increase with offshore distance, particularly in the surface layer and entrainment zone where steam-fog and cumulus clouds form.

The lidar data was used to determine the aerosol motion vector field offshore with 250 m spacing. For the case of January 10, the vector field derived from PPI scans revealed quite homogeneous acceleration and veering of the flow and the possible wake effect of a large building at the shore. On January 13, the vector field derived from PPI scans revealed a localized wind-speed maximum which is probably the result of flow that was influenced by Sheboygan Point. Aerosol structure motion derived from RHI scans on 13 January were also used to show the redistribution of momentum in the vertical as a function of downstream distance. It is likely that no other instrument, except for perhaps one or two Doppler lidars, could have provided these flow measurements.

8.2 From the LES

It appears that the organization of convection near the shore (the first few kilometers) is strongly influenced by the presence of, or lack of, eddies advecting offshore. For example, when laminar flow is advecting offshore, a region of convection spin-up must occur in the first several kilometers immediately downstream of the shoreline. This same process happens in the Nieuwstadt CBL simulation of with an overshoot of TKE as many vigorous eddies form initially in response to the accumulation of potential energy near the surface. To have a realistic simulation of the observed cases, it was necessary to have a fully-developed CBL over the land.

In order to sustain fully-developed, horizontally-homogeneous turbulence over the land, a perturbation recycling method was used to maintain a turbulent inflow boundary condition. In addition to this, a precursor LES was run to spin-up turbulence that is characteristic of the upwind boundary layer and generate a mean inflow condition for the IBL domain.

The simulations showed that the vertical thermodynamic structure of the atmosphere over the western shore on 13 January ducted gravity waves. This became especially evident when precursor simulations where run for several hours and the wave amplitude in the capping inversion became so large that it completely dominated the large-eddy motions of the mixed layer. This problem was eliminated when the depth of the domain was limited to just 1 km. However, this removed the apparent organizing effect of the gravity waves on convective plumes in the mixed layer as discussed in the previous section.

January 13 was chosen as the day to simulate because of the availability of excellent PPI, RHI and RHI volume scan data and a steady-state 400 m boundary layer depth. Although the data from the 10th was more homogeneous, the 1 km deep boundary layer required too much computer resource with 15 m grid-spacing. 15-m grid spacing was chosen in order to resolve turbulent structures similar to that which the lidar was capable of resolving. The 11th of January presents another excellent case for simulation because of the relatively shallow boundary layer and availability of excellent data, however the boundary layer depth steadily decreases throughout the day which may be difficult to duplicate in the simulation.

The eddy structure generated by the LES is sensitive to the eddy viscosity coefficient (DKR) and the amount of numerical filtering used. Unfortunately, none of the three simulations that were compared with the lidar observations proved to be any better than the other. This suggests that something common to all the simulations is causing them to be different from the observations.

The LES was also used to estimate the difference between aerosol structure motion and wind. This difference is so small that it has not been possible to measure it given the large sampling errors of conventional wind measurement systems. However, this result is dependent on the models ability to generate and advect eddies properly and should be verified in a future field experiment.

8.3 Recommendations for future work

Eye-safe volume-imaging lidars are needed to eliminate the hazard of the current system. Scanning eye-safe systems will also permit measurements close to the ground in populated areas. For example, if the VIL had been eye-safe during Lake-ICE, data from over the land would have been collected during our deployment. That data could have been used as an observational constraint for the simulation of eddy structure over the land. In the current study, there is no observational confirmation of the very linear coherent structures which the LES produces over land with weak positive surface heat flux.

Faster volume scanning is needed in order to measure aerosol structure motion at multple altitudes simultaneously. Currently, two to three minutes are required to collect one volume scan and during this time enough decorrelation occurs due to turbulence that the aerosol motion cannot be obtained. Higher sensitivity is also needed so that the backscatter values are not constant in regions of homogeneous scattering. Fortunately, a next generation volume imaging lidar is under development.

Improved simulation of lidar aerosol scattering should include a relationship between LES water content and optical scattering. Additional simulations should be run that include (1) much deeper domains and (2) allowing the mean condition on the inflow wall to change, or float, with time. These adjustments may allow the simulation of stronger gravity waves which could act to organize convection within the boundary layer below them. A series of numerical experiment should also be conducted to see how the presence of buildings and shoreline shape effect the turbulence structures over the lake. The algorithm to determine and output model fluxes should also be examined to determine the cause of the systematic vertical stripes in figs. 5.31 and 5.32. Comparison of the mean (vertical *and horizontal*) momentum fluxes as shown in fig. 5.32 with differences between coherent structure motion and wind (as shown in fig. 7.2) may be very interesting.

Finally, this work suggests that a field campaign should be conducted whereby the turbulence structure and wind field over the land and water could be measured using both volume imaging and Doppler lidars simultaneously. In addition to the lidars, several types of in situ measurements are necessary. First, a surface meteorological

station with radiosonde launching capability should be deployed upwind of the shore as was done in Lake-ICE. Colocated at that site, or near the lidar site at the shore, should be a facility for determining the optical scattering as a function of relative humidity. A micrometeorological station with flux measurement capability should be installed on a floating platform for verification of offshore conditions. Such a campaign will allow us to determine if the LES is generating correct coherent structures over the land before the flow experiences the abrubt change in surface forcing. It will also allow determination of the difference between coherent structure motion and the wind.

A UW-NMS Formulation

The University of Wisconsin Nonhydrostatic Modeling System (UW-NMS) is a quasi-compressible, nonhydrostatic, primitive equation model. It is formulated to conserve dynamic properties of the flow including vorticity, kinetic energy, *and enstrophy in the 2D limit.* This is accomplished by casting the Navier-Stokes equations in the Bernoulli, or vorticity, form in such a way that the three components of absolute vorticity and kinetic energy are uniquely defined for all three Cartesian equations of motion. Moreover, all three dimensions are treated similarly, except for gravity, so that motion is not biased by a differing coordinate system in the vertical and horizontal directions. For more details of model formulation see Tripoli (1992).

Conservation of enstrophy (the mean vorticity squared) is used to increase the accuracy of the numerical advection scheme. This numerical constraint reduces systematic biases of truncation errors that lead to numerical enstrophy cascade. This approach increases the accuracy of the nonlinear aspects of the advecting and therefore makes the simulated scale interactions more physical.

The model is cast on a rotated spherical Arakawa C grid for scalability purposes at virtually no cost. This enables the definition of large domains which conform to the shape of the earth or small domains where curvature is not important. This framework also permits nesting if desired from large to small scales.

Although not used for the work presented here, topography can be represented by a variably stepped coordinate that conforms to the exact mean topographical height over a grid box.

All variables in this appendix are defined in table A.1. Primed variables denote perturbations from the base state and double-primed variables indicate turbulent deviations relative to the grid average.

1 Equations of motion

Accelerations for the air at each grid point are calculated from the three equations of motion. In UW-NMS they are defined as:

$$\frac{\partial u}{\partial t} + \theta_v \frac{\partial \pi'}{\partial x} = \eta_z v^* - \eta_y w^* - \frac{\partial k}{\partial x} - F_{1u} + F_{2u} \tag{A.1}$$

$$\frac{\partial v}{\partial t} + \theta_v \frac{\partial \pi'}{\partial y} = -\eta_z u^* + \eta_x w^* - \frac{\partial k}{\partial y} - F_{1v} + F_{2v} \tag{A.2}$$

$$\frac{\partial w}{\partial t} + \theta_v \frac{\partial \pi'}{\partial z} = \eta_y u^* + \eta_x v^* - \frac{\partial k}{\partial z} - F_{1w} + F_{2w} - g\frac{\theta'}{\theta_0} \tag{A.3}$$

where subgrid-scale turbulence is represented by

$$F_{1u} = \frac{1}{\rho}\left[\frac{\partial \rho\tau_{11}}{\partial x} + \frac{\partial \rho\tau_{12}}{\partial y} + \frac{\partial \rho\tau_{13}}{\partial z}\right] \tag{A.4}$$

$$F_{1v} = \frac{1}{\rho}\left[\frac{\partial \rho\tau_{12}}{\partial x} + \frac{\partial \rho\tau_{22}}{\partial y} + \frac{\partial \rho\tau_{23}}{\partial z}\right] \tag{A.5}$$

$$F_{1w} = \frac{1}{\rho}\left[\frac{\partial \rho\tau_{13}}{\partial x} + \frac{\partial \rho\tau_{23}}{\partial y} + \frac{\partial \rho\tau_{33}}{\partial z}\right]. \tag{A.6}$$

The components of the stress matrix are parameterized by

$$\tau_{ij} = l e^{1/2}\left(\frac{\partial u_i}{\partial x_j} + \frac{\partial u_j}{\partial x_i}\right) - \frac{2}{3}\delta_{ij} e. \tag{A.7}$$

where the length scale l is set to the cube-root of the product of the grid-spacing:

$$l = (\Delta x \Delta y \Delta z)^{1/3}. \tag{A.8}$$

The time-tendency of turbulent kinetic energy e is predicted from

$$\begin{aligned}\frac{\partial e}{\partial t} = &-\frac{1}{\rho}\left[\frac{\partial \rho u e}{\partial x} + \frac{\partial \rho v e}{\partial y} + \frac{\partial \rho w e}{\partial z}\right] + e\frac{\delta_\rho}{\rho} \\ &-\frac{1}{\rho}\left[\frac{\partial \rho u'' e''}{\partial x} + \frac{\partial \rho v'' e''}{\partial y} + \frac{\partial \rho w'' e''}{\partial z}\right] + F_e + S_e\end{aligned} \tag{A.9}$$

where

$$S_e = \mathrm{c}_1 l D^2\sqrt{e} + \mathrm{c}_1 l\frac{K_h}{K_m}N^2\sqrt{e} - \frac{2}{3}D_v^2 e - c_\epsilon\frac{e^{3/2}}{l}. \tag{A.10}$$

and

$$F_e = \frac{1}{e}\left[\frac{\partial \rho e}{\partial x} + \frac{\partial \rho e}{\partial y} + \frac{\partial \rho e}{\partial z}\right]. \tag{A.11}$$

The four terms to the right of the equal sign in eqn. A.10 in order from left to right are mechanical source, buoyant source, divergence and dissipation, respectively. c_1 is a mixing coefficient previously called DKR in chapter 5. In eqn. A.10, D is velocity deformation

$$D = \left(\frac{\partial u_i}{\partial x_j} + \frac{\partial u_j}{\partial x_i}\right) \tag{A.12}$$

and D_v is divergence

$$D_v = \frac{\partial u}{\partial x} + \frac{\partial v}{\partial y} + \frac{\partial w}{\partial z}. \tag{A.13}$$

The mechanical and thermal eddy viscosities are computed from

$$K_m = c_1 l e^{1/2} \qquad \text{and} \qquad K_h = 3K_m. \tag{A.14}$$

In the equations of motion, relative and absolute vorticites with axes of rotation in the three Cartesian directions are defined in the following equations respectively.

$$\eta_x = \frac{\zeta_x + f_x}{\rho_m} \qquad \zeta_x = -\frac{1}{m}\left(\frac{\partial mv}{\partial z} - \frac{\partial mw}{\partial y}\right) \tag{A.15}$$

$$\eta_y = \frac{\zeta_y + f_y}{\rho_m} \qquad \zeta_y = -\frac{1}{m}\left(\frac{\partial mu}{\partial z} - \frac{\partial mw}{\partial x}\right) \tag{A.16}$$

$$\eta_z = \frac{\zeta_z + f_z}{\rho_m} \qquad \zeta_y = -\frac{1}{m}\left(\frac{\partial mu}{\partial y} - \frac{\partial mv}{\partial x}\right) \tag{A.17}$$

The kinetic energy is defined as

$$k = \frac{1}{2m}\sqrt{(mu)^2 + (mv)^2 + (mw)^2}. \tag{A.18}$$

A numerical filter is applied in the horizontal and vertical directions to combat any numerical noise and physical enstrophy cascade not absorbed by the physical turbulence scheme. In the horizontal a minimal 6th order filter of magnitude $\Delta x^6/(640\Delta t)$ $\mathrm{m}^6\ \mathrm{s}^{-1}$ is used and in the vertical a 4th order filter of $\Delta z^4/(8000\Delta t)$ $\mathrm{m}^4\ \mathrm{s}^{-1}$ is applied.

2 Thermodynamics

The models thermodynamics are based on the prediction of a moist entropy variable (θ_{il}) that is designed to be conserved over all ice and liquid adiabatic processes (Tripoli and Cotton 1981). Its transport equations, cast in density weighted flux form, enforce the conservation in anelastic flow. In addition, pressure in the form of the Exner function π is predicted quasi-compressibility, precipitating ice and liquid are predicted and total water content is predicted. Cloud droplets are assumed to form and evaporate instantaneously so as to maintain no supersaturation, rendering cloud water, vapor, pressure, potential temperature and temperature diagnostically through a rapidly converging iterative process. This system ensures the ability to perfectly conserve moist for all moist adiabatic processes and provides a simple way to calculate diabatic tendencies to these quantities due to precipitation processes or radiative transfer. This moist thermodynamics system is especially appropriate for

turbulent boundary layer moist processes where its use makes most of the rapid scale processes implicit to the system since they will not affect the predictive moist entropy variable on the grid scale.

Moist entropy, or ice-liquid water potential temperature, is defined as

$$\theta = \theta_{il} = \left(1 + \frac{L_{vl} r_l + L_{il} r_i}{c_p \max(\mathrm{T}, 253)}\right) \tag{A.19}$$

and the Exner function is defined as

$$\pi = c_p \left(\frac{P}{P_{00}}\right)^{R/c_p}. \tag{A.20}$$

The time-tendency of moist-entropy is computed from

$$\begin{aligned} \frac{\partial \theta_{il}}{\partial t} = &- \frac{1}{\rho}\left[\frac{\partial \rho u \theta_{il}}{\partial x} + \frac{\partial \rho v \theta_{il}}{\partial y} + \frac{\partial \rho w \theta_{il}}{\partial z}\right] + \theta_{il}\frac{\delta_\rho}{\rho} \\ &- \frac{1}{\rho}\left[\frac{\partial \rho u'' \theta_{il}''}{\partial x} + \frac{\partial \rho v'' \theta_{il}''}{\partial y} + \frac{\partial \rho w'' \theta_{il}''}{\partial z}\right] + F_{\theta_{il}} + S_{\theta_{il}} \end{aligned} \tag{A.21}$$

and the time-tendency of the Exner function from

$$\frac{\partial \pi'}{\partial t} + \alpha_s \delta_{\rho\theta_v} = 0. \tag{A.22}$$

Here, α_s is a coefficient related to the artifical reduction of the speed of sound for computational efficiency. c_s' is the adjusted sound speed and c_s is the true speed of sound.

$$\alpha_s = \left(\frac{c_s'}{c_s}\right)^2 \frac{R}{c_v}\frac{\pi_0}{\rho_0 \theta_0} \tag{A.23}$$

The time-tendency of total water mixing ratio is computed from

$$\begin{aligned} \frac{\partial r_T}{\partial t} = &- \frac{1}{\rho}\left[\frac{\partial \rho u r_T}{\partial x} + \frac{\partial \rho v r_T}{\partial y} + \frac{\partial \rho w r_T}{\partial z}\right] + \theta_{il}\frac{\delta_\rho}{\rho} \\ &- \frac{1}{\rho}\left[\frac{\partial \rho u'' r_T''}{\partial x} + \frac{\partial \rho v'' r_T''}{\partial y} + \frac{\partial \rho w'' r_T''}{\partial z}\right] + F_{r_T} \end{aligned} \tag{A.24}$$

where diagnostic cloud water is computed from

$$r_c = \max[0, \mathrm{r_T} - \mathrm{r_{vs}}(\mathrm{T}, \mathrm{p})] \tag{A.25}$$

Finally, in any of the above equations

$$\delta_A = \left(\frac{\partial Au}{\partial x} + \frac{\partial Av}{\partial y} + \frac{\partial Aw}{\partial z}\right) \tag{A.26}$$

$$A^* = \rho_m A \tag{A.27}$$

$$A'(x_i, y_j, z_k) = A(x_i, y_j, z_k) - A_0(z_k) \tag{A.28}$$

where A can be replaced by whatever variable is used in the equation. Other equations used in the model include

$$T = \theta \frac{\pi}{c_p} \qquad \text{(Poisson's equation)} \tag{A.29}$$

$$\pi^{c_v/c_p} = \frac{\rho R \theta_v}{P_{00}^{R/c_p}} \qquad \text{(Equation of state)} \tag{A.30}$$

and

$$\theta_v = \theta(1 + 0.61 r_v) \qquad \text{(Virtual temperature).} \tag{A.31}$$

Variable	Description
a	radius of the earth
A	any predicted variable
c_1	eddy mixing coefficient (also DKR)
c_p	specific heat at constant pressure
c_p	specific heat at constant volume
c_ϵ	dissipation constant 0.7
c_s, c_s^1	speed of sound, modified speed of sound
D	3D deformation
D_v	3D velocity divergence
e	turbulent kinetic energy
F_1	stress terms
F_2	numerical filter
g	gravity
k	kinetic energy
K_m	mechanical eddy viscosity
K_h	thermal eddy viscosity
l	length scale
L_{vl}	latent heat (vapor to liquid)
L_{il}	latent heat (ice to liquid)
m	spherical transformation function $cos\phi$
N	Brunt Vaisala frequency
r_T	total water mixing ratio
r_i, r_l	mixing ratio for ice, mixing ratio for liquid
P, P_0, P_{00}	pressure, base-state pressure, 1000 mb
R	gas constant
S	source term
t	time
T	temperature
u, v, w	components of velocity in x, y, and z
u^*, v^*, w^*	ρu, ρv, and ρw
x, y, z	Cartesian coordinates
δ_{ij}	1 if $i = j$, 0 if $i \neq j$
$\delta_{\rho\theta_v}$	
δ_ρ	
Δx, Δy, Δz	grid spacing
η_x, η_y, η_z	relative vorticity in x, y and z
ζ_x, ζ_y, ζ_z	absolute vorticity in x, y and z
ρ	density
τ	stress
α_s	
θ	potential temperature
θ_0	potential temperature
θ_v	virtual potential temperature
θ_{il}	moist ice-liquid entropy
$\delta_{\rho\theta_v}$	
δ_ρ	
θ_0	
ϕ	latitude
λ	longitude
π	Exner function (see eqn. A.20)

Table A.1: Definitions of variables used in model appendix.

B 2D CCFs from 11 January

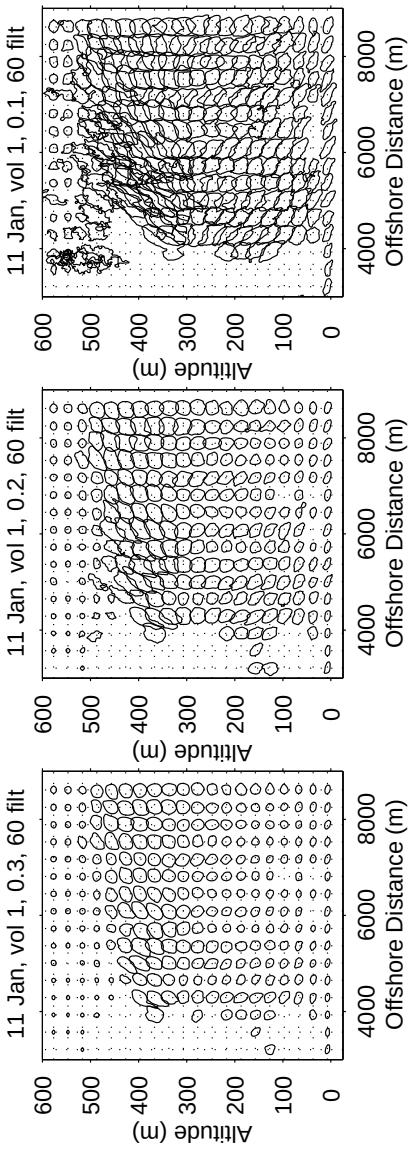

Figure B.1: Contours of 0.3 (left), 0.2 (middle) and 0.1 (right) from cross-correlation functions of aerosol backscatter on CAPPIs on 11 January from 11:51-12:16 UT.

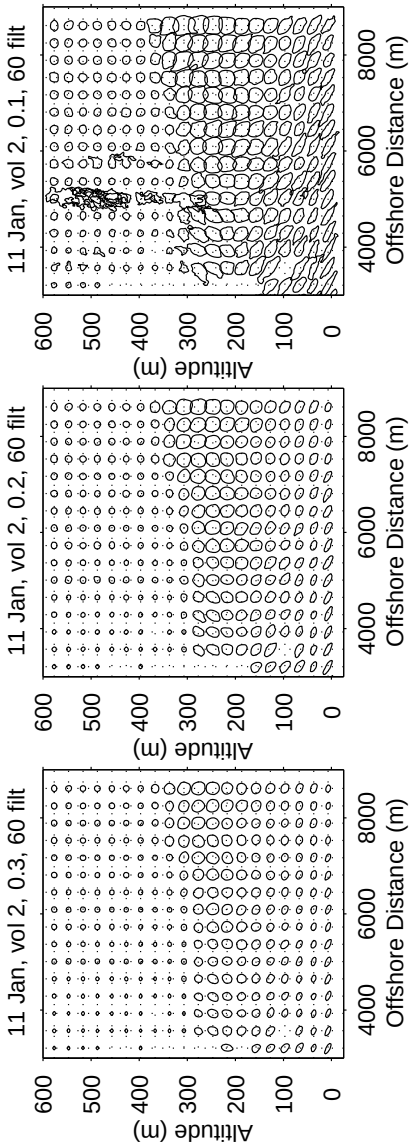

Figure B.2: Contours of 0.3 (left), 0.2 (middle) and 0.1 (right) from cross-correlation functions of aerosol backscatter on CAPPIs on 11 January from 13:47-14:30 UT.

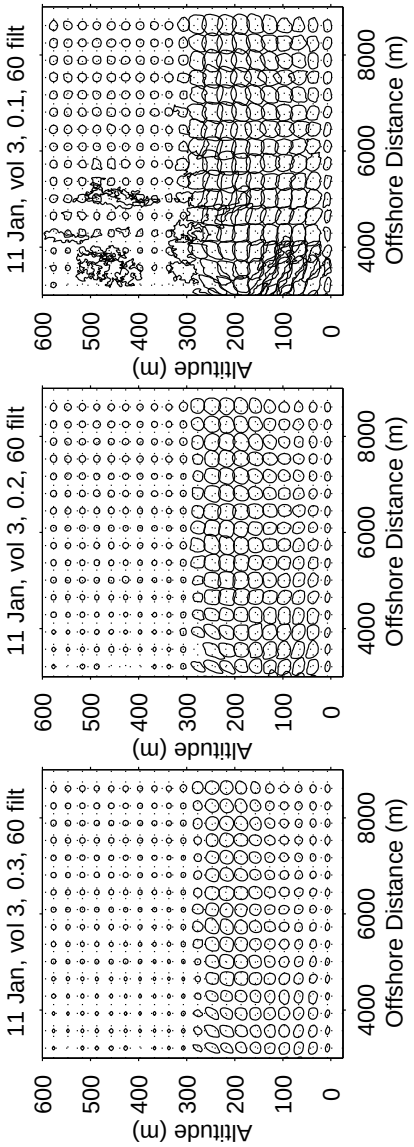

Figure B.3: Contours of 0.3 (left), 0.2 (middle) and 0.1 (right) from cross-correlation functions of aerosol backscatter on CAPPIs on 11 January from 15:29-16:23 UT.

References

Agee, E. M. and Hart, M. L. (1990): Boundary layer and mesoscale structure over Lake Michigan during a wintertime cold air outbreak. *J. Atmos. Sci.*, **47**, pp. 2293–2316.

Andren, A., Brown, A. R., Graf, J., Mason, P. J., Moeng, C.-H., Nieuwstadt, F. T. M., and Schumann, U. (1994): Large-eddy simulation of a neutrally stratified boundary layer: A comparison of four computer codes. *Quart. J. R. Met. Soc.*, **120**, pp. 1457–1484.

Arakawa, A. and Lamb, V. R. (1981): A potential enstrophy and energy conserving scheme for the shallow water equations. *Mon. Wea. Rev.*, **109**, pp. 18–36.

Atkinson, B. W. and Zhang, J. W. (1996): Mesoscale shallow convection in the atmosphere. *Rev. Geophys.*, **34**, pp. 403–431.

Ayotte, K. W., Sullivan, P. P., Andren, A., Doney, S. C., Holtslag, A. M., Large, W. G., McWilliams, J. C., Moeng, C.-H., Otte, M. J., Tribbia, J. J., and Wyngaard, J. C. (1996): An evaluation of neutral and convective planetary boundary-layer parameterizations relative to large eddy simulations. *Bound. Layer Meteor.*, **79**, pp. 131–175.

Bevington, P. R. (1969): *Data Reduction and Error Analysis for the Physical Sciences.* McGraw-Hill, New York.

Bilbro, J., Fichtl, G., Fitzjarrald, D., Krause, M., and Lee, R. (1984): Airborne Doppler Lidar Wind Field Measurements. *Bull. Amer. Meteor. Soc.*, **65**, pp. 348–359.

Bluestein, H. B. (1990): Observations of steam devils over a lake during a cold-air outbreak. *Mon. Wea. Rev.*, **118**, pp. 2244–2247.

Boers, R. and Eloranta, E. W. (1986): Lidar measurements of the atmospheric entrainment zone and the potential temperature jump across the top of the mixed layer. *Bound. Layer Meteor.*, **34**, pp. 357–375.

Boers, R., Eloranta, E. W., and Coulter, R. L. (1984): Lidar observations of mixed layer dynamics: tests of parameterized entrainment models of mixed layer growth rate. *J. Clim. Appl. Meteor.*, **23**, pp. 247–266.

Bohren, C. F. and Albrecht, B. A. (1998): *Atmospheric Thermodynamics.* Oxford University Press, New York.

Carruthers, D. J. and Moeng, C.-H. (1987): Waves in the overlying inversion of the convective boundary layer. *J. Atmos. Sci.*, **44**, pp. 1801–1808.

Chang, S. S. and R. R. Braham, J. (1991): Observational study of a convective internal boundary layer over Lake Michigan. *J. Atmos. Sci.*, **48**, pp. 2265–2279.

Coleman, G. N., Ferziger, J. H., and Spalart, P. R. (1990): A numerical study of the turbulent Ekman layer. *J. Fluid Mech.*, **213**, pp. 313–348.

Coleman, G. N., Ferziger, J. H., and Spalart, P. R. (1992): Direct simulation of the stably stratified turbulent Ekman layer. *J. Fluid Mech.*, **244**, pp. 677–712.

Covert, D. S., Charlson, R. J., and Ahlquist, N. C. (1972): A study of the relationship of chemical composition and humidity to light scattering by aerosols. *J. Appl. Meteor.*, **11**, pp. 968–976.

Deardorff, J. W. (1972): Numerical investigations of neutral and unstable planetary boundary layers. *J. Atmos. Sci.*, **29**, pp. 91–115.

Deardorff, J. W. (1974): Three-dimensional numerical study of turbulence in an entraining mixed layer. *Bound. Layer Meteor.*, **7**, pp. 199–226.

Deardorff, J. W. (1974): Three-dimensional study of the height and mean structure of a heated planetary boundary layer. *Bound. Layer Meteor.*, **7**, pp. 81–106.

Deardorff, J. W. (1980): Laboratory studies of the entrainment zone of a convectively mixed layer. *J. Atmos. Sci.*, **100**, pp. 41–64.

Elliott, W. P. (1958): The growth of the atmospheric internal boundary layer. *Trans. Amer. Geophys. Union*, **39**, pp. 1048–1054.

Eloranta, E. W. and Forrest, D. K. (1992): Volume-imaging lidar observations of the convective structure surrounding the flight path of a flux-measuring aircraft. *J. Geophys. Res*, **97**, pp. 18383–18393.

Eloranta, E. W., King, J. M., and Weinman, J. A. (1975): The determination of wind speeds in the boundary layer by monostatic lidar. *J. Appl. Meteor.*, **14**, pp. 1485–1489.

Fedorovich, E., Nieuwstadt, F. T. M., and Kaiser, R. (2001): Numerical and laboratory study of a horizontally evolving convective boundary layer. Part I: transition regimes and development of the mixed layer. *J. Atmos. Sci.*, **58**, pp. 70–86.

Ferrare, R. A., Eloranta, E. W., and Coulter, R. (1991): Lidar observations of banded convection during BLX83. *J. Appl. Meteor.*, **30**, pp. 312–326.

Fitzgerald, J. W., Hoppel, W. A., and Vietti, M. A. (1982): The size and scattering coefficient of urban aerosol particles at Washington DC as a function of relative humidity. *J. Atmos. Sci.*, **39**, pp. 1838–1852.

Gander, W., Golub, G. H., and Strebel, R. Fitting of circles and ellipses least squares solution. Technical Report 217, ETH Zurich, Departement Informatik, Institut fur Wissenschaftliches Rechnen, CH-8092 Zurich, 1994.

Garratt, J. R. (1990): The internal boundary layer – a review. *Bound. Layer Meteor.*, **50**, pp. 171–203.

Glendening, J. W. (1995): Horizontally integrated atmospheric heat flux from an Arctic lead. *J. Geophys. Res*, **100**, pp. 4613–4620.

Glendening, J. W. (1996): Lineal eddy features under strong shear conditions. *J. Atmos. Sci.*, **53**, pp. 3430–3449.

Glendening, J. W. (1999): Large-eddy simulation of internal boundary layers. In *AMS 13th Conference on Coastal Prediction*, Boston. pp. 13–16.

Glendening, J. W. and Burk, S. D. (1992): Turbulent transport from an arctic lead: a large-eddy simulation. *Bound. Layer Meteor.*, **59**, pp. 315–339.

Gossard, E. E. and Strauch, R. G. (1983): *Radar observations of clear air and clouds.* Elsevier, New York.

Grant, W. B. (1991): Differential absorption and Raman lidar for water vapor profile measurements: a review. *Opt. Eng.*, **30**, pp. 40–48.

Grund, C. J. and Eloranta, E. W. (1991): University of Wisconsin High Spectral Resolution Lidar. *Opt. Eng.*, **30**, pp. 6–12.

Hack, J. J. and Schubert, W. H. (1981): Lateral boundary conditions for tropical cyclone models. *Mon. Wea. Rev.*, **109**, pp. 1404–1420.

Halir, R. (2000): Robust bias-corrected least squares fitting of ellipses. In *8th International Conference in Central Eurpoe on Computer Graphics, Visualization and Interactive Digital Media*, Plzen, Czech Republic. pp. 36–43.

Halir, R. and Flusser, J. (1998): Numerically stable direct least squares fitting of ellipses. In *WSCG98. The sixth international conference in central Europe on computer graphics and visualization*, Plzen, Czech Republic. pp. 125–132.

Hauf, T. and Clark, T. L. (1989): Three-dimensional numerical experiments on convectively forced internal gravity waves. *Quart. J. R. Met. Soc.*, pp. 309–333.

Hooper, W. P. and Eloranta, E. W. (1986): Lidar measurements of wind in the planetary boundary layer: the method, accuracy and results from joint measurements with radiosonde and kytoon. *J. Clim. Appl. Meteor.*, **25**, pp. 990–1001.

Hsu, S. A. (1983): Measurements of the height of the convective surface boundary layer over an arid coast on the Red Sea. *Bound. Layer Meteor.*, **26**, pp. 391–396.

Hsu, S. A. (1983): On the growth of a thermally modified boundary layer by advection of warm air over a cooler sea. *J. Geophys. Res*, **88**, pp. 771–774.

Hsu, S. A. (1986): A note on estimating the height of the convective internal boundary layer near shore. *Bound. Layer Meteor.*, **35**, pp. 311–316.

Kelly, R. D. (1984): Horizontal roll and boundary-layer interrelationships observed over Lake Michigan. *J. Atmos. Sci.*, **41**, pp. 1816–1826.

Khanna, S. and Brasseur, J. G. (1998): Three-dimensional buoyancy- and shear-induced local structure of the atmospheric boundary layer. *J. Atmos. Sci.*, **55**, pp. 710–743.

Klemp, J. B. and Lilly, D. K. (1980): Mountain waves and momentum flux. In *Orographic effects in planetary flows*, volume GARP Publ. Ser. No. 23, ICSU/WMO, Case Postale No. 5, CH-1211 Geneva 20, Switzerland. World Meteorological Organization, pp. 116–141.

Klemp, J. B. and Wilhelmson, R. B. (1978): The simulation of three-dimensional convective storm dynamics. *J. Atmos. Sci.*, **35**, pp. 1070–1096.

Kolev, I., Parvanov, O., Kaprielov, B., Donev, E., and Ivanov, D. (1998): Lidar observations of sea-breeze and land-breeze aerosol structure on the Black Sea. *J. Appl. Meteor.*, **37**, pp. 982–995.

Konrad, T. G. (1970): The dynamics of the convective process in clear air as seen by radar. *J. Atmos. Sci.*, **27**, pp. 1138–1147.

Kristovich, D. A. R., Young, G. S., Verlinde, J., Sousounis, P. J., Mourad, P., Lenschow, D., Rauber, R. M., Ramamurthy, M. K., Jewett, B. F., Beard, K., Cutrim, E., DeMott, P. J., Eloranta, E. W., Hjelmfelt, M. R., Kreidenweis, S. M., Martin, J., Moore, J., III, H. T. O., Rogers, D. C., Scala, J., Tripoli, G., and

Young, J. (2000): The Lake-Induced Convection Experiment and the Snowband Dynamics Project. *Bull. Amer. Meteor. Soc.*, **81**, pp. 519–542.

Kropfli, R. A. and Hildebrand, P. H. (1980): Three-dimensional wind measurements in the optically clear planetary boundary layer with dual-Doppler radar. *Radio Sci.*, **15**, pp. 283–296.

Kuettner, J. P., Hildebrand, P. A., and Clark, T. A. (1987): Convection waves: observations of gravity waves over convectively active boundary layers. *Quart. J. R. Met. Soc.*, **113**, pp. 445–467.

Kunkel, K. (1978): *Measurement of upper convective boundary layer parameters by means of lidar.* PhD thesis, University of Wisconsin, Madison.

Kunkel, K. E., Eloranta, E. W., and Shipley, S. T. (1977): Lidar observations of the convective boundary layer. *J. Appl. Meteor.*, **16**, pp. 1306–1311.

Kunkel, K. E., Eloranta, E. W., and Weinman, J. (1980): Remote determination of winds, turbulence spectra and energy dissipation rates in the boundary layer from lidar measurements. *J. Atmos. Sci.*, **37**, pp. 978–985.

Lamb, R. G. (1978): A numerical simulation of dispersion from an elevated point source in the convective planetary boundary layer. *Atmos. Environment.*, **12**, pp. 1297–1304.

LeMone, M. A. (1990): Some observations of vertical velocity skewness in the convective planetary boundary layer. *J. Atmos. Sci.*, **47**, pp. 1163–1169.

Lenschow, D. H. (1973): Two examples of planetary boundary layer modification over the Great Lakes. *J. Atmos. Sci.*, **30**, pp. 568–581.

Lenschow, D. H. and Stankov, B. B. (1986): Length scales in the convective boundary layer. *J. Atmos. Sci.*, **43**, pp. 1198–1209.

Lenschow, D. H., Wyngaard, J. C., and Pennell, W. T. (1980): Mean-field and second-moment budgets in a baroclinic convective boundary layer. *J. Atmos. Sci.*, **37**, pp. 1313–1326.

Lin, C.-L. (1999): Near-grid-scale energy transfer and coherent structures in the convective planetary boundary layer. *Phys. Fluids*, **11**, pp. 3482–3494.

Lin, C.-L., McWilliams, J. C., Moeng, C.-H., and Sullivan, P. P. (1996): Coherent structures and dynamics in a neutrally stratified planetary boundary layer flow. *Phys. Fluids*, **8**, pp. 2626–2639.

Lin, C.-L., Moeng, C.-H., Sullivan, P. P., and McWilliams, J. (1997): The effect of surface roughness on flow structures in a neutrally stratified planetary boundary layer flow. *Phys. Fluids*, **9**, pp. 3235–3249.

Louis, J. F. (1979): A parametric model of vertical eddy fluxes in the atmosphere. *Bound. Layer Meteor.*, **17**, pp. 187–202.

Lund, T. S., Wu, X., and Squires, K. D. (1998): Generation of turbulent inflow data for spatially-developing boundary layer simulations. *J. Comp. Phys.*, **140**, pp. 233–258.

Lyons, W. A. and Pease, S. R. (1972): Steam devils over Lake Michigan during a January arctic outbreak. *Mon. Wea. Rev.*, **100**, pp. 235–237.

Mahrt, L. (2000): Surface heterogeneity and vertical structures of the boundary layer. *Bound. Layer Meteor.*, **96**, pp. 33–62.

Mason, P. J. (1989): Large-eddy simulation of the convective atmospheric boundary layer. *J. Atmos. Sci.*, **46**, pp. 1492–1516.

Mayor, S. D. and Eloranta, E. W. (2001): Two-dimensional vector wind-fields from Volume Imaging Lidar data. *J. Appl. Meteor., In Press.*

Mayor, S. D., Eloranta, E. W., Kuehn, R. E., and Ponsardin, P. (1998): Summary of volume imaging lidar preliminary results from the Lake-Induced Convection Experiment. In *Nineteenth International Laser Radar Conference.* NASA/CP-1998-207671/PT1, pp. 469–472.

Mayor, S. D., Eloranta, E. W., and Tripoli, G. J. (2000): Eddy resolving lidar measurements and numerical simulations of the convective internal boundary layer. In *14th Symp. on Boundary Layers and Turbulence.* AMS, pp. 271–274.

Mayor, S. D., Spalart, P. R., and Tripoli, G. J. (2001): Effective turbulent inflow conditions for large-eddy simulation of internal boundary layers. *Submitted to J. Atmos. Sci.*

Mayor, S. D., Tripoli, G. J., Eloranta, E. W., and Hoggatt, B. (1999): Comparison of microscale convection patterns seen in lidar data and large-eddy simulations. In *13th Symp. on Boundary Layers and Turbulence.* AMS, pp. 271–274.

Moeng, C.-H. (1984): A large-eddy simulation model for the study of boundary layer turbulence. *J. Atmos. Sci.*, **41**, pp. 2052–2062.

Moeng, C.-H., Cotton, W. R., Bretherton, C., Chlond, A., Khairoutdinov, M., Krueger, S., Lewellen, W. S., MacVean, M. K., Pasquier, J. R. M., Rand, H. A., Siebesma, A. P., Stevens, B., and Sykes, R. I. (1996): Simulation of a

stratocumulus-topped planetary boundary layer: intercomparison among different numerical codes. *Bull. Amer. Meteor. Soc.*, **77**, pp. 261–278.

Moeng, C.-H. and Rotunno, R. (1990): Vertical velocity skewness in the buoyancy-driven boundary layer. *J. Atmos. Sci.*, **47**, pp. 1149–1162.

Moeng, C.-H. and Sullivan, P. P. (1994): A comparison of shear and buoyancy driven planetary boundary layer flows. *J. Atmos. Sci.*, **51**, pp. 999–1022.

Moin, P. and Kim, J. (1997): Tackling turbulence with supercomputers. *Scientific American*, **275**, pp. 62–68.

Nieuwstadt, F. T. M. and Brost, R. A. (1986): Decay of convective turbulence. *J. Atmos. Sci.*, **43**, pp. 532–546.

Nieuwstadt, F. T. M., Mason, P. J., Moeng, C.-H., and Schumann, U. (1993): Large-eddy simulation of the convective boundary layer: a comparison of four computer codes. *Turbulent Shear Flows*, **8**, pp. 343–367.

Ogawa, Y. and Ohara, T. (1985): The turbulent structure of the internal boundary layer near the shore. *Bound. Layer Meteor.*, **31**, pp. 369–384.

Okland, H. and Gotaas, Y. (1995): Modelling and prediction of steam fog. *Beitr. Phys. Atmosph.*, **68**, pp. 121–131.

Orlanski, I. (1976): A simple boundary condition for unbounded hyperbolic flows. *J. Comp. Phys.*, **21**, pp. 251–269.

Passarelli, R. E. J. and Brahm, R. R. (1981): The role of the winter land breeze in formation of Great Lake snow storms. *Bull. Amer. Meteor. Soc.*, **62**, pp. 482–491.

Piironen, A. K. and Eloranta, E. W. (1995): Accuracy analysis of wind profiles calculated from volume imaging lidar data. *J. Geophys. Res*, **100**, pp. 25559–25567.

Pinto, J. O. and Curry, J. A. (1995): Atmospheric convective plumes emanating from leads 2. Microphysical and radiative processes. *J. Geophys. Res*, **100**, pp. 4333–4642.

Raynor, G. S., Sethuraman, S., and Brown, R. M. (1979): Formation and characteristics of coastal internal boundary layers during onshore flows. *Bound. Layer Meteor.*, **16**, pp. 487–514.

Redelsperger, J. L. and Sommeria, G. (1982): Methode de representation de la turbulence associe aux precipitations dans un modele tri-dimensionnel de convection nuageuses. *Bound. Layer Meteor.*, **24**, pp. 231–252.

Rothermel, J., Cutten, D. R., Hardesty, R. M., Menzies, R. T., Howell, J. N., Johnson, S. C., Tratt, D. N., Olivier, L. D., and Banta, R. M. (1998): The Multi-center Airborne Coherent Atmospheric Wind Sensor. *Bull. Amer. Meteor. Soc.*, **79**, pp. 581–599.

Sadourny, R. (1975): The dynamics of finite-difference models of the shallow-water equations. *J. Atmos. Sci.*, **32**, pp. 680–689.

Sasano, Y., Hirohara, H., Yamasaki, T., Shimizu, H., Takeuchi, N., and Kawamura, T. (1982): Horizontal wind vector determination from the displacement of aerosol distribution patterns observed by a scanning lidar. *J. Appl. Meteor.*, **21**, pp. 1516–1523.

Sassen, K. (1991): The polarization lidar technique for cloud research: a review and current assessment. *Bull. Amer. Meteor. Soc.*, **72**, pp. 1848–1866.

Saunders, P. M. (1964): Sea smoke and steam fog. *Quart. J. R. Met. Soc.*, **90**, pp. 156–165.

Schmidt, H. and Schumann, U. (1989): Coherent structures of the convective boundary layer derived from large-eddy simulations. *J. Fluid Mech.*, **200**, pp. 511–562.

Schnell, R. C. and Coauthors, . (1989): Lidar detection of leads in arctic sea ice. *Nature*, **339**, pp. 530–532.

Schoenberger, L. M. (1986): Mesoscale features of the Michigan land breeze using PAM II temperature data. *Wea. Forecasting*, **1**, pp. 127–135.

Schols, J. L. and Eloranta, E. W. (1992): The calculation of area-averaged vertical profiles of the horizontal wind velocity from volume imaging lidar data. *J. Geophys. Res*, **97**, pp. 18395–18407.

Smedman, A.-S., Bergstrom, H., and Grisogono, B. (1997): Evolution of stable internal boundary layers over a cold sea. *J. Geophys. Res*, **102**, pp. 1091–1099.

Smythe, G. R. and Zrnic, D. S. (1983): Correlation analysis of Doppler radar data and retrieval of the horizontal wind. *J. Clim. Appl. Meteor.*, **22**, pp. 297–311.

Sommeria, G. (1976): Three-dimensional simulation of turbulent processes in an undisturbed trade wind boundary layer. *J. Atmos. Sci.*, **33**, pp. 216–241.

Spalart, P. R. (1988): Direct simulation of a turbulent boundary layer up to $R_\theta = 1140$. *J. Fluid Mech.*, **187**, pp. 61–98.

Sroga, J. T., Eloranta, E. W., and Barber, T. (1980): Lidar measurements of wind velocity profiles in the boundary layer. *J. Appl. Meteor.*, **19**, pp. 598–605.

Straka, J. M., Wilhelmson, R. B., Wicker, L. J., Anderson, J. R., and Droegemeier, K. K. (1993): Numerical solutions of a non-linear density current: a benchmark solution and comparisons. *Inter. J. Num. Meth. Fluids*, **17**, pp. 1–22.

Stull, R. B. (1988): *An Introduction to Boundary Layer Meteorology*. Kluwer, Boston.

Stunder, M. and Sethuraman, S. (1985): A comparative evaluation of the coastal internal boundary-layer height equations. *Bound. Layer Meteor.*, **32**, pp. 177–204.

Tennekes, H. and Lumley, J. L. (1972): *A First Course in Turbulence*. The MIT Press, Cambridge, Massachusetts.

Tripoli, G. J. (1992): A nonhydrostatic mesoscale model designed to simulate scale interaction. *Mon. Wea. Rev.*, **120**, pp. 1342–1359.

Tripoli, G. J. and Cotton, W. R. (1981): The use of ice-liquid water potential temperature as a thermodynamic variable in deep atmospheric models. *Mon. Wea. Rev.*, **109**, pp. 1094–1102.

Tripoli, G. J. and Mayor, S. D. (2000): Numerical simulation of the neutral boundary layer: a comparison of enstrophy conserving with momentum conserving finite difference schemes. In *AMS 14th Symposium on Boundary Layers and Turbulence*, Boston. pp. 376–379.

Tuttle, J. D. and Foote, G. B. (1990): Determination of the boundary layer airflow from a single Doppler radar. *J. Atmos. Ocean. Technol.*, **7**, pp. 218–232.

Venkatram, A. (1977): A model of internal boundary layer development. *Bound. Layer Meteor.*, **11**, pp. 419–437.

Weckwerth, T. M., Wilson, J. W., Wakimoto, R. M., and Crook, N. A. (1997): Horizontal convective rolls: determining the environmental conditions supporting their existence and characteristics. *Mon. Wea. Rev.*, **125**, pp. 505–526.

Werner, C. and Coauthors (2001): Wind infrared Doppler lidar instrument. *Optical Engineering*, **40**, pp. 115–125.

Willis, G. E. and Deardorff, J. W. (1979): Laboratory observations of turbulent penetrative-convection planforms. *J. Geophys. Res*, **84**, pp. 295–302.

Wulfmeyer, V. and Bosenberg, J. (1998): Ground-based differential absorption lidar for water-vapor profiling: assessment of accuracy, resolution and meteorological applications. *Appl. Optics*, **37**, pp. 3825–3844.

Wulfmeyer, V. and Feingold, G. (2000): On the relationship between relative humidity and particle backscattering coefficient in the marine boundary layer determined with a differential absorption lidar. *J. Geophys. Res*, **105**, pp. 4729–4741.

Wyngaard, J. C. and Brost, R. A. (1984): Top-down and bottom-up diffusion of a scalar in the convective boundary layer. *J. Atmos. Sci.*, **41**, pp. 102–112.

Xu, Q. and Qiu, C.-J. (1995): Adjoint-method retrievals of low-altitude wind fields from single-Doppler reflectivity and radial wind data. *J. Atmos. Ocean. Technol.*, **12**, pp. 1111–1119.

Young, G. S., Cameron, B. K., and Hebble, E. E. (2000): Observations of the entrainment zone in a rapidly entraining boundary layer. *J. Atmos. Sci.*, **57**, pp. 3145–3160.